Micromechanical Study of Rock Fracture and Fragmentation under Dynamic Loads using Discrete Element Method

THÈSE N^{O} 5008 (2011)

PRÉSENTÉE LE 8 AVRIL 2011
À LA FACULTÉ ENVIRONNEMENT NATUREL, ARCHITECTURAL ET CONSTRUIT
LABORATOIRE DE MÉCANIQUE DES ROCHES
PROGRAMME DOCTORAL EN MÉCANIQUE

ÉCOLE POLYTECHNIQUE FÉDÉRALE DE LAUSANNE

POUR L'OBTENTION DU GRADE DE DOCTEUR ÈS SCIENCES

PAR

Tohid KAZERANI

acceptée sur proposition du jury:

Prof. I. Botsis, président du jury
Prof. J. Zhao, directeur de thèse
Prof. L. Jing, rapporteur
Prof. J.-F. Molinari, rapporteur
Dr J. A. S. Vieira de Lemos, rapporteur

ÉCOLE POLYTECHNIQUE
FÉDÉRALE DE LAUSANNE

Suisse
2011

To the Iranians

the people, who are standing up and withstanding

Contents

Acknowledgements

I would first and foremost like to thank my thesis advisors *Jian Zhao*, without whose constant support and encouragement none of this would be achieved. I am also ever so grateful to my previous mentor, *Vahid Lotfi* who has immensely contributed to my research career over my graduate years.

I am in appreciation of *Carlos Carranza–Torres*, *Gao–Feng Zhao*, *Rafael Rojas Fuentes*, *Jean–François Mathier*, *Jean–Paul Dudt*, *Rosa Ana Turielle*, and everyone in the laboratory whom I have encountered in my four years working with the LMR. I would also like to thank my knowledgeable thesis jury for accepting the invitation, and agreeing to share this last part of my graduate student experience.

Although naming my friends here will inevitably cause some else to be neglected, I need to mention those fellows who have kindly shared their life, time and advices with me. I am deeply grateful to *Azad*, *Navid*, *Jennifer*, and *Pooneh*, without whose support I never was able to benefit new features of life and professional career over the years of my degree.

I need to mention *Vessal*, my younger brother, whose ideas have ever made me inspired and hopeful. I am in appreciation of his endless encouragements.

Lastly, I offer my regards and blessings to *Nahid* and *Hassan*, my parents who always set an amazing example for me growing up and pushed me towards a successful academic path. They are really the inspiration for my life. They did not have a fancy education but it never stopped them from supporting and encouraging me to achieve more. Their tireless example of hard work in the face of many challenges provided me with the ideals and values that are so needed to persevere.

Abstract

The study presented in this thesis aims to numerically explore the micro–mechanisms underlying rock fracture and fragmentation under dynamic loading. The approach adopted is based on the Discrete Element Method (DEM) coupled to the Cohesive Process Zone (CPZ) theory. It assumes rock material as assemblage of irregular–sized deformable fragments joining together at their cohesive boundaries. The simulation, which is referred to as Cohesive Fragment Model (CFM), takes advantage of DEM particle/contact logic to handle the fragments and boundaries in between. In this idealization, mechanical properties of particle and more dominantly those of contact control macroscopic response of the particle assemblage. A rate–dependent orthotropic cohesive law is developed for DEM contacts to capture rock material specific features, e.g. brittleness, anisotropy and rate–dependency. Rock experimental behavior is then modeled in order to assess individually the sensitivity of results to grain size, confining pressure, micromechanical parameters, stored strain energy, loading rate etc.

The thesis is organized to approach the problem systematically. First, CFM application for static analysis is examined. It is shown that CFM quantitatively and qualitatively predicts compressive and tensile failure of hard and soft rocks as well as shear strength, dilatancy and degradation of rough rock joints. CFM micro–parameters, i.e., stiffness of particle and strength, stiffness, and friction of contact are calibrated using a combination of statistical disciplines and original closed–form expressions. The calibration process provides useful physical interpretation for each micro–parameter in terms of standard rock mechanical properties. These interpretations enable to understand how macroscopic behavior of rock material originates from its mineral microstructure.

Energy needed to fully open a contact, the contact energy numerically represents material fracture energy in CFM. Experimental investigations suggest that fracture energy is independent of loading rate in quasi–static circumstances. Thus, contact energy is simply assumed as constant in static analysis. However, simulation on fast fracturing by CFM warns that this assumption causes serious deviations in fracture dynamic analysis.

Laboratory observations reveal that fast-moving fracture consumes more energy than slow-moving one does. This inspires to consider contact energy as variable and rate-dependent to provide the model with the appropriate prediction of the fracture energy release process. Applying this new approach, fracture behavior of PMMA plates is investigated under different levels of stored strain energy.

As the final stage, dynamic fracture toughness of rock samples, measured by the split-Hopkinson pressure bar test, is simulated and promising results are obtained. They demonstrate how numerical modeling can practically aid experimental methods in terms of measurement verification, error estimation, and performing appropriate corrections.

The studies suggest that DEM is an effective and convenient tool to investigate fracture and fragmentation problems. While predictions by continuum models are restricted only to crack initiation, simulation by DEM made it possible to track both the initiation and progression of fracture over time by following consecutive damage of contacts. Moreover, the research specifically demonstrates that the proposed contact model properly predicts the experimental behavior of rock fracture under static and dynamic loading. This result verifies the model validity and adequacy for rock fracture analysis.

Key words: discrete element method, cohesive fragment model, micro-parameter, rate-dependency, rock dynamics, fracture, fragmentation

Résumé

L'étude présentée dans cette thèse vise à explorer les micro-mécanismes de la rupture et la fragmentation des matériaux rocheux soumis aux charges dynamiques. L'approche numérique utilisée est basée sur le couplage de la méthode des éléments discrets (DEM) et la théorie de la zone cohésive. Le matériau rocheux est supposé être un assemblage de fragments irréguliers déformables reliés par leurs bords cohésifs. La méthode, qui est appelée le modèle des fragments cohésifs (CFM), tient compte de la logique particule/contact de la méthode DEM pour traiter les fragments et l'interaction entre eux. Dans cette idéalisation, la réponse macroscopique de l'assemblage est contrôlée par les paramètres mécaniques associés aux particules et, de façon plus importante, à ceux des contacts. Une loi cohésive orthotropique dépendant du taux de chargement est développée pour les contacts afin de saisir les caractéristiques du matériau rocheux, i.e. fragilité, anisotropie et dépendance au taux de chargement. Le comportement expérimental du matériau est ensuite modélisé afin d'évaluer la sensibilité des réponses à la taille des grains, la pression de confinement, les paramètres micromécaniques, l'énergie stockée par la déformation, taux de chargement, etc.

Cette thèse est organisée de façon à aborder le problème systématiquement. Tout d'abord, l'application statique du CFM est examinée. Il est montré que le CFM peut prédire quantitativement et qualitativement la rupture en compression et en traction de roches dures et tendres, ainsi que la résistance au cisaillement, la dilatance et la dégradation des joints rocheux rugueux. Les micro-paramètres du CFM, i.e., la rigidité des particules et leur résistance, la rigidité et le frottement des points de contact, sont étalonnés par des méthodes statistiques et analytiques originales. Le processus d'étalonnage fournit une interprétation utile pour chaque micro-paramètre en fonction des paramètres mécaniques standards du matériau rocheux. Ces interprétations permettent de comprendre comment le comportement macroscopique du matériau dépend de sa microstructure minérale.

L'énergie de contact, i.e., l'énergie nécessaire pour ouvrir entièrement un contact, représente numériquement l'énergie de rupture en CFM. Les études expérimentales suggèrent que l'énergie de rupture est indépendante des taux de chargement en conditions quasi-statiques. Par conséquent, l'énergie de contact peut simplement être supposée constante dans les analyses statiques. Cependant, les simulations des fissures rapides par le CFM montrent que cette hypothèse crée des déviations importantes dans l'analyse dynamique de la rupture.

Les observations expérimentales révèlent qu'une fissure qui se propage rapidement consomme plus d'énergie que celle qui se propage lentement. Cela incite à considérer l'énergie de contact comme une variable dépendant des taux d'ouverture du contact pour doter le modèle de prédictions appropriées du processus de libération d'énergie de fracturation. Avec l'application de cette nouvelle approche, le comportement de la rupture des plaques du PMMA est étudié selon différents niveaux de l'énergie stockée par déformation.

Au final, la ténacité dynamique des échantillons rocheux, mesurée à l'aide d'un essai de pression à la barre de Hopkinson, est simulée et les résultats obtenus sont satisfaisants. Ils démontrent comment la modélisation numérique peut aider pratiquement les méthodes expérimentales en termes de vérification de mesures, d'estimation d'erreurs, et comment effectuer les corrections adéquates.

Ces études suggèrent que le DEM est un outil efficace et pratique pour étudier les problèmes de rupture et de fragmentation. Lorsque les prédictions par des modèles continus sont limitées seulement à l'initiation des fissures, les simulations par la DEM rendent possible de retracer à la fois l'initiation et aussi la progression des fractures au cours du temps en suivant les endommagements des contacts. De plus, cette recherche montre spécifiquement que le modèle de contact proposé, prédit convenablement le comportement expérimental des fractures rocheuses soumises aux chargements statiques et dynamiques. Ce résultat vérifie la validité du modèle et l'adéquation pour l'analyse des fractures rocheuses.

Mots-clés : méthode des éléments discrets, modèle des fragments cohésifs, micro-paramètre, dépendance au taux de déformation, dynamique des roches, fissure, fragmentation

CHAPTER 1

Introduction

Rock dynamics, as a branch of rock mechanics deals with dynamic load, deformation and failure of rock in relation with time. It covers a wide scope ranging from the formation and transmission of dynamic loads in stress waveforms, fracturing and damage of rock materials and rock masses under dynamic loading, to support of engineering structures in and on rock under dynamic conditions (Zhou and Zhao 2011). However, complex and heterogeneous nature of rock substance makes its dynamic response much more complicated than any artificial or manufactured material, such that it could not be studied through only conventional experimental and numerical methods.

As a critical aspect of rock dynamics, rock fracture and fragmentation is of significant influence on the stability and integrity of rock material. Understanding the micro-mechanics behind fracture and fragmentation is very important for a vast verity of applications involved in rock dynamics. Applications range from the characterization of natural fractures influencing rock mass strength to the examination of rock–cutter interaction to assess the performance of Tunnel Boring Machines.

As the most prevalent fracture parameter, fracture toughness is utilized to express the resistance of material against fracturing. It helps asses the probability of fracture initiation and characterize how fracture propagates through material. Many numerical and experimental studies have been carried out on static fracture over the years. These studies have extensively examined fracture response under static loads and measured fracture toughness for different types of material. They revealed that fracture initiation toughness in majority of brittle materials including rock does not markedly change during static propagation. Hence, static fracturing is considered as a *rate–independent* phenomenon as its response is independent of fracture propagation velocity and loading rate.

The characteristics of material fracturing under dynamic circumstances are not actively explored yet. Experimental studies arranged over last decade have mostly focused on ceramics, polymers and metal alloys to examine fracture toughness, propagation velocity and bifurcation patterns. The Split–Hopkinson Pressure Bar (SHPB) technique, originally developed by Kolsky (1949, 1963), has been extensively used by many investigators to obtain dynamic compressive properties of materials. This technique has mostly been used to study the plastic flow stress of metals that undergo large strains at high strain rates. The experimental observations have revealed that materials exhibit various fracturing behaviors depending on fracture propagation speed and dynamic loading rate applied. Hence, fracture response is then referred to as *rate–dependent*.

Limited number of the experimental studies has been performed on rock. Using the SHPB technique, rock specimens have been tested to measure rock dynamic fracture toughness and strength under high–rate loading. The experiments have confirmed that rock material, like alloys and polymers, follows a rate–dependent fracture behavior where its compressive and tensile strength as well as fracture toughness varies with the loading rate applied. Nevertheless, all the laboratory attempts on rock fracture are limited to macroscopic measurements. The micromechanics behind the observed rate–dependent quality has not been fully explored yet. In other words, it is not clearly understood yet how rock micro–structure plays role in material rate–dependent behavior. This subject requires more investigation which is aimed by this thesis.

1.1. Research objectives

Mechanical behavior of rock, as a heterogeneous and grained composite material, is deeply affected by its microstructure, which is constituted by minerals (grains) and mineral cement (if any). Rock minerals are of different molecular structure and size. Igneous rocks are made of minerals with the average size of 1 to 5 *mm*, while metamorphic and sedimentary rocks are of less coarse texture. Grain size is generally reported between 0.5 to 3 *mm* for metamorphic and less than 2 *mm* for sedimentary rock (e.g. Deer et al. 1992). In addition to mineral properties, the cement pasting sediment grains together configures the microstructure of sedimentary rocks.

As experimentally observed (e.g. Whittles 2006), rock fractures though the weakest mineral, grains interface, or mineral cement. Therefore, rock fracture and fragmentation behavior expectedly can be interpreted in terms of mineral and cement properties.

To understand the micro–mechanisms underlying rock fracture and fragmentation, this research specifically explores how rock micro–structure controls

- rock strength and failure in compression, tension, and shear,
- rock fracture behavior and dynamic fracture toughness,
- and fracture rate–dependent behavior observed in macroscopic scale.

Replying these questions will hopefully broaden our scope to encompass rock fracture and fragmentation mechanisms. This will help us handle the engineering applications involved in rock dynamics more accurately.

1.2. Methodology

We have chosen numerical simulation as the research tool. First, a numerical model needs to be developed, and then it must be verified by simulating certain laboratory tests and comparing the numerical predictions to the test measurements. To cover all the expected objectives, verification simulations should comprise static experiments on rocks and rock joints as well as dynamic tests on homogeneous and heterogeneous materials.

Up to the present, numerical developments related to rock dynamic fracture propagation are not extensive. Most of the attempts have been performed by adopting *continuum models*, which are not basically able to simulate fracture explicitly. To overcome this issue, *discontinuum models* were introduced. With regard to fracture and fragmentation purposes, the advantages of discontinuum to continuum models can be briefly counted as follows.

- Discontinuum models are not engaged with flow rule and potential function, which continuum models need to perform nonlinear analysis.
- Discontinuum models are capable of representing large crack separation as well as reattachment of fragmented parts at new contact points whilst continuum models are not.
- While predictions by continuum models are restricted to implicit representation of fracture, the use of discontinuum models make it possible to demonstrate fracture initiation and propagation over time explicitly by tracking consecutive separation of structural elements.

According to the heterogeneous and grained texture of rock material, discontinuum models reproduce its structure as aggregate of particles connecting together by structural bonds. Very predominantly, particles are taken as rigid random–sized discs or spheres depending on the two– or three–dimensional state of modeling. Therefore, contact between the particles inevitably occurs at points where two particles touch each other. However, the material constituting rock can be more realistically described as an assemblage of deformable and sharp–cornered fragments where contacts are not necessarily punctual and frictional contact planes can exist. This idealization is more analogous to rock texture and reproduces its fragmentation pattern more accurately.

Referred to as Cohesive Fragment Model (CFM), the numerical approach adopted in this research is based on the Discrete Element Method (DEM) coupled to the Cohesive Process Zone (CPZ) theory. It assumes rock material as collection of deformable irregular–sized triangular fragments joining together at their boundaries, which are acting as cohesive frictional surfaces.

To implement CFM, we have selected the Universal Distinct Element Code (UDEC) (Itasca 2009) due to its helpful capabilities and relative ease of development. CFM takes advantage of UDEC particle/contact logic to handle the fragments and boundaries in between. Using two–dimensional Delaunay triangulation (Delaunay 1934), a pre–processor program has been separately developed to generate arbitrarily sized triangular particles. They are then discretized into CST elements (i.e. constant–strain triangles) to produce deformable fragments.

In this study, an orthotropic rate–dependent cohesive law has been developed for UDEC contacts to capture the specific properties of rock material, e.g., brittleness, anisotropy and rate–dependency. Contact orthotropy is provided by assuming contact to follow different tensile and shear behaviors in terms of strength, stiffness and ultimate displacement.

UDEC can be developed by user. Any development for particle or contact constitutive model as well as definition of new material properties can be carried out by creating Dynamic Link Libraries (DLL) in Visual C++ environment. The created DLL files are then attached to the UDEC conventional software, and enable it to perform requested tasks.

1.3. Thesis outline

The thesis has been organized to approach the problem systematically. Its structure has been tried to follow a continuous flow to ultimately reach the designed objectives. For this purpose, we first focus on the model description, and then its applications are examined. The model is also employed to explore the micro–mechanism of rock fracture, fragmentation and failure.

1.3.1. *Model description and implementation*

This part includes half of the thesis through four chapters. In Chapter 2, we start with explaining fundamentals of rock fracture mechanics and the cohesive presses zone theory. Then, different features of rock failure surveyed in different observation scales are phenomenologically compared. According to rock natural texture and its failure fashion in micro–scale, the numerical idealization based on which CFM has been built is ultimately described.

In Chapter 3, existing literature regarding the thesis subject is vastly reviewed in terms of numerical and experimental studies. Comparing all the possible numerical methods and considering their capabilities and disadvantages, DEM is finally presented as the most efficient tool for our purpose.

Chapter 4 focuses on CFM implementation in UDEC. It begins with a brief description of UDEC and explains its fundamentals specifically the concept of particle and contact.

Following this, some critical maters related to the solution stability are reviewed. This Chapter also explains the adopted particle generation algorithm, and includes a statistical study on the size distribution of particles generated. As mentioned earlier, the designed pre–processor program makes use of Delaunay triangulation to produce particle assemblage.

In Chapter 5, we explain the orthotropic cohesive contact model developed. This chapter describes the concept of micro–parameter and establishes some original closed–form equations expressing micro–parameters in terms of material macroscopic properties. There is illustrated the algorithm used to create DLL files and to implement the contact model into UDEC.

1.3.2. *Model applications*

This section comprises the last four chapters. In Chapter 6, we examine the CFM applicability for rock static analysis. First, CFM capability for reproduction of fracture mechanics behavior is examined. Then, standard laboratory tests of rock is modeled to asses the sensitivity of results to the model micro–parameters and confining pressure. Using the obtained results, an established calibration process is proposed, which leads to a unique set of the micro–parameters.

Chapter 7 particularly focuses on rock joint shear behavior, where CFM is used to examine strength, dilatancy, and asperity degradation in plaster–made rock joints. Obtained numerical results are compared qualitatively and quantitatively to laboratory data, and similarities are discrepancies will be discussed in detail.

In Chapter 8, we explore the CFM application for dynamic problems in homogeneous material. For this purpose, dynamic fracture tests on PMMA plates (Shioya and Zhou 1995) are modeled. The simulations reveal that the fracture behavior of PMMA samples is not satisfactorily predicted, unless rate effects are appropriately introduced into the contact constitutive model.

Ultimately, Chapter 9 shows the CFM capabilities for investigating rock fracture features observed in the split–Hopkinson pressure bar test. As a representative case, we have chosen the semi–circular bend test method proposed by Chen et al. (2009). Simulation of the test demonstrates how the test measurements are controlled by the rock micromechanics and specimen boundary condition.

CHAPTER 2

Fracture process zone theory and description of Cohesive Fragment Model (CFM)

This chapter briefly introduces the theory of rock fracture mechanics and presents some key developments. The reader is introduced to the terminology regarding fracture in rocks as well as mechanical background of fracturing in terms of stress intensity factor, and the theory of fracture process zone.

Empirically investigating rock failure patterns, a numerical idealization for rock material, based on its microstructure and the process zone theory, is eventually proposed, which is expected to reproduce and explain the failure process.

2.1. Discontinuities in rock

In the literature, terms regarding the description of discontinuities and in particular fractures are frequently used in not clearly specified meanings. This might be due to different nomenclatures in different disciplines. The terms used in this thesis are explained in this section.

A *crack* is any separation in rock body that has one or two dimensions much smaller than the third. The width to length ratio, termed crack aspect ratio, is typically between 10^{-3} to 10^{-5} (Simmons and Richter 1976). Cracks can be divided into three scale classes, i.e., micro, meso and macro. *Micro–cracks* are planar discontinuities with their longest dimension in the order of one to few grain diameters. This might be about one to one thousand microns. Based on their occurrence within the rock, they can be divided into *grain boundary* cracks (located at the interface between grains), *intra–granular* cracks (cracks restricted within one grain), and *inter–granular* cracks (cracks cutting more than one grain) (Engelder 1987). A *meso–crack* is a discontinuity spanning a larger number of grains than a micro–crack, formed by a complicated rupture event and eventually connecting several micro–cracks. The extension is one to few millimeters.

The *macro–crack* spans several millimeters to decimeters. Meso– and macro–cracks are referred to as *fracture*.

As seen in Figure 2–1, a fracture system consists of the through–going main separation and the surrounding *Fracture Process Zone* (*FPZ*) (e.g. Hoagland et al. 1973; Atkinson 1987). This process zone includes micro–cracks and meso–cracks. Prior to the main fracture growth, extensive micro–/meso–cracking occurs. Meso– or macro–cracks propagating off the fracture are called *branching cracks*.

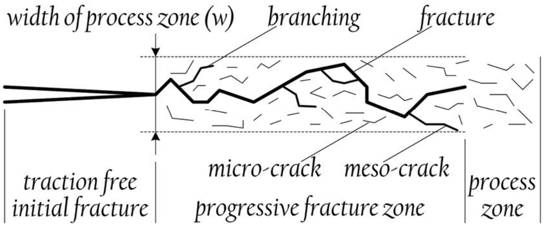

Figure 2–1: Nomenclature of a fracture system (modified after Liu et al. 2000)

The width of the fracture process zone depends on grain size and loading nature (e.g. Hoagland et al. 1973; Labuz et al. 1985; Zang et al. 2000; Zhou et al. 2005). The size of the FPZ is typically about five to ten times the average grain size (e.g. Hoagland et al. 1973; Zang et al. 2000). However, greater values up to 40 grain–diameters have been reported (Whittaker et al. 1992). Broberg (1999) defines the process zone as the area in the state of decohesion, in front of the fracture tip and the wake of it, where micro–cracks coalesce to form the through–going main separation. Non–elastic deformation within the FPZ is caused by stress concentrations at the fracture tip.

Figure 2–2 schematically presents the progression of fracturing, where sequence A–D shows micro–, meso–, and macro–crack development with increasing load. Evolution of the load and number of micro–cracks is given in the below bars.

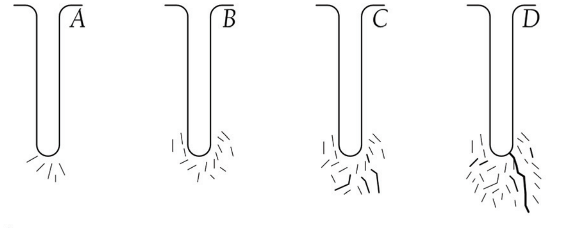

Figure 2–2: Development of fracture and fracture process zone under tensile load perpendicular to starter notch (modified after Hoagland et al. 1973)

In tectonics and structural geology, the genesis of fractures and fracture networks is indicated by the terms *joint* and *fault*. A joint is a discontinuity that shows a displacement normal to its surface or trace and no displacement parallel to its surfaces. Joints are in parallel sets, and often formed during cooling or tectonic movements. A fault has been generated by a shear deformation, therefore showing displacement parallel to the surfaces (Pollard and Aydin 1988). In general, these types of discontinuities are much larger than fractures. Figure 2–3 shows the length classification from micro–crack to fault. In laboratory work, fracture and joint are often interested. This study specifically focuses on rock fracture and joint.

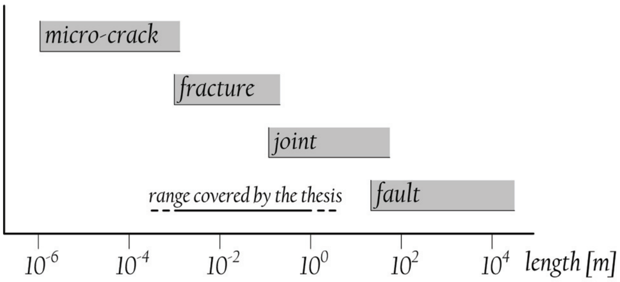

Figure 2–3: Length range of different types of discontinuities in rock

2.2. Theory of fracture mechanics

2.2.1. *Modes of fracturing*

In fracture mechanics, cracks or fractures are usually subdivided into three basic types, namely *Mode–I*, *Mode–II* and *Mode–III*, from a mostly mathematical viewpoint (Irwin 1958). The division, which is based on the crack surface displacement or crack tip loading, is generally indicated as either *mode of crack propagation*, *mode of fracturing* or *mode of loading*. Relating the modes of fracturing to the modes of loading (with the assumption that the fracture propagates within its own plane) is appropriate for most metals (Rao et al. 2003). In rocks, a specific *mode of loading*, however, is not necessarily leading to the same *mode of fracturing*. Note that the reference of mode regarding the applied loading and fracture propagation is often mixed up in the literature. For the sake of clarity, an apparent distinction between *mode of loading* (for applied boundary stresses) and *mode of fracturing* or *failure* (for mechanical breakdown process defined by relative displacement) is respected by the thesis.

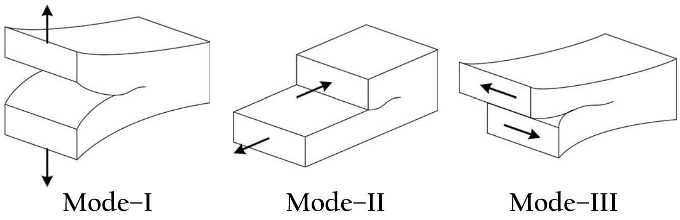

Figure 2–4: Basic modes of fracturing

In terms of crack surface displacement, i.e., mode of fracturing, the modes can be classified as depicted in Figure 2–4. In Mode–I, also called tensile mode, the crack tip is subjected to a displacement perpendicular to the crack plane. Propagation of the crack is in its plane direction, where it carries no shear traction and no record of shear displacement is visible. In Mode–II, the crack faces move relatively to each other in the crack plane, and the crack propagates perpendicular to the crack front. Shear traction parallels the plane of the crack. In the third mode of fracturing, Mode–III, shear displacement is acting parallel to the front in the crack plane.

Any combination of the three basic modes is referred to as *mixed mode*. The principle of superposition is applicable to describe the most general case of crack tip deformation (Atkinson 1987).

2.2.2. *Stress distribution within fractured area*

Inglis (1913) showed mathematically that the local stress concentrated at a sharp tip is several times larger than the applied stress. Therefore, any microscopic flaws or even inhomogeneities, within rock body, can be considered as a potential plane of weakness. This stress concentration concept yields

$$\frac{\sigma_n}{\sigma_f} = \frac{1}{\rho} \tag{2–1}$$

where σ_n is the stress at the crack tip, σ_f is the applied stress and ρ is the curvature of the crack tip. The ratio in Equation 2–1 is an elastic stress concentration factor and it depends on the shape (curvature) of the crack or corner.

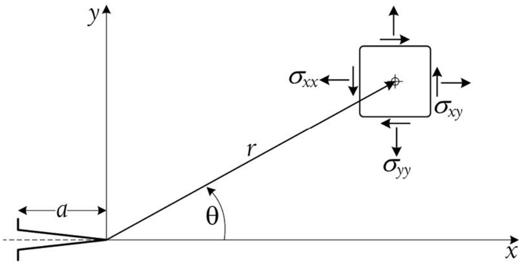

Figure 2–5: Notations for stress tensor around an edge notch

Stresses and displacements at the tip of an existing crack with a sharp tip, i.e., $\rho \approx 0$, can be calculated using Westergaard's and Sneddon's stress functions (Westergaard 1939; Sneddon 1945). Derivation and formulation of the stress and displacement functions can be found in Lawn (1993). The stress formulations can be reduced to the simple form

$$\sigma_{ij} = \frac{K_k}{\sqrt{2\pi r}} f_{ij}(\theta) \tag{2–2}$$

where σ_{ij} is the stress tensor in the Cartesian coordinates, and i and j represent the Cartesian coordinate axes. f_{ij} is a geometric stress factor depending solely on the angle θ (see Figure 2–5). K_k is a multiplier depending on the boundary conditions, i.e., applied loading and geometry, where the subscript k refers to the corresponding mode. In the theory of fracture mechanics, K_k is referred to as *stress intensity factor* that gives the grade of stress concentration at the tip of a notch of length *a* and at a given loading. It has the dimension of stress times square root of length, e.g. *Pa√m* in the SI units. When $\theta = 0$,

$$K_k = \sigma_f \sqrt{\pi a} = \sigma_{ij} \sqrt{2\pi r} \qquad (2\text{–}3)$$

One must be aware that the concept developed is for the case of a fracture propagating in its own plane due to the corresponding modes of loading. Any deflection from this plane will result in mixed mode conditions.

2.2.3. *Griffith' theory and energy release rate*

Most materials fail when stressed beyond some critical level. From this point of view, crack initiation will occur, when the stress intensity factor reaches a critical value called *fracture toughness*, K_{kC}. To clarify the essence of this phenomenon, Griffith tried to examine it from an energy viewpoint. For this purpose, he formulated a criterion for extension of an isolated crack within elastic solids. Introducing the fundamental energy theorems of classical mechanics and thermodynamics, He modeled the crack as a reversible thermodynamic system. The energy–balance concept by Griffith is given by the following equilibrium requirement,

$$\frac{d\Psi}{dr} = 0 \qquad (2\text{–}4)$$

where $d\Psi$ is the change in the system energy and *dr* is the crack extension. If equilibrium is not maintained, a crack would extend or retract reversibly, according to whether the left hand side of Equation 2–4 is negative or positive. The failure load, σ_u is therefore defined by the Griffith's strength relation as follows.

$$\sigma_u = \sqrt{\frac{2E'\gamma}{\pi a}} \qquad (2\text{–}5)$$

$E' = E$ for plane–stress and $E/(1-\nu^2)$ for plane–strain, where *E* is the Young's modulus, ν the Poisson's ratio, and γ the crack surface energy.

As long as applied boundary stress, σ_f, is lower than σ_u, the crack remains stationary. As σ_u is exceeded, it propagates spontaneously. The logical extension of this idea, expounded by Griffith, yields the concept of *energy release rate*, *G*, which indicates that crack extension occurs as *G* exceeds the *critical energy release rate*, G_f.

Rearranging the Griffith's strength relation leads to

$$G_f = 2\gamma = \frac{\pi a \sigma_u^2}{E'} \qquad (2\text{–}6)$$

Irwin (1958) could show the equivalence of the energy release rate and stress intensity factor, i.e., $K_k = K_{kC} \leftrightarrow G = G_f$. The fracture toughness and the critical energy release rate should be therefore related together. For example, if $\sigma_f = \sigma_u$ in Mode–I, Equation 2–3 suggests

$$K_{IC} = \sigma_u \sqrt{\pi a} \tag{2–7}$$

Combining Equation 2–6 and 7,

$$G_f = \frac{K_{IC}^2}{E'} \tag{2–8}$$

As the principle of superposition applied to the relationship, it yields

$$G_f = \frac{K_{IC}^2}{E'} + \frac{K_{IIC}^2}{E'} + \frac{K_{IIIC}^2}{E'}(1+\nu) \tag{2–9}$$

2.3. Concept of cohesive process zone

2.3.1. *Fracturing process*

The process of fracturing in rock and rock like materials has been frequently studied. This was done under different loading condition and for different materials, and by means of different observation scales and techniques, e.g. interpretation of mechanical data, microscopy at different scales and detection and interpretation of acoustic emission events. The reader is referred to textbooks and reviews such as Pollard and Aydin (1988), Atkinson (1991), and Dresen and Guéguen (2004).

When subjecting a plate with an isolated fracture to an increasing tensional stress perpendicular to the fracture, it will generally fail by rapid Mode–I fracture propagation. The fracture accelerates approaching speeds whose maximum is governed by the speed of elastic waves.

Experimental work on inclined single or multiple prefabricated fractures (notches) subjected to compressive loads was carried out by, e.g. Brace and Bombolakis (1963), Hoek and Bieniawski (1984) and Sammis and Ashby (1986) in glass, e.g. Erdogan and Sih (1963), Horii and Nemat–Nasser (1985), Ashby and Hallam (1986), and Petit and Barquins (1988) in PMMA, e.g. Shen et al. (1995), Bobet and Einstein (1998), Park et el. (2001), Tang et al. (2001), Wong et al. (2001), and Sagong and Bobet (2002) in model materials, and, e.g. Petit and Barquins (1988) in rock samples.

As recognized in the meso and macroscopic observation of rocks, both tensile and shear stress concentrations develop at preexisting inclined inhomogeneities under boundary compressive loading. As the compression applied to the sample increases further, tensile cracks will be initiated at the tips of the preexisting fractures. These are called *wing cracks* and grow progressively in the direction of the remote major principal stress and finally stop (e.g. Brace and Bombolakis 1963; Kemeny and Cook 1987, Petit and Barquins 1988). At the early stages of propagation, the growth of the stable wing crack is dominated by the stress field of the original fracture. As it extends, it starts interacting with neighboring micro–cracks, where this interaction might lead to coalescence and eventually ultimate failure.

Depending on geometry and pattern of the interacting fractures also stress condition, different coalescence behavior was observed. In general, the wing cracks initiate at the fracture tips at uniaxial and low confinement biaxial condition (Figure 2–6). Bobet and Einstein (1998) reported that the location of crack initiation moves to the middle of the flaw, as confining pressure increases. The wing cracks disappear completely at higher confining stresses. Later, secondary fractures are likely to connect the preexisting fractures. They propagate unstably and follow the direction of shear (Sagong and Bobet 2002). Figure 2–6 illustrates the most preferable configuration of the developing shear fractures, which is a setup with two co–planar initial fractures as well with as without confining pressure (Bobet and Einstein 1998).

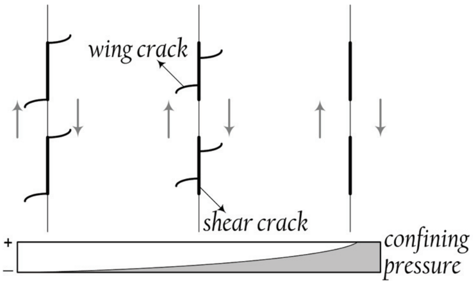

Figure 2–6: Setup for fracture coalescence in shear and influence of confining pressure (Bobet and Einstein 1998)

Intrinsic limits are reported for growth of 3D cracks, i.e. cracks with not planar but curved surface. For further details on this rarely studied subject, refer to, e.g. Dyskin et al. (2003) and Germanovich and Dyskin (2000).

While, e.g. Brace and Bombolakis (1963) or Horii and Nemat–Nasser (1985) indicated that shear fractures observed in glass will not propagate in their own plane in the micro–/meso–scale, rock shear fractures were found to grow in–plane (e.g. Petit and Barquins 1988; Reches and Lockner 1994; Moore and Lockner 1995) at least in the macro–scale.

On the micro–scale, Bažant and Pfeiffer (1986) describe the shear fracture resulted from Mode–II loading as a zone of inclined tensile micro–cracks subsequently connected by shearing. The shear fracture or shear band consists of inclined struts of the material between inclined cracks. Shear failure requires these struts to be crushed in compression.

According to Lockner (1995), shearing will take place along surfaces oblique to the maximum tensile stress and play an important role in the development of local stress concentrations. Induced near a fracture tip and loaded in shear, the local stresses contain a component of tension as well as shear. This will in general lead to tensile failure before shear failure is achieved.

Two processes may take place simultaneously during loading the fractures in compressive shear. First, propagation of the extensional cracks decreases stress intensity, so that additional deviatoric stress must be applied to cause further fracture propagation. At some point, the extensional crack propagates outward the area of high stress concentration and subsequently ceases. Second, diagonal flaws propagate out–of–plane and in parallel with the orientation of the maximum tensile stress. These flaws are favorably oriented to act as initiation points for shear failure. When the flaw density evolves sufficiently for crack interaction to occur, en–echelon arrays of cracks will develop (Costin 1987; Lockner 1995). Finally, the stress concentration is high enough to initiate shear fractures propagating in plane and being governed by their own stress field. The expanse of damaged rock is asymmetrically distributed around the Mode–II fracture (Moore and Lockner 1995). Similar observations on PMMA and sandstone were reported by Petit and Barquins (1988). They state "various […] examples show that Mode–II propagation from a defect cannot induce the formation of a single crack co–planar with the defect as is suggested by the fracture mechanics model. A macroscopically […] shear zone involving Mode–I minor fractures (micro–cracks) can, however, propagate to prolong the defect" (p. 1254).

Acoustic emission data, recorded in compressive cylindrical samples, in combination with micro–structural observations yielded a description for the formation of shear fractures. I.e. below yield strength, many dilatant micro–cracks are formed in a random distribution; near peak strength nucleation, local increase of crack density causes the process zone to expand that leads shear fracture to be created by crushing, buckling and rotation (e.g. Lockner et al. 1992; Reches and Lockner 1994; Zang et al., 2000).

Glaser and Nelson (1992) did detection of AE events during Mode–I and Mode–II loading of dolostone samples. They observed that in both the loading cases the most common waveform recorded comes from tensile crack propagation. In fact, Mode–II cracking occurs due to the growth and coalescence of local tensile cracks which, in aggregate, create the shear failure plane observed in macro–scale. They did not detect any signal before the peak point in Mode–I loading, which is in direct contrast to the observations reported by Hoagland et al. (1973). Evidences, implying for crack growth before peak load, are clearly recognized at the onset of nonlinear deformation recorded in the load–deflection curve of acoustic emission (Ouchterlony 1982). This has been also confirmed by Stanchits et al. (2003) for Mode–I loading of granite samples.

Since most usually $K_{IIC} > K_{IC}$, tensile fracture is consequently identified as dominant in rocks and rock–type materials. Even in situations where Mode–II seems to be favorable, Mode–I takes over (Melin 1989). This is manifested in, e.g. the formation of the wing fractures on shear cracks. The wing fractures propagate stably and often stop when aligned parallel to the direction of maximum tensile stress. Mode–II fractures are then initiated at the wings tips and in parallel with the shear crack. They form an array of en–échelon cracks, which are later connected. Mostly propagating unstably, the fractures are asymmetrically distributed with respect to the shear plane. Confining pressure enhances the growth of Mode–II fractures and suppresses development of Mode–I wing cracks.

2.3.2. *Static–dynamic versus stable–unstable fracture growth*

There exist two terminology frames for fracture propagation process. One is based on fracture propagation velocity, and the second is defined by stress intensity factor. The velocity–dependent definition differentiates between *static* and *dynamic*, while the latter deals with the concepts of *stable* and *unstable*. Figure 2–7 shows the different regimes of fracture propagation.

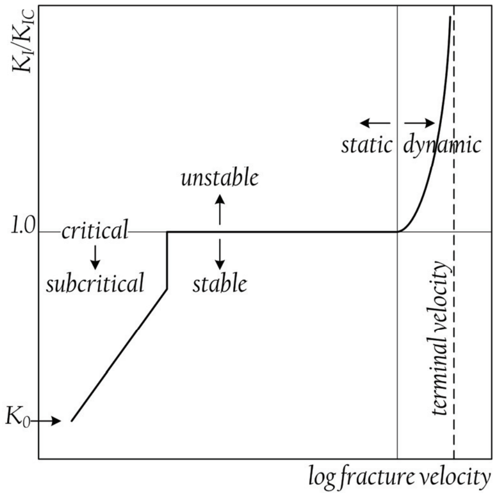

Figure 2–7: Schematic variation of Mode–I stress intensity factor, K_I, versus fracture velocity (after Zhang et al. 1999)

The necessary condition for instability of a crack is that stress intensity reaches material fracture toughness, i.e., $K_k = K_{kC}$, and the derivative of K_k with respect to the crack length remains positive. (Lawn 1993). Otherwise, the crack is stable. A stable crack extends comparably slow and can be stopped at any stage, i.e., requires an increase in stress for each increment of crack growth. An unstable crack will be accelerated by excess energy and propagates at the speed approaching the terminal velocity, which is governed by the material elastic wave speed. This situation is referred to as dynamic. Instability can be either achieved by reaching a critical crack length or by impact loading. The term *critical* is used for the onset of the unstable crack growth, i.e., the transition from stable to unstable. The stress intensity factor corresponding to this transition is fracture toughness, K_{kC}. Any fracture propagation taking place at fractions of K_{kC} is referred to as *subcritical* crack growth (e.g. Atkinson 1984), which is governed by some competing mechanisms including diffusion, dissolution, ion exchange, micro–plasticity, and stress corrosion. The latter is important in rocks, whilst the others have been mainly shown as active in ceramics and glass. Subcritical fracture propagation takes place at slow speeds. The transition from critical cracking to stress–corrosion–dominated propagation is reported at a crack propagation velocity of about 10^{-3} *m/s* (Atkinson 1984). At stress intensities lower than K_0, no subcritical crack growth is initiated.

2.3.3. *Fracture process zone model*

In the previous section, static stress and displacement fields at the vicinity of a loaded crack were introduced in terms of the stress intensity factor, K_k. Assuming linear elastic behavior, Equation 2–2 suggests an infinite or singular stress at the crack tip, i.e., $r \to 0$, providing any nonzero K_k. This is, in fact, a manifestation of Hooke's law applied beyond its limits of validity. Physically, the stress–bearing capacity of a material is limited by its yield strength. Hence, a small plastic region is expected immediately ahead of the crack tip. This region is called *plastic zone* in metallic materials (Irwin, 1958); however, it has been demonstrated to be a micro–crack–smeared zone or a fracture process zone in rock (e.g. Hoagland et al. 1973).

Some fracture process zone models have been so far proposed. According to Whittaker et al. 1992, the most important and popular ones are the maximum normal stress criterion (Schmidt 1980) and the cohesive crack model (Dugdale 1960; Labuz et al. 1983). The maximum normal stress criterion is based on the assumption that the formation of the FPZ takes place when the local tensile stress in the vicinity of the crack tip reaches the ultimate uniaxial tensile strength of the rock material. The theory provides formulations for size and shape of the process zone.

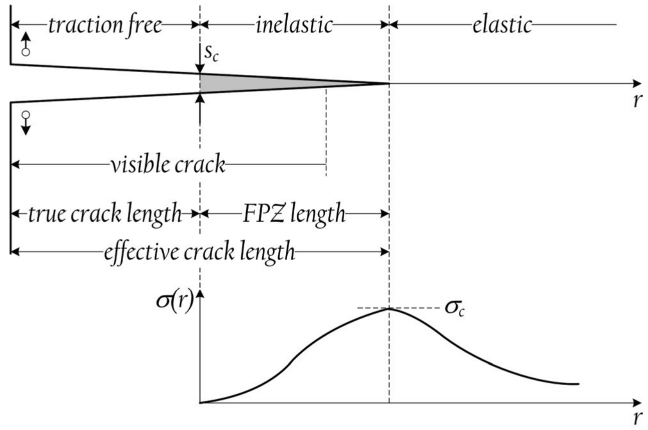

Figure 2–8: The schematic layout and nomenclature of the cohesive crack model

Describing the FPZ for Mode–I fracturing in rocks, the cohesive crack model is a modification to the Dugdale's crack model initially introduced for metals. The model assumes a crack to be represented by an effective length (see Figure 2–8). This length is divided into a traction free portion (true crack length) and a length over which cohesive stress applies. The cohesive stress tends to close the crack and refer to the FPZ. The material in the process zone, indicated by the shaded area in Figure 2–8, is partially damaged but still able to withstand some stress, which is transferred from one surface to the other. The material outside the FPZ is assumed linear elastic.

The FPZ starts expanding if the maximum tensile stress, induced over the FPZ, reaches the ultimate tensile strength, σ_c, while the true crack tip displacement, i.e., opening is still zero. As the crack tip opens up, the stress decays to zero, and eventually the true crack tip displacement reaches a critical maximum value, s_c. Hence, the stress singularity problem is overcome. From now on, the true crack tip displacement is briefly named crack displacement, Although Dugdale's assumption suggests that the crack–closing cohesive stress is constant and equal to the yield strength, it is, in reality, thought to depend on some other parameters, e.g. the instantaneous value of crack displacement, loading nature etc.

2.4. Rock failure phenomenology

Experimental observations show that since the rock minerals have different strength and hardness, rock expectedly fractures through the weakest minerals (e.g. Hazzard and Young 2000). Subsequently, coalescence of fractures causes rock to fragment irregularly as observed in macro–scale (Figure 2–9). This process is known as *fragmentation* in which material turns into several or even numerous intact fragments, where each fragment has the same texture with that of the original rock, and consequently, inherits physical properties from that.

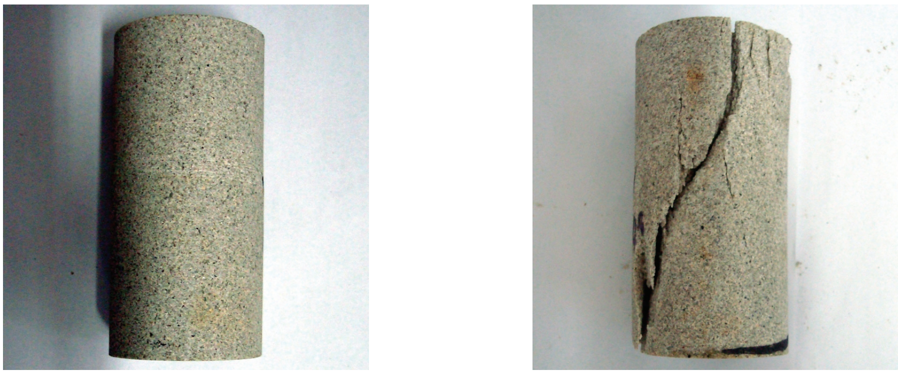

a. compressive sample in low–rate static testing

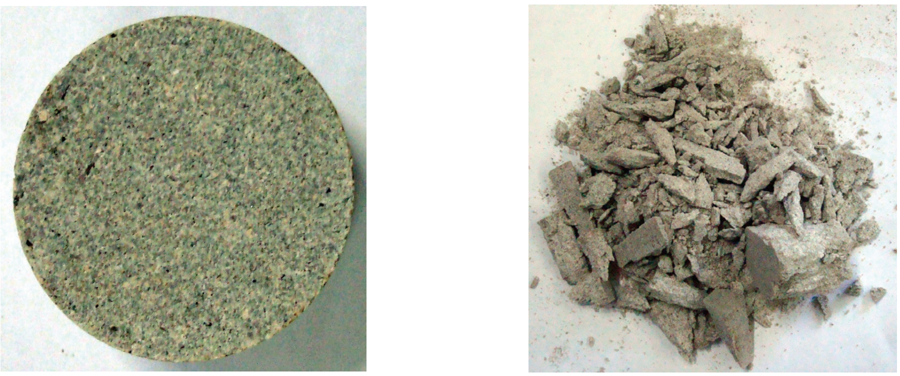

b. compressive sample in high–rate dynamic testing

Figure 2–9: Pre– and post–failure appearance of sandstone samples under low– and high–rate loading (Gong 2010)

Fragment size depends on the rock texture and more significantly on the loading nature that the rock endures. As observed in laboratory tests done on compressive and tensile samples, rock breaks into few pieces in static loading, where distinct failure surfaces are observed. On the contrary, the material violently smashes under high–rate loading. Figure 2–9 (previous page) compares the post–failure appearance of sandstone samples observed under different loading rates. Gradation of the fragments produced by the sample, illustrated in Figure 2–9b, is presented in Figure 2–10.

a. sample core (20 mm), very big fragments (12-15 mm)

b. big fragments (6-12 mm)

c. moderate fragments (3-6 mm)

d. small fragments (2-3 mm)

e. very small fragments (1-2 mm)

f. fine fragments and minerals (<1 mm)

Figure 2–10: Fragments size gradation of the sample shown in Figure 2–9b (Gong 2010)

2.4.1. *Rock failure in different scales*

Material failure can be interpreted differently in different observation scales. In macro–scale, strength criteria, e.g. Mohr–Coulomb are used to express the failure phenomenon irrespective of the role of rock microstructure. However, as discussed before, micro–cracks, initiated within the weak grains or mineral cement and propagating throughout the rock structure, are the origin of rock failure. Furthermore, mechanical properties of each rock mineral depend on its molecular structure, where attractive and repulsive forces between molecules govern the mineral strength and stiffness. In such a structure, excessive separation of molecules, interpreted as *bond break*, is the origin of mineral fracture. Figure 2–11 (next page) schematically presents how a single rock failure phenomenon can be independently investigated at different observation levels.

Molecular bond rupture is, in fact, the origin of any material failure observed in whether micro– or macro–scale. However, its numerical simulation requires extremely fine discretization, which is too effortful by current computational facilities. This problem turns more serious when laboratory specimens with few centimeters size are aimed to be modeled. That is exactly why micro–scale simulations are vastly preferred, although molecular effects cannot be explicitly included into them. However, if relations between the model parameters and the material molecular properties are somehow established, these effects can be implicitly introduced into the calculations.

Accepting this logic, this thesis aims to establish a micro–scale model in order to explore how micromechanical properties of rock characterize and control its macroscopic response. This model will help for rock strength prediction under different loading rates, and hopefully provides a clear understanding about rock failure process.

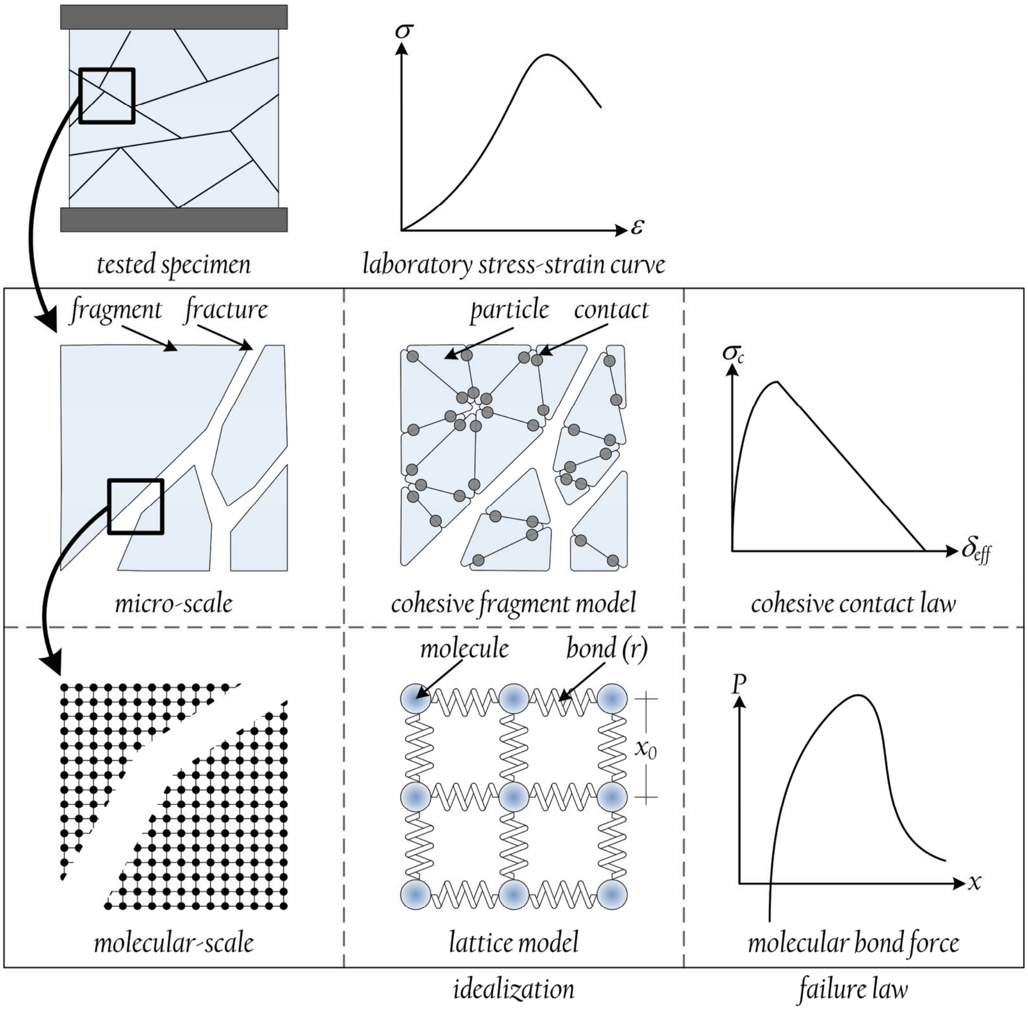

Figure 2–11: Rock failure in different observation scales, and its idealization in micro– and molecular–scale modeling

2.5. Cohesive fragment model

Considering the presented explanations, the microstructure of rock material can be idealized as a collection of fragments cohesively stuck together along their boundaries (see the second row in Figure 2–11). The fragments are regarded as a miniature of the rock material with the same texture and elastic properties, where the interface between the fragments represents a potential fracture. As formerly illustrated in Figure 2–8, force–

displacement relation in the interfaces should follow a cohesive law in order to mode the fracture process zone.

Global behavior of this idealization can be studied in three distinct stages:

- Pre–failure or elastic stage where all the fragments are connected together, and no fracture, i.e., interface separation exists. The assemblage follows therefore the same elastic response with that of the tested rock.
- Failure stage; once traction force between two or several fragments exceeds its ultimate limit, the fragments start separating from each other, and fracturing is triggered. The assemblage loses its strength and exhibits a softening behavior.
- Post–failure stage; if loading keeps increasing, number of fragments detached increases and fractures densely propagate throughout the body. Depending on the model specifics, this process may create a distinct failure surface or intensively shatter the assemblage.

This simulation approach, which can be applied to a verity of brittle materials, e.g. rock, ceramics, polymer and concrete, is called Cohesive Fragment Model (CFM) in this thesis.

2.5.1. *Numerical method for CFM implementation*

The CFM requires a numerical method capable of handling both the fragments and interfaces. The method must be also able to treat the cycles of fragments separation and reattachment. To choose the best option for the CFM implementation, all the numerical methods, related to fracture and fragmentation, should be examined in terms of their capabilities and limitations. This is done in the next chapter, where the most efficient numerical method to carry out the CFM will be introduced.

CHAPTER 3

Numerical models and laboratory tests for rock fracture study

The entire research on rock fracture can be classically divided into two parts, i.e., experimental studies and numerical simulations. Each part involves particular difficulties. Precise sample preparation is always necessary for laboratory tests and any inaccuracy may totally alter the measurements. Moreover, high–speed cameras and sensitive data logger systems are needed for dynamic tests to accurately record the dynamic event, which occurs within a fraction of microsecond. On the other hand, advanced computational facilities are required to handle massive numerical models with very high degrees of discretization. These obstacles delayed rock fracture research until resent years. However, studies done in the last decade attained promising achievements, which have not only extended geomechanics, but also been helpful for the other branches of material science.

This chapter reviews the major progresses achieved in rock fracture simulation and briefly explains their basics, assumptions, consequences, and limitations. Laboratory tests mainly for measuring static and dynamic fracture toughness are also described. Finally, all the numerical methods are compared and the most efficient option in terms of the CFM implementation is selected.

3.1. Numerical modeling

Subsequent to rapid advancements in computer technology, numerical methods have provided powerful tools in rock dynamics study. For example, numerical modeling has been used to simulate dynamic response of fractured rock mass (Chen et al. 2000; Hildyard and Young 2002), fracture propagation in rock and concrete under static and dynamic loading conditions (Bennett 1991; Du et al. 1989; Kaiser and Tang 1998; Liang et al. 2004; Prisco and Mazars 1996; Tang and Kaiser 1998; Zhu and Tang 2006), wave propagation in jointed rock masses (Chen and Zhao 1998; Lei et al. 2006), and acoustic emission in rock (Hazzard and Young 2000b). A large number of numerical methods have been applied to rock mechanics problems, such as the finite element method, finite difference method, finite volume method, discrete element method etc. These methods will be explained in detail by categorizing them into continuum, discontinuum, and coupled methods (Jing 2003).

3.2. **Continuum methods**

3.2.1. *Finite difference method*

The Finite Difference Method (FDM) is one of the oldest numerical techniques used for solving partial differential equations. The FDM implementation is simple for both two- and three-dimensional cases. Unlike other methods, that does not need for any trial or interpolation functions. However, the conventional FDM with regular grid systems does suffer from inherent inflexibilities in dealing with fractures, complex boundary conditions and material heterogeneity. These shortcomings constrain its application for rock mechanics. Some FDM developments target at getting rid of these deficiencies. For example, the Finite Volume Method (FVM) is considered as an extensional FDM. That is not only free of regular mesh constrains but also is specially suited to simulate non-linear behavior of solids (Jing and Hudson 2002).

Introduced by Yee (1966), the Finite-Difference Time-Domain (FDTD) is another development of the FDM, which bases on two-layer grid-based differential time-domain methodology. The FDTD was widely used for electromagnetic data processing in rock mechanics, e.g. imaging electromagnetic data for cross-hole (Ernst et al. 2006; Holliger et al. 2001; Yu et al. 1998). By using double grid methodology, the FDTD can deal with inhomogeneous problems. It can also be used for determining rock hydraulic conductivity (Lesnic et al. 1997) and wave propagation problem in homogeneous and heterogeneous media (Barkhatov 2007; JafarGandomi and Takenaka 2007; Sato 2006; Schroder and Scott 2000; Schubert et al. 1998; Wang and Tang 2003).

Based on the FDM fundamental idea, some truly meshless methods have been proposed, such as the Generalized Finite Difference Method (GFDM) (Liszka and Orkisz 1980) and the Finite Point Method (FPM) (Onate et al. 2001). Despite of many constrains of the FDM, its basic idea has been widely used in many numerical methods, especially for dynamic analysis, such as the discrete element method, molecular dynamics etc.

3.2.2. *Boundary element method*

The Boundary Element Method (BEM) seeks a weak solution at global level through a numerical solution of an integral equation derived using Betti's reciprocal theorem and Somigliana's identity. The main advantage of the BEM is to reduce the model dimensions by one, with much simpler mesh generation and much faster calculation speed. The BEM is more suitable for solving fracture problems in inhomogeneous and linearly elastic bodies (Gray et al. 2004; Pan et al. 1997; Saez and Dominguez 2001; Wearing and Burstow 1994; Zhao et al. 1999).

Recent BEM developments can be summarized as follows: The Boundary Contour Method (BCM) (Nagarajan et al. 1996) that further reduces computational model dimensions; the Galerkin Boundary Element Method (GBEM) (Bonnet et al. 1998; Maier and Frangi 1998) which paves the way for the variation formulation of the BEM to solve non–linear problems; and the BEM–based mesh–free methods (Liu and Gu 2004; Nicolazzi et al. 2005) that overcome the conventional drawback of the BEM on requiring boundary element.

However, according to the literature, the BEM does not sound efficient in dealing with material heterogeneity, material non–linearity, and damage evolution process.

3.2.3. *Finite element method*

The term Finite Element Method (FEM) was first used by Clough (1960) for plane stress problems. Nowadays the FEM has become the mainstream numerical tool in engineering sciences, including rock mechanics and rock engineering. The FEM has a great flexibility in treatment with material heterogeneity, non–linear deformability, complex boundary conditions, in situ stresses and gravity. These merits made it become the most extensive numerical method used in engineering and scientific research (Jing and Hudson, 2002). Special development of the FEM in rock mechanics are the *joint elements* (Goodman et al. 1968; Katona 1983; Mahtab and Goodman 1970; Zienkiewicz et al. 1970) which are targeting at simulation of jointed rock mass.

An overview on the exiting literature shows that the FEM approaches for fracture simulation can be classified into two groups, i.e., *element degradation method* and *element boundary breaking method*.

The idea of element degradation approach is treating the fracturing process as a sequence of element degradation. The removal technique provided in the ABAQUS is an example of this kind of approach, which deletes the elements where the failure criterion is locally satisfied, and crack propagation track is visualized as the path of removed elements (ABAQUS 2005). The most representative method of the element degradation approach is the Continuum Damage Mechanics (CDM), which is widely used in brittle fracturing analysis (Bonora 1997; Brooker and Ronalds 2001; Kuna–Ciska and Skrzypek 2004). Combination of the CDM with the Weibull’s distribution enables the FEM to represent material heterogeneity. This is a common technique for describing damage evolution and crack propagation in rock and concrete under static and dynamic loading conditions (Bennett 1991; Du et al. 1989; Liang et al. 2004; Prisco and Mazars 1996; Tang and Kaiser 1998; Zhu and Tang 2006).

Another degradation technique for representing cracked medium is to work with equivalent continuum concept of elastic degradation and/or softening plasticity

(Zienkiewicz et al. 1980). Introduced by Rashid (1968), the smeared crack modeling is a known representation of this method. It is commonly used in concrete fracturing analysis, and very popular because of its computational convenience (Abdollahi 1996; Espandar and Lotfi 2003; Lotfi and Espandar 2004). This method has been also used for concrete fracture analysis under high strain rate, thermo–mechanical behavior of concrete and failure of ceramic refractory materials (Ali, 1996, Andreev and Harmuth 2003; Tedesco et al. 1993). It is introduced into some commercial FEM codes like the ANSYS (ANSYS 2008) and ATENA (Wolfel 2007).

The main advantage of the element degradation method is avoiding re–meshing and adding new degrees of freedom during the calculation process. However, this method does not give an explicit interpretation of the fracturing phenomenon.

Elements boundary breaking approach represents fracturing process by separation through the inter–element boundaries. Failure in inter–element boundaries may be based on either the fracture mechanics theory or a failure criterion governing the detachment of inter–element boundaries. The first approach has been used in several FEM codes like the ABAQUS (ABAQUS 2005), FRANC (Agrawal and Sun 2004) and MARC (MSC Software 2007). The second method inserts interface elements along the inter–element boundaries. That is mostly applied to concrete or rock material (Alfaiate et al. 1997; Cho et al. 2003; Cho and Kaneko 2004). The most successful development of the element boundary breaking approach is the Cohesive Zone Modeling (CZM), which dates back to the work of Hillerborg et al. (1976) and Belytschko et al. (1976). The CZM has been successfully used in the simulation of fracture and fragmentation in brittle materials, multiple discrete crack propagation, and dynamic crack growth in ceramic materials (Block et al. 2007; Camacho and Ortiz 1996; Elmarakbi et al. 2009; Karedla and Reddy 2007; Li et al. 2004a; Molinari et al. 2007; Murphy and Ivankovic 2005; Pinho et al. 2006; Remmers et al. 2008; Tomar et al. 2004; Yang and Chen 2005; Zhai et al. 2004; Zhou and Molinari 2004b; Zhou et al. 2005a).

Application of these techniques is usually coupled with a re–meshing algorithm to eliminate stress singularity and element dependence problems happening at the crack tip (Yang and Chen 2005). Re–meshing techniques (Bocca et al. 1990; Bocca et al. 1991; Molinari and Ortiz 2002; Wawrzynek and Ingraffea 1989) require rather complicated programming, and may accumulate calculation errors through the variable mapping. As the worse effect, adaptive re–meshing can hardly be used to simulate complex cracking aspects such as crack coalescence or crack bifurcation.

Generally speaking, the continuum assumption makes the FEM unsuitable to deal with the complete detachment and large–scale fracture opening problems (Jing and Hudson 2002; Jing 2003), which are the most concerned issues in micromechanical modeling of rock material failure. The locking effects including element locking and numerical locking, i.e., ill–conditioning are other shortcomings of the FEM (Arnold 1981; Babuska and Suri 1992; Chilton and Suri 1997; Suri 1996; Szabo 1990). They have more or less negative influences on the FEM application in brittle material fracturing.

Recently, the FEM has been specifically extended to deal with fracturing problems in continua. Two main streams in this way are categorized as follows.

a. Extended finite element method

The Extended Finite Element Method (XFEM) (Belytschko and Black 1999) is based on the Partition of Unity Method (PUM) (Babuska 1997) which allows for addition of a priori knowledge about the final solution into the approximation space of the numerical solution. The XFEM treats cracking at element level by using the Level Sets Technique (Prabel et al. 2007; Stolarska 2001). Usually Heaviside function and asymptotic functions are used to deal with the discontinuity and singularity problems. Compared with the classical FEM, the XFEM has several advantages in terms of mesh independence. In the XFEM, elements containing a crack are not required to conform to crack edges, and consequently mesh generation is much simpler than the classical FEM. The most important aspect of the XFEM is to perform crack extension without any re–meshing effort. That was successfully applied to dynamic crack propagation, multiple cracks and three–dimensional cracking (Asadpoure and Mohammadi 2007; Asferg et al. 2007b; Pedro and Belytschko 2005; Prabel et al. 2007; Rethore et al. 2005a, b; Sukumar et al. 2003b).

Fracture propagation analysis in quasi–brittle and polycrystalline materials (Mergheim et al. 2005; Sukumar et al. 2003a), dynamic fracturing and time–dependent problems (Cavin et al. 2005; Rethore et al. 2005b) have been also handled by using the XFEM. Its recent developments include dealing with cohesive fracturing (Asferg et al. 2007a, b; Belytschko et al. 2003; Zi and Belytschko 2003), explicit reformulation (Menouillard et al. 2006, 2007), anisotropic problems (Asadpoure and Mohammadi 2007; Asadpoure et al. 2006), and assuming contact between cracks (Khoei and Nikbakht 2007; Ribeaucourt et al. 2007).

Although the XFEM can deal with weak and strong discontinuities and profits from mesh independency (Fernandez–Mendez and Huerta 2004), it suffers from some defects. For example, the global stiffness matrix may become singular, if crack truncates a very small part of a finite element (Markus Peters 2005). The XFEM implementation in available commercial codes is a little difficult, because additional degrees of freedom are introduced (Stéphane et al. 2007). And all of these methods would suffer from ill–conditioning when using higher order trial functions (Strouboulis et al. 2007).

b. Meshless methods

In recent years, a large family of *meshless methods* has been invented to eliminate the troubles associated with model discretization involved in solving partial differential equations. In these methods, only discrete modes are generated and distributed within the concerned medium, while no fixed element–node topological relation is predicted as it is in the FEM. The basic idea of meshless methods is therefore to provide numerical solutions using a set of arbitrarily distributed points without any element to connect them. Compared to mesh generation algorithms, it is relatively simpler to create only a node distribution and adapt it locally.

There are many versions of meshless method, such as the Smoothed Particle Hydrodynamics (SPH) (Monaghan 1988; Randles and Libersky 1996), the Diffuse Element Method (Nayroles et al. 1992), the Element–Free Galerkin Method (EFGM) (Belytschko et al. 1992; Belytschko et al. 1994b), the Reproducing Kernel Particle Method (Chen et al. 1996; Liu et al., 1996; Liu et al. 1997b), the H–p Clouds Method (Liszka et al. 1996), the Partition of Unity Method (PUM) (Melenk and Babuska 1996), the Finite Point Method (FPM) (Onate et al. 1996a, b; Perazzo et al. 2008), the Method of Finite Spheres (De and Bathe 2000), the Natural Element Method (NEM) (Sukumar et al. 1998) etc. A vast review on these methods is given by Belytschko et al. (1996) and Jing (2003).

Depending on the methodology used to handle the equations, meshless methods can be classified into two major categories, i.e., *meshless strong–form methods* and *meshless weak–form methods*. Most of meshless weak–form methods such as the EFGM (Belytschko et al. 1992) are "meshless" only in terms of the numerical approximation of field variables. They have to adapt a background mesh to perform numerical integration of a weak form over the problem domain, which is computationally expensive. Meshless strong–form methods such as the Generalized Finite Difference Method (Liszka and Orkisz 1979) often use the Point Collocation Method to satisfy governing partial differential equations and boundary conditions. These are easy to implement and computationally efficient. Since they do not need any background mesh, they are purely "meshless". In this review, only two mainstream meshless methods of the Element–Free Galerkin Method (EFGM) and the Smoothed Particle Hydrodynamics (SPH) method are presented.

The EFGM (Belytschko et al. 1992), which is based on the Moving Least Square (MLS) interpolants, requires only nodal data and no element connectivity is needed. This makes the method attractive particularly for dynamic crack problems, since in which re–meshing algorithm is avoided. The EFGM application and development includes various fields, such as static crack growth (Belytschko et al. 1994a), dynamic problems (Belytschko et al. 1995; Belytschko and Tabbara 1996; Lu et al. 1995), 3–D material non–linearity (Belytschko et al. 1997), adaptive approach (Haussler–Combe and Korn 1998), dynamic propagation of arbitrary 3–D cracks (Krysl and Belytschko 1999), mixed–mode dynamic crack propagation and probabilistic fracture mechanics (Belytschko et al., 2000; Rahman and Rao 2002; Rao and Rahman 2002), parallel EFGM algorithms (Singh and Jain 2005a, b), and multiple cracking and cohesive crack growth (Muravin and Turkel 2006; Soparat and Nanakorn 2008).

Furthermore, contact logic, based on a penalty method, is introduced into the EFGM by Belytschko and Fleming (1999), and that is applied for the analysis of jointed rock masses with block–interface models (Zhang et al. 2000). These advances make the EFGM capable of handling rock mechanics problems, although it is entangled with high computational cost.

The SPH method was initially invented to deal with astrophysical problems (Monaghan 1988). The elasto–dynamic equations were first studied by Libersky and Petschek (1991). The SPH application mainly includes fragmentation analyses, such as dynamic fragmentation in brittle elastic solid (Benz and Asphaug 1994, 1995), high distortion impact computations (Johnson et al. 1996; Medina and Chen 2000), concrete fragmentation under explosion loading (Rabczuk and Eibl 2003), formation of cracks around magma chambers (Gray and Monaghan 2004) and strain rate effect on heterogeneous brittle materials (Ma et al. 2006a). However, it exhibits an instability, known as *tensile instability*, and suffers from *zero–energy modes*. Hence, that requires special treatments to produce stable and accurate results (Campbell et al. 2000; Dyka et al. 1997; Gray et al. 2001). Furthermore, the SPH results are vastly affected by the kernel function adopted (Fulk and Quinn 1996). Generally speaking, the SPH method has some advantages in dynamic fragmentation, but precision and computational time is still a problem for its further application in rock mechanics.

As the main advantage, the meshless approaches sharply reduce the expenses for domain discretization compared to the standard FEM or FVM. However, they involve several troublesome defects including difficulty in enforcement of essential boundary conditions, stability, and high computational cost. The interpolation functions are non–polynomial that makes the integration more demanding for the weak–form approach. The strong–form approach do not need integration, however it would suffer from unstable solutions.

From a pure computational viewpoint, the meshless methods have not yet outperformed the FEM. However, due to their flexibilities in fracture simulation, they are potentially applicable for civil engineering and geomechanical purposes.

3.3. Discontinuum methods

3.3.1. *Discrete element method*

The key concept of the Discrete Element Method (DEM) is that the domain of interest is treated as assemblage of rigid or deformable *blocks/particles/bodies* (Cundall 1971). The DEM is capable of analyzing multiple interacting deformable continuous, discontinuous or fracturing bodies undergoing large displacements and rotations. Formulation and development of the DEM have progressed over a long period of time since the pioneering study of Cundall (1971). The DEM were widely used in underground works (Lemos 1993; Sofianos and Kapenis 1998; Souley et al. 1997; Zhao et al. 1999), laboratory test simulations and constitutive model development (Jing et al. 1993; Jing et al. 1994; Min and Jing 2003), rock dynamics (Cai and Zhao 2000), wave propagation in jointed rock masses (Chen and Zhao 1998; Lei et al. 2006; Zhao et al. 2006), nuclear waste repository design and performance assessment (Jing et al. 1995), rock fragmentation process (Gong and Zhao 2007), and acoustic emission in rock (Hazzard and Young 2000b).

Contact detection and *contact interaction* are the most important aspects of the DEM, as many researchers distinguish the DEM from other methods because of its ability for new contacts detection during calculation. There are several contact detection algorithms aiming efficiency of computation time and memory space. Details on this topic are provided by Munjiza (2004).

Mechanical interaction between two contacting blocks has a great influence on the mechanical behavior of a DEM simulation. It is usually characterized by two finite stiffness springs in normal and tangential direction. Other improvements for block interaction are reported. For example, Donze et al. (1999) and Hentz et al. (2004) have extended the classical DEM by introducing an interaction range and using a modified Mohr–Coulomb rupture criterion. Kemeny (2005) also implemented a first order differential equation for contact cohesion. Jing and Stephansson (2007) have extensively provided the fundamentals of the DEM and its application in rock mechanics.

According to the solution algorithm used, the DEMs can be divided into two groups of explicit and implicit formulation.

a. Explicit DEM (distinct element method)

As the explicit formulation of the DEM, the distinct element method appeared in the early 1970s by a fundamental paper on progressive movement of rock mass as a 2–D assemblage of rigid blocks (Cundall 1971). It became more presented by Cundall and Strack (1979), Cundall and Hart (1992), Hart (1993), Lemos et al. (1985), Lemos (1994) and Curran and Ofoegbu (1993). The most popular numerical representation of the explicit DEM has been implemented with the computer codes of PFC2D and UDEC in 2D and PFC3D and 3DEC in 3D modeling (Itasca 2008, 2009). Other developments were made behind or in parallel with these two. The distinct element method appear to be the main direction of the DEM implementations for rock mechanics problems, although the term discrete element method is more universally adopted.

In explicit algorithm, there also exist two kinds of approaches, i.e., *static relaxation* and *dynamic relaxation*. In static relaxation, blocks displacement at the next time step is figured out by the equilibrium equations. Examples of the DEM with static relaxation are found in Taylor (1983) and Williams and Mustoe (1987). Dynamic relaxation uses Newton's second law to get the displacement of blocks at the next time step (Cundall 1988; Hart et al. 1988). Static relaxation iterates faster than dynamic one and has no need to set damping, but it cannot examine the dynamic effects.

One use of the explicit DEM is to represent rock–type material as a dense packing of irregular–sized particles interacting at their contact. This method has been already known as the Bonded Particle Method (BPM) (Potyondy and Cundall 2004). Many have employed the BPM with circular particles, to capture different failure features of rock material and other grained media (Azevedo et al. 2008; Cho et al. 2007; Hazzard et al 2000a; Jensen et al. 1999; Potyondy 2007; Schöpfer 2009; Tan 2008; Tan 2009; Yoon 2007; Wanne and Young 2008), and some others have made use of polygonal particles (Camborde et al. 2000; Damjanac et al. 2007; Kazerani and Zhao 2010; Kazerani et al. 2010b).

b. *Implicit DEM (discontinuous deformation analysis)*

As the DEM implicit formulation, the Discontinuous Deformation Analysis (DDA) was proposed by Shi (1988) to analyze mechanical behavior of blocky systems. The DDA is somewhat similar to the FEM, but accounts for the interaction of independent blocks along discontinuities in fractured and jointed rock masses. The DDA is typically formulated as a work–energy method, and can be derived using the principle of minimum potential energy or Hamilton's principle.

The applications of the DDA are mainly on tunneling, caverns, earthquake effects, and fracturing and fragmentation process of geological and structural materials (Hatzor et al. 2004; Hsiung and Shi 2001; Jiao et al. 2007b; Zhang et al. 2007). The DDA developments include discretizing the blocks with finite elements (Shyu 1993), handling the contacts as stiff joints and removing penetration criteria to improve the efficiency and to accelerate the convergence (Cheng 1998), coupled stress–flow problems (Kim et al. 1999), 3D block system analysis (Jiang and Yeung 2004), higher order elements (Hsiung 2001), more comprehensive representation of the fractures (Zhang and Lu 1998), and viscous boundary for modeling stress wave propagation (Jiao et al. 2007a).

The DEM has had wide application in rock mechanics, mainly because of its conceptual attraction in explicit crack representation. In addition, its theory is simple and easy to understand. However, the DEM is relatively new and its performance, particularly for dynamic analysis, is not fully explored yet.

3.3.2. *Molecular dynamics*

The Molecular Dynamics (MD) is a form of computer simulation in which atoms and molecules are allowed to interact for a period of time under potential laws of physics. It is regarded as an interface between laboratory experiment and theory, and can be assumed as a virtual experiment. This technique was originally conceived in theoretical physics in the late 1950's (Alder and Wainwright 1959).

Since early time, the MD has been used for crack modeling at atomic scale, where the obtained results were in agreement with the continuum and fracture mechanics (Dienes and Paskin 1987; Mullins and Dokainish 1982; Paskin et al. 1980; Paskin et al. 1983). Other applications of the MD can be summarized as follows: transition between brittle to ductile propagation of a sharp crack and favorable crack propagation direction in crystallize material (Cheung and Yip 1990; Kohlhoff et al. 1991), failure mechanism of micro granular material (Farkas et al. 2002; Hasnaoui et al. 2003), crack propagation of Mode–I in an icosahedral quasicrystal model (Rosch et al. 2005) and Yoffe's linear theory of dynamic brittle fracture (Abraham 2005). Nowadays, the MD is widely used in material science and biochemistry to interpret some phenomena at atomic level.

Rock mechanics related problems solved by the molecular dynamics include interaction between complex granular particles (Poschel and Buchholtz 1995), creation of polycrystalline computer materials (Krivtsov and Wiercigroch 2001), visco–elastic behavior of granite rock (Ichikawa et al. 2001) and influence of porosity on elastic strength properties of polycrystalline specimens (Krivtsov 2003).

Potential laws used for crack propagation includes the Lennard–Jones potential (Paskin et al. 1980), Hooke's law (Abraham 2005, 2006), the EAM potentials (Farkas et al. 2002; Hasnaoui et al. 2003), and the ReaxFF reactive force field (Buehler et al. 2006). The Lennard–Jones potential and Hooke's law are simple but do not have much physical reality. The EAM potentials were successfully used in metal simulation. However, they suffer from some problems when facing with non–metal material (Buehler et al. 2006). Suitable for non–metal materials, the ReaxFF reactive force field has been developed to describe many different elements across the periodic table (Buehler et al. 2006).

The key problem of any MD simulation is that the adapted potential function strongly affects on the results, while no verified manner is proposed yet to correctly pick the potential function.

Although, the MD is a powerful tool for studying crack propagation mechanism at microscopic level, long time simulations are mathematically ill–conditioned, that makes the MD problematic to perform long period processes. Furthermore, simple potential functions are not sufficiently accurate to reproduce molecular systems while complicated functions usually are computationally expensive. The explained time and space barriers make the MD inefficient for rock mechanics. Nevertheless, the MD techniques are still promising for people interested in micro–mechanics.

3.3.3. *Lattice model*

Formulated by Brandtzaeg (1927), the *lattice model*, assumes a continuum as a network of bar or beam elements. Hrennikoff (1941) demonstrated that a regular triangular lattice of bars, i.e., a truss, is capable of solving problems of continuum elasticity with a Poisson's ratio fixed at one third. Because of computational limits, further work stalled until Herrmann et al. (1989) proposed the use of beam elements instead of bars and using regular or random lattice for fracture simulation in heterogeneous solid.

The classical lattice models basically aim to describe how concrete or reinforced concrete fails due to fracturing (Katsman and Aharonov 2006; Sands et al. 2007; Schlangen and van Mier 1992a, b). Fracture process is modeled by removing elements which exceed their tensile strength. Material heterogeneity can be also introduced by assigning different properties to lattice elements (Reuschle 1998). The most prevalent applications of the lattice modeling can be summarized as follows: deformational response and fracturing process subjected to dynamic loading (Song and Kim 1996), 3D fracture processes in brittle materials (Chen et al. 2002, 2003; Donze and Magnier 1995; Kazerani et al. 2010a; Kozicki 2007; Lilliu and van Mier 2003; Zhao 2010), multi physical simulation (Eker and Akin 2006; Jimenez-Hornero et al. 2005; Szymczak and Ladd 2004), and dynamic fracture simulations of brittle solid and seismic wave radiation (Mora and Place 1994; Wang et al. 2006b; Wang et al. 2000).

The lattice model combined with the digital imaging method and the principal-tensile-stress fracture law seems to give quite realistic crack patterns (Liu et al. 2008; Schlangen and Garboczi 1997). There are many other numerical methods, which use the basic idea of the lattice modeling, including the Virtual Internal Bond (VIB) model (Gao and Klein 1998; Klein and Gao 1998), the irregular lattice model (Berton 2003), the cellular automata model (Li et al. 2004b) and the fractal lattices (Babadagli 2005).

3.4. Coupled methods

3.4.1. *Continuum-discontinuum coupled methods*

Continuum and discontinuum methods are respectively unsuitable for modeling the post-failure and pre-failure behavior of rock. A combination of the both sounds to be helpful in many geophysical applications in order to predict the formation and interaction of fragments (Morris et al. 2006). Coupled methods can take advantages of each method while avoiding the disadvantages. Creating fractured zones with a discontinuum-based method and intact zones with a continuum-based one forms a direct simple coupled methodology. Examples of this kind of coupled method include hybrid DEM/BEM models (Lorig et al. 1986), combinations of the DEM, DFN and BEM approaches (Wei and Hudson 1988), and most popularly hybrid DEM/FEM models (Chen and Zhao 1998; Pan and Reed 1991; Munjiza et al. 1999; Morris et al. 2006; Cai 2008).

The combined finite-discrete element method (Munjiza et al. 1999; Munjiza et al. 2004; Munjiza and John 2002; Munjiza et al. 1995) aims at simulating failure, fracture and fragmentation in solids. In this way, each block, viewed as a single discrete element, interacts with neighboring discrete elements, while it is itself discretized into finite elements and may break into smaller blocks during calculation. This approach has been widely used to simulate fracturing process of rock. For example, Morris et al. (2006) developed the FEM/DEM code of LDEC to investigate the effects of explosion and impact loading on geological media. Karami and Stead (2008) used their FEM/DEM model to simulate crack propagation under mixed mode loading. Ariffin et al. (2006) created a hybrid FEM/DEM code to study joint surface damage and tensile failure in near–surface intact rock.

As a hybrid DDA/FEM, the Numerical Manifold Method (NMM) was developed by Shi (1991). This method employs two sets of system, one is mathematical and to define domain approximations, and the other is physical and defines integration fields. The NMM main advantage is getting rid of meshing and combining discontinuum and continuum problems into a single framework. For this reason, the NMM is reported as suitable for fracture simulation (Chiou et al. 2002; Zhang et al. 1997). The Finite Cover Method (FCM) has been proposed by Terada et al. (2003) to enhance the NMM for dealing with heterogeneous materials by using Lagrange multipliers. Terada and Kurumatani (2005) and Terada et al. (2007) have recently developed the method for 3D.

3.4.2. *Multi–scale coupled methods*

Multi–scale modeling has been regarded as a promising methodology for the simulation of cracking process (de Borst 2008; Guidault et al. 2007; Hettich et al. 2008). The purpose of multi–scale modeling is to reduce computational expense (Wu and Lin 2008) and to obtain directly material macroscopic response from micromechanical properties (Sansoz and Molinari 2007). This methodology has been widely used in coupling the molecular dynamics with continuum mechanics approaches such as the FEM (Mullins and Dokainish 1982), analytical solutions (Hasnaoui et al. 2003) and the Generalized Interpolation Material Point (GIMP) method (Ma et al. 2006b).

As another example, the Quasi–Continuum (QC) method is a coupled continuum and atomistic method, which is proposed by Tadmor et al. (1996a, b) for simulating the mechanical response of polycrystalline materials. The QC method is basically designed for metal material studies, such as effects of structure and size on deformation of bicrystals in copper (Sansoz and Molinari 2007), atomic scale fracturing (Miller et al. 1998), and deformation and failure of metal material controlled by atomic scale properties (Miller and Tadmor 2007).

Other examples of multi–scale modeling include the three–scale computational method (Takano and Okuno 2004; Vernerey et al. 2008), the multi–scale BEM (Sfantos and Aliabadi 2007) and the Voronoi cell FEM with a non–local Gurson Tvergaard Needleman (GTN) model (Hu et al. 2007).

Most popularly, the double scale approaches are applied to fracture analysis. In this solution, domain of interest is split into two parts, i.e., an overall coarse mesh, which is unchanged during crack propagation and a dense discretization with a nonlinear analysis over a small part of solution space (Haidar et al. 2003; Guidault et al. 2007; Stefan Loehnert 2007; Belytschko 2007).

The wavelet theory is a powerful mathematic tool for multi–scale analysis. It has been used in solving partial differential equations (Kaminski 2005; Ko et al. 1995) and crack tip singularity (Shen and Yi 2000; Spanos and Rao 2001). It has been also employed as an upscaling technique to obtain rock properties from geological data at small scale (Chu et al. 1998). There are some wavelet–based numerical methods such as the Reproducing Kernel Particle Methods (RKPM) (Liu et al. 1997a) and the multi–resolution FEM based on the second generation wavelets (Han et al. 2005; He et al. 2007).

Some numerical methods have been specifically designed for multi–scale analysis. For example, the Multi–scale Finite Element Method (MsFEM) (Hou and Wu 1997) was created for solving a class of elliptic problems. And the Finite Difference Heterogeneous Multi–scale Method (FD–HMM) (Abdulle and Weinan 2003) was designed to solve multi–scale parabolic problems.

3.5. Experimental studies

Although this chapter mainly discusses about numerical modeling of rock fracture, a summary of related laboratory tests are reviewed as well. These experimental studies produce benchmarks to verify numerical models in terms of algorithm correctness, approach validity and adequacy.

First, static measurement techniques are outlined and then dynamic tests are reviewed.

3.5.1. *Static tests*

The most matured laboratory works are the Mode–I testing methods evidently in three ISRM *suggested methods*. Some Mode–II methods exist, but most are insufficient to provide reliable results. There are very few methods available to provide Mode–III loading condition (e.g. Cox and Scholz 1988; Yacoub–Tokatly et al. 1989). Mode–I and–II fracture toughness testing methods are summarized below and the effective factors on measurement are discussed. At the end, some typical data measured are provided.

a. Mode–I fracture toughness testing methods

Several testing methods for the Mode–I fracture toughness, K_{IC}, have been introduced, e.g. the Semicircular Core in three point Bending (SCB) test (Chong and Kuruppu 1984), the chevron–notched SCB test (Kuruppu 1997), the Brazilian Disc (BD) test (Guo et al. 1993), the Radial Cracked Ring (RCR) test (Shiryaev and Kotkis 1982), the Modified Ring (MR) test (Thiercelin and Roegiers 1986), and the Double Torsion (DT) test (Evans 1972). Reviews of the methods can be found in, e.g. Whittaker et al. (1992) and Chang et al. (2002). The DT test is of special importance, as it has been also applied to the study of subcritical crack growth in rock (Atkinson 1984).

Three testing methods have been introduced by the International Society for Rock Mechanics (ISRM) as suggested methods (Ouchterlony 1988; Fowell 1995).

In 1988, the Chevron Bend (CB) and Short Rod (SR) methods were introduced as ISRM suggested methods (Figure 3–1a and b). The CB method uses cores with a prefabricated chevron shaped notch that is subjected to three–point bending.

The SR method uses the remaining halves of the CB method. A notch is introduced into the core in long axis direction and is subjected to tension. This combination of CB and SR method provides the possibility to study anisotropy effects, i.e., determination of K_{IC} parallel and perpendicular to the core axis.

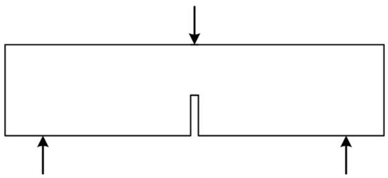

a. Chevron Bend (CB) method

b. Short Rod (SR) method

c. Cracked Chevron Notched Brazilian Disc (CCNBD) method

Figure 3–1: ISRM suggested methods for determination of Mode–I fracture toughness

The Cracked Chevron Notched Brazilian Disc (CCNBD) was introduced in 1995 by the ISRM as suggested method (Fowell 1995). It uses Brazilian discs (Brown 1981) with a notch in the centre of the specimen (Figure 3–1c). The evaluation of K_{IC} from this method is still under discussion (e.g. Wang and Xing 1999; Wang et al. 2003).

b. Mode–II fracture toughness testing methods

Several methods for the Mode–II fracture toughness, K_{IIC}, have been introduced. Most of the procedures have been developed for metals but later applied to rocks. Only those that have been applied to rock or rock like materials, e.g. concrete, are mentioned.

Ingraffea (1981) introduced the antisymmetric four–point bending test for application of both mixed Mode I–II and Mode II loading (Figure 3–2a). Swartz and Taha (1990) numerically analyzed this test method and stated that tensile stresses inevitably exist around the notch tips, even under pure shear loading. Despite of not being able to avoid the tensile stresses, the antisymmetric four–point bending cube test has been applied to concrete and rock by Barr and Derradj (1990) (Figure 3–2d).

Watkins (1983) introduced the rectangular punch through shear test (Figure 3–2c) and argued numerically that failure takes place in Mode–II (Davies et al. 1986).

The compression–shear cube test (Figure 3–2f) (Jumikis 1979) was shown to be a potential method for determining K_{IIC} (Izumi et al. 1986). This method was employed by Rao (1999) to determine K_{IIC} of granite and marble.

The short beam compression test (Figure 3–2e) with a special notch orientation was developed by Watkins and Liu (1985). The notches are orientated perpendicular to the loading direction. The K_{IIC} values determined in this test are always less than the K_{IC} values, despite K_{IC} is thought to be lower than K_{IIC}. The result that K_{IIC} measured is smaller than K_{IC} is not reasonable for brittle rock, because experiments generally show shear strength larger than tensile strength (Rao et al. 2003). An exception to this might be very porous materials like some sandstones, mortar and concretes.

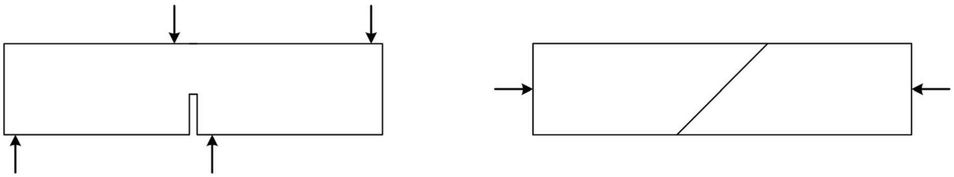

a. antisymmetric four–point bending **b. triaxial compression**

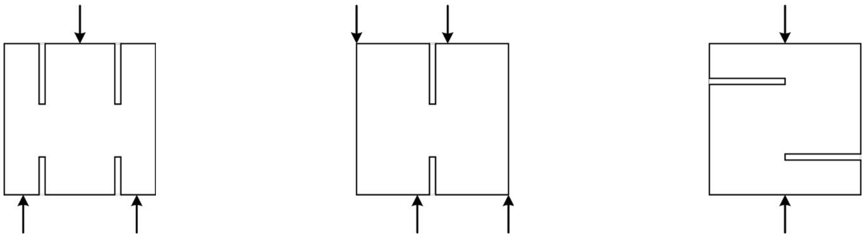

c. punch through shear **d. antisymmetric four–point bending cube** **e. short beam compression**

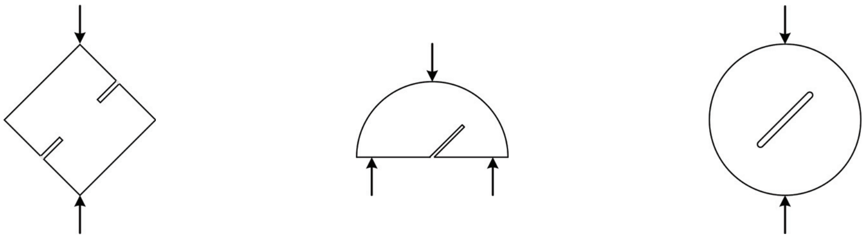

f. compression–shear cube **g. three–point bending semi–disc** **h. centrally cracked Brazilian disc**

Figure 3–2: Mode–II fracture toughness testing methods

Several other testing methods for K_{IIC} have been introduced. Some were first developed for determination of stress intensity factor in Mode–I or mixed mode. However, as the stress intensity factor depends on the angle between applied load and fracture plane (Atkinson et al. 1982), they were modified to perform K_{IIC} testing. For example, Mode–II loading can be induced in the CCNBD, if the slot is distinctly inclined (Figure 3–2h), but slight inaccuracy in the test setup may result in mixed mode condition. Therefore, this method is not practical for Mode–II. Nevertheless, Chang et al. (2002) claim the CCNBD method is suitable for mixed mode as well as Mode–II determination.

The same problem and discussion as for the CCNBD test is evident with the three–point bending semi–disc test (Chong and Kuruppu 1984), which uses a half Brazilian disc with an introduced notch at diagonal cut (Figure 3–2g).

An evaluation method for the triaxial compression test was introduced by Hakami and Stephansson (1990) to estimate the Mode–II energy release rate (Figure 3–2b). It showed that the energy release rate and, hence, fracture toughness is influenced by confining pressure.

c. *Influential factor on fracture toughness*

Fracture toughness was introduced in Chapter 2. The critical stress intensity factor is a mechanical property for any material that may vary with changing environmental and loading condition.

Winter (1983) could show experimentally that K_{IC} increases with increasing confining pressure. Tests on three–point bending specimen with increasing confining pressures on e.g. Ruhr sandstone showed a linear increase of fracture toughness by a factor of five up to 100 *MPa* confining pressure. Thallak et al. (1993) confirm the linear increase of K_{IC} with confining pressure for laboratory hydro–fracture experiments. Al–Shayea et al. (2000) applied confining pressures up to 28 *MPa* to centrally cracked Brazilian disc specimens. K_{IC} for a limestone increased 274% with an increase of 28 *MPa* of confining pressure, while K_{IIC} increased 137% only (see Table 3–1) for the same increase in confining pressure. Rao (1999) varied the loading angle and confining pressure in the compression–shear cube testing for determination of K_{IIC}, that was found to linearly increase with increasing confining pressure. For marble, K_{IIC} increased approximately 2.5 times for an increase of confining pressure from ambient conditions to 20 *MPa*. K_{IIC} of granite increased by a factor of 1.7 at 10 *MPa* confinement.

Other variations in boundary condition have shown to influence fracture toughness. These are, e.g. temperature (Al–Shayea et al. 2000; Dwivedi et al. 2000) or moisture content. Dwivedi et al. (2000) noted K_{IC} to increase with decreasing temperature, i.e., +30° to –50° *C*, in the CCNBD specimen. They related this effect to the remaining moisture content in the samples, where the water freezes and the fracture toughness of the ice adds to the one of the rock. Changing the moisture content changes the degree of K_{IC} variation with temperature change. With increasing temperature, K_{IC} increases slightly until approximately 100° *C*, and then starts dropping (Al–Shayea et al. 2000). K_{IIC} was shown to slightly increase with temperature, at least for temperatures up to 120° *C* (Al–Shayea et al. 2000).

For the influence of loading rate on fracture toughness, do refer to Section 2.3.2 and, e.g. Zhang et al. (1999) and Atkinson (1984). This topic is to be extensively discussed in Chapter 8 and 9 of the thesis.

Fracture toughness can be related to physico–mechanical properties of rock, like the Young's modulus, uniaxial compressive strength, tensile strength, point–load index, the Poisson's ratio, compressive wave velocity, grain size, grain contact length, and dry density (e.g. Whittaker et al. 1992; Bearman 1999; Zhang 2002; Alber and Brardt 2003).

Table 3–1 summarizes the typical values of K_{IC} and K_{IIC} for several rock types. In general, K_{IIC} is larger than K_{IC} in rock, a factor of 2 to 3 is usually assumed for ambient conditions (e.g. Rao et al. 2003). Lockner (1995) even suggests a factor of 15.

Table 3–1: Fracture toughness for different rocks, P: confinement, ^{1}CB, ^{2}SR, ^{3}antisymmetric four–point bending, ^{4}compression–shear cube, ^{5}centrally cracked Brazilian disc

rock type	K_{IC}	K_{IIC}	K_{IC}/K_{IIC}	reference
granite	~2.0	~2.2	~1.1	Ingraffea (1981)^3
	1.88	4.90	2.6	Rao et al. (2003)$^{1/4}$
	0.65–2.47			Müller and Rummel (1984)^1, Ouchterlony (1988)^1
		1.75–2.60		Singh and Sun (1989)
limestone	~0.8	~0.9	~1.1	Ingraffea (1981)^3
	0.82–2.21			Bearman et al. (1989)^1, Guo (1990)^1
$P = 0.1\ MPa$	0.42	0.92	2.1	Al–Shayea et al. (2000)^5
$P = 28\ MPa$	1.57	2.18	1.4	
marble	2.21	6.1	2.8	Rao et al. (2003)$^{1/4}$
	0.46–2.25			Guo (1990)^1, Ouchterlony (1988)^2
		3.33–6.36		Rao (1999)^4
sandstone	1.67		3.0	Rao et al. (2003)$^{1/4}$
	0.67–2.56			Guo (1990)^1, Ouchterlony (1988)$^{1/2}$
		0.32–0.41		Singh & Sun (1989)
$P = 0.1\ MPa$	1.08			Müller (1984)^1
$P = 40\ MPa$	2.21			
$P = 80\ MPa$	2.54			

3.5.2. *Dynamic tests*

All the dynamic experiments have been performed in two major groups, i.e., dynamic fracture toughness tests (Chen et al. 2009; Dia et al. 2009; Dia et al. 2008; Jun et al. 2006; Kidane and Shukla 2010; Kim and Chao 2007; Nasseri et al. 2007; Sahraoui et al. 2009; Weerheijm and Van Doormaal 2007) and rock strength testing or fragmentation under high loading rates (Chlup et al. 2010; Cho et al. 2003; Dai et al. 2010; Fukui et al. 2004; Huang et al. 2010; Jeong et al. 2006; Qi et al. 2009; Wang et al. 2006a; Whittles et al. 2006; Xia 2006; Xia et al. 2008; Zhai et al. 2008; Zhao and Li 2000; Zhou and Yang 2007).

Different toughness testing methods with various specimen geometries have been so far proposed to capture fracture initiation toughness, fracture propagation toughness, fracture energy, and fracture velocity. Conventional sample geometries include the three–point bend specimen, the wedge–shaped specimen, and the compact compression specimen (Bayoui et al. 1984; Popelar et al. 2000; Sahraoui et al. 2009; Yokoyama and Kishida 1989). The Brazilian disc specimen (also called central cracked circular disc) has been widely used to measure fracture properties of brittle materials (Fowell and Xu, 1994; Liu et al. 1998; Shetty et al. 1987), because its configuration can cover the entire mode mixity range from pure Mode–I to pure Mode–II by changing the loading angle, i.e., the angle of crack inclination relative to the line of loading.

Using the notched Semi–Circular Bend (SCB) specimen, Chen et al. (2009) and Dia et al. (2009) have developed and validated a method to simultaneously measure the Mode–I fracture parameters. Fracture initiation toughness is obtained from the peak load given by dynamic force equilibrium. A Laser Gap Gauge (LGG) has been developed to monitor crack opening displacement, from which fracture propagation velocity and fracture energy are calculated. The method can be also adapted to evaluate dynamic tensile strength of brittle solids (Dia et al., 2008).

a. Split–Hopkinson pressure bar test

Originally developed by Kolsky (1949, 1963), the Split–Hopkinson Pressure Bar (SHPB) technique has been comprehensively used by many investigators to reproduce high–rate loading in laboratory.

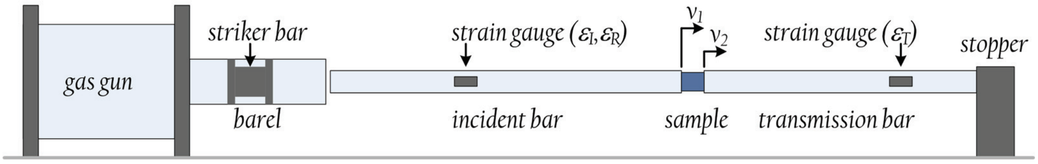

Figure 3–3: Schematic plot of a conventional split–Hopkinson pressure bar

As shown in Figure 3–3, a conventional SHPB consists of a striker bar, an incident bar, a transmission bar and a sample placed between the incident and transmission bars. A gas gun launches the striker bar at the incident bar. The produced impact creates an elastic compressive wave traveling through the incident bar toward the sample. Assuming the elementary theory for wave propagation, the sample response can be recorded from measurements taken with strain gages mounted on the incident and transmission bars. The evolution of this experimental method and recent advances are discussed by Follansbee (1985), Gray (1999), Gray and Blumenthal (1999), Nemat–Nasser et al. (1991), Nicholas (1982), and Ramesh and Narasimhan (1996).

For an ideal SHPB experiment, the sample should be in dynamic stress equilibrium and should deform at a constant strain rate over most the duration of the test. To closely approximate these ideal conditions for the specimens tested, a pulse shaper, e.g. a thin copper disc is placed on the impact surface of the incident bar. It causes that a non–dispersive ramp pulse propagates within the incident bar.

Assuming a uniform deformation for the sample, its strain rate is given by

$$\dot{\varepsilon}_s = \frac{d\varepsilon_s}{dt} = \frac{v_1(t) - v_2(t)}{l_0} \tag{3–1}$$

where l_o is the sample length.

Subscripts 1 and 2 represent the locations of the ends of the sample as shown in Figure 3–3. v_1 and v_2, which are the particle velocities at the sample–bar interfaces, can be written as follows,

$$v_1(t)=c\left[\varepsilon_I(t)-\varepsilon_R(t)\right] \text{ and } v_2(t)=c\left[\varepsilon_T(t)\right] \tag{3–2}$$

where ε_I, ε_R and ε_T denote respectively the incident, reflected and transmitted strain recorded by the gauges mounted on the bars. Note that compressive stress and contractive strain are assumed positive, and positive particle velocity is toward right.

By substituting the velocities into Equation 3–1,

$$\dot{\varepsilon}_s=\frac{c}{l_0}\left[\varepsilon_I(t)-\varepsilon_R(t)-\varepsilon_T(t)\right] \tag{3–3}$$

where c is the compressive wave speed. Thus, the stresses at the ends of the sample are

$$\sigma_1(t)=\frac{EA}{A_s}\left[\varepsilon_I(t)+\varepsilon_R(t)\right] \text{ and } \sigma_2(t)=\frac{EA}{A_s}\left[\varepsilon_T(t)\right] \tag{3–4}$$

E is the Young's modulus, A the cross–sectional area of the bars, and A_s that of the sample. Assuming dynamic stress equilibrium of the sample, $\sigma_1 = \sigma_2$, therefore

$$\varepsilon_I(t)+\varepsilon_R(t)=\varepsilon_T(t) \tag{3–5}$$

Finally, the stress, σ_s, the strain, ε_s, and the strain rate for the sample are given by

$$\sigma_s(t)=\frac{\sigma_1(t)+\sigma_2(t)}{2}=\frac{EA}{A_s}\left[\varepsilon_I(t)+\varepsilon_R(t)\right] \tag{3–6}$$

$$\dot{\varepsilon}_s=\frac{-2c}{l_0}\varepsilon_R(t) \text{ and } \varepsilon_s=\frac{-2c}{l_0}\int\varepsilon_R(t)dt \tag{3–7}$$

3.6. Discussion and conclusion

As the studies reviewed show, each numerical method benefits from some advantages, and suffers from some shortcomings. It is therefore impossible to find a perfect one to satisfy all the requisites of the problems related to rock dynamics.

As any discontinuous deformation is intrinsically banned in continuum methods, they are unsuitable to handle the problems involving large–scale fracture opening or complete detachment, which are the most concerned issues in rock dynamics. These methods cannot consequently help solve the problems related to material post–failure state or jointed medium.

Discontinuum methods model rock material or rock mass as an assemblage of blocks, particles or bars. Rock fracture process is therefore represented by the failure of inter–block contacts, inter–particle bonds or bars. Although discontinuum methods provide a realistic prospect to the failure process, they are relatively ineffective for stress distribution analysis in the pre–failure state. As described earlier, coupled approaches have been basically created to optimize the capabilities of each method.

Table 3–2 summarizes the weakness and strength points of every method, and compares their attributes together.

Table 3–2: Comparison of reviewed numerical methods in terms of their capabilities for rock mechanics applications

purpose	FEM	XFEM	DEM	lattice	MD	coupled	multiscale
static	■	■	▨	░	░	▨	▨
dynamic	■	■	■	■	■	■	■
pre–failure	■	■	░	░	░	■	■
post–failure	░	░	■	■	■	■	▨
rock material	■	■	░	■	░	■	▨
rock mass	░	░	■	░	░	■	▨
fracture	▨	▨	■	■	■	■	■
fragmentation	░	░	■	■	■	■	■

(■ : strong/easy to apply; ▨: applicable but with treatment; ░: weak/hard to apply)

Since the thesis objective is to investigate rock fracture and fragmentation, none of the continuum methods can be chosen. However, pre–failure behavior of rock is also needed to be examined. That is why a pure discontinuous method may not be perfectly helpful, and some items of continuous techniques must be also employed. Hence, a coupled model may be proposed, in which the discontinuous side is more participating than the continuous one. This idea leads to the choice of a DEM code, provided it supplies the deformability of particles.

As it will be explained in the next chapter, the Universal Distinct Element Code (UDEC), as a coupled discrete element/finite difference model, satisfactorily provides these requirements. Its discrete element basics guarantee properly treating the separation and reattachment of the CFM fragments, where its finite difference formulation allows handling their deformation.

CHAPTER 4

UDEC and implementation of CFM

As a finite deference–discrete element coupled code, the Universal Distinct Element Code (UDEC) permits 2D plane–strain and plane–stress analyses (Itasca 2009). As explained in Chapter 2, the CFM suggests to model rock material as assemblage of distinct deformable fragments interacting at their boundaries. The CFM makes use of the particle/contact logic of UDEC to model the fragments and the interfaces in between, where each particle is composed of the Constant–Strain Triangular (CST) elements, as seen in Figure 4–1.

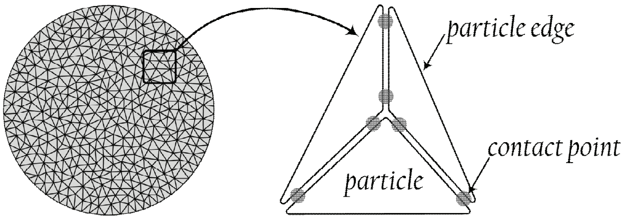

Figure 4–1: A representative CFM particle assemblage used for the Brazilian test simulation, and configuration of model–constructing particles and contacts

A perturbation within this particle assemblage, caused by an applied excitation, propagates through the whole system and leads to the particles movement. A series of calculations, tracing the particles motion, give the induced contact forces in this dynamic process, and the perturbation propagation speed will depend on the physical properties of the discrete system.

In coming sections, the particle and contact numerical representation in UDEC as well as the formulation of the governing equations is explained in detail. Then, the process developed for particle generation according to the CFM assumptions will be described.

4.1. **Particle and contact representation**

4.1.1. *Contact detection and identification*

The interface between fragments is numerically represented as a contact surface formed between two particle edges. In general, for each pair of particles that touch (or are separated by a small enough gap), data elements are created to represent contact points. In UDEC, adjacent particles can touch along a common edge segment or at discrete points where a corner meets an edge or another corner.

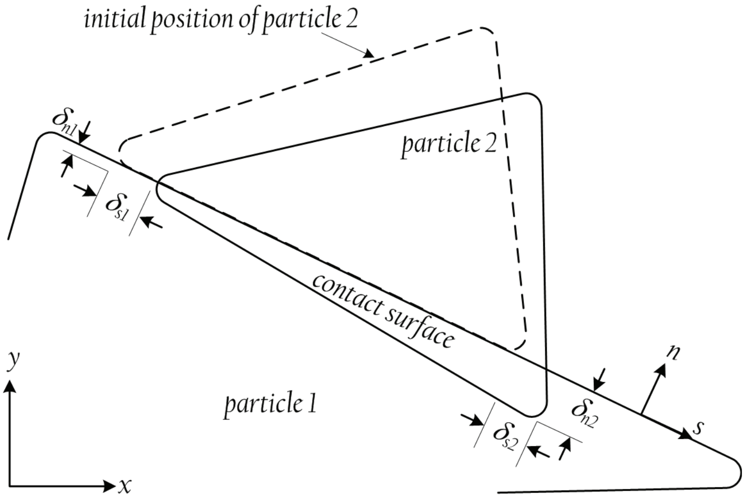

Figure 4–2: Contact between to particles

Figure 4–2 illustrates a scheme for the representation of contacts. For rigid particles, a contact is created at each corner interacting with a corner or edge of an opposing particle. If the particles are deformable, i.e., internally discretized by the CST elements, contact points are created at all grid–points located on the particle edge in contact. Thus, the number of contact points can be increased as a function of the internal discretization of adjacent particles.

a. corners rounding using constant rounding length, r_0

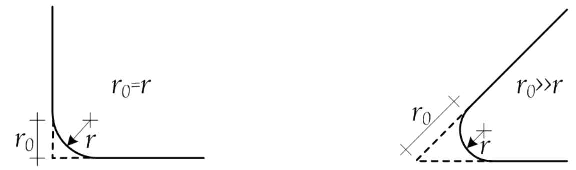

b. corners rounding using constant rounding radius, r, demonstrating unacceptable truncation of acute angled corner

Figure 4–3: Definition of corner rounding length, r_0

A specific problem with contact schemes is the unrealistic response that can result when particle interaction occurs close to or at two opposing particle corners. Numerically, particles may become locked or hung–up. This is a result of the modeling assumption that particle corners are sharp or have infinite strength. In reality, crushing of the fragment corners would occur as a result of a stress concentration. Explicit modeling of this effect is impractical. However, a realistic representation can be achieved by *rounding* the corners of the particles so that they can smoothly slide past one another when two opposing corners interact. Corner rounding is used in UDEC by specifying a circular arc for each particle corner. The arc is defined by the distance from the true apex to the point of tangency with the adjoining edges. Examples are shown in Figure 4–3. By specifying this distance rather than a constant radius, truncation of sharp corners is not severe (compare Figure 4–3a to Figure 4–3b).

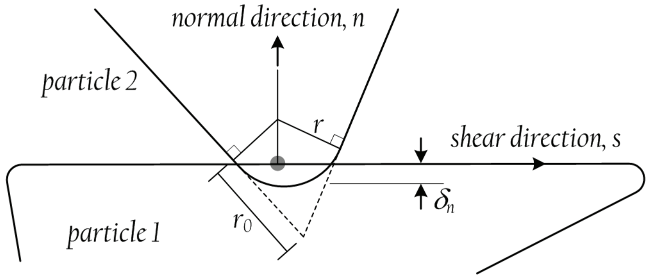

a. details of rounded corner–to–edge contacts (rounding length is exaggerated)

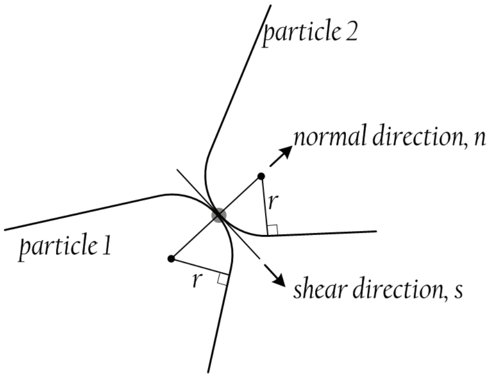

b. smooth interaction of corner–to–corner contact

Figure 4–4: Definition of contact point, contact normal and shear direction (contact point is indicated by gray rigid circle)

The point of contact between a corner and an edge is located at the intersection between the edge and the normal taken from the centre of the radius of the circular arc at the corner with the edge (see Figure 4–4a). If two corners are in contact, the point of contact is the intersection between the line joining the two opposing centers of radii and the circular arcs (Figure 4–4b). If the edges of two deformable particles are in contact, i.e., edge–to–edge contact, the points of contact are still treated as corner–to–edge contacts. However, they are located at the intersections of the normal to the grid–points along the edge of one particle and the edge of the other particle; corner rounding is not used in this case. If a grid–point along the edge of one deformable particle is created at the same location as a grid–point along the edge of another deformable particle, two contacts will be created; one contact for each grid–point. This provides for better accuracy, particularly if the two grid–points slide past each other.

The directions of normal and shear force acting at each corner–to–corner or corner–to–edge contact are defined with respect to the direction of the contact normal, as illustrated in Figure 4–4.

Corner rounding only applies to the contact mechanics calculation in UDEC. All other calculations and properties are based on the entire particle. Corner rounding can introduce inaccuracy in the solution if the rounding is too large. If the rounding length is kept to approximately one percent of the representative particle edge length in the model, good accuracy is achieved (Cundall 1987).

4.1.2. *Domain contact detection*

Contact points are updated automatically as particle motion occurs. The algorithms to perform this updating must be computationally efficient, particularly for dynamic analysis, where large displacements may require deleting and adding hundreds of contacts during the dynamic simulation. UDEC takes advantage of a network of *domains* created by the 2D particle assemblage. Domains are the regions of space between particles which are defined by the contact points, as are D_1 and D_2 in Figure 4–5. During one time step, new contacts can only be formed between corners and edges within the same domain, so local updates can be executed efficiently whenever some prescribed measure of motion is reached within the domain. The main disadvantage of this scheme is that it cannot be used for very loose systems because the domain structure is ill–defined.

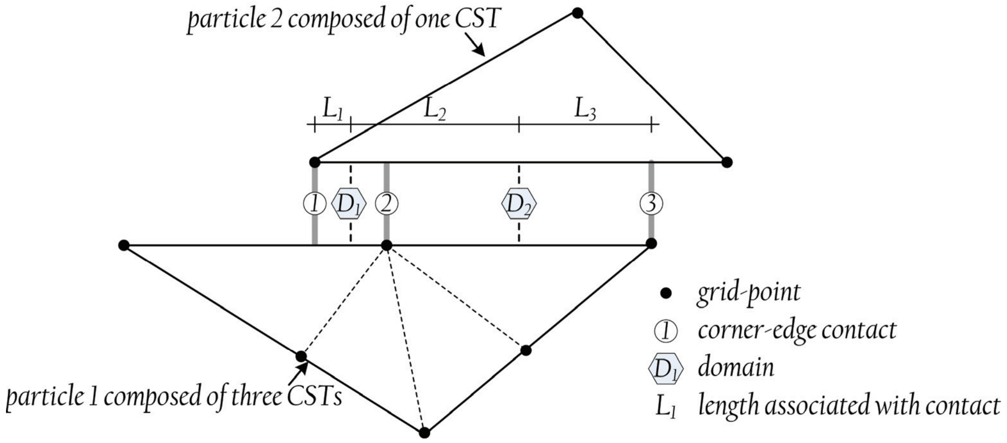

Figure 4–5: Configuration of deformable particles, CST elements, contacts, and domains between to particles

Contact updating is triggered by significant relative motion within a domain. A fictitious displacement is accumulated for each domain, and this displacement is related to the relative motion that has taken place in the domain since the previous update. The fictitious displacement is the accumulated maximum relative velocity between any two corners in a domain times the time step. When this displacement exceeds a certain tolerance, i.e., 35% of the rounding length, an update is triggered. This ensures that contacts are always detected before physical contact is made.

During an update, new contacts are made and old ones deleted depending on the relative motion at each contact. For example, if two blocks are found to be separated by a gap that is equal to or less than half of the rounding length, a contact is created. Conversely, if an existing contact acquires a separation greater than a predefined tolerance, the contact is deleted. The default value for this tolerance is 55% of the rounding length.

For particles sliding past each other, if the relative shear displacement at a contact exceeds two times the rounding length, a new contact is formed. For large shear displacements, contact updating must ensure that contact forces are preserved when contacts are added or deleted such that a smooth transition will exist between neighboring states. This is particularly important for dynamic analyses with high stress gradients.

The logic described above ensures that the data structure for all potential contacts is in place before physical contact takes place. It also ensures that contact searching is only done for moving particles; there is no time wasted on relatively inactive ones.

4.2. UDEC solution procedure and formulation

Dynamic behavior is numerically represented by a time stepping algorithm in which time step duration is limited by the assumption that velocities and accelerations are constant within the time step. The solution scheme is identical to that used by the explicit finite difference method for continuum analysis. Solving procedure in UDEC alternates between the application of a stress–displacement law at all the contacts and the Newton's second law for all the particles. The contact stress–displacement law is used to find the contact stresses from the known and fixed displacements. The Newton's second law gives the particles motion resulting from the known and fixed forces acting on them. The motion is calculated at the grid points of the triangular constant–strain elements within the elastic particle. Then, application of the material constitutive relations gives new stresses within the elements. Figure 4–6 (next page) schematically presents the calculation cycle in UDEC along with a brief review of the basic equations, which are fully explained in coming sections.

4.2.1. *Equations of particle motion*

The motion of an individual particle is determined by the magnitude and the direction of the resultant out–of–balance moment and forces acting on it. Considering a one–dimensional motion for a single mass acted on by a varying force $F^{(t)}$, the Newton's second law of motion can be written in the form

$$\frac{d\dot{u}}{dt} = \frac{F^{(t)}}{m_p} \tag{4–1}$$

where $\dot{u}$ is the velocity, t is the time, and m_p denotes the particle mass. The central difference scheme for the left–hand side of Equation 4–1 at time t can be written as

$$\frac{d\dot{u}}{dt} = \frac{\dot{u}^{(t+\Delta t/2)} - \dot{u}^{(t-\Delta t/2)}}{\Delta t} \tag{4–2}$$

Substituting Equation 4–2 in Equation 4–1 and rearranging yields

$$\dot{u}^{(t+\Delta t/2)} = \dot{u}^{(t-\Delta t/2)} + \frac{F^{(t)}}{m_p}\Delta t \tag{4–3}$$

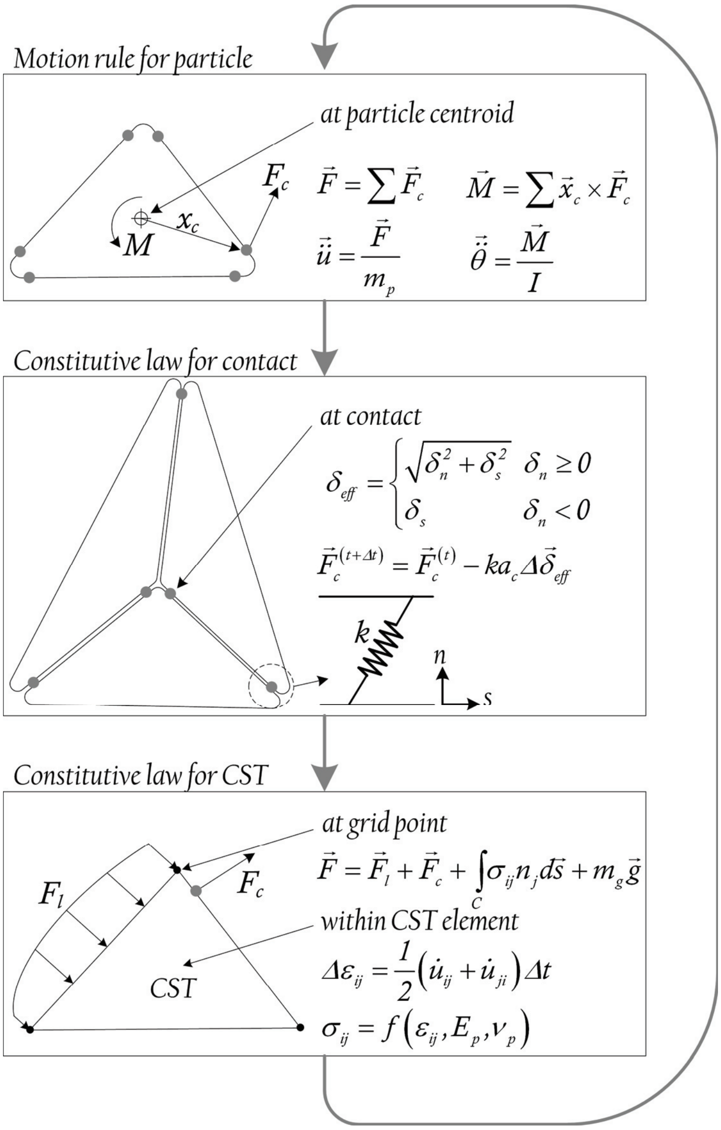

Figure 4–6: Calculation cycle in UDEC: particle motion calculation, application of contact constitutive law to obtain contact forces acting on particle as its force boundary condition, and application of elasticity rules for CST elements to calculate stress and stain field within particle

Displacement can be expressed in terms of the velocities stored at the half time step point:

$$u^{(t+\Delta t)} = u^{(t)} + \dot{u}^{(t+\Delta t/2)}\Delta t \tag{4–4}$$

Because the force depends on the displacement, the force–displacement calculation is done at one time instant. The central difference scheme is *second–order accurate*, i.e., first–order error terms vanish from the solution. This is an important characteristic that prevents long–term drift in a discrete element simulation.

For the particles, acted upon by several forces as well as the gravity, the velocity equations become

$$\begin{aligned} \vec{\dot{u}}^{(t+\Delta t/2)} &= \vec{\dot{u}}^{(t-\Delta t/2)} + \left(\frac{\vec{F}^{(t)}}{m_p} + \vec{g}\right)\Delta t \\ \vec{\dot{\theta}}^{(t+\Delta t/2)} &= \vec{\dot{\theta}}^{(t-\Delta t/2)} + \left(\frac{\vec{M}^{(t)}}{I}\right)\Delta t \end{aligned} \tag{4–5}$$

where $\vec{\dot{u}}$ and $\vec{\dot{\theta}}$ are the vectors of the linear and angular velocity of the particle, respectively. I is its moment of inertia about the centroid. $\vec{F}$ and $\vec{M}$ denote the vectors of the total force and moment acting on the particle, and $\vec{g}$ is the gravitational acceleration vector (see Figure 4–6).

New velocities in Equation 4–5 are used to determine the updated particle location according to

$$\begin{aligned} \vec{x}^{(t+\Delta t)} &= \vec{x}^{(t)} + \vec{\dot{u}}^{(t+\Delta t/2)}\Delta t \\ \vec{\theta}^{(t+\Delta t)} &= \vec{\theta}^{(t)} + \vec{\dot{\theta}}^{(t+\Delta t/2)}\Delta t \end{aligned} \tag{4–6}$$

where $\vec{x}$ is the location vector pointing to the particle centroid, and $\vec{\theta}$ is the particle rotation vector about its centroid. Note that the rotations are not stored, and instead, the incremental rotations are used to update the positions of the particle vertices. In summary, each time step produces the new particle position that generates the new contact forces. The resultant forces and moments are used to calculate the linear and angular accelerations of each particle. The velocities and displacements of the particle are determined by the integration over the time increments. The procedure is repeated until a satisfactory state of equilibrium or continuing failure results.

4.2.2. *Force–displacement equation in contact*

Having individual particle motion, the position of the particles within the assemblage is updated. Then the displacement for each contact is calculated by the relative displacements of the two particles creating it.

Given the contact displacement, contact constitutive law calculates the contact force, F_c, which actually acts as the force boundary condition for the neighboring particles. This law is, in fact, an algebraic function of the contact stiffness coefficient, k, contact normal displacement, δ_n, contact shear displacement δ_s, and some additional parameters:

$$F_c = f\left(k,\delta_n,\delta_s,...\right) \tag{4–7}$$

The additional parameters are to introduce the particular features of rock behavior into the model, i.e., anisotropy, brittleness, rate dependency, and residual strength.

Under certain circumstances, if the stress or displacement within one or more contacts exceeds its ultimate value, the contact breaks, i.e., its stress decays and it endures an increasing displacement. This procedure causes that a limited amount of energy gets numerically dissipated, and the model loses some extent of its macroscopic stiffness and strength. Note that since the CFM particles are assumed to have an elastic behavior, the model global failure is controlled only by the contact constitutive law.

Details of the developed contact model will be presented in Chapter 5.

4.2.3. *Particle deformability*

Particles are internally discretized into the finite–difference triangular elements. The complexity of the deformation at each particle depends on the number of elements into which the particle is divided. The vertices of the triangular elements are called grid point (see Figure 4–5). The grid point force at each time step $\vec{F}^{(t)}$ is obtained as the sum of the four terms as follows

$$\vec{F}^{(t)} = \vec{F}_l + \vec{F}_c + \int_C \sigma_{ij} n_j d\vec{s} + m_g \vec{g} \tag{4–8}$$

where $\vec{F}_l$ is the external applied load, as illustrated in Figure 4–6. $\vec{F}_c$ results from the contact forces, and exists only for the grid points along the particle boundary. σ_{ij} is the element stress tensor, and n_j is the unit outward normal to the contour C, which follows the closed polygonal line defined by the straight segments which bisect the element edges converging on the grid point under consideration. Finally, m_g is the lumped gravitational mass at the grid point, defined as the sum of one–third of the masses of the triangles connected to the grid point. The grid point will be accelerated by $\vec{F}^{(t)}$ according to the finite difference form of the Newton's second law of motion,

$$\vec{\dot{u}}^{(t+\Delta t/2)} = \vec{\dot{u}}^{(t-\Delta t/2)} + \vec{F}^{(t)} \frac{\Delta t}{m_g} \tag{4–9}$$

where $\vec{\dot{u}}$ is the velocity vector at the grid point, and the superscripts show the time at which the corresponding variable is evaluated.

During each time step, the element strain rate $\dot{\varepsilon}_{ij}$ is related to the nodal displacements in the following usual fashion,

$$\dot{\varepsilon}_{ij} = \frac{1}{2}\left(\dot{u}_{ij} + \dot{u}_{ji}\right) \tag{4–10}$$

where $\dot{u}_{ij}$ denotes the partial derivative of the i^{th} component of $\vec{u}$ with respect to the j^{th} component of the Cartesian coordinate frame. The incremental strain tensor is then calculated as

$$\Delta\varepsilon_{ij} = \dot{\varepsilon}_{ij}\Delta t \tag{4–11}$$

The constitutive relations for the deformable particles are used in an incremental form so that the implementation on the nonlinear problems can be accomplished easily. Since the particles are assumed to have an elastic isotropic behavior, the relation of stress to strain in plane–stress is expressed by the Hook's law as

$$\begin{aligned}
\Delta\sigma_{11} &= \alpha_1\Delta\varepsilon_{11} + \alpha_2\Delta\varepsilon_{22}\\
\Delta\sigma_{22} &= \alpha_2\Delta\varepsilon_{11} + \alpha_1\Delta\varepsilon_{22}\\
\Delta\sigma_{12} &= \Delta\sigma_{21} = \alpha_3\Delta\varepsilon_{12}\\
\Delta\sigma_{33} &= \alpha_2\left(\Delta\varepsilon_{11} + \Delta\varepsilon_{22}\right)
\end{aligned} \tag{4–12}$$

where

$$\alpha_1 = \frac{\left(1-\nu_p\right)E_p}{\left(1+\nu_p\right)\left(1-2\nu_p\right)},\ \alpha_2 = \frac{\nu_p E_p}{\left(1+\nu_p\right)\left(1-2\nu_p\right)} \text{ and } \alpha_3 = \frac{E_p}{1+\nu_p} \tag{4–13}$$

E_p and ν_p are the particle Young's modulus and Poisson's ratio, respectively.

In plane–stress these equations become

$$\begin{aligned}
\Delta\sigma_{11} &= \beta_1\Delta\varepsilon_{11} + \beta_2\Delta\varepsilon_{22}\\
\Delta\sigma_{22} &= \beta_2\Delta\varepsilon_{11} + \beta_1\Delta\varepsilon_{22}\\
\Delta\sigma_{12} &= \Delta\sigma_{21} = \beta_3\Delta\varepsilon_{12}\\
\Delta\sigma_{33} &= 0
\end{aligned} \tag{4–14}$$

where

$$\beta_1 = \alpha_1 - \frac{\alpha_2^2}{\alpha_1},\ \beta_2 = \alpha_2 - \frac{\alpha_2^2}{\alpha_1} \text{ and } \beta_3 = \alpha_3 \tag{4–15}$$

4.3. **Analysis stability**

4.3.1. *Time step determination*

The solution scheme used in UDEC is conditionally stable. A limiting time step that satisfies both the stability criterion for calculation of particle deformation as well as that for contact displacement is determined. The time step required for the stability of particle deformation computations is estimated as

$$\Delta t_n = 2\,min\left(\frac{m_i}{\kappa_i}\right)^{1/2} \tag{4–16}$$

where m_i is the mass associated with grid–point i; and κ_i is the measure of stiffness of the elements surrounding the grid–point. The ratio of mass to stiffness is related to the highest eigenfrequency in a linear elastic system.

The stiffness term, κ_i, must account for both the particles and contacts stiffnesses. It is calculated as the sum of the two components.

$$\kappa_i = \kappa_i^{con} + \sum \kappa_i^{CST} \tag{4–17}$$

The first term on the right–hand side denotes the contact stiffness and exists only for grid–points located on the particle boundary. It is taken as the product of the contact stiffness coefficients, k, and the sum of the lengths of the two particle edge segments adjacent to the grid–point i.

The second term represents the sum of the contributions of the stiffness of all the CST elements connected to the grid–point i, which are estimated as

$$\kappa_i^{CST} = \frac{8}{3}\left(\frac{E_p\left(1-v_p\right)}{\left(1+v_p\right)\left(1-2v_p\right)}\right)\frac{b_{max}^2}{h_{min}} \tag{4–18}$$

where E_p and v_p are the Young's modulus and the Poison's ratio of the particle, respectively; b_{max} is the largest CST element edge, and h_{min} is the minimum height of them.

For calculations of contact displacement, the limiting time step is calculated by analogy to a single degree–of–freedom system, as

$$\Delta t_c = 2C_1\left(\frac{M_{min}}{K_{max}}\right)^{1/2} \tag{4–19}$$

where M_{min} is the mass of the smallest particle in the system; and K_{max} is the maximum contact stiffness. The multiplier C_1 is a user–supplied value that accounts for the fact that a single particle may be in contact with several particles simultaneously. A typical value for C_1 is 0.1.

The controlling time step for a quasi–static or a moderate–rate dynamic analysis is

$$\Delta t_s = min\left(\Delta t_n, \Delta t_c\right) \tag{4–20}$$

However, the time step suggested above may not guarantee the stability of the analysis under high–rate dynamic loading. In fact, high particle speed, which has not been introduced into the formulation yet, may be the critical factor in this case. Therefore, the Courant–Friedrichs–Lewy (CFL) (Courant 1967) condition is additionally applied to provide a more conservative limitation for the time step. The critical time step, suggested by the CFL condition, is calculated as follows,

$$\Delta t_{CFL} = C_2\, min\left(\frac{b_j}{c_p + v_j} \right) \tag{4–21}$$

where c_p is the material adiabatic sound speed; b_j is the smallest edge size for particle j; v_j is the particle speed, and C_2 is a constant factor around 0.3. Finally, the time step for the analysis under high–rate loading is

$$\Delta t = min\left(\Delta t_s , \Delta t_{CFL} \right) \tag{4–22}$$

4.3.2. *Mechanical Damping*

There are several designs for the mechanical damping in UDEC. For the CFM, *local damping* is the most convenient choice in which the damping force on a node is proportional to the magnitude of the unbalanced force. In this scheme, the direction of the damping force is such that energy is always dissipated. For this purpose, the equations of motion (Equation 4–9) are replaced by the following equation, which incorporates local damping,

$$\dot{\vec{u}}^{(t+\Delta t/2)} = \dot{\vec{u}}^{(t-\Delta t/2)} + \left\{ \vec{F}^{(t)} - \alpha \left| \vec{F}^{(t)} \right| sgn\left(\dot{\vec{u}}^{(t-\Delta t/2)} \right) \right\} \frac{\Delta t}{m_g} \tag{4–23}$$

where α is a constant. This type of damping has several advantages including that the magnitude of damping constant, α, is dimensionless and is independent of the model properties or boundary condition. Moreover, the amount of damping varies from point to point (Cundall 1987).

4.4. **Implementation of CFM in UDEC**

In UDEC, the discrete–element information is all stored within a linked–list data structure that corresponds to the topological structure of the physical system. Each physical entity, such as a particle or contact, is represented by a data element that is linked by pointers to the data structure from a main accessible storage array. The topological nature of the data structure permits a direct translation of the model structural data into UDEC. The physical characteristics describing particle size and shape and the contact locations are translated directly into data elements and linked to the data structure.

Importing the particle data into UDEC, each particle is independently discretized into a mesh of triangular elements. The automatic mesh generator performs the internal particle discretization and stores the CST elements information in the data structure. Other data for constitutive models, material properties and initial and boundary conditions are also linked to the data structure during model generation. The structure facilitates the assignment of different constitutive models, properties and conditions to user–selected locations in the model. The data structure can easily be accessed via the UDEC internal programming language, FISH (Section 4.5.2).

4.4.1. *Particle generation*

Since the CFM simulates material as the collection of irregular triangular particles, a preprocessor program is needed to produce a mesh of triangles with random size. This process is implemented by developing a separate computer code, which creates a particle/contact data file importable into UDEC. For this purpose, the pre–processer algorithm is designed to insert points into the domain of interest such that the spacing between each two is not smaller than a limit value of d_l. d_l is actually the lower bound of the future particle edge size, d_p. The x– and y–coordinates of the points are produced by the conventional pseudorandom number generators imbedded in any compiler used, e.g. the function *rand()* in Visual C++ 6.0 (Zaratian 1997). The point insertion continues until a specific criterion in terms of the minimum number of the points inserted, n_{min}, is satisfied.

Using 2D Delaunay triangulation (Delaunay 1934), the triangular net is then constructed on the preinserted points. The algorithm proposed by Du (1996) is used to implement the Delaunay triangulation.

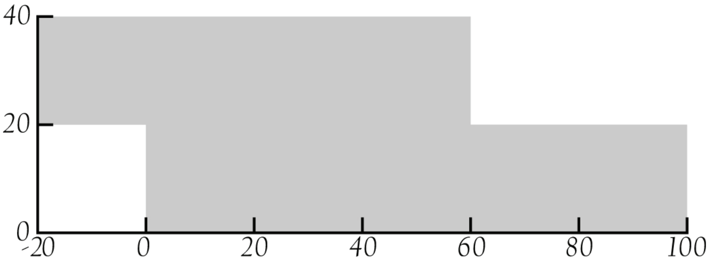

a. domain geometry

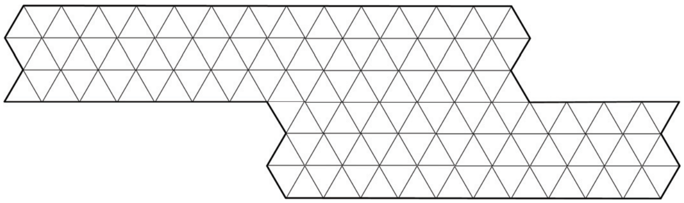

b. regular discretization of domain with n_{max} inserted points

Figure 4–7: An irregular domain designed for verification and its regular discretization

Four tests on an irregular concave domain as illustrated in Figure 4–7a are designed to verify the adequacy of the proposed particle generation algorithm, and to find a valid estimation for n_{min}. If the domain was estimated by a collection of equilateral triangles with the edge size of d_l (see Figure 4–7b), the number of points inserted, which was the maximum number possible, would be

$$n_{max} = \frac{2S_D}{\sqrt{3}d_l^2} - \frac{P_D}{2d_l} + 1 \tag{4–24}$$

where S_D is the surface area of the domain of interest into which the points are being added, and P_D is its perimeter which is highlighted by the thick black line in Figure 4–7b.

Using four values for d_l, i.e., 1, 2, 3 and 4, the preprocessor is run. Over fifty million cycles of point generation is tried to ensure that no more point can be inserted into the domain, and the mesh generated, i.e., particle assemblage, is shown in Figure 4–8.

The histograms of the percentage distribution of the particles edge size for each particles assemblage is presented by Figure 4–9, where the horizontal axes are normalized to d_l.

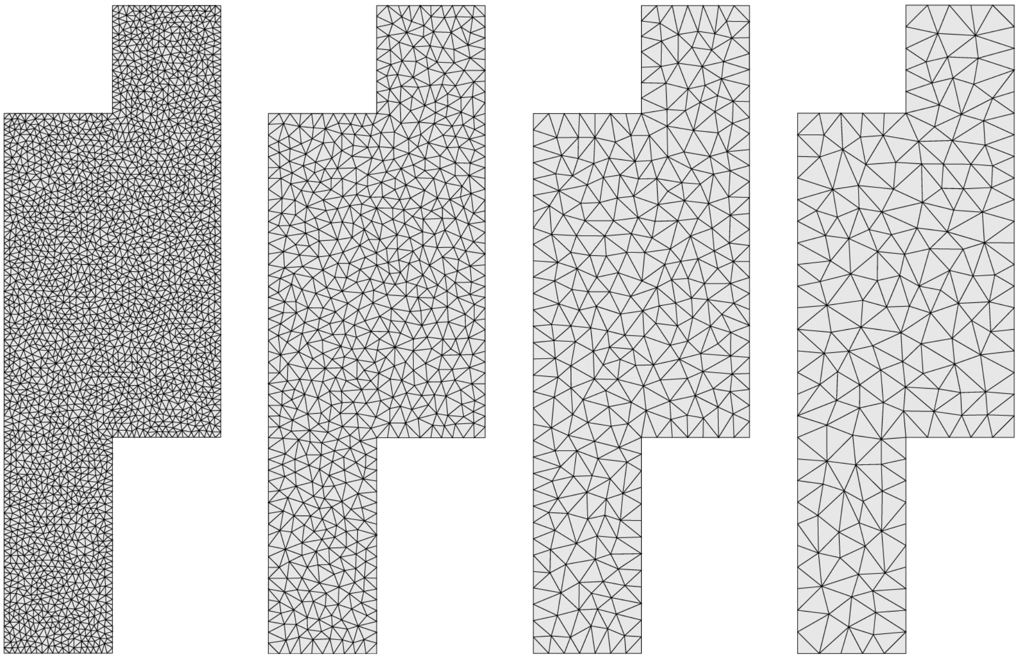

a. T1 (d_l = 1.0) b. T2 (d_l = 2.0) c. T3 (d_l = 3.0) d. T4 (d_l = 4.0)

Figure 4–8: Four different particle assemblages generated by different d_l values

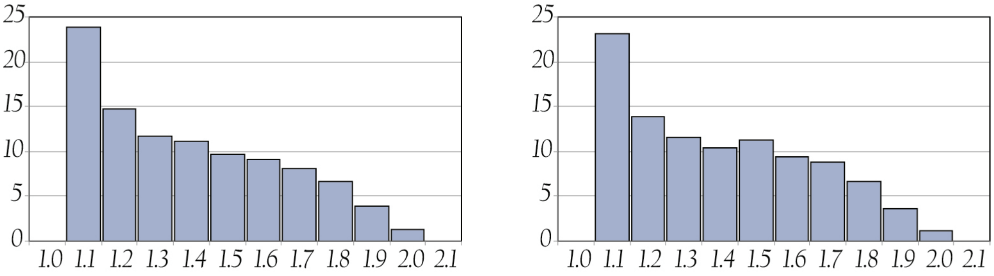

a. model T1 b. model T2

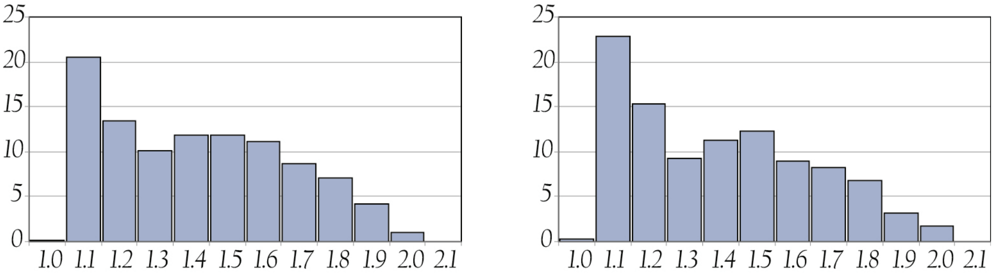

c. model T3 d. model T4

Figure 4–9: Histograms of percentage distribution of particles edge size

Figure 4–9 clearly shows that all the samples follows nearly the same particle edge size distribution. Regardless of d_l, the majority (over 90%) of the particles generated have an edge size between 1.1d_l to 1.8d_l, where the mean value declines to the left, i.e., 1.1d_l. This result can be also observed in Table 4–1, where the minimum (d_{min}), maximum (d_{max}), and average (d_{mean}) values of the normalized edge size are listed. As seen, d_{mean} is fixed at about 1.35, and the ratio of the ultimately inserted points, n_{insert}, to n_{max} is around 0.57.

Table 4–1: Tests results in terms of number of points inserted, number of triangles and edges created and minimum, maximum, and mean length of particles edge

Test	d_l	n_{max}	n_{insert}	n_{insert}/n_{max}	$n_{triangle}$	n_{edge}	d_{min}	d_{max}	d_{mean}
T1	1	3997	2346	0.59	5010	7355	1.0000	1.9914	1.3369
T2	2	960	548	0.57	1254	1801	1.0000	1.9936	1.3445
T3	3	409	223	0.55	552	774	1.0002	1.9957	1.3622
T4	4	220	123	0.56	324	446	1.0003	1.9842	1.3413

All the results presented yield to this conclusion that to generate a particle assemblage with the average edge size of d_p, d_l should be taken as 0.75d_p, and at least 0.57n_{max} points must be randomly inserted into the domain. Then, the majority of triangles created will have an edge size between 0.85 to 1.35 times d_p.

To verify these results, particle generation is repeated again to produce an assemblage with the average edge size of d_p = 2.0. As suggested above, d_l = 1.5 and since n_{max} calculated by Equation 4–24 is 1741, n_{insert} = 992. Finally, as Figure 4–10 shows, more that 90% of the triangles generated have the expected edge size, with the mean value of 2.03.

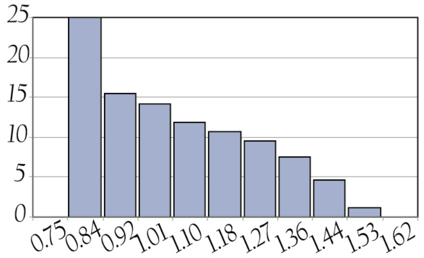

Figure 4–10: Histogram of percentage distribution of particles edge size for a model generation with d_p = 2.0 (horizontal axis is normalized to d_p)

4.4.2. *Built–in programming*

FISH is the programming language embedded within UDEC that enables the user to define new variables and functions. As mentioned earlier, FISH functions have access to the linked–list data structures. The global indices that point to these data structures are provided as FISH scalar variables, which are contained in a series of files supplied with UDEC.

These functions are vastly used for the CFM implementation to extend the model usefulness and to add user–defined features, e.g. to plot and print variables associated with the CFM, to implement special model generators, to apply servo–control for numerical tests, and to perform calibration process and parametric studies.

CHAPTER 5

Orthotropic cohesive contact model

The model failure behavior is controlled by the contact constitutive law. Hence, the failure characteristics of rock, i.e., anisotropy, brittleness and rate–dependency, must be appropriately reflected in the CFM contact model. This chapter describes the cohesive contact model developed for this purpose. A cohesive contact acts like some glue cohering particles together, which follows an orthotropic behavior at the same time. It is also assumed to have a decaying stiffness in the pre–failure stage in order to represent the damage behavior of the fracture process zone. The necessity of this assumption will be justified in this chapter and additionally in Chapter 8, where loading rate effects are needed to be introduced into the formulation.

Depending on whether a contact undergoes tension or shear, it endures either gradual or perfect stress softening after its strength is exceeded. In tension, the supposed glue gradually loses its stress and is stretched up to a length called *contact cohesive displacement*, beyond which the contact will no longer endure stress. In shear, the contact stress abruptly decreases to a residual frictional strength, which represents the friction acting on the fractured surface.

5.1. Formulation

In the cohesive contact model, the stress σ applied on the contact surface is defined as

$$\sigma=\sigma\left(\delta_{eff},k_t,k_s,t_c,c_c,\phi_c,D\right) \tag{5–1}$$

where δ_{eff} is the contact effective displacement, and k_t and k_s denote the contact initial stiffness coefficients in tension and shear, respectively. The parameters t_c, c_c, and ϕ_c characterize the strength of contact. They respectively referred to as contact tensile strength, contact cohesion, and contact friction angle. D is the contact damage variable.

In mixed–mode separation, i.e., concurrent existence of normal and shear displacements of contact, δ_{eff} is defined as

$$\delta_{eff} = \begin{cases} \sqrt{\delta_n^2 + \delta_s^2} & \delta_n \geq 0 \\ \delta_s & \delta_n < 0 \end{cases} \tag{5–2}$$

where δ_n and δ_s are the normal separation and shear sliding over the contact surface (see Figure 4–2). δ_n is assumed positive where the contact undergoes opening (tension).

A review of various types of fracture laws is given by, e.g. Shet and Chandra (2002). Presented in Figure 5–1, the contact model developed for the CFM can be regarded as a combination of those given by Xu et al. (2003) and Zhou et al. (2005a). However, it contains additional parameters to account for the initial stiffness of the cohesive surface and the irreversibility of separation with damage.

5.1.1. *Tensile behavior of contact*

Contact cohesive stress in tension is expressed as

$$\sigma = \begin{cases} k_t \delta_{eff} \, exp(-\delta_{eff}/\delta_{ct}) & \delta_{eff} \leq \delta_{ct} \\ \left.\begin{matrix} t_c(1-D) & \delta_{eff} = \delta_{max} \\ k_{red}\delta_{eff} & \delta_{eff} < \delta_{max} \end{matrix}\right\} & \delta_{ct} < \delta_{eff} \leq \delta_{ut} \\ 0 & \delta_{eff} > \delta_{ut} \end{cases} \tag{5–3}$$

In hardening stage ($\delta_{eff} \leq \delta_{ct}$), the governing equation is the exponential traction–separation law described by Xu and Needleman (1995). δ_{ct} is the critical tensile displacement of contact beyond which cohesive softening happens, and δ_{ut} is the ultimate tensile displacement of contact at which contact entirely loses its cohesive strength. In this stage, stress–displacement behavior elastic, i.e., the unloading and reloading paths are the same and no energy dissipation occurs within contact.

Substituting $\sigma = t_c$ and $\delta_{eff} = \delta_{ct}$, and solving for δ_{ct}, it is obtained as follows where $e = exp(1)$ is the base of the natural logarithm.

$$\delta_{ct} = e\frac{t_c}{k_t} \tag{5–4}$$

In softening stage ($\delta_{ct} < \delta_{eff} \leq \delta_{ut}$), contact is permitted to release energy during unloading–reloading cycles. δ_{max} is then defined as the maximum effective displacement that contact has ever undergone (Figure 5–1a). δ_{max} is δ_{eff}, when contact is increasingly opened, and held fixed as it undergoes unloading and reloading until δ_{eff} again reaches δ_{max}.

The damage variable is defined as follows.

$$D = \frac{\delta_{max} - \delta_{ct}}{\delta_{ut} - \delta_{ct}} \tag{5–5}$$

As contact undergoes softening, D irreversibly increases from 0 to 1 or remains constant, even if multiple unloading–reloading cycles happens.

In unloading–reloading cycles ($\delta_{eff} < \delta_{max}$), contact follows a linear stress–displacement path, where k_{red} is defined as the secant stiffness at the point with an effective displacement equal to δ_{max} (see Figure 5–1a).

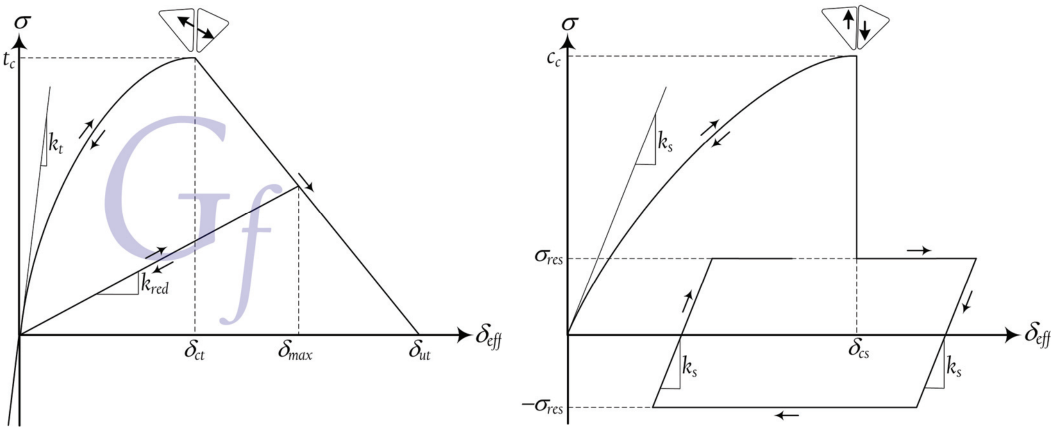

a. tensile behavior b. compressive–shear behavior

Figure 5–1: Schematic stress–displacement behavior of cohesive contact, arrows denote loading, unloading and reloading paths (displacements at peak points are exaggerated)

5.1.2. *Compressive–shear behavior of contact*

When contact is sheared under compression, the stress–displacement law is described as

$$\sigma = \begin{cases} k_s \delta_{eff} \, exp(-\delta_{eff} / \delta_{cs}) & \delta_{eff} \leq \delta_{cs} \\ \sigma_{res} = -k_t \delta_n \, tan(\phi_c) & \delta_{eff} > \delta_{cs} \end{cases} \tag{5–6}$$

Similarly, the critical shear displacement of contact is calculated as follows.

$$\delta_{cs} = e \frac{c_c}{k_s} \tag{5–7}$$

The unloading–reloading path of contact is linear as demonstrated in Figure 5–1b, where the contact stress increment (or decrement) is calculated as

$$\Delta\sigma = \begin{cases} k_s \Delta\delta_{eff} & \sigma < \sigma_{res} \\ 0 & \sigma = \sigma_{res} \end{cases} \tag{5–8}$$

In each solution iteration, $\Delta\sigma$ is calculated and added to the current value of the contact stress to produce its new value.

Finally, the normal component of contact force is obtained as

$$F_n = \begin{cases} -\sigma \dfrac{\delta_n}{\delta_{eff}} a_c & \delta_n \geq 0 \\ -k_t \delta_n a_c & \delta_n < 0 \end{cases} \tag{5–9}$$

where a_c is the contact surface area which is defined based on the contact domain and length. Contact shear force is calculated in a similar way using

$$F_s = -\sigma \frac{\delta_s}{\delta_{eff}} a_c \tag{5–10}$$

5.1.3. *Contact fracture energy*

According to the Griffith–Irwin's fracture criterion, the condition necessary for fracture propagation is if sufficient energy is provided to detach material thereby increase the fractured surface. This energy should be supplied by the loading system and the elastic energy stored in the body. By definition, the Griffith's fracture energy, G_f is the rate of this energy per unit area along the fracture edge. The area under the curve in Figure 5–1a represents the energy needed to fully open the unit area of contact surface. Since contact is the numerical representation of fracture, the area under the curve should be equal to G_f.

$$G_f = \int_0^{\delta_{ut}} \sigma d\delta_{eff} = t_c \delta_{ct}(e-2) + t_c \frac{\delta_{ut} - \delta_{ct}}{2} \tag{5–11}$$

5.2. CFM micro–parameters

The parameters involved in modeling are classified under the term *micro–parameter*. Table 5–1 lists them along with the analogous material properties.

Table 5–1: Material properties and CFM micro–parameters

material property	model micro–parameter
Young's modulus (E)	particle Young's modulus (E_p)
Poisson's ratio (ν)	particle Poisson's ratio (ν_p)
fracture toughness in Mode–I (K_{IC})	contact initial tensile stiffness coefficient (k_t)
fracture toughness in Mode–II (K_{IIC})	contact initial shear stiffness coefficient (k_s)
Brazilian strength (σ_t)	contact tensile strength (t_c)
internal cohesion (C)	contact cohesion (c_c)
internal friction angle (ϕ)	contact friction angle (ϕ_c)
uniaxial compressive strength (σ_c)	contact ultimate tensile displacement (δ_{ut})

Since any CFM simulation is deeply affected by the micro–parameters, they must be appropriately set such that the model reproduces a response similar to that of the physical material. To reach this purpose, the relation between the micro–parameters and the model behavior should be investigated. This is done by establishing analytical and statistical equations, which explicitly define each model macroscopic response in terms of the micro–parameter. These equations, in fact, express the physical interpretation of the micro–parameters.

5.2.1. *Physical interpretation of contact stiffness coefficient*

In numerical simulation of structures involving bodies in contact, the effect of ill–conditioning may destabilize the solution. Briefly speaking, this problem is raised due to the lack of appropriate judgment about the contact stiffness. As commonly thought, the ideal choice for the contact stiffness is to take it as infinite to prevent any reduction in the global stiffness of the structure. However, this assumption causes numerical inconsistencies within the FEM solver or the DEM contact force algorithm (e.g. Babuska and Suri 1992; Chilton and Suri 1997). Therefore, contact stiffness is arbitrarily reduced, but not so much as the structure global stiffness is altered. That is why no exact suggestion for the contact stiffness is provided yet, and it is always assumed as an arbitrary parameter, which is estimated by empirical formula (e.g. Zhai et al. 2004; Pinho et al. 2006; Elmarakbi et al. 2009).

However, the fracture cohesive zone theory suggests that the fracture process must be regarded as the combination of material detachment and the cohesive zone, i.e., damaged area surrounding the crack–tip. Since the model assumes no damage for particles, contact stiffness must represent the stiffness of the damaged material of the cohesive zone. Thus, before fracture initiation, the contact (initial) stiffness coefficient should be as follows for tension and shear,

$$k_t = \frac{E}{w} \text{ and } k_s = \frac{G}{w} \tag{5–12}$$

where E and G are the Young's and shear modulus of the undamaged material, and w is the thickness of the cohesive zone, perpendicular to the orientation of crack propagation.

Contact should gradually lose its stiffness upon opening or sliding in order to represent the cohesive zone damage. That is why the nonlinear (exponential) curves are adopted for the contact hardening behavior in tension and shear (see Figure 5–1), where their derivative at the origin equals the suggestions provided by Equation 5–12. The slope of the curves then gradually decays with the contact displacement increase, and ultimately it reaches zero. In tension, the softening stage then begins and contact starts losing its cohesive stress, and in shear, contact friction is mobilized on the fractured surface.

As a matter of fact, the assumption of infinite contact stiffness signifies that the cohesive zone in the model has no thickness, which is in contradictory with the cohesive zone theory. Therefore, the usual assumption of huge contact stiffness is not only needed, but also incorrect.

a. Estimation of cohesive zone thickness

There are several descriptions to formulate the length of the cohesive zone (e.g. Anderson 1995), but not for its thickness. This section provides an estimation for the cohesive zone thickness in terms of the material mechanical properties.

a.1. Material strength in molecular mechanics

A material cracks when the sufficient stress and energy are applied to break the inter–molecular bonds. These bonds hold the molecules together and their strength is supplied by the attractive forces between the molecules. Many equations have been proposed to formulate this force and its potential energy. The Lennard–Jones potential (Griebel et al. 2007) is a simple and extensively used function in this way,

$$\Psi(x)=\alpha\varepsilon\left[\left(\frac{\xi}{x}\right)^{n}-\left(\frac{\xi}{x}\right)^{m}\right] \tag{5–13}$$

where $m < n$. x denotes the separation distance between two adjacent molecules, and

$$\alpha=\frac{1}{n-m}\left(\frac{n^{n}}{m^{m}}\right)^{\frac{1}{n-m}} \tag{5–14}$$

This potential is parameterized by ξ and ε. As depicted in Figure 5–2, ε describes the depth of the potential and thereby the strength of the repulsive and attractive forces. The value ξ parameterizes the zero crossing of the potential. The integer m and n are dependent of the material molecular nature and are more commonly among 6 to 16.

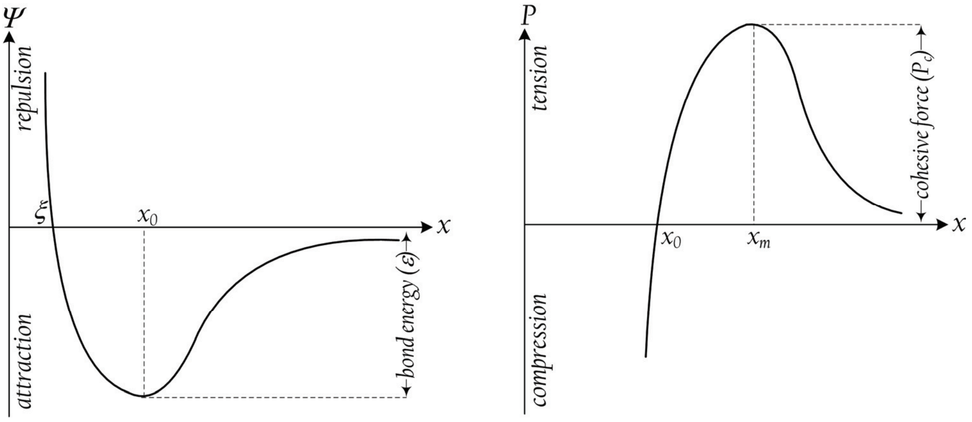

Figure 5–2: Plots of Lennard–Jones' potential function (left) and intermolecular force (right)

As the potential derivative with respect to x, the inter–molecular force $P(x)$ is written as

$$P(x)=\frac{\partial\Psi}{\partial x}=\frac{\alpha\varepsilon}{x}\left[-n\left(\frac{\xi}{x}\right)^{n}+m\left(\frac{\xi}{x}\right)^{m}\right] \tag{5–15}$$

The peak value of the inter–molecular force, which is called cohesive force, P_c, happens at x_m as shown in Figure 5–2. Solving the derivative of $P(x)$ for x,

$$x_m=\xi\left(\frac{n(n+1)}{m(m+1)}\right)^{\frac{1}{n-m}} \tag{5–16}$$

Substituting x_m into Equation 5–15 leads to

$$P_c=\alpha\frac{\varepsilon}{\xi}\left(-n\left(\frac{n(n+1)}{m(m+1)}\right)^{\frac{-n-1}{n-m}}+m\left(\frac{n(n+1)}{m(m+1)}\right)^{\frac{-m-1}{n-m}}\right) \tag{5–17}$$

The equilibrium spacing between two molecules, x_o occurs when the potential energy is at a minimum or the force is zero (see Figure 5–2). Thus if solving Equation 5–15 for x,

$$x_0=\xi\left(\frac{n}{m}\right)^{\frac{1}{n-m}} \tag{5–18}$$

In unit volume of a perfect material, there should ideally exist $1/x_0^3$ molecules and $3/x_0^3$ bonds. However, the number of molecules and bonds in reality never reaches these predictions because of material imperfections as molecular vacancies and nano–fractures. Therefore, the number of existing bonds, n_b, can be defined as

$$n_b=\gamma\frac{3}{x_0^3} \tag{5–19}$$

where γ is a multiplier, smaller than one, that indicates the rate of the existing bonds per unit volume of the physical material.

For perfect material, P_c/x_0^2 estimates the material tensile strength, σ_t. However, σ_t never reaches P_c/x_0^2 again due to material imperfections. Given the definition of γ, σ_t can be estimated as

$$\sigma_t=\gamma\frac{P_c}{x_0^2} \tag{5–20}$$

a.2. Material fracturing

A tensile force is required to increase the separation distance from the equilibrium value. If this force exceeds the cohesive force, the bond is completely severed, and the material starts cracking. The energy needed to break a single bond, called bond energy, is calculated as follows.

$$U=\int_{x_0}^{\infty}P(x)dx=\Psi(x)\Big]_{x_0}^{\infty}=-\Psi(x_0)=\varepsilon \tag{5–21}$$

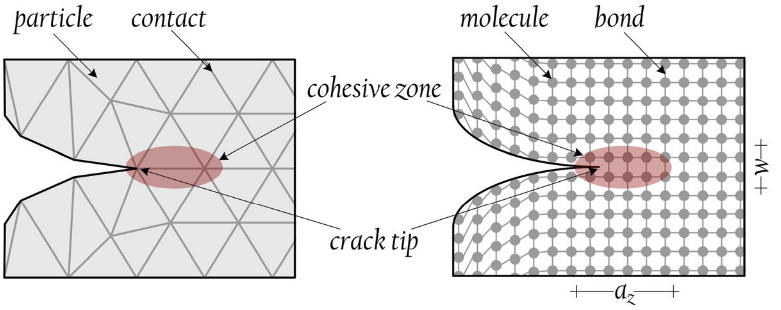

Figure 5–3: Fracture representation in CFM simulation (left) and molecular–scale (right)

As discussed in Chapter 2, there is a high stress concentration at the areas close to the crack tip during crack propagation process. Therefore, bond rupture takes place across an extended crack tip, i.e., fracture process zone. As Figure 5–3 suggests, the number of bonds located at the cohesive zone, n_{bc} can be estimated by the multiplication of n_b by the volume of the cohesive zone:

$$n_{bc} = 3\gamma \frac{w a_z}{x_0^3} \tag{5–22}$$

where w and a_z denotes the thickness and the surface of the cohesive zone, respectively.

When a bond breaks, a quantity of energy equal to U is dissipated. The accumulation of these energies over the cohesive zone surface supplies the energy dissipation through fracturing. Therefore, the Griffith's fracture energy G_f, defined as the rate of total energy release per unit cracked area, is expressed as

$$G_f = \frac{n_{bc}\varepsilon}{a_z} = 3\gamma \frac{w\varepsilon}{x_0^3} \tag{5–23}$$

Substituting the parameter ε obtained from Equation 5–17 into the above relation,

$$G_f = 3\frac{\gamma}{\alpha}\frac{w\xi}{x_0^3}P_c\left(-n\left(\frac{n(n+1)}{m(m+1)}\right)^{\frac{-n-1}{n-m}} + m\left(\frac{n(n+1)}{m(m+1)}\right)^{\frac{-m-1}{n-m}}\right)^{-1} \tag{5–24}$$

Substituting P_c by Equation 5–20, x_0 by Equation 5–18, and solving for w, the cohesive zone thickness is estimated in terms of σ_t and G_f as

$$w = \frac{1}{3\beta}\frac{G_f}{\sigma_t} \tag{5–25}$$

where

$$\beta = \frac{\frac{1}{m} - \frac{1}{n}}{\left(\frac{m+1}{n+1}\right)^{\frac{m+1}{n-m}} - \left(\frac{m+1}{n+1}\right)^{\frac{n+1}{n-m}}} \tag{5–26}$$

depends on the integers m and n. Table 5–2 shows that β is relatively constant at 0.25 for common values of $m \in [8,12]$ and $n \in [13,18]$.

Table 5–2: Values of β for common values of m and n

m	n = 13	n = 14	n = 15	n = 16	n = 17	n = 18
8	0.30	0.29	0.28	0.27	0.26	0.26
9	0.28	0.27	0.26	0.25	0.25	0.24
10	0.26	0.25	0.24	0.24	0.23	0.22
11	0.25	0.24	0.23	0.22	0.22	0.21
12	0.24	0.23	0.22	0.21	0.21	0.20

In mixed mode fracture, G_f is stated as

$$G_f = \frac{K_{IC}^2}{\tilde{E}} + \frac{K_{IIC}^2}{\tilde{E}} \tag{5–27}$$

where $\tilde{E} = E$ for plain–stress, and $\tilde{E} = E/(1-\nu^2)$ for plain–strain. If contact undergoes pure tension,

$$w = \frac{1}{3\beta}\frac{K_{IC}^2}{\tilde{E}\sigma_t} \tag{5–28}$$

and in case of pure sliding

$$w = \frac{1}{3\beta}\frac{K_{IIC}^2}{\tilde{E}\sigma_t} \tag{5–29}$$

Given Equation 5–12, the contact initial stiffness coefficients in plane–stress are,

$$k_t = 3\beta\frac{E^2\sigma_t}{K_{IC}^2} \text{ and } k_s = 3\beta\frac{GE\sigma_t}{K_{IIC}^2} \tag{5–30}$$

and in plane–strain,

$$k_t = 3\beta\frac{E^2\sigma_t}{\left(1-\nu^2\right)K_{IC}^2} \text{ and } k_s = 3\beta\frac{GE\sigma_t}{\left(1-\nu^2\right)K_{IIC}^2} \tag{5–31}$$

The ratio of the initial stiffness coefficients is

$$\frac{k_s}{k_t} = \frac{1}{2(1+\nu)}\left(\frac{K_{IC}}{K_{IIC}}\right)^2 \tag{5–32}$$

5.2.2. *Particle elastic properties*

Particle stiffness and that of contact together determine the model global stiffness. If contact stiffness is much higher than that of particle, its effect can be neglected. As a measure of particle deformability, E/d_p can be compared with the contact stiffness coefficients to examine the validity of this condition, where d_p denotes the particle edge size. Table 5–3 lists the value of k_t, obtained from Equation 5–31, in comparison to the ratio of E/d_p for different materials studied in the thesis.

Table 5–3: Values of contact stiffness coefficient versus particle deformability ratio for brittle materials studied in thesis[1]

material type	Augig granite	Laurentian granite	Transjurane sandstone	gypsum plaster	PMMA
k_t [MPa/mm]	2.60e+6	3.79e+7	8.30e+5	2.61e+3	6.64e+5
E/d_p [MPa/mm]	6.45e+3	1.80e+5	6.25e+3	6.50e+2	3.09e+4

Since the contact stiffness is one to three orders greater than the particle deformability ratio, contacts do not have considerable effect on the model global elasticity. Therefore,

---

[1] Further information on Augig granite and Transjurane sandstone is found in Chapter 6; for gypsum plaster in Chapter 7; for PMMA in Chapter 8; and for Laurentian granite in Chapter 9.

the Young's modulus and the Poisson's ratio of the model particles are assumed equal to those of the materials to make the model reproduce their Young's modulus and Poisson's ratio:

$$E_p = E \text{ and } \nu_p = \nu \tag{5–33}$$

5.2.3. *Contact strength parameters*

Although the micro–parameters related to the model elasticity, i.e., E_p, ν_p, k_t, and k_s, are explicitly calculated through Equations 5–30 to 5–33, the others, i.e., t_c, c_c, and ϕ_c, are still unknown (note that given G_f and k_t, δ_{ut} is related to t_c and calculated through Equation 5–11). A calibration process in which the model response is compared with that of physical material is required to obtain t_c, c_c, and ϕ_c. The calibrated micro–parameters should be unique and result in the best quantitative and qualitative agreement between the model response and that of tested rock in terms of the Brazilian tensile strength, uniaxial compressive strength, internal cohesion and internal friction angel. Note that these four parameters are dependent of each other. In other words, if having three of them for a typical material, the forth is predictable by the Mohr–Coulomb equations. Therefore, tensile strength, internal cohesion, and internal friction angle are considered as the parameters characterizing material mechanical response.

Since the model failure is controlled by the contact model, tensile strength, internal cohesion, and internal friction angle of the modeled material are related to t_c, c_c and ϕ_c of contact. If finding these relations in an explicit algebraic form, there will be three equations with the same number of unknowns, i.e., t_c, c_c, and ϕ_c, that will lead to a unique solution.

As described in the next chapter, the calibration process estimates these equations by a statistical approach called Design Of Experiment (DOE). The DOE provides a limited number of suggestions for the micro–parameters to simulate the laboratory tests. Using the obtained results from the simulations, the DOE eventually offers the equations on a polynomial form of desirable order.

5.3. **Implementation of developed contact model in UDEC**

The source code of UDEC is needed to be developed to implement the proposed contact model. Since the source code is originally written in Visual C++ 6.0, any development of UDEC requires sufficient knowledge about this programming environment, particularly the object–oriented features.

The flowchart presented in Figure 5–4 (next page) illustrates the algorithm used to carry out the formulation of the cohesive contact model. Note that it includes merely those equations that are related to the contact stress calculation. The rest of the formulation, e.g. contact force calculation, as well as the functional or object–oriented design of the code, i.e., input data management, interface with the code main body and class structure, are not comprised in Figure 5–4.

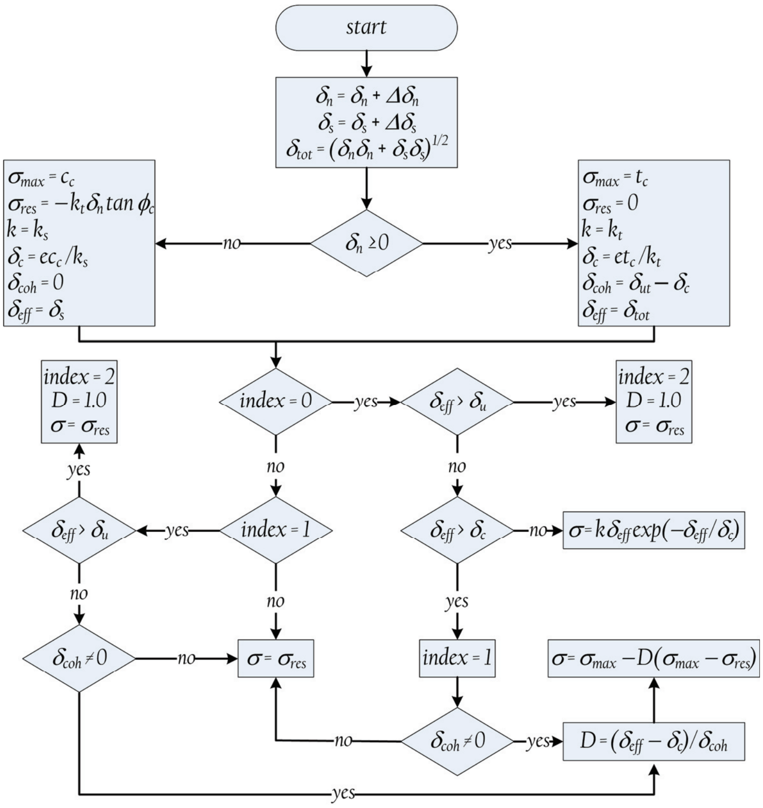

Figure 5–4: Flowchart illustrating the algorithm adopted to calculate contact stress in terms of contact separation mode and effective displacement

CHAPTER 6

Compressive and tensile failure of rock material

The CFM applicability for rock static analysis is explored in this chapter. First, the CFM capability for the reproduction of fracture mechanics behavior is examined. The results of this part approves that the CFM can reproduce the patterns of stress distribution at the crack tip as the Linear Elastic Fracture Mechanics (LEFM) suggests.

The standard laboratory tests of rock are then modeled to verify the model adequacy for rock simulation. The presented results show that a unique set of the micro–parameters exists using which the CFM properly reproduces the material macroscopic response as observed in the tests.

6.1. Reproduction of fracture mechanics behavior

Although contact failure in a particle assemblage might sound conceptually different from cracks propagating in a brittle continuum, a formal link could be established between the CFM numerical mechanism and the LEFM. For this purpose, pure tensile failure, defined as Mode–I, is simulated. Meanwhile, some mathematical developments are derived to establish closed–form expressions describing the relationship between contact tensile strength, particles size, and material fracture toughness.

6.1.1. *Simulation of material fracture in Mode–I*

Consider the 2D square plate shown in Figure 6–1 (next page), in which a crack, i.e., a line of contacts with no strength, is created in a packing of equilateral triangles of the side length $d_p = 0.4$ *mm*. No contact failure is assumed to let the plate have perfect elastic behavior. Width of the plate is 100 *mm* and it is subjected to an extension strain normal to the crack. The material properties assumed for the plate are the Young's modulus, E =

18000 *MPa* and the Poisson's ratio, $\nu = 0.26$. The contact stiffness coefficients in tension and shear are taken as $k_t = k_s = 1.0\times10^8$ *MPa/mm*.

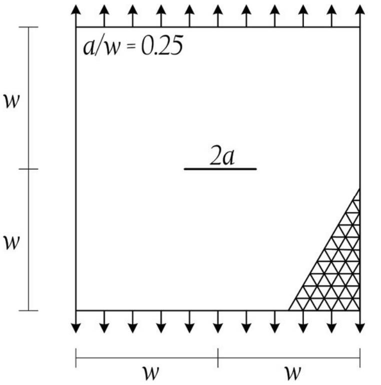

Figure 6–1: Plate particle assemblage with deformable particles

The crack with half–width of $a = 12.2$ *mm* contains 61 particles along its width. The model boundaries are at a distance of 4*a* and 3*a* above and in front of the crack, respectively.

According to the LEFM (Anderson 1995), for a through–thickness crack of half–width *a* in a wide plate of isotropic linear elastic material subjected to a remote tensile stress, σ_f, acting normal to the crack, the induced stress, σ_n, acting on the crack plane near the crack tip, i.e., r ‹‹ a, is

$$\sigma_n = \sigma_f \sqrt{a/2r}\cdot C\left(a/w\right) \tag{6–1}$$

where *r* is the distance from the crack tip and *C* is a function of model geometry as presented by Equation 6–2.

$$C\left(a/w\right) = \sqrt{sec\left(\pi a/2w\right)}\left(1-0.025\left(a/w\right)^2+0.06\left(a/w\right)^4\right) \tag{6–2}$$

The force F_p acting over a line segment as long as the particle side, d_p, at a mean distance of *r* is given by

$$F_p = \int_{r-d_p/2}^{r+d_p/2}\sigma_n dr = \sigma_f\sqrt{a/2}\int_{r-d_p/2}^{r+d_p/2} r^{-1/2}\, dr\cdot C\left(a/w\right) \tag{6–3}$$

Carrying out the above integration and assuming $r = (2m-1)d_p$ where *m* is a positive integer denoting the particle sequence number (e.g. for the particle next to crack tip, $m = 1$, for the next one it is 2 and so on),

$$F_p = \sigma_f\sqrt{2ad_p}\left(\sqrt{m}-\sqrt{m-1}\right)\cdot C\left(a/w\right) \tag{6–4}$$

As Equation 6–4 suggests, the largest contact tensile force occurs at the contact just adjacent the crack tip, where $m = 1$. Therefore,

$$F_p^{max} = \sigma_f \sqrt{2ad_p} \cdot C\left({}^{a}\!/_{w}\right) \tag{6-5}$$

The normalized contact forces acing along the crack plane are obtained as the division of F_p by its maximum value as follows.

$$\bar{F}_p = \frac{F_p}{F_p^{max}} = \sqrt{m} - \sqrt{m-1} \tag{6-6}$$

Figure 6–2 compares tensile forces obtained from Equation 6–6 with those calculated by the CFM simulation in which sum of tensile forces acting on both contacts of each particle creates F_p. As seen, the force magnitude obtained by the CFM fairly fits those of the LEFM that would be induced over a finite line segment near crack tip in an isotropic linear elastic continuum.

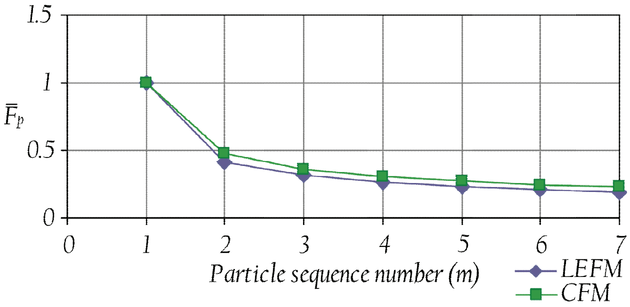

Figure 6–2: Variation of contact tensile force versus particle sequence number, m

This result confirms the CFM capabilities in reproducing the LEFM solutions, while the problematic singularities, discussed extensively in fracture mechanics references, do not arise in a discontinuous model. There is thus no need to propose some devices, such as plasticity assumptions, to eliminate the crack–tip singularity. This also verifies the LEFM validity as a tool to derive closed–from expressions needed to link micro– and macro–properties involved in the CFM.

The foregoing analysis is based on incipient failure and does not address the condition for propagation of a crack. Assuming contact fails with no cohesive displacement, the new induced force, F_p', following breakage of the contact nearest the crack tip, is found by substituting the new crack length in Equation 6–5 for the original crack length.

$$F_p' = \sigma_f \sqrt{2\left(a+d_p\right)d_p} \cdot C\left({}^{a}\!/_{w}\right) = F_p^{max} \sqrt{1+d_p/a} \tag{6-7}$$

Thus, the new maximum contact force is always greater than the previous maximum and consequently greater than the contact tensile strength. This condition determines that the crack will be propagating in an unstable fashion, if the contacts have no cohesive behavior. Thus, crack stability aspects, e.g. crack arrest, bifurcation, and propagation speed, can be controlled by adjusting contact ultimate displacement. This topic will be discussed in Chapter 8.

6.1.2. *Developing closed–form expressions*

Figure 6–3 offers a cutout of a representative particle collection, within which a finite number of contacts are already broken to form a cracked surface. Assuming that the boundary is sufficiently far from the crack, concentrated force on the first contact point, just adjacent the crack tip, is calculated by an integration similar to Equation 6–3,

$$F_c = \int_0^{d_p/2} \sigma_n dr = \sigma_f \sqrt{ad_p} \cdot \tilde{C} \tag{6–8}$$

where $\tilde{C}$ is a multiplier with a definition like $C(a/w)$ to introduce the geometry effects.

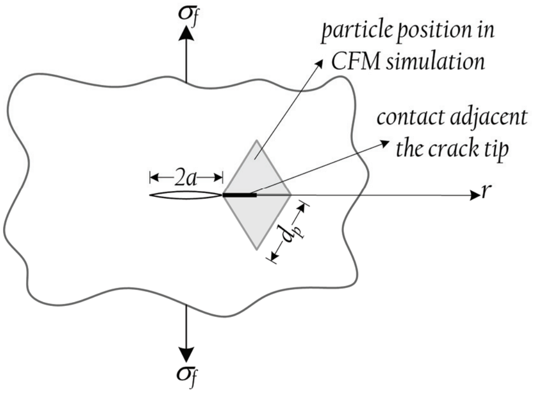

Figure 6–3: Crack representation within a particle assemblage

As soon as F_c exceeds the assumed contact strength, the contact breaks and the crack expands. Since the Mode–I stress intensity factor for the system is defined as

$$K_I = \sigma_f \sqrt{\pi a} \tag{6–9}$$

Equation 6–8 can be re–written as

$$F_c = K_I \sqrt{d_p/\pi} \cdot \tilde{C} \tag{6–10}$$

Therefore, the tensile stress created at the first contact point is evaluated by

$$\sigma_c = \frac{F_c}{(d_p - 2r_0)/2} = \frac{2K_I}{d_p - 2r_0} \sqrt{d_p/\pi} \cdot \tilde{C} \tag{6–11}$$

where r_0 denotes the particle rounding length which is most often taken 2 to 5% of the particle edge size, d_p (see Chapter 4).

For a regularly packed assemblage loaded along packing direction, at the incipient failure or crack extension, $\sigma_c = t_c$ and $K_I = K_{IC}$, where t_c is the contact tensile strength and K_{IC} is the Mode–I fracture toughness. Substituting them into Equation 6–11 yields

$$t_c = \frac{2K_{IC}}{d_p - 2r_0} \sqrt{d_p/\pi} \cdot \tilde{C} \tag{6–12}$$

Equation 6–12 indicates that contact tensile strength can be physically interpreted in terms of the material fracture toughness and depends on the particle size employed. If solving Equation 6–12 for K_{IC}, and neglecting r_0 as it is so small compared to d_p,

$$K_{IC} \approx t_c \sqrt{\pi \cdot {d_p}/{4}} \tag{6–13}$$

This result is anticipated, as the concept of fracture toughness implies an internal length scale, whereby the ratio of fracture toughness to material strength has the dimension of square root of length. The particle size supplies this internal length scale in the CFM.

a. *Interpretation of contact tensile strength in terms of the Brazilian strength*

Zhang (2002), Gunsallus and Kulhawy (1984), Bhagat (1985), Haberfield and Johnston (1989), and Harison et al. (1994) separately tested a vast range igneous, metamorphic and sedimentary rocks to explore how rock strength and fracture toughness are related together, and proposed few empirical formula. As suggested by Zhang (2002), a good estimation of the Brazilian strength, σ_t, with a coefficient of determination $r^2 = 0.94$ is provided by

$$\sigma_t = 6.88 K_{IC} \tag{6–14}$$

where the dimension of the parameters involved is expressed with the SI units.

Failure of a Brazilian specimen can be fairly estimated by the idealization presented in Figure 6–4, where sample failure initiates with tensile fracture due to the tensile stress induced at the specimen centre and along the loading axis. Similarity of Figure 6–4 to 6–3 may indicate that Equation 6–13 could be applied for the Brazilian specimen too. If substituting Equation 6–14 into 6–13,

$$\sigma_t \propto t_c \sqrt{d_p} \tag{6–15}$$

Equation 6–15 suggests that the Brazilian tensile strength predicted by the CFM varies with contact tensile strength and particle size, while it is independent of the other contact micro–parameters. Choosing a specific size of particle, t_c can be found through a trial and error procedure.

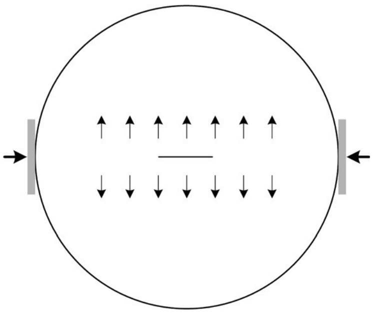

Figure 6–4: An idealized Brazilian specimen at tensile failure

6.2. Reproduction of compressive and tensile response of a hard rock

As mentioned in Chapter 2, the CFM represents brittle material as a dense packing of irregular–sized particles interacting at their boundaries. Whereas continuum models indirectly represent damage through empirical flow rules and complicated potential functions, the CFM utilizes breakage of individual structural units, i.e., contacts, to represent material failure directly.

It should be noted that some other researchers have tried similar approaches to handle the discontinuum modeling of rock. The most implementations in this way have been carried out by the Particle Flow Code (PFC) which is commercially available and used to solve many rock engineering and geomechanics problems (e.g. Potyondy and Cundall 2004; Cho et al. 2007; Yoon 2007; Wanne and Young 2008; Schöpfer et al. 2009; Tan et al. 2009). It has been applied in modeling static behavior of rocks, particularly damage and non–linear behaviors. However, there is a serious disconcerting result, i.e., PFC predicts the Brazilian Tensile Strength (BTS) of rock approximately 0.25 of its Uniaxial Compressive Strength (UCS) (Diederich 2000; Potyondy and Cundall 2004; Cho et al. 2007). Comparing various types of rocks, this value is unrealistically high, where the ratio of tensile to compressive strength is typically reported around 0.05 to 0.1 (Hoek and Brown 1998).

In addition, Potyondy and Cundall (2004) reported that calibrating PFC to the uniaxial strength gives a very low triaxial strength. They argued that the so–called *cluster logic* is required to improve the results. Cho et al. (2007) proposed the *clump logic* to resolve these shortcomings. Yoon (2007) applied a statistical approach for calibrating PFC parameters to fit mechanical properties of modeled material excluding its tensile strength.

These problems are arising because PFC generates material by rigid rounded discs, which do not appropriately represent the irregular–shaped and interlocked grains of rock. As neglecting interlocking, PFC parameters have to be chosen disproportionately large to fit the material compressive strength. Therefore, the model tensile strength will become exceedingly higher than that of rock.

The proposed logics, i.e., cluster and clump, seem to be only a way to eliminate this intrinsic defect of PFC. However, in addition to execution difficulties, these logics are suffering from some disadvantages. For example, since each cluster or clump is composed of several particles, its size is perforce much larger than that of the actual rock minerals. Moreover, PFC works with 10 parameters some of which, e.g. coefficient of friction, contact modulus, and parallel bond modulus, have no effect on the model global response, i.e., these parameters are deprived of any physical sense (Diederich 2000; Potyondy and Cundall 2004).

As Kazerani and Zhao (2010) mentioned, using polygonal rigid particles removes the discussed shortcomings, and provides a useful picture of material behavior.

This section examines the CFM capabilities to simulate mechanical behavior of a granite. It will show that the CFM is fully able to meet this objective, where no troublesome extra logic or modification is needed.

6.2.1. *Solution process*

A numerical simulation by the CFM requires proper selection of the unknown micro–parameters, i.e., t_c, c_c, and ϕ_c, by means of a calibration process in which the model responses are directly compared to the observed responses of the physical material. Depending on the application intended by the CFM, these comparisons can be made either at laboratory scale, e.g. uniaxial or triaxial and static–fatigue testing, or at field scale, e.g. evolution and extent of damage around various excavations.

From now on in this chapter, any micro–parameter expressing contact strength, i.e., t_c, c_c, or ϕ_c, is briefly called micro–parameter. The objective of this section is to develop an approach that calculates proper micro–parameters for model generation. With this approach, a set of micro–parameters is obtained by which the generated model closely reproduces physical properties of the rock material.

Once the unknown micro–parameters are obtained, they are used to generate the model. Simulation of the Brazilian tension and uniaxial compression is then carried out on the generated model and the results, in terms of strength parameters, elastic constants, and crack distribution, are compared to those of the laboratory tests. If a fair agreement is met, solution adequacy and credibleness will be verified for further applications.

6.2.2. *Numerical simulation of experiments*

As explained, a series of the conventional experiments, i.e., uniaxial/triaxial compression and the Brazilian tension, must be modeled to implement the CFM calibration. Meanwhile, the obtained results will describe how macroscopic response of a CFM simulation is influenced by the micro–parameters.

a. *Material properties*

Since Augig granite has been extensively tested by the rock mechanics laboratory (LMR) in EPFL, it is selected as a representative hard rock. As a coarse aggregate rock, it is composed of minerals ranging from 2 to 6 *mm* (4 *mm* on average). The mechanical properties of Augig granite are listed in Table 6–1.

Table 6–1: Mechanical properties of Augig granite

Young's modulus, E	25.8 GPa	internal cohesion, C	21 MPa
Poisson's ratio, ν	0.23	internal friction angle, ϕ	53°
fracture toughness in Mode–I, K_{IC}	1.5 $MPa\sqrt{m}$	Brazilian tensile strength, BTS	8.8 MPa
fracture toughness Mode–II, K_{IIC}	3.0 $MPa\sqrt{m}$	uniaxial compressive strength, UCS	122 MPa

The values of fracture toughness are average for different testing orientations. K_{IC} is measured in the EPFL LMR laboratory according to the ISRM suggested testing method for chevron bend specimens (Ulusay and Hudson 2007). However, K_{IIC} is an estimated value by those reported in the literature for other types of granite.

b. Discrete element mesh

According to the specimens' geometry and condition, a plane–strain (axisymmetric) and a plane–stress analysis are respectively adopted for the compressive and Brazilian models. The compressive cylindrical sample is 80 *mm* in diameter and 160 *mm* high, and the Brazilian specimen is a disc with a diameter of 80 *mm*. They are placed between two steel platens whose interfacial friction angle is assumed 5°. The geometry and the boundary condition of the samples modeled are illustrated in Figure 6–5.

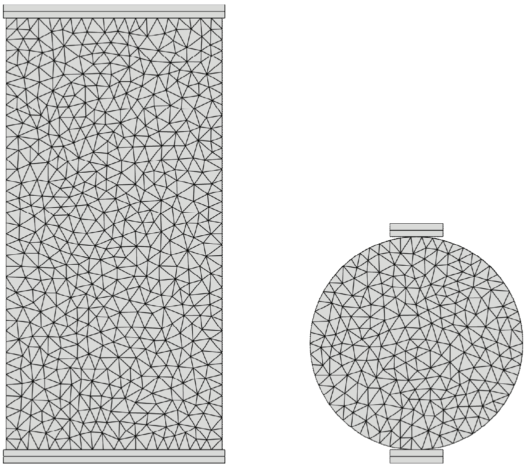

Figure 6–5: Model geometry for simulation of compression and Brazilian tension tests

The particle assemblage is generated arbitrarily to capture the material heterogeneity and diverse fracture patterns. Both the samples are generated as explained in Chapter 4, and consist of irregular triangular particles with an average edge size of d_p = 4.0 *mm*, corresponding to 1122 and 452 particles for the compressive and tensile samples, respectively. d_p has been chosen according to the granite grain size. Each particle consists of one CST element.

c. Quasi–static analysis

Using Equation 5–33, the particle's Young's modules and Poisson's ratio are held fixed at $E_p = 25.8$ *GPa* and $\nu_p = 0.23$.

Assuming $\beta = 0.25$ in Equation 5–30 and 5–31, the tensile and shear initial stiffness coefficients of contact are obtained as $k_t = 1.95\times10^6$ *MPa/mm* and $k_s = 1.98\times10^5$ *MPa/mm* for the Brazilian sample and $k_t = 2.06\times10^6$ *MPa/mm* and $k_s = 2.10\times10^5$ *MPa/mm* for the compressive one.

As explained earlier, UDEC basically works with a dynamic algorithm. To simulate static test condition, loading rate must be set the same as the practice, i.e., 0.02 *mm/s*. Considering that the time step calculated by the code is about 10^{-7} *sec*, half a billion steps are needed to move the platen for 1.0 *mm* (ultimate deformation of Augig granite at its compressive failure), that it is quite inefficient.

The only way feasible to keep the solution efficient is raising the loading rate up to a reasonable level as well as applying a sufficiently high numerical damping (e.g. $\alpha = 0.85$ in Equation 4–23) to avoid any probable dynamic effect and unexpected increase in material strength. The loading rate is therefore set to 10 *mm/sec* for both the compression and tension tests. The probable effects of the loading rate on the model response will be studied later.

Although the over damping removes any dynamic oscillations, it causes stress wave to decelerate. Thus, a stress delay may happen between two ends of the sample that possibly annuls the necessary quasi–static equilibrium. To overcome this problem, the upper and lower platens are simultaneously moved toward together with an identical speed of 5 *mm/sec*. During this process, the reaction force at both the upper and lower support are continuously recorded to generate stress–strain curves and to estimate the samples strength. For the Brazilian sample, tensile strength is measured through the following equation

$$\sigma_t = \frac{2F_{max}}{\pi t D} \tag{6–16}$$

where F_{max} is the maximum axial force recorded. D and t denote the sample diameter and thickness, where $t = 1$ for 2D simulation.

6.2.3. *Parametric study*

A parametric study is needed to determine which micro–parameters have the largest impacts on which macroscopic responses of the model. A set of micro–parameters should be initially chosen to carry out the study. As a starting point, contact cohesion and friction angle are assumed equal to the rock UCS and internal frictional angle, respectively. Thus $c_c = 122$ *MPa*, and $\phi_c = 53°$.

a. Effect of contact tensile strength

A series of simulations are designed to explore how the model global strength is related to the contact tensile strength. Considering Equation 5–27, the mixed–mode fracture energy, G_f, of Augig granite is calculated to be 413.0 and 436.0 J/m^2 for plain–strain and plain–stress, respectively, i.e., for the compressive and Brazilian samples. Given G_f, contact ultimate displacement, δ_{ut}, can be calculated by Equation 5–11 for different values of t_c as listed in Table 6–2 (next page).

Table 6–2: Values of contact tensile strength and corresponding ultimate displacement for each simulation

t_c [*MPa*] (t_c/BTS)	8.8 (1)	17.6 (2)	26.4 (3)	35.2 (4)
δ_{ut} for compressive test [*mm*]	0.094	0.047	0.031	0.023
δ_{ut} for Brazilian test [*mm*]	0.099	0.050	0.033	0.025

Based on the behavior of a CFM system, one could recognize that the model global strength is dependent of t_c. Figure 6–6 confirms that and indicates a linear relation between t_c and the Brazilian strength predicted by the model, σ_t. This result is in agreement with the earlier prediction by Equation 6–15. The relationship for the uniaxial compressive strength, σ_c, is nonlinear. Note that the axes in Figure 6–6 are normalized to the rock corresponding strengths, where BTS = 8.8 *MPa*, and UCS = 122 *MPa*.

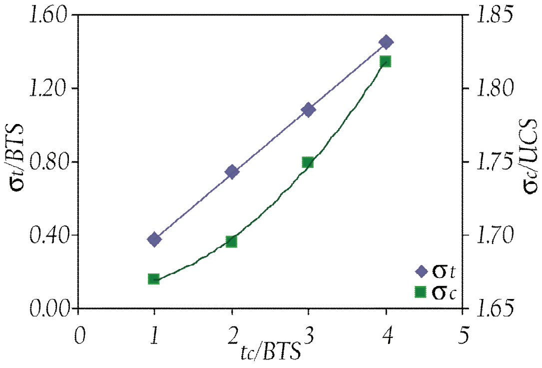

Figure 6–6: Tensile and compressive strength of the model versus contact tensile strength, t_c

By establishing a linear regression fit to the data, t_c is predicted 24.15 *MPa* to fit the tensile strength of the rock. Repetition of the simulation with t_c = 24.15 *MPa* verifies this anticipation and gives σ_t = 8.73 *MPa*, which is very near the Augig granite tensile strength.

b. Effect of contact friction angle and cohesion

Having t_c = 24.15 *MPa*, the sensitivity of the model to c_c and ϕ_c are examined as presented in Figure 6–7 and 6–8, where the values of c_c and ϕ_c are normalized to their reference values, i.e., the uniaxial compressive strength and the internal friction angle of the rock, respectively.

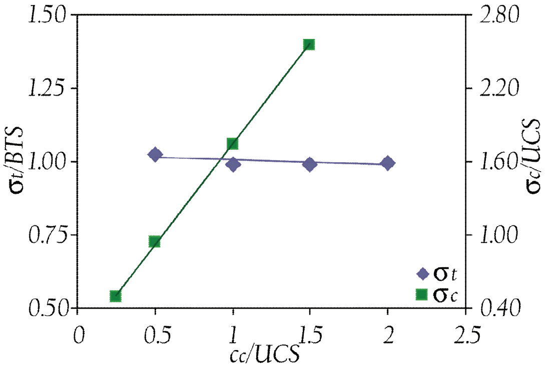

Figure 6–7: Tensile and compressive strength of the model versus contact cohesion, c_c

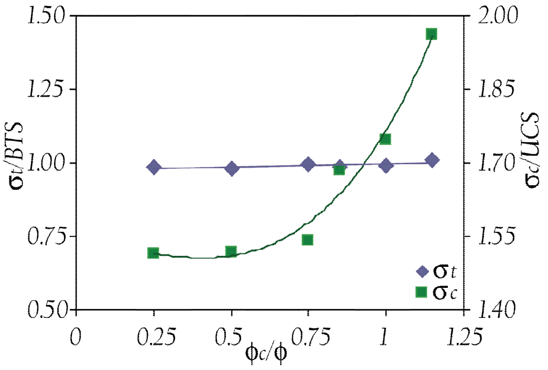

Figure 6–8: Tensile and compressive strength of the model versus contact friction angle, ϕ_c

The pictures show that the model Brazilian strength is independent of both c_c and ϕ_c, while predicted uniaxial compressive strength is highly influenced by them. Figure 6–8 illustrates that the model uniaxial compressive strength will not change with ϕ_c any more, when ϕ_c goes bellow a certain threshold, i.e., about 0.75ϕ. All these results yield the fact that the predicted tensile strength in the Brazilian test simulation depends on the contact tensile strength only. Therefore the obtained t_c = 24.15 *MPa* is the ultimate solution for the contact tensile strength. However, the relationship between the other two micro–parameters (c_c and ϕ_c) and the model global response is not explicit yet and needs more investigations.

6.2.4. *Design of experiment*

Consisting a group of statistical techniques, the Design Of Experiment (DOE) is an efficient, structured and organized discipline to quantitatively evaluate the relations between the measured *responses* of an experiment and the given input variables called *factors* (NIST/SEMATECH 2003). The objective of the DOE is to observe how and to what extent changes in the factors influence on the response variables. It is also used for planning experiments so that the results obtained can be analyzed to yield valid and objective conclusions. There are many different DOE methods. The best choice depends on the number of factors involved and the accuracy level required. Kennedy and Krouse (1999) presented the details for different DOE methods and categorized them based on the experimental objectives they meet.

The DOE begins with the definition of the experiment objectives and the selection of the input/output variables. In our purpose, the unknown micro–parameters, i.e., c_c and ϕ_c, are chosen as the factors; and the assemblage macroscopic responses, in terms of the internal cohesion C, and internal friction angle ϕ, are considered as the responses.

a. *Estimation of lower and upper bounds of factors*

The DOE needs to define a range for each factor. For this purpose, the results of the parametric study are used. As Figure 6–7 presents, if the contact cohesion is about half the rock compressive strength, the model reproduces a uniaxial compressive strength approximately equal to that of Augig granite. Therefore, the range of c_c is defined between 0.25×UCS and 0.75×UCS, i.e., 30.50 to 91.50 *MPa*. Since the model response does not vary when ϕ_c is below 0.75ϕ (Figure 6–8), the range of ϕ_c is assumed between 0.85ϕ to 1.15ϕ, i.e., 45.05° to 60.95°.

Table 6–3: Range of model micro–parameters to perform DOE on Augig granite test results

micro–parameter	lower bound	upper bound	centre (mean)
contact cohesion, c_c [*MPa*]	0.25×UCS	0.75×UCS	0.50×UCS
contact friction angle, ϕ_c [°]	0.85ϕ	1.15ϕ	1.00ϕ

b. *Response surface analysis*

Depending on the level of accuracy required, a complete description of the response behavior might need a linear, a quadratic or even a higher–order DOE. Under some circumstances, a design involving only main effects and interactions may be appropriate to describe a response surface when analysis of the results reveals no evidence of pure quadratic curvatures in the response of interest. As the curvature observed in Figure 6–8 implies, there is, however, a probability of existing interaction between the factors. It causes to believe that a linear design does not satisfy our objective; and a quadratic model is strongly necessary.

For this purpose, the Response Surface Method (RSM) is applied for the estimation of non–linear relations between the two unknown micro–parameters and the CFM macroscopic responses. One of the methods used to predict response quadratic curvature is the Central Composite Design (CCD).

b.1. Application of the central composite design

The CCD provides high quality prediction of a response surface over the entire design space, including linear, quadratic, and interaction effects. It contains an imbedded factorial or fractional factorial design with *centre points* that are augmented with a group of *star points* that allows estimation of curvature (see Table 6–5). If the distance from the design space centre to a *factorial point* is assumed ±1 unit for each factor, the distance from the design space centre to a star point will be $\pm\alpha$. The precise value of α depends on the number of factors involved. Since there are two factors in the model (c_c, and ϕ_c), $\alpha = 2^{1/2} \approx 1.414$, and the number of factorial runs will be four (NIST/SEMATECH 2003).

Table 6–4: Definition of factors and numerical value of micro–parameters at each coded level

factor	corresponding micro–parameter	value of micro–parameters at coded levels					transformation formula
		$-\alpha$	−1	0	+1	$+\alpha$	
x_1	contact cohesion, c_c	17.87	30.50	61.00	91.50	104.13	c_c = 30.50×[coded level] + 61.00
x_2	contact friction angle, ϕ_c	41.76	45.05	53.00	60.95	64.24	ϕ_c = 7.95×[coded level] + 53.00

The levels ±1 represent the upper and lower bounds assumed for the factors. The value of each factor at the centre point is defined as the arithmetic mean of the upper and lower bound values. Considering the lower and upper bounds presented in Table 6–3, the centre, factorial, and star points are calculated as listed in Table 6–4.

The CCD offers a limited number of combinations for the factors. These combinations are collected in a matrix called design matrix as listed in Table 6–5. This matrix can be converted to the matrix of the real factors, i.e., micro–parameters, by the transformation formula expressed at the last column in Table 6–4. The laboratory tests are then simulated using each set of the CCD–suggested micro–parameters, and the model results are obtained as recorded in Table 6–6. These tests include the uniaxial and triaxial compressive tests on the sample shown in Figure 6–5, where the confining pressure, σ_3, of 0, 4, and 8 *MPa* is applied. Using the compressive strengths obtained at each run, internal cohesion and internal friction angle of the model are calculated as the DOE responses.

Table 6–5: Complete design matrix for central composite design

run	point type	factor 1 (x_1)	factor 2 (x_2)
1	corner (1)	−1	−1
2	corner (2)	+1	−1
3	corner (3)	−1	+1
4	corner (4)	+1	+1
5	star (a)	−1.414	0
6	star (b)	+1.414	0
7	star (c)	0	−1.414
8	star (d)	0	+1.414
9	centre (i)	0	0
10	centre (ii)	0	0
11	centre (iii)	0	0
12	centre (iv)	0	0
13	centre (v)	0	0

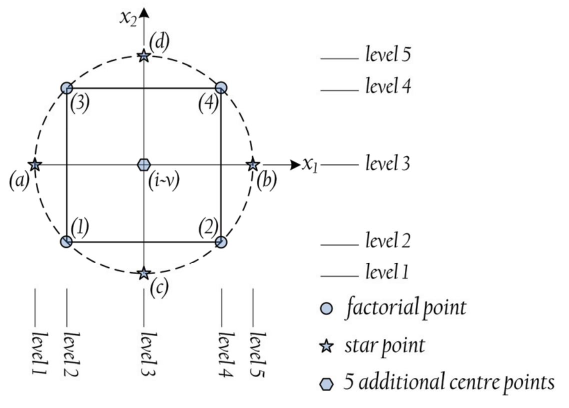

Table 6–6: CCD–suggested design matrix and obtained results

	micro–parameters matrix		DOE responses		CFM results for compressive models		
run	c_c	ϕ_c	C	ϕ	$\sigma_3 = 0\,MPa$	$\sigma_3 = 4\,MPa$	$\sigma_3 = 8\,MPa$
1	30.53	45.05	7.2	57.6	55.98	84.10	151.04
2	91.58	45.05	35.7	38.9	147.32	171.56	182.38
3	30.53	60.95	15.1	73.7	181.74	460.30	570.00
4	91.58	60.95	13.7	74.1	180.57	433.50	590.34
5	17.88	53.00	3.9	69.8	35.87	183.62	287.03
6	104.22	53.00	26.4	56.4	181.09	205.94	268.65
7	61.05	41.76	35.3	21.9	104.08	114.09	121.63
8	61.05	64.24	17.3	74.8	245.97	510.31	694.55
9	61.05	53.00	11.4	67.0	115.40	200.89	308.71
10	61.05	53.00	12.1	64.6	107.89	183.33	264.81
11	61.05	53.00	10.1	69.5	114.47	227.16	358.74
12	61.05	53.00	10.2	70.2	106.14	269.88	369.24
13	61.05	53.00	11.8	63.6	103.95	165.91	248.86

For each run, the particle assemblage is separately created. In addition, the simulations are repeated for five times with the same micro–parameters at the centre points (see runs

9 to 13 in Table 6–6). That is because the particle assemblage is generated arbitrarily and two CFM runs might produce slightly different results. Hence, the CCD predictively carries out this repetition to minimize the variability in modeling.

The targeted response parameters are statistically analyzed by applying the above data in statistical software of JMP (Sall et al. 2007). The individual parameters are evaluated using the Fischer test, and quadratic models of the form

$$Y = \beta_0 + \beta_1 x_1 + \beta_2 x_2 + \beta_3 x_1 x_2 + \beta_4 x_1^2 + \beta_5 x_2^2 \tag{6–17}$$

are generated for each response parameter using multiple linear regression analysis and analysis of variance. Y stands for the level of the measured response, i.e., C and ϕ here. β_0 is the intercept; β_1 to β_5 are the regression coefficients. x_1 and x_2 stand for the coded factors; x_1x_2 is the interaction between the main effects; x_1^2 and x_2^2 are the quadratic terms of the independent variables that are used to simulate the curvature of the designed surface. Predictor equations containing only the significant terms are generated using a backward elimination procedure. A numerical optimization procedure using desirability approach is used to locate the optimal settings of the formulation variables in view to obtain the desired response (Park and Park 2010).

Using the data presented in Table 6–6, the following equations between the model macroscopic response and the coded factors are constructed.

$$C = 11.12 + 7.36x_1 - 4.94x_2 - 7.48x_1x_2 + 1.32x_1^2 + 6.89x_2^2 \tag{6–18}$$

$$\phi = 66.98 - 4.66x_1 + 15.76x_2 + 4.78x_1x_2 - 0.60x_1^2 - 7.98x_2^2 \tag{6–19}$$

Comparing the multipliers in the above equations, the necessity of a quadratic RSM is clearly justified. Solving them for C = 21 MPa and ϕ = 53° of Augig granite, x_1 = 0.443 and x_2 = −0.533. These are coded factors and have to be transformed to uncoded values using the transformation equations that eventually leads to c_c = 74.57 MPa, and ϕ_c = 48.76° as the target micro–parameters.

6.2.5. *Solution verification*

The proposed calibration process is expected to provide the best micro–parameters for the model generation and give the closest match between the laboratory results and those of the simulation. The validity of the solution can be verified through quantitative and qualitative comparisons of these two sets of results.

a. Quantitative comparison

For a quantitative comparison, the results of the Brazilian tension, uniaxial and triaxial compression tests on Augig granite are reproduced again. The results of laboratory test were previously inserted into the obtained system of equations and the target set of the micro–parameters is calculated. They are then used as input for the new simulations, which are expected to give the closest match with the laboratory test in terms of the Young's modulus, Poisson's ratio, Brazilian tensile strength, uniaxial compressive strength, internal cohesion, and internal frictions angle.

If the discrepancy between the experiment and simulation is limited to a reasonable range, the CFM solution can be admitted as adequate for modeling any target rock material and can be further applied for more complicated problems.

Table 6–7 presents the complete list of the micro–parameters, which have been obtained by the closed–formed expressions, parametric study, and CCD calculation.

Since different assemblage arrangements result in different model strength, five models with different particle arrangement but the same micro–parameters as Table 6–7 are created. The results of mean, standard deviation, and relative error percentage are listed in Table 6–8, which show fair agreement with the experimental measurements, where the relative error is always less than 5%.

Table 6–7: List of target micro–parameters for simulation of Augig granite

E_p [*GPa*]	ν_p	k_t [*TPa/mm*]	k_s [*TPa/mm*]	t_c [*MPa*]	c_c [*MPa*]	ϕ_c [°]
25.80	0.23	1.95 / 2.06	0.198 / 0.21	24.15	74.57	48.76

Table 6–8: Experimental properties of Augig granite versus CFM predictions

property	E [*GPa*]	ν	σ_t [*MPa*]	σ_c [*MPa*]	C [*MPa*]	ϕ [°]
experimental value	25.8	0.23	8.8	122.0	21.0	53.0
numerical mean	25.2	0.24	8.7	125.4	20.9	53.5
standard deviation	0.21	0.01	0.16	2.35	0.85	1.12
relative error %	2.33	4.35	1.14	2.79	0.48	0.94

Though the target set of the micro–parameters is expected to provide a close match, little variations in the numerical results are unavoidable because of the inherent randomness of particle placement in the model generation. Note that this is not regarded at all as the CFM disadvantage, when even two separate experimental tests on rock material do not lead necessarily to identical results due to rock intrinsic heterogeneity. In fact, the randomness of the particle arrangement relatively represents rock heterogeneity, while material anisotropy is introduced into the model by the adopted orthotropic contact law.

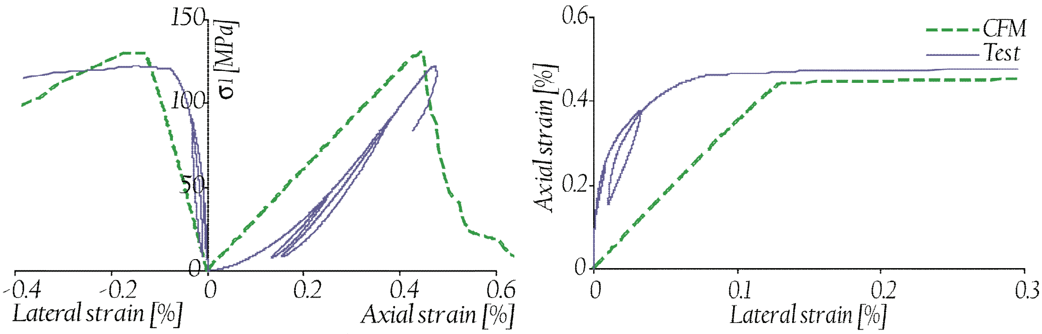

a. axial stress versus axial and lateral strain **b. axial strain versus lateral strain**

Figure 6–9: Comparison of predicted stress–strain curves with those obtained in laboratory

Comparisons between the curves of axial stress versus axial and lateral strain for the laboratory test and a representative simulation are presented in Figure 6–9. Note that some special aspects for rock behavior such as sliding at grain boundaries or closure of initial flaws and pores are not captured by the CFM. This causes stress–strain curves in the simulation to be slightly different from those of the laboratory tests, particularly where the initial nonlinearity is not reflected in the modeling.

The elastic constants for the laboratory testing were obtained from the middle portions of the curves where relatively linear relation between stress and strain is maintained. For numerical simulation, those are computed using stress and strain increments occurring between the start of the test and the point at which one half of the peak stress has been obtained (tangent method).

Figure 6–10 illustrates the CFM predictions for the Brazilian, uniaxial and triaxial simulations in comparison with the laboratory measurements. The Hoek–Brown failure envelops are also plotted for the both. As seen, the curves show fair agreements.

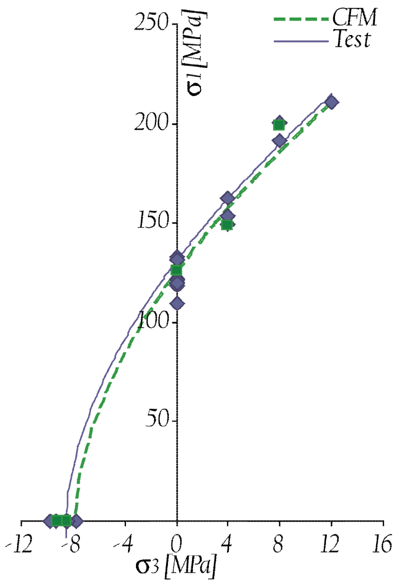

Figure 6–10: The Hoek–Brown failure envelop for Augig granite

b. Qualitative comparison

Some specific features of the simulation, e.g. failure mode or fracturing pattern, cannot be adequately quantified. A qualitative comparison can be as an alternative to complete the verification of the CFM solution. For this purpose, the solution correctness is investigated by comparing the mentioned features obtained from the laboratory test with those from the CFM simulation.

b.1. Compressive failure mode

As shown by Paterson (1987), rocks exhibit higher ductility under triaxial circumstances than uniaxial. Figure 6–11 offers that this phenomenon is fairly captured by the CFM. The simulation gives further yielding and plastic deformation with confinement, whilst an abrupt softening at post–peak region is observed in the laboratory results.

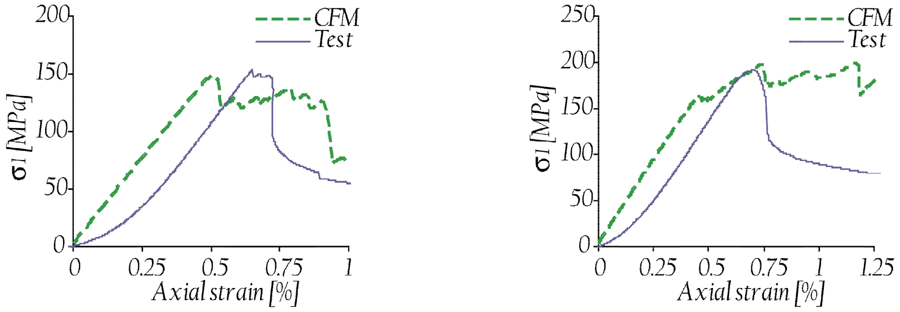

a. σ_3 = 4.0 MPa b. σ_3 = 8.0 MPa

Figure 6–11: Experimental stress–strain response of Augig granite compared with the CFM predictions in triaxial compression

As Wawersik and Fairhurst (1970) describes, rock failure in unconfined circumstances occurs in two distinct modes of axial splitting (cleavage failure) and shear rupture (faulting). Axial cleavage generally precedes faulting for hard rocks and characterizes failure initiation. On the contrary, failure of soft rocks usually starts with shear faulting. Figure 6–12 shows that this phenomenon is clearly observed by the CFM, where the predicted failure mode shows typical cleavage happening in the laboratory tests.

Figure 6–12: Comparison of laboratory compressive failure of Augig granite with CFM predictions under unconfined condition

b.2. Tensile fracturing pattern

In the CFM simulation, tensile failure initially starts at about sample centre, and then the induced fracture rapidly propagates in parallel with the loading axis. That is why sample resistance suddenly decays after failure starts. Further increasing the load causes more contacts break around the major fracture, particularly beneath the platens.

The post–failure picture for Augig granite and the CFM simulation is plotted in Figure 6–13 (next page). The failure features, in terms of the major fault induced into the sample and the wedge–shaped zone created at the contact points with the platens, are fairly captured.

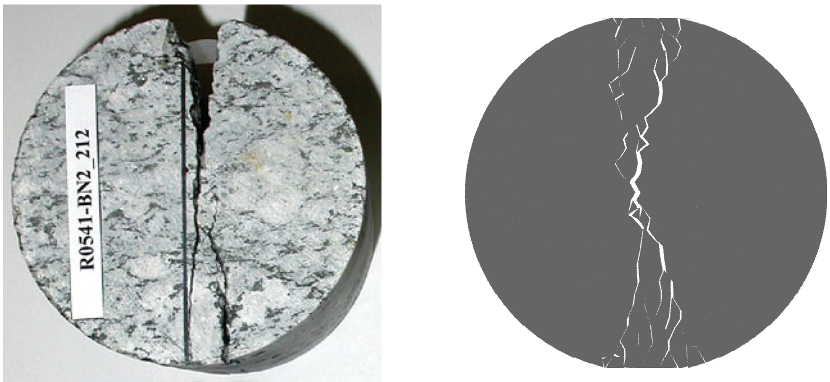

Figure 6–13: Comparison of laboratory tensile failure with the CFM predictions

6.2.6. *Complementary investigations*

a. *Effect of particle size*

Equation 6–15 predicts that the Brazilian strength predicted by the CFM is affected by particle size. A series of simulations are carried out to numerically examine this analytical prediction. They consist of particles with the average edge size between 2 to 7.5 *mm*. This range of particle size is chosen regarding the Augig granite grain size. The details for some of the models are presented in Figure 6–14.

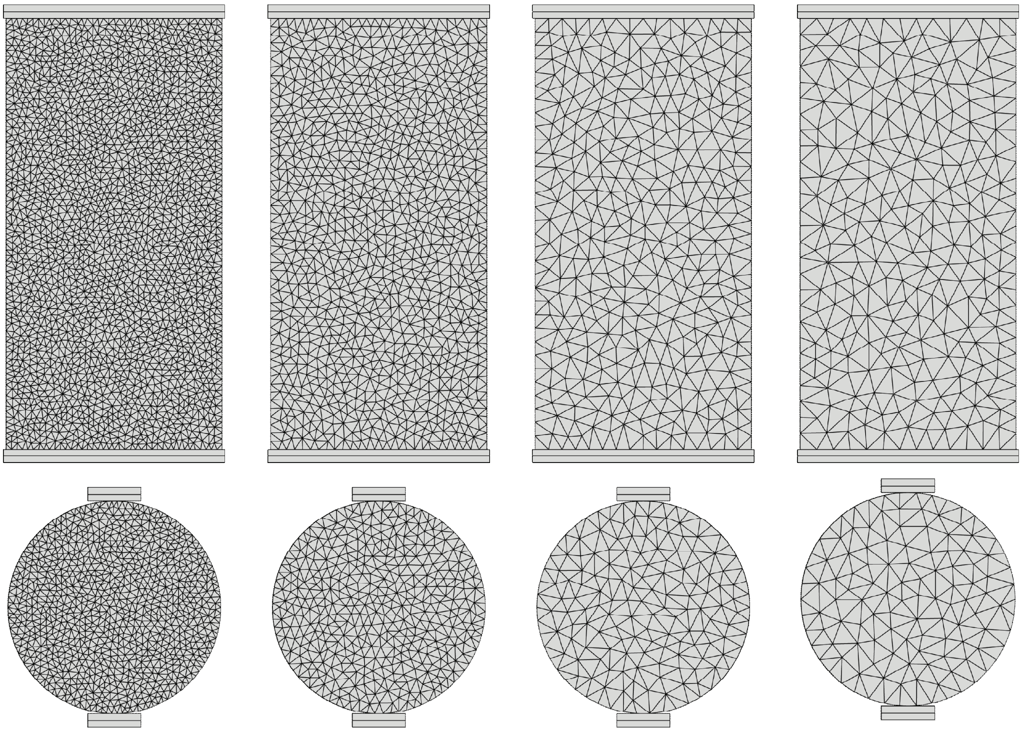

a. d_p = 2.0 mm **b. d_p = 3.0 mm** **c. d_p = 5.0 mm** **d. d_p = 6.0 mm**

Figure 6–14: Some of particle assemblages created to explore particle size effects

The results, presented in Figure 6–15, indicate that although the compressive strength has nearly no change, the Brazilian strength decreases with the particle size decrease, and follows a trend similar to that predicted by Equation 6–15. The CFM results are compared with Equation 6–15 by fitting a power–law curve, with an exponent of 0.39, to the numerical data. However, the equation suggests a power of one–half. This discrepancy may be explained through the argument that the power will be one–half, if the LEFM conditions apply. However, such conditions are not valid here, because (1) the CFM's contacts follow a cohesive behavior, i.e., $\delta_{ut} \neq 0$, and (2) despite of the ideal plate shown in Figure 6–3 in which only one single contact breaks at every instant of crack growth, an accumulation of contact failures represents the Brazilian sample rupture.

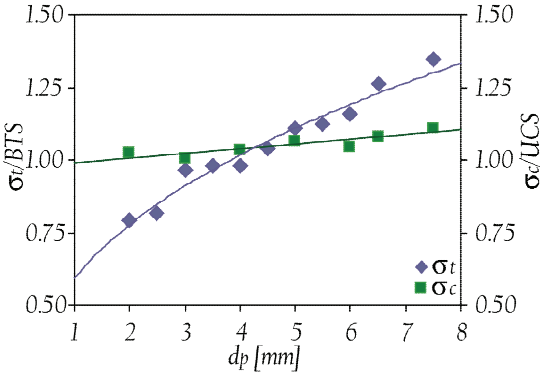

Figure 6–15: Variation of compressive and Brazilian strength versus particle size

These results yield to this conclusion that the CFM's particles are not needed to be extremely small. They, in fact, must be sufficiently small to allow the model to exhibit the actual failure fashion of the rock, particularly in terms of the frequency of the dominant cracks controlling the failure procedure. For grained media, particle size is chosen mainly by the material texture and its average grain size.

b. *Effect of loading rate*

As discussed earlier, due to efficiency limitations, the model has to be loaded with a rate much higher than that of practice. This increased–rate loading is suspected to alter the strength and failure of the model. Hence, a series of compressive and tensile models are loaded with different rates varying from 2 to 1000 *mm/sec* to explore how the CFM predictions are affected.

Figure 6–16 (next page) shows that the model response approaches to an asymptotic value, as loading rate decreases. However, the results are seriously impacted after the rate of loading exceeds 100 *mm/sec*.

It also suggests that the Brazilian models are more sensitive to the loading rate than the compressive ones. The results presented confirm that the rate adopted in the CFM, i.e., 10 *mm/sec*, has no effect on the model responses, and the quasi–static equilibrium is properly satisfied.

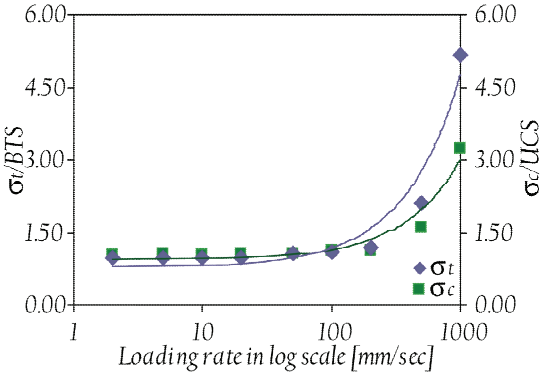

Figure 6–16: Variation of CFM macroscopic response versus loading rate exerted

6.3. Reproduction of compressive and tensile response of soft rocks

For additional verification, the same procedure is applied to reproduce the mechanical properties of Transjurane sandstone as a soft rock.

6.3.1. *Numerical simulation of experiments*

a. *Material properties and elastic micro–properties*

As a moderately coarse aggregate rock, Transjurane sandstone is composed of the grains with the average size of 1.75 *mm*. Its mechanical properties are listed in Table 6–9.

Table 6–9: Mechanical properties of Augig granite

Young's modulus, E	12.5 *GPa*	internal cohesion, C	8.5 *MPa*
Poisson's ratio, ν	0.3	internal friction angle, ϕ	41.0°
fracture toughness in Mode–I, K_{IC}	0.7 $MPa\sqrt{m}$	Brazilian tensile strength, BTS	2.8 *MPa*
fracture toughness Mode–II, K_{IIC}	0.8 $MPa\sqrt{m}$	uniaxial compressive strength, UCS	40.0 *MPa*

Using Equation 5–33, the particle's Young's modules and Poisson's ratio are held fixed at E_p = 12.5 *GPa* and ν_p = 0.3. Given Equation 5–30 and 5–31, the contact initial stiffness coefficients in tension and shear are calculated as $k_t = 7.31\times10^5$ *MPa/mm* and $k_s = 1.97\times10^5$ *MPa/mm* for the Brazilian sample and $k_t = 8.03\times10^5$ *MPa/mm* and $k_s = 2.17\times10^5$ *MPa/mm* for the compressive one.

b. *Discrete element mesh*

A plane–strain and a plane–stress analysis are adopted for the compressive and Brazilian models, respectively. The compressive cylindrical sample is 30 *mm* in diameter and 70 *mm* high, and the Brazilian specimen is a disc with a diameter of 70 *mm*. Both the samples are generated by irregular triangular particles with an average edge size of d_p = 2.0 *mm*, corresponding to 740 and 1134 particles for the compressive and tensile samples, respectively. Each particle consists of one CST. Friction angle between the rock and steel platens is assumed 5°, and loading rate is set 10 *mm/sec*.

The geometry and boundary condition of the samples are presented in Figure 6–17.

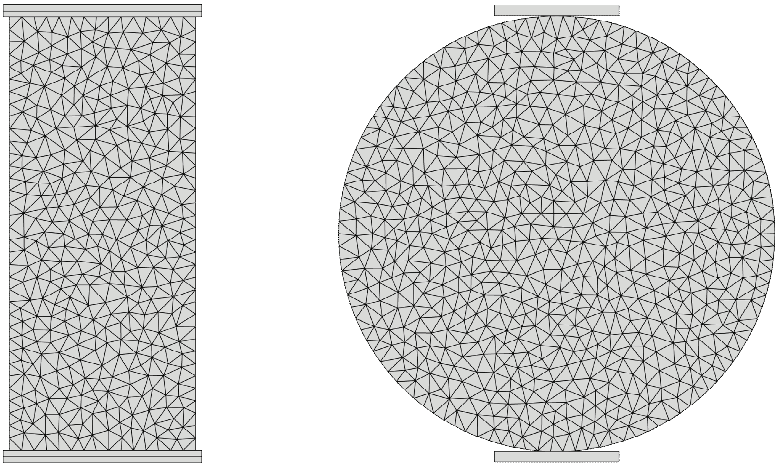

Figure 6–17: Model geometry for compression and Brazilian tension tests simulation

6.3.2. *Parametric study*

The parametric study is repeated for Transjurane sandstone. Considering the results of the Augig granite simulation, the initial set of the micro–parameters are chosen as c_c = UCS/2 = 20 *MPa* and $\phi_c = \phi = 41°$. A series of Brazilian samples are the designed to study the effects of the contact tensile strength on the model global tensile strength. The values assumed for t_c and δ_{ut} are listed in Table 6–10. Given Equation 5–11, G_f for Transjurane sandstone is calculated as 87.1 J/m^2 for plain–stress.

Table 6–10: Values of contact ultimate displacement for the Brazilian tension models

t_c [*MPa*] (t_c/BTS)	2.8 (1)	5.6 (2)	8.4 (3)	11.2 (4)	14.0 (5)	16.8 (6)	19.6 (7)
δ_{ut} for Brazilian test [*mm*]	0.0566	0.0283	0.0189	0.0142	0.0113	0.0094	0.0081

Similar to Augig granite and as anticipated by Equation 6–15, the Brazilian strength of the model is linearly dependent of t_c (see Figure 6–18). The linear regression fit predicts t_c as 10.97 *MPa* to produce the laboratory measured tensile strength, BTS = 2.8 *MPa*. Repetition of the simulation with the obtained t_c provides σ_t = 2.90 *MPa*, which is very close to the rock tensile strength.

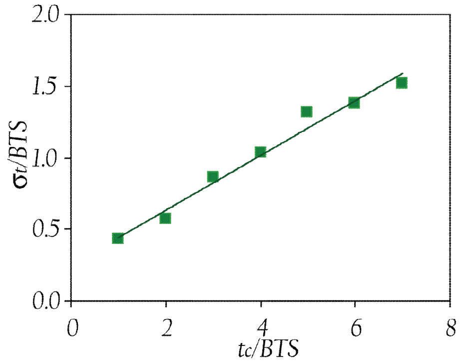

Figure 6–18: Variation of tensile strength of the model versus contact tensile strength, t_c

Having t_c = 10.97 *MPa*, the sensitivity of the model response to c_c and ϕ_c are examined through simulating a series of the Brazilian and compressive samples. Like Augig granite, the Brazilian strength of the sandstone model is not affected by any of the two micro-parameters. Therefore t_c = 24.15 *MPa* is the target value for the contact tensile strength.

Figure 6–19 shows that the compressive behavior of the model is highly influenced by c_c and ϕ_c. However, the results do not change any more with ϕ_c, when it is lower than 0.50ϕ.

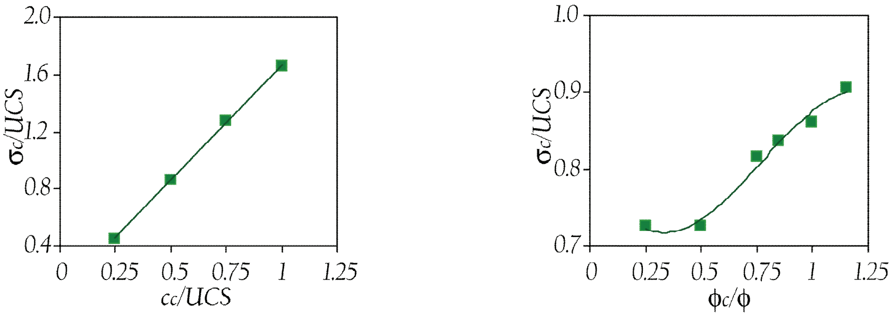

Figure 6–19: Variation of uniaxial compressive strength of the model versus contact cohesion, c_c, and contact friction angle, ϕ_c

6.3.3. *Design of experiment*

a. *Estimation of lower and upper bounds of factors*

Regarding Figure 6–19, the range of c_c and ϕ_c is defined as listed in Table 6–11.

Table 6–11: Applied range of micro–parameters to implement DOE on Transjurane sandstone

micro–parameter	lower bound	upper bound	centre (mean)
contact cohesion, c_c [*MPa*]	0.25×UCS = 10.00	0.75×UCS = 30.00	0.50×UCS = 20.00
contact friction angle, ϕ_c [°]	0.85ϕ = 34.85	1.15ϕ = 47.15	1.00ϕ = 41.00

b. *Central composite design*

According to the design matrix in Table 6–5, and the micro–parameters range presented in Table 6–11, the centre, factorial, and star points, corresponding to the sandstone properties, are calculated in Table 6–12.

Table 6–12: Definition of factors and numerical value of micro–parameters at coded levels

factor	corresponding micro–parameter	value of micro–parameters at coded levels					transformation formula
		$-\alpha$	−1	0	+1	$+\alpha$	
x_1	contact cohesion, c_c	5.86	10.00	20.00	30.00	34.14	c_c = 10.0×[coded level] + 20.00
x_2	contact friction angle, ϕ_c	32.30	34.85	41.00	47.15	49.70	ϕ_c = 6.15×[coded level] + 41.00

The CCD–suggested micro–parameters and the obtained results, under confining pressures of 0, 3, and 6 *MPa*, are listed in Table 6–13 (next page). Using the data presented there, the following equations between the model macroscopic responses, i.e., *C* and ϕ, and the coded factors are constructed.

$$C = 8.00 + 5.52x_1 - 3.07x_2 - 2.20x_1x_2 + 0.83x_1^2 + 0.16x_2^2 \tag{6–20}$$

$$\phi = 37.60 - 8.18x_1 + 16.89x_2 + 2.48x_1x_2 + 0.66x_1^2 + 0.44x_2^2 \tag{6–21}$$

Solving them for C = 8.5 MPa and ϕ = 41° of the sandstone, x_1 = 0.292 and x_2 = 0.323. After converting x_1 and x_2 to the uncoded values, c_c = 22.92 MPa and ϕ_c = 42.99° are finally obtained as the target micro–parameters.

Table 6–13: CCD–suggested design matrix and obtained results

	micro–parameters matrix		DOE responses		CFM results for compressive models		
run	c_c	ϕ_c	C	ϕ	$\sigma_3 = 0\,MPa$	$\sigma_3 = 3\,MPa$	$\sigma_3 = 6\,MPa$
1	10.00	34.85	4.1	33.5	17.19	21.46	37.97
2	30.00	34.85	18.2	16.4	48.23	55.12	58.96
3	10.00	47.15	2.6	60.2	19.02	62.57	103.91
4	30.00	47.15	7.9	53.0	53.39	61.10	107.10
5	5.86	41.00	1.7	51.4	10.65	33.22	59.71
6	34.14	41.00	19.2	22.3	56.59	65.35	69.94
7	20.00	32.30	13.6	11.0	33.01	37.71	41.84
8	20.00	49.70	4.6	61.8	36.07	85.14	130.87
9	20.00	41.00	8.0	37.6	34.45	40.61	59.25
10	20.00	41.00	5.7	48.9	35.81	40.23	78.54
11	20.00	41.00	6.1	45.9	34.03	40.35	70.58
12	20.00	41.00	6.0	48.7	36.41	43.14	78.68
13	20.00	41.00	5.6	48.7	34.91	40.57	77.11

6.3.4. *Solution verification*

a. *Quantitative comparison*

All the calibrated micro–parameters for the sandstone simulation are listed in Table 6–14. Using this data, the tensile and compressive simulations are again repeated for five times. The results in terms of mean, standard deviation and relative error are presented in Table 6–15, where they show perfect agreements with the experimental measurements.

Table 6–14: List of the target micro–parameters for simulation of Transjurane sandstone

E_p [GPa]	v_p	k_t [TPa/mm]	k_s [TPa/mm]	t_c [MPa]	c_c [MPa]	ϕ_c [°]
12.5	0.30	0.731 / 0.803	0.197 / 0.217	11.97	22.92	42.99

Table 6–15: Experimental properties of Transjurane sandstone versus CFM predictions

property	E [GPa]	v	σ_t [MPa]	σ_c [MPa]	C [MPa]	ϕ [°]
experimental value	12.5	0.30	2.8	40.0	8.5	41.0
numerical mean	12.7	0.31	2.9	39.8	8.5	40.7
standard deviation	0.30	0.01	0.36	1.85	0.51	1.24
relative error %	1.61	3.33	3.57	0.50	0.00	0.73

The experimental and numerical stress–strain curves are compared in Figure 6–20 (next page). Like Augig granite simulation, the initial nonlinearity is not reflected in the modeling. As Figure 6–21 (next page) presents, the model predicts higher ductility under triaxial than uniaxial condition, which agrees with the general compressive behavior of rocks (Paterson 1978).

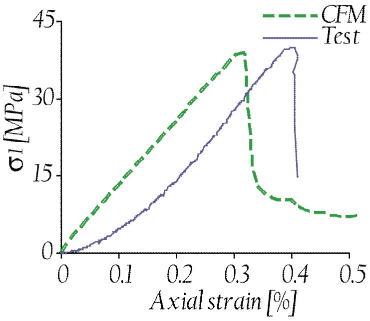

Figure 6–20: Comparison of laboratory and CFM–predicted results for uniaxial compressive behavior of Transjurane sandstone

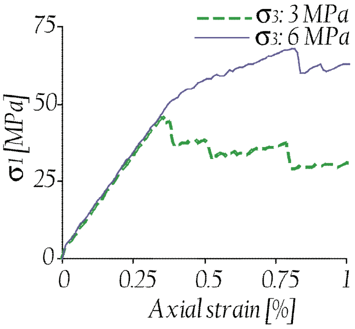

Figure 6–21: Triaxial compression results predicted by CFM for different confinements

Figure 6–22 plots the CFM predictions for the model compressive and tensile strengths in comparison with the laboratory measurements obtained from the uniaxial, triaxial and Brazilian tests. As seen, the CFM results follow nearly the same pattern with the laboratory data. The Hoek–Brown failure envelops are also drawn for both the numerical and experimental data, where fair agreement is observed.

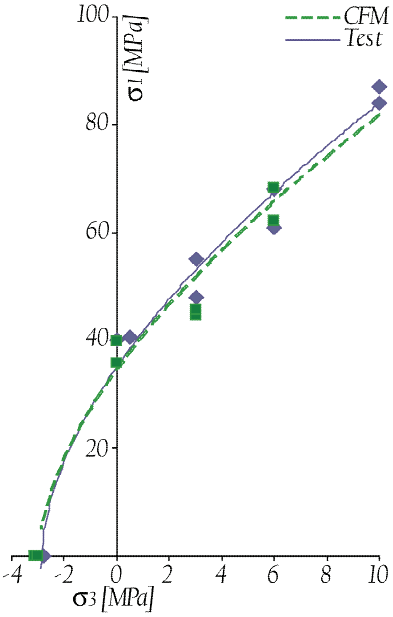

Figure 6–22: The Hoek–Brown failure envelop for Transjurane sandstone

b. Qualitative comparison

Figure 6–23 compares the experimental failure mode of the sandstone with that predicted by the CFM. The experimental picture illustrates a typical failure observed in soft rocks, where shear faulting is more dominant than cleavage failure (Wawersik and Fairhurst 1970). The picture on the right shows that this phenomenon is clearly captured by the CFM, where the model is sheared over an inclined surface; thereby the upper part of the simulation is sliding down.

Figure 6–23: Comparison of experimental compressive failure of Transjurane sandstone with CFM predictions under unconfined condition

6.4. Conclusion

The results presented in this chapter ensured there is a unique set of the CFM micro-parameters by which the model, not only quantitatively but also qualitatively, can reproduce the rock experimental behavior in compression and tension. Using them, good predictions for the laboratory response of both strong and weak rocks are obtained.

The results also showed how rock macroscopic behavior is influenced by its micromechanical properties, i.e., grain size, inter–granular contact strength and friction. In addition, it was seen how static loading rate and lateral confinement affects on the model predictions.

CHAPTER 7

Shear failure and degradation of rock joint

Formed in sets, natural rock joints are the most common preexisting weak discontinuity within rock masses. Their scale in terms of length and spacing may vary from centimeters to meters. Understanding their mechanical behavior is of prime importance for many applications such as tunnel excavation and support, slope stability and foundation design. Since the 1970s, numerous investigations have been conducted to determine the mechanical properties of rock joints and the influence of externally applied normal and shear stress (Barton and Choubey 1977; Ladanyi and Archambault 1977; Patton 1996; Zhao 1997a). Roughness of the joint walls was identified early on as a key parameter of the mechanical behavior of rock joints (Barton 1971; Barton 1976). However, it is not constant as the joint morphology evolves upon shearing (Grasselli et al. 2002; Hans and Boulon 2003; Zhao 1997b). In fact, very high local stresses are generated within the joint during shearing which leads to a progressive breakage of the asperities. This phenomenon induces a reduction in shear strength and dilation, usually visible at residual state and particularly for cyclic shearing, as has been discussed extensively in the literature (Barton and Choubey 1977; Huang et al. 1993; Yang and Chiang 2000; Lee et al. 2001; Jafari et al. 2003).

Asperity degradation is of major significance to the mechanical behavior of rock joints and therefore has been included in models to accurately assess the joint shear strength (Plesha 1987; Nguyen and Selvadurai 1998; Lee et al. 2001). The joint roughness governs the dilation of the joint (Barton, Bandis et al. 1985) and progressive joint closure is observed when asperities are worn off.

Regarding experimental controllability and sample preparation ease, artificially made joints with simplified geometries such a saw–tooth are more preferred than natural rock joints whose surface profiles are complex and non–repeatable. The artificial joints are normally made of cement or gypsum mortar for small-size samples and concrete for big-size ones.

This chapter examines the capability of the CFM for modeling asperity degradation within plaster-made joints under shearing. For this purpose, the CFM micro-parameters are initially calibrated by the compressive and tensile test data of the plaster material. Using the target micro-parameters and with no additional modification, shear tests on the plaster joint specimens are then modeled. Ultimately, the obtained results are qualitatively and quantitatively compared to the experimental data, and the agreements and discrepancies are discussed in detail.

7.1. Experimental data

The geometry of the present numerical rock joints corresponds to that used by Yang and Chiang (2000). They tested a series of the plaster-made specimens under different levels of normal stress. They first focused on the shear behavior of two single-tooth joints (joints A and B with a tooth angle of 15° and 30°, respectively) before combining the two teeth in joints AB and BA (see Figure 7-1). In all the specimens tested, the tooth height is fixed at 5.0 *mm*, and the joint surface area is 10×10 cm^2.

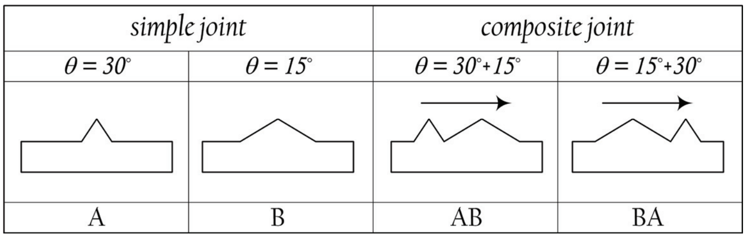

Figure 7-1: Rock joint models used by Yang and Chiang (2000)

The tests demonstrated that the tooth geometry and the normal stress very much affect on the strength and dilatancy response of the joints.

This chapter makes use of the CFM to investigate these issues for joints A and AB.

7.1.1. *Material properties*

The plaster mortar, used to make the specimens, is made of plaster and water mixed by the weight ratio of 1:0.65. All the specimens are cured for 5 days inside a chamber with the temperature of 25° *C* and the relative humidity of 55%. The mechanical properties of the plaster are listed in Table 7-1.

Table 7-1: Mechanical properties of the plaster

Young's modulus, E	1.3 *GPa*	internal cohesion, C	1.75 *MPa*
Poisson's ratio, ν	0.2	internal friction angle, ϕ	40°
fracture toughness in Mode-I, K_{IC}	0.9 $MPa\sqrt{m}$	Brazilian tensile strength, BTS	1.6 *MPa*
fracture toughness Mode-II, K_{IIC}	1.1 $MPa\sqrt{m}$	uniaxial compressive strength, UCS	7.5 *MPa*

Yang and Chiang (2000) have not reported K_{IC} and K_{IIC} of the tested plaster. Hence, those parameters were estimated by the values reported for other types of plaster made of similar mixtures and having nearly the same mechanical properties with the tested plaster (Saadaoui et al 2000; Eve et al. 2002; Gmouh et al. 2003).

7.2. **Model calibration**

The standard compressive and tensile tests are simulated to find the target micro–parameters. As described in Chapter 6, the calibration process begins with the definition of the experiment objectives and the selection of the input/output variables.

All the three unknown micro–parameters, i.e., t_c, c_c and ϕ_c, are chosen as factors, and the CFM predictions for the Brazilian strength σ_t, internal cohesion, C, and internal friction angle, ϕ, of the plaster are regarded as responses. Therefore, each CCD run must include a Brazilian simulation in addition to the uniaxial and triaxial ones.

7.2.1. *Reproduction of compressive and tensile test data*

A plane–strain and a plane–stress analysis are adopted for the compressive and Brazilian models, respectively. The compressive cylindrical sample is 54 *mm* in diameter and 130 *mm* high, and the Brazilian specimen is a disc with a diameter of 54 *mm*. They are placed between two steel platens whose interfacial friction angle is assumed negligible. The geometry and boundary condition of the samples are shown in Figure 7–2 (next page).

The both groups of the samples are generated as explained in Chapter 4, and consist of irregular triangular particles with the average edge size of d_p = 2.0 *mm*. d_p is believed to be sufficiently small to allow the simulation to provide the actual failure fashion of the plaster, as observed in laboratory.

Using Equation 5–33, the particle's Young's modules and Poisson's ratio are fixed at E_p = 1.3 *GPa* and ν_p = 0.2. Given Equation 5–30 and 5–31, the tensile and shear initial stiffness coefficients of contact are obtained as k_t = 2.61×10^3 *MPa/mm* and k_s = 7.27×10^2 *MPa/mm* for the compressive sample, and k_t = 2.50×10^3 *MPa/mm* and k_s = 6.98×10^2 *MPa/mm* for the Brazilian one.

As explained earlier, the over damping, introduced in order to eliminate dynamic effects, makes the material unnaturally viscous and therefore decelerates stress wave speed. Consequently, stress delay inevitably happens between the two ends of the sample and its middle points, which may annul the static equilibrium needed for each solution step. To overcome this inconvenience, the loading process is divided into *stages*. During each stage, each platen moves for 0.01 *mm* that causes the sample to be compressed as one hundredth of its ultimate deformation at failure. Then, loading stops and the sample is let reach stress equilibrium. These stages repeat until the sample fails. At the end of each stage, the sample deformation and the reaction force of the platens are recorded in order to generate stress–strain curve and to estimate the sample strength.

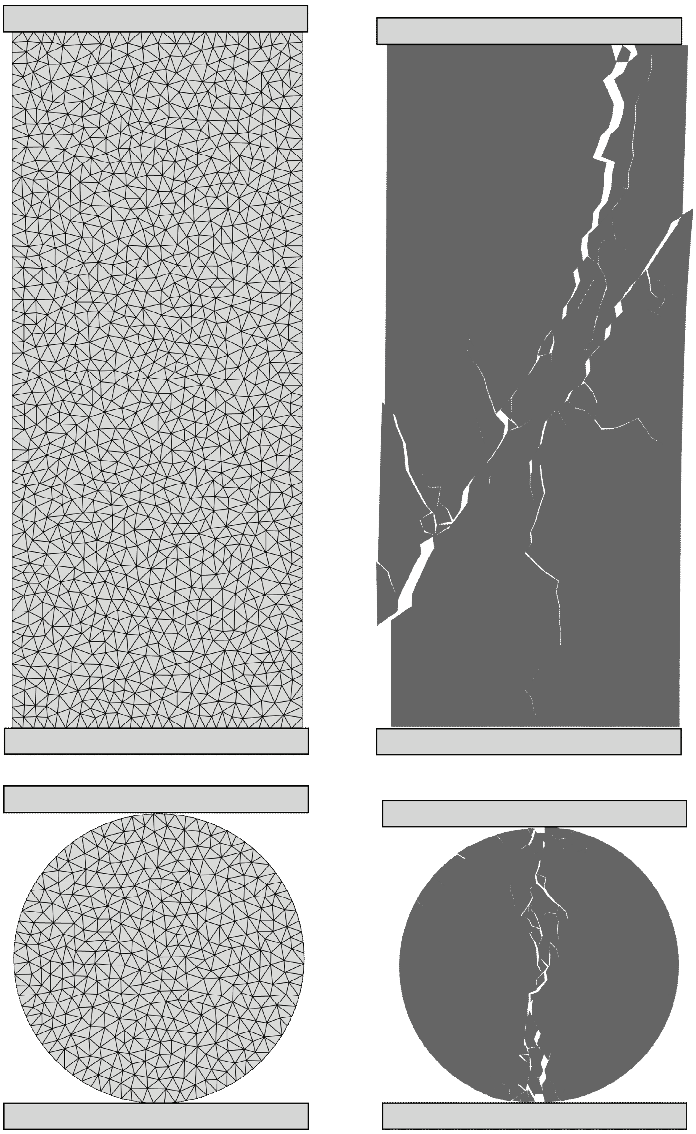
a. geometry and boundary condition before failure

b. predicted failure mode using target micro–parameters

Figure 7–2: Plaster models for simulation of compression and Brazilian tension tests

7.2.2. *Design of experiment*

a. Estimation of lower and upper bounds of factors

Regarding the discussion provided in Chapter 6, the upper and lower bounds for c_c and ϕ_c are assumed as listed in Table 7–2 (next page). Since t_c obtained for the hard and soft rocks, examined in Chapter 6, is 2.8 and 3.9 times their BTS, respectively, its target value for the plaster has been guessed to be between 1.5×BTS to 4.5×BTS, i.e., 2.4 to 7.2 *MPa*.

Table 7–2: Upper and lower bound of CFM micro–parameters for plaster simulation

micro–parameter	lower bound	upper bound	centre (mean)
contact tensile strength, t_c [MPa]	1.50×BTS	4.50×BTS	3.00×BTS
contact cohesion, c_c [MPa]	0.25×UCS	0.75×UCS	0.50×UCS
contact friction angle, ϕ_c [°]	0.85ϕ	1.15ϕ	1.00ϕ

b. Application of the central composite design

Since there are three factors involved in the design, $\alpha = 2^{3/4} \approx 1.682$, and the number of factorial runs is eight (NIST/SEMATECH 2003). Considering the lower, upper and mean values presented in Table 7–2, the centre, factorial, and star points are calculated as listed in Table 7–3. In three–dimensional space, the factorial points denote eight vertices of a cube centred at the origin, with edges parallel to the Cartesian axes representing x_1, x_2 and x_3 and with an edge length of 2. The centre points are then placed on the origin, and the star points are represented by the intersection of the axes and the circumscribed sphere of the cube.

Table 7–3: Definition of factors and numerical value of micro–parameters at each coded level

factor	corresponding micro–parameter	value of micro–parameter at coded levels					transformation formula
		$-\alpha$	–1	0	+1	$+\alpha$	
x_1	contact tensile strength, t_c	0.76	2.4	4.80	7.20	8.84	$t_c = 2.40\times$[coded level] + 4.80
x_2	contact cohesion, c_c	0.60	1.88	3.75	5.63	6.90	$c_c = 1.88\times$[coded level] + 3.75
x_3	contact friction angle, ϕ_c	29.91	34.00	40.00	46.00	50.09	$\phi_c = 6.00\times$[coded level] + 40.0

Table 7–4: Complete design matrix for central composite design

run	point type	factor 1 (x_1)	factor 2 (x_2)	factor 3 (x_3)
1	corner (1)	–1	–1	–1
2	corner (2)	1	–1	–1
3	corner (3)	–1	1	–1
4	corner (4)	1	1	–1
5	corner (5)	–1	–1	1
6	corner (6)	1	–1	1
7	corner (7)	–1	1	1
8	corner (8)	1	1	1
9	star (a)	–1.682	0	0
10	star (b)	1.682	0	0
11	star (c)	0	–1.682	0
12	star (d)	0	1.682	0
13	star (e)	0	0	–1.682
14	star (f)	0	0	1.682
15	centre (i)	0	0	0
16	centre (ii)	0	0	0
17	centre (iii)	0	0	0
18	centre (iv)	0	0	0
19	centre (v)	0	0	0
20	centre (vi)	0	0	0

Table 7–4 offers the CCD design matrix for three factors (NIST/SEMATECH 2003). Using the transformation formula expressed at the last column of Table 7–3, this matrix can be converted to the matrix of the real factors, i.e., micro–parameters matrix at Table

7–5. The laboratory tests are then simulated using each set of the CCD–suggested micro–parameters. These tests include the Brazilian tension, uniaxial and triaxial compression tests on the samples shown in Figure 7–2a, where the confining pressures applied in triaxial tests, σ_3, equals 0.5 and 1 *MPa*. Finally, the model macroscopic results, in terms of tensile strength, internal cohesion, and internal friction angle are recorded as the DOE responses (Table 7–5), where internal cohesion and internal friction angle are calculated based on the obtained uniaxial and triaxial compressive strengths.

Table 7–5: CCD–suggested micro–parameters and obtained results

	micro–parameters matrix			DOE responses			CFM results for compressive models		
run	t_c	c_c	ϕ_c	σ_t	C	ϕ	$\sigma_3 = 0\,MPa$	$\sigma_3 = 0.5\,MPa$	$\sigma_3 = 1.0\,MPa$
1	2.40	1.88	34.00	0.38	0.69	49.58	3.75	7.44	11.71
2	7.20	1.88	34.00	0.47	1.91	21.78	5.65	6.74	7.85
3	2.40	5.63	34.00	0.38	0.60	69.79	6.79	22.54	41.05
4	7.20	5.63	34.00	1.04	1.86	62.67	15.27	23.73	33.18
5	2.40	1.88	46.00	0.31	0.60	62.89	5.00	13.60	23.15
6	7.20	1.88	46.00	0.81	2.09	39.91	8.95	11.24	13.89
7	2.40	5.63	46.00	0.31	1.59	70.77	18.77	36.19	54.00
8	7.20	5.63	46.00	1.11	1.81	70.57	21.11	38.16	57.70
9	0.76	3.75	40.00	0.07	1.15	61.35	9.01	16.68	24.54
10	8.84	3.75	40.00	1.14	2.55	50.97	14.39	18.37	22.84
11	4.80	0.60	40.00	0.10	0.49	33.06	1.79	3.49	5.53
12	4.80	6.90	40.00	0.70	0.87	73.53	11.96	35.83	62.55
13	4.80	3.75	29.91	0.70	1.10	56.53	7.33	12.86	19.25
14	4.80	3.75	50.09	0.76	1.68	66.39	16.10	27.55	40.93
15	4.80	3.75	40.00	0.70	1.71	57.46	11.75	17.62	23.98
16	4.80	3.75	40.00	0.63	1.77	60.41	13.39	20.56	28.32
17	4.80	3.75	40.00	0.80	1.93	56.67	12.91	18.49	24.33
18	4.80	3.75	40.00	0.90	2.14	53.39	12.93	17.50	22.80
19	4.80	3.75	40.00	0.71	1.53	60.82	11.76	19.14	26.83
20	4.80	3.75	40.00	0.79	1.71	57.67	11.80	17.75	24.62

Again, the simulations are predictively repeated for several times with the same micro–parameters at the centre point to minimize the variability in modeling.

Using the data presented in Table 7–5, the following equations between the model macroscopic response and the coded factors are constructed.

$$\begin{aligned}\sigma_t &= 0.75 + 0.28x_1 + 0.14x_2 + 0.03x_3 + 0.11x_1x_2 + 0.07x_1x_3 - 0.03x_1x_3 \\ &\quad - 0.05x_1^2 - 0.12x_2^2 - 0.002x_3^2\end{aligned} \tag{7–1}$$

$$\begin{aligned}C &= 1.80 + 0.48x_1 + 0.09x_2 + 0.15x_3 - 0.15x_1x_2 - 0.10x_1x_3 + 0.11x_2x_3 \\ &\quad + 0.04x_1^2 - 0.37x_2^2 - 0.12x_3^2\end{aligned} \tag{7–2}$$

$$\begin{aligned}\phi &= 57.77 - 5.53x_1 + 12.28x_2 + 4.17x_3 + 5.43x_1x_2 + 1.47x_1x_3 - 2.82x_2x_3 \\ &\quad - 0.75x_1^2 - 1.77x_2^2 + 1.12x_3^2\end{aligned} \tag{7–3}$$

Equations 7–1 to 7–3 form a quadratic system of simultaneous equations for the coded factors. Solving it for σ_t = 1.6 *MPa*, C = 1.75 *MPa* and ϕ = 40° of the plaster, x_1 = 0.871, x_2 = 0.675 and x_3 = –0.583. Using the transformation equations, the uncoded factors are t_c = 6.89 *MPa*, c_c = 5.02 *MPa*, and ϕ_c = 36.50° as the target micro–parameters.

7.2.3. *Calibration verification*

The target micro-parameters obtained are listed in Table 7-6. Using this set of data, the tensile and compressive simulations are again repeated for five times. The results in terms of mean, standard deviation and relative error are listed in Table 7-7, where they show perfect agreements with the experimental measurements.

Table 7-6: List of target micro-parameters for simulation of the plaster

E_p [GPa]	v_p	k_t [GPa/mm]	k_s [GPa/mm]	t_c [MPa]	c_c [MPa]	ϕ_c [°]
1.30	0.20	2.50 / 2.61	0.698 / 0.727	6.89	5.02	36.50

Table 7-7: Experimental properties of the plaster versus CFM predictions

property	E [GPa]	v	σ_t [MPa]	σ_c [MPa]	C [MPa]	ϕ [°]
experimental value	1.3	0.20	1.6	7.5	1.75	40.0
numerical mean	1.3	0.20	1.6	7.4	1.77	40.3
standard deviation	0.01	0.01	0.04	0.16	0.04	0.59
relative error %	1.54	4.03	3.13	4.01	3.43	2.51

The CFM predictions for failure mode of the Brazilian tension and uniaxial compression tests have been plotted in Figure 7-2b. As seen, the characteristic failure reported for soft rocks is reproduced, as shear faulting is the major rupture process (Paterson 1978).

7.2.4. *Discussion*

Comparing the multipliers in Equations 7-1 to 7-3, necessity of a quadratic RSM is justified (See Section 6.2.4 for the description of the RSM). Equation 7-1 shows that the model tensile strength is more dependent of the contact tensile strength than its cohesion, while it is not very affected by the contact friction angle. The first and second order variables in Equation 7-2 show that the model cohesion is more significantly related to the contact tensile strength than its cohesion and friction angle. Equation 7-3 presents that the contact tensile strength has an important role on the model friction angle, although the most significant effect comes from the contact cohesion.

These results indicate that contact tensile strength is the critical micro-parameter, as it mainly characterizes the sample strength in the CFM simulations. This agrees with the experimental observations by Hazzard and Young (2000) mentioning that failure in rocks starts with the creation of inter-mineral tensile fractures in parallel with the applied load. Then, coalescence of these micro-fractures creates a major failure surface as observed in the numerical modeling as well as the laboratory.

7.3. **Rock joint modeling**

7.3.1. *Specimen geometry and boundary condition*

The model geometry corresponds to that chosen by Yang and Chiang (2000). Figure 7-3 offers a schematic view of the joint samples together with the assigned boundary condition. The joint lower half is free to displace horizontally while vertically restrained. Conversely, the upper part is quite bonded by a rigid body prevented from any movement in the lateral direction. The rigid body is to obstruct the upper half from any global rotation. Consequently, dilation is allowed while rotation is not. These are the standard circumstances under which the rock joint shear tests are normally preformed.

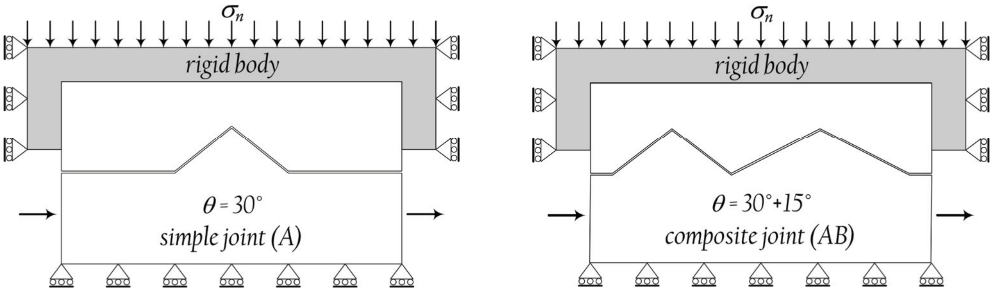

Figure 7–3: Schematic representation of joint samples and applied boundary condition

As shown by Yang and Chiang (2000), the material damage zone is limited to the joint tooth. Hence, only the teeth are permitted to break and the other parts of the specimen are assumed as elastic. The damage zone, i.e., the joint tooth, is discretized by particles with the average edge size of 0.2 *mm*. Figure 7–4 illustrates the particle assemblage forming a 30° asperity. A total of 393 and 1241 particles have been taken part in model A and AB, respectively.

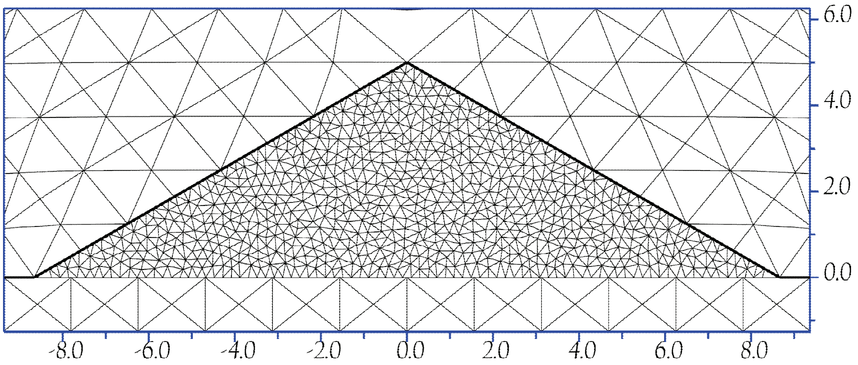

Figure 7–4: Particle assemblage in a 30° joint asperity (units in millimeter)

The test proceeds by first compressing the joints to reach the prescribed normal stress. Adopting a plain–stress analysis, the joints are then sheared by a controlled lateral displacement horizontally exerted to the lower half. To limit the computation time, a rate of 2 *mm/s* has been applied.

7.3.2. *Predictions and discussion*

The joints mechanical response is examined under normal stress of 0.39 and 1.47 *MPa*. A Coulomb friction law is assigned to the joint surface illustrated by the black thick line in Figure 7–4. The penalty parameter to control surface interpenetration is assumed 2.50

GPa/mm, equal to k_n for plain–strain. This value is large enough to avoid any excessive overlap between the upper and lower parts of the specimen. The shear stiffness coefficient of the joint surface is fixed at 10 *MPa/mm* to best fit the elastic deformation of the joint in the pre–failure region. The friction angle of the joint surface is 35°.

a. Single–tooth joint

As shown in Figure 7–5, the overall trend of the experimental response of the discontinuity, in terms of the joint strength and dilatancy, is satisfactorily reproduced, and the maximum and tail values of the shear stress are properly predicted.

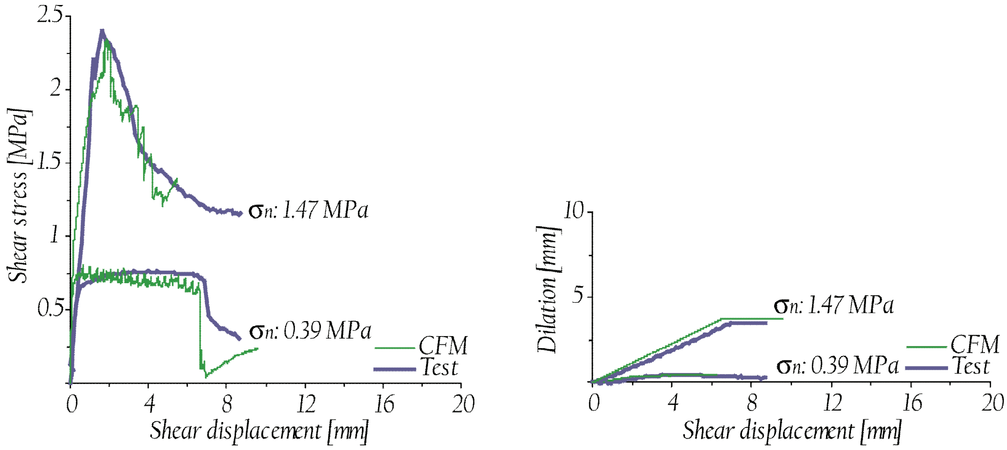

Figure 7–5: Shear stress and dilation versus shear displacement for the simple joint

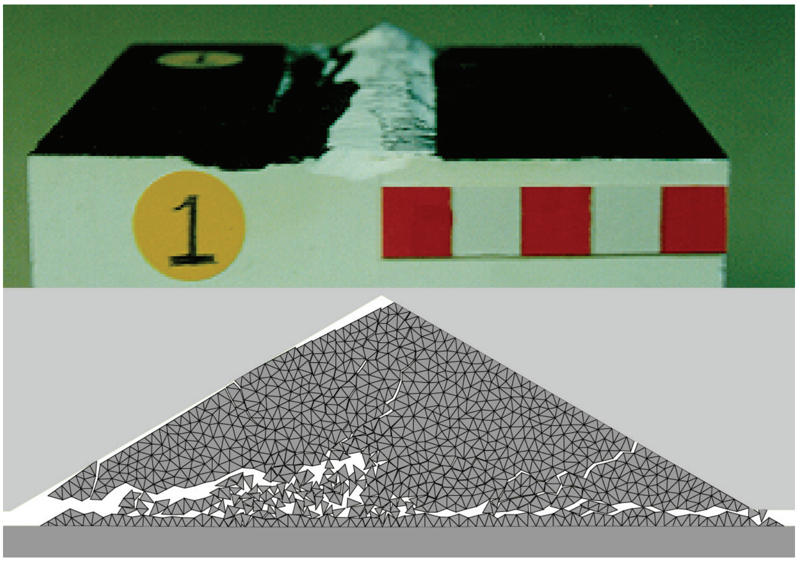

Figure 7–6: Numerical and experimental failure modes for the simple joint under 1.47 MPa

Every time that one or several contacts fail, a sudden drop in the numerical response happens. However, the initial normal stress causes the broken contacts to get closed, and therefore the joint shear stress evolves again. These sequences of the drop and evolution give an oscillating appearance to the model shear response. Figure 7–6 demonstrates that the numerical and experimental failure patterns eventually are fairly similar.

b. Double–tooth joint

Both the high and low values of the normal pressure are applied on the composite joint. Although the peak shear strength is fairly reproduced under 1.47 *MPa*, there is a qualitative difference between the laboratory results and the numerical response in the post–failure stage (see Figure 7–7). Comparing the test measurement, the model does not reproduce the flat zone and shows a larger drop in the shear stress, after which stress increases again. This is typical of a staggered contribution to the shear strength, i.e., the 30° tooth breaks and subsequently the 15° one is mobilized. This phenomenon causes a sudden fall in the joint shear response. On the contrary, the smooth inclination in the experimental observation suggests that both the teeth are somehow sheared simultaneously. The reason of this difference might be a matter of the experimental boundary condition, which is uncertain, or the 2D state of the numerical simulation versus the 3D nature of the experiment. Note that the numerical instabilities (mainly excessive particles interpenetration) caused the calculation to stop after 5 *mm* of shearing. To remove this inconvenience, we have to reduce the time step further, which makes the solution inefficient.

As seen in Figure 7–7, the laboratory measurements are better predicted under normal stress of 0.39 *MPa* than 1.47 *MPa*, where both the peak and residual shear strengths are properly reproduced.

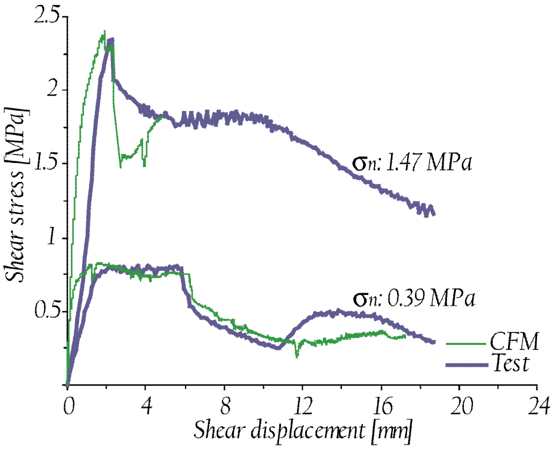

Figure 7–7: Shear stress versus shear displacement for the composite joint

7.4. Conclusion

Using the CFM, two types of the plaster–made rock joints were modeled. The results for the simple joint were excellent. Shear strength, dilation and failure mode of the joint were properly predicted, where no additional modification or effort was required.

The model fitted the pre–failure response and the peak strength for the composite joint as well. However, there was a qualitative difference between the experiment and the numerical reproduction under high normal pressure, where the model showed a significant drop in shear stress following its peak value. Nevertheless, the model succeeded to match the laboratory results of the composite joint under low normal pressure.

The presented results demonstrate that the CFM is able to predict rock joints shear response, when the micro–parameters used are obtained from the standard compressive and tensile test data of the rock.

CHAPTER 8

Dynamics fracturing in homogeneous material

This chapter examines the CFM application for dynamic problems specifically in terms of homogeneous materials. First, related studies, concerning crack propagation in metals and polymers, are briefly reviewed. Following this, a distinctive experimental study, chosen for the verification of the simulation, will be explained in detail. Modeling the test and comparing the obtained results with those of the experiment, the capabilities and deficiencies of the CFM simulation will be explored. Finally, necessary developments will be adopted in order to incorporate dynamic effects into the CFM.

8.1. Dynamic fracture in homogenous material

A major objective in studying dynamic fracture is to predict crack dissemination pattern and velocity. The linear elastic fracture mechanics suggests the Rayleigh surface wave speed, c_R, as the upper limit for the material cracking velocity, v_{cr} (Freund 1990; Broberg 1999). However, in rapid cracking of brittle solids, the crack–tip zone undergoes a series of complex mechanisms such as large and nonlinear deformation, high strain rate, plasticity, micro–crack nucleation, heat diffusion and subsequent thermal softening. These mechanisms cause the fracture energy release rate, G_f, to increase when the crack velocity increases. For most materials, when v_{cr} approaches a critical value called terminal velocity, v_L, G_f infinitely increases, and finally the crack stops further accelerating (Ravi–Chandar and Knauss 1984; Dally et al. 1985; Fineberg et al. 1991; Sharon et al. 1996).

Several approaches have been applied to examine dynamic fracturing. Nishioka (1995) and Nishioka et al. (2001) introduced the dynamic J–integral into a moving finite element mesh that needs a re–meshing algorithm with a very fine mesh around the crack tip. Belytschko and Black (1999) and Moes et al. (1999) suggested an extended FEM (XFEM) solution with crack propagation through the ordinary elements which gives a smooth crack path with minimal re–meshing effort. However, discontinuities must be considered in the shape functions to model broken elements. This makes the solution too effortful when cracks intersect.

Introduced by Dugdale (1960) and Barenblatt (1962), the cohesive finite element methods which are based on the cohesive zone concept, have been extensively used in recent years. Xu and Needleman (1994, 1995, 1996) applied an elastic–exponentially decaying cohesive law. Camacho and Ortiz (1996, 1997) proposed a rigid–linear law in 2D space. Later on, Pandolfi et al. (1999, 2000) and Ruiz et al. (2000) carried it out for 3D analysis. Zhai et al. (2004) analyzed dynamic fracture in two–phase Al_2O_3/TiB_2 ceramic composite microstructures using the cohesive element. The model integrates cohesive surfaces along all finite element boundaries as an intrinsic part of the material description. This approach obviates the need for any specific fracture criteria and assigns models with the capability of predicting fracture paths and fracture patterns. Karedla and Reddy (2007) applied high inertia zone theory to a cohesive finite element model to examine crack branching in PMMA. Nevertheless, the crack propagation speed was not fully discussed. In all the research mentioned, the cohesive laws used are rate–independent, i.e., the traction mobilized within the crack is just a function of its separation but independent of its opening speed.

Much attention has been paid recently to the rate–dependent cohesive models. Li and Bazant (1997a, 1997b) proposed a visco–elastic rate–dependent law to analyze a stationary crack under dynamic loading in concrete that results in cohesive forces extremely exceeding the material ultimate strength. Lee and Prakash (1999) studied dynamic fracturing in high–strength brittle steels. They found that the rate–dependency assumption is crucial to reproduce the experimental results.

Zhou et al. (2005b) introduced a linear decaying law into the cohesive interface elements to reproduce the laboratory results of PMMA cracking. However, their numerically predicted v_{cr} was not limited to v_L. Block et al. (2007) developed the cohesive nodal force method which needed a compulsory continuum damage model for solid elements to control the model energy dissipation at high loading rates.

8.2. Dynamic crack propagation in PMMA plates

In this section, the experimental work done by Shioya and Zhou (1995) on fracture behavior of the pre–strained PMMA strips is presented. More explanation in terms of the test setup and the experimental results is published by Zhou et al. (2005a), and a detailed description is presented by Zhou (1996).

8.2.1. *Experimental setup and measurement*

Polymethyl Methacrylate (PMMA) rectangular plate (3 *mm* thick) was used as the test material. Before crack propagation, a universal test machine loaded the specimen in tension. The magnitude of the loading was measured by the load cell in the test machine. After reaching a given load level, a small sharp crack was initiated at the middle point of one specimen end by a razor. Since the material is very brittle, the crack quickly propagated straight across the specimen.

To record the crack propagation during the test, electric conductive lines were drawn on the specimen surface. They were connected to an electronic logic circuit. When the crack propagated, the time at which it cut each line was recorded by a digital memory. From this record and the position of each line, the crack propagation history and its velocity were obtained.

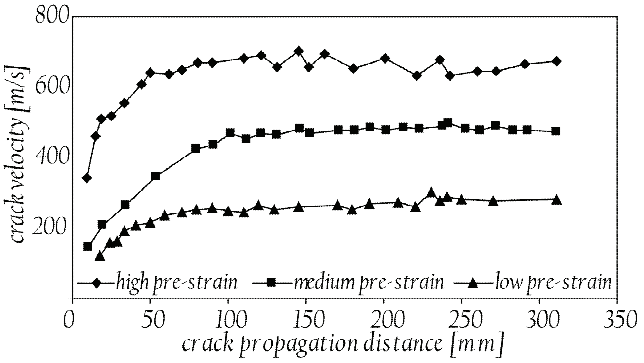

Figure 8–1: Crack velocity recorded under various levels of loading (Zhou et al. 2005a)

As presented in Figure 8–1, the test data showed that the crack velocity tends to a steady asymptotic value, and this steady propagation state continues until the crack tip reaches the opposite edge of the specimen. The average steady velocity of the crack is called crack velocity and is denoted by v_{cr}.

8.2.2. *Test results*

Various specimens with different geometries were tested. By changing the induced tension and size of the specimen, different values of elastic strain energy, W, were obtained. From each test, a data point of (W,v_{cr}) was produced some of which are plotted in Figure 8–2.

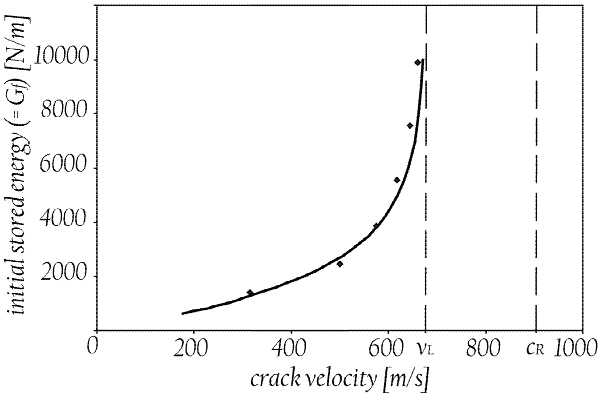

Figure 8–2: Initial stored energy versus crack propagation velocity (Zhou et al. 2005a)

During the fracture process, the vast majority of the specimen strain energy is consumed through material fracture, and the rest is converted to kinetic energy. Since the initial deformation applied to each specimen was small compared to its size, the material kinetic energy in the region behind the crack front can be assumed negligible. Therefore, the strain energy stored per unit length of the specimen is approximately equal to the energy consumed by unit length of the crack propagation, i.e., the dynamic fracture energy release rate, G_f. This equality is verified by Zhou et al. (2005a).

Hence, Figure 8–2 demonstrates, in fact, the variation of G_f versus v_{cr}. If fitting a monotonically–increasing curve to the points in Figure 8–2, the relation ship between the material fracture energy and the crack propagation speed can be expressed by the following empirical equation, where $v_L = 675$ *m/s* and $G_0 = 1000$ *N/m*.

$$G_f = G_0 \frac{v_L}{v_L - v_{cr}} \tag{8–1}$$

8.2.3. *Crack branching (bifurcation)*

It was observed the crack surface becomes rougher with increasing crack velocity. As described by Zhou et al. (2005a), under low pre–strain ($W < 4000$ *N/m*) the crack propagation velocity was low ($v_{cr} < 450$ *m/s*), and the fractured surface was smooth. In moderate values of pre–strain ($W = 4000–8000$ *N/m*), the crack velocity was higher ($v_{cr} = 450–600$ *m/s*), and some streaks and roughness were observed on the crack surface. At first, these streaks were not remarkable. However, when the crack velocity approached 600 *m/s*, they became more evident and deeper (0.01 *mm* order), but the crack still ran in a single straight path.

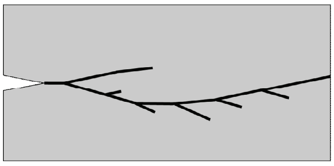

Figure 8–3: Schematic plot of crack bifurcation under very high pre–strain

Under very high pre–strain ($W > 8000$ *N/m*), the crack velocity exceeded 600 *m/s*, and some small cracks started branching from the main crack (Figure 8–3). Generally, in the velocity range about 600–650 *m/s*, these small cracks stopped further propagating and created the micro–branches seen in the laboratory. However, when $v_{cr} > 650$ *m/s*, one or few of these small cracks continued running as far as 1 *mm* or more, and crack bifurcation happened.

8.3. Reproduction of the dynamic crack velocity by CFM

Validity of the CFM for dynamic fracture simulation is examined here through modeling the experimental data.

8.3.1. *Material properties*

Mechanical properties of the model are assumed the same with the experiment.

Table 8–1: Mechanical properties of PMMA

Young's modulus, E	3090 MPa	Poisson's ratio, ν	0.35
Mode-I fracture toughness, K_{IC}	0.96 $MPa\sqrt{m}$	fracture energy, G_f	300 N/m
Mode-II fracture toughness, K_{IIC}	0.83 $MPa\sqrt{m}$	tensile strength, σ_t	75 MPa

The Mode–II fracture toughness has been measured using the semi–circular bend specimen at the crack angle of 50° (reported by Ayatollahi and Aliha 2006).

The PMMA density is 1180 kg/m^3. According to the elastic wave equations (Bedford and Drumheller 1996), the longitudinal, shear and Rayleigh surface wave speed are obtained as c_L = 1618 m/s, c_S = 985 m/s, and c_R = 906 m/s, respectively. Therefore the experimental terminal velocity of crack propagation, v_L, is about 75% of c_R.

8.3.2. *Model geometry and boundary condition*

The PMMA plate modeled is l = 32 mm long, h = 16 mm high and contains a 4 mm long slit along the centerline. The plate is made of 204,800 right isosceles triangular particles with the hypotenuse of d_p = 0.1 mm, where each particle consists of one CST. The model totally has 2,457,600 degrees of freedom. Its geometry and a part of the particle assemblage are shown in Figure 8–4.

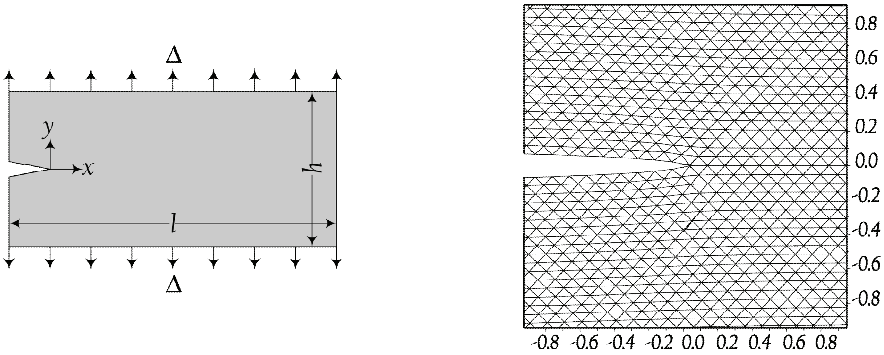

Figure 8–4: Model geometry and boundary condition (left) and a part of particle assemblage focusing initial crack–tip (right), dimensions in millimeter

8.3.3. *Analysis procedure*

The plate is initially loaded by a prescribed tensile displacement, Δ, along the upper and lower boundaries in the y–direction, while the crack is not allowed to propagate. The specimen is not constrained in the x–direction. A plane–stress static analysis is then conducted to calculate the initial strain and stress state of the plate with the stationary crack. To reach this purpose, the local damping factor, α, is taken as 0.8 to secure the quasi–static equilibrium of the plate. Under these loading circumstances, the strain energy, stored per unit area of the (pre–strained) plate, is

$$W = \frac{1}{2}\frac{E(2\Delta)^2}{h} = \frac{2E\Delta^2}{h} \tag{8–2}$$

After the static calculation, the plate is allowed to fracture, where its boundary condition is kept fixed. An explicit dynamic analysis is performed by assuming $\alpha = 0$. As suggested in the classical numerical methods, e.g. FEM and DEM, the time step in an explicit analysis must be shorter than the time of P–wave propagation through the particle length, which is calculated as 6×10^{-8} *sec* for the model. As the time step suggested by UDEC is 4×10^{-9} *sec*, numerical stability of the dynamic analysis is therefore guaranteed.

At the end of the static analysis, a high stress concentration is induced at the tip of the pre–existing crack. This stress far exceeds the contact strength and thus may lead to a sudden and extensive failure over the zone close to the crack tip at the beginning of the dynamic analysis. However after a short time, the crack is seen to propagate in a steady state similar to the laboratory observations (see Figure 8–5).

8.3.4. *Micro–parameters*

The orthotropic cohesive contact law was completely explained in Chapter 5. Since PMMA is considered as an isotropic homogeneous material, the contact law can become simplified, e.g. both the tensile and shear peak strengths of contact can be assumed equal to the PMMA tensile strength, i.e., $t_c = c_c = 75$ *MPa*. Moreover, as the plate is subjected to the Mode–I loading, contact shear failure is not expected to occur, and therefore numerical fracture propagation is only controlled by the tensile parameters of contact. Consequently, the contact friction angle can be assumed an arbitrary value, e.g. zero.

Given Equation 5–30, the contact stiffness coefficients in tension and shear are calculated as $k_t = 5.83\times10^5$ *MPa/mm* and $k_s = 2.89\times10^5$ *MPa/mm*. The ultimate tensile opening of contact, δ_{ut}, is obtained through Equation 5–11 as 7.54 *μm* for $G_f = 300$ *N/m*.

8.3.5. *Calculation results*

The CFM predictions in terms of crack propagation velocity are compared with the laboratory data for different amounts of loading. The prescribed boundary displacement, Δ is chosen as 0.06, 0.08, 0.10, 0.12, 0.14, and 0.16 *mm*. Given Equation 8–2, the stored energy, W is then calculated as 1391, 2472, 3863, 5562, 7571, and 9888 *N/m*, respectively.

Since no rate effect is introduced into the model, this modeling exercise is referred to as Rate–Independent (RI) model, in which the strength and the ultimate displacement of contact are constant regardless the loading rate. NCRI (Non–Cohesive RI) denotes a particular RI model where the ultimate tensile displacement of contact is assumed equal to its critical displacement. NCRI is brought into consideration to evaluate how much contact cohesiveness affects on the model dynamic response.

The particle size adopted is the minimum possible regarding efficiency considerations. However, it is much larger than the size of the streaks and micro–branches observed on the crack surface when applying low or moderate pre–strain. Therefore, crack branching is not allowed in the numerical model except under very high pre–strain, where the branch size is larger than the mesh size.

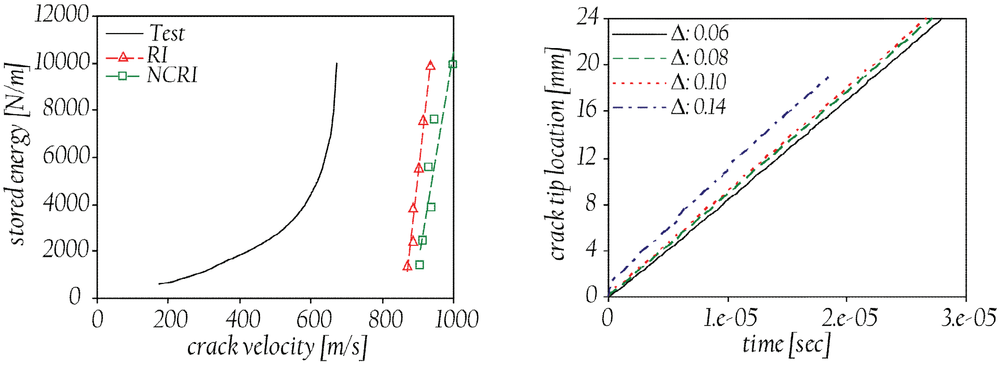

Figure 8–5: Variation of crack propagation velocity calculated using a constant G_f (left) and crack tip location versus time (right) for the RI simulation

For low and moderate loading, i.e., $\Delta \leq 0.14$ *mm*, where crack branching is permitted, the crack reaches the steady velocity after a short acceleration stage, and propagates straight forward until halves the specimen. v_{cr} is then obtained from the curves of the crack tip distance versus time as presented in Figure 8–5. For $\Delta = 0.16$ *mm*, bifurcation is allowed that causes messy crack dissemination (see Figure 8–18a). v_{cr} is there estimated as the average velocity of the crack front.

Figure 8–5 manifestly shows that v_{cr} increases with W, which is qualitatively in accord with the laboratory observations. However, significant deviations are recognized, where under the same level of stored energy, the calculated steady velocity is excessively beyond the test data. The calculated v_{cr} reaches the theoretical crack velocity, i.e., the Rayleigh surface wave speed, even if crack bifurcation is allowed.

The reason of this deviation can be attributed to the process of fracture energy release in the model. Fracture is numerically represented by contact opening that always releases a constant amount of energy, i.e., $G_f = 300$ *N/m*. This energy is much smaller than the strain energy stored in the unit length of the plate (W), as W varies from 1391 to 9888 *N/m*. This means that the fracture driving energy, i.e., W, is much larger than the contact fracture energy, i.e., G_f, which undertakes the model resistance against fracturing. This energy unbalance causes the numerical fracture to propagate much faster than that observed in the experiment, where the fracture energy release is adaptively changing with the instant speed of fracture propagation.

Note that assuming a larger G_f parameter does not effectively resolve this deviation. For example, given $G_f = 3000$ *N/m*, the crack stops propagating for $W < 3000$ *N/m*. The reason is the fracture driving energy is not then adequate to overcome the contact resistance against fracturing. If there is sufficiently high value of W (> 3000 *N/m*), crack will propagate, but its steady state velocity again approaches c_R.

8.3.6. *Discussion*

The presented results reveal that the rate–independent cohesive law with constant G_f cannot satisfactorily reproduce the experimental measurements. This means that structural inertia alone cannot explain the velocity–toughening effect.

Review of the experimental observations can help explore the reason. As schematically illustrated in Figure 8–6, the experimental observations suggest that the main crack propagates straight forward at low crack velocities (Section 8.2.3). Micro–cracking deformation is not then significant, and thus the fracture surface is smooth. On the contrary, many micro–cracks are developed within the process zone when the fracture propagates at high speed. Consequently, dynamic fracture process happens in an expanded damage zone that causes larger amount of energy to be dissipated. Hence, the velocity–toughening phenomenon can be attributed to these microscopic deformations and damage mechanisms happening at the fracture process zone (Shioya et al. 1995).

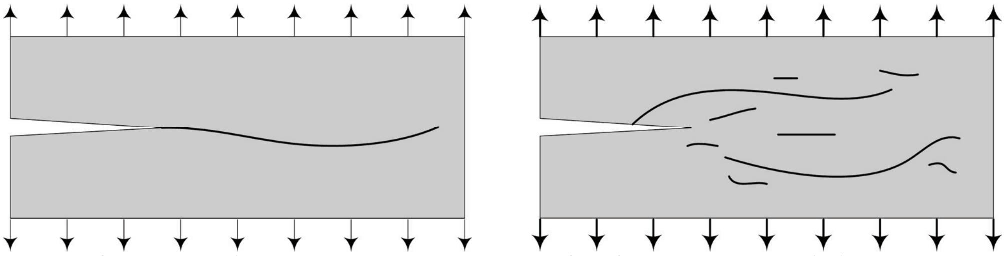

a. slow fracture with small process zone **b. fast fracture in extended process zone**

Figure 8–6: Schematic formation of micro–cracks at fracture process zone

One may argue that the correct macroscopic behavior of crack propagation would be captured, if incorporating the fracture process zone's details into the model by adopting an extremely fine mesh, e.g. 0.01 *mm*. This solution is practically impossible due to several reasons. First, crack propagation will not be then limited to the process zone and instead spreads over the whole specimen size. Second, such a CFM simulation will contain, e.g. 245,760,000 degrees of freedom, and is most likely too huge to be implemented by current computer facilities. Third, deformation mechanisms in the process zone, e.g. large deformation, nonlinear hardening, visco–plasticity, and thermal softening are so complex that their full numerical simulation seems out of reach.

An alternative solution would be creating a rate–dependent model by somehow introducing the rate effects into the contact cohesive law.

8.4. Rate–dependent cohesive model

In the rate–dependent model, the fracture energy of contact, which represents the material fracture energy, G_f, is assumed to change with the crack propagation velocity. However, since this velocity is a macroscopic quantity, it cannot be directly introduced into the contact constitutive law. Alternatively, the contact opening speed, $\dot{\delta}_{eff}$, is assumed as the factor that controls energy release process within the crack–tip zone:

$$\dot{\delta}_{eff} = \frac{\partial \delta_{eff}}{\partial t} \tag{8–3}$$

With an explicit relationship between the numerical crack propagation velocity and the contact opening speed, the (contact) fracture energy, expressed by Equation 8–1, can be reformulated in terms of the contact opening speed. Since the strength and ultimate displacement of contact define its fracture energy, the relationship between each of them and the contact opening speed will be therefore configured.

8.4.1. *Introducing rate effects into the cohesive contact model*

The NCRI results suggest that the modeled crack propagates at the Rayleigh surface wave speed, when no contact cohesive behavior is assumed, i.e., $\delta_{ut} = \delta_{ct}$. Therefore, the time needed for the crack to pass through the edge of a particle is

$$\Delta t = \frac{d_p}{c_R} \tag{8–4}$$

With contact cohesiveness, this time will be definitely longer. The time extension is assumedly proportional to the time needed for a cohesive contact to fully open. In fact, contact cohesiveness delays the stress evolution at the next contact points. Hence, the fracture will propagate slower than the Rayleigh surface wave.

Assuming constant speed for contact opening, the discussed time is defined as

$$\delta t = \frac{\delta_{fin}}{\dot{\delta}_{eff}} \tag{8–5}$$

where δ_{fin} is the final effective displacement that contact undergoes until failure. $\delta_{fin} = \delta_{ut}$ for the rate–independent model. It may be however larger, if taking the rate–dependency into account. Therefore, for the cohesive contact model

$$\Delta t = \frac{d_p}{c_R} + \gamma \delta t \tag{8–6}$$

where γ is the proportion factor. As in fact Δt is represented by d_p / v_{cr},

$$\frac{d_p}{v_{cr}} = \frac{d_p}{c_R} + \gamma \frac{\delta_{fin}}{\dot{\delta}_{eff}} \tag{8–7}$$

Finally, the explicit relation between v_{cr} and $\dot{\delta}_{eff}$ takes the following form.

$$\frac{1}{v_{cr}}=\frac{1}{c_R}+\gamma\frac{\delta_{fin}}{d_p\dot{\delta}_{eff}} \tag{8–8}$$

If assuming no cohesive contact displacement ($\delta_{fin} \approx 0$), Equation 8–8 predicts the crack propagation velocity equal to the Rayleigh surface wave speed, which is in accord with the NCRI results and the LEFM suggestions. However, if admitting the cohesive contact assumption ($\delta_{fin} > 0$, e.g. $\delta_{fin} = \delta_{ut}$ as in the RI model), a lower v_{cr} is predicted which agrees with the results obtained from the RI simulation.

Substituting v_{cr} from Equation 8–8 into Equation 8–1, and assuming $v_L = \alpha c_R$ ($\alpha = 0.75$),

$$G_f=G_0\left[1+\frac{\dot{\delta}_{eff}}{r_G-(1-\alpha)\dot{\delta}_{eff}}\right] \tag{8–9}$$

where

$$r_G=\gamma\frac{\delta_{fin}}{d_p}v_L \tag{8–10}$$

is called reference opening speed of contact. Note that Equation 8–9 and 8–10 suggest that the rate effects, represented by the contact opening speed, would be neglected (constant G_f assumption), if an extremely small mesh size was adopted, i.e., $d_p \to 0$. As explained earlier, this is however impossible with the current modeling practice.

Equation 8–9 provides a pattern for the contact energy variation in terms of the contact opening speed. Since G_f is numerically the product of contact peak strength and ultimate displacement, one or both of them may be assumed to follow a similar pattern. Hence,

$$\delta'_{ut}=\delta_{ut}\left[1+\left(\frac{\dot{\delta}_{eff}}{r_\delta-(1-\alpha)\dot{\delta}_{eff}}\right)^{\eta}\right] \tag{8–11}$$

$$t'_c=t_c\left[1+\left(\frac{\dot{\delta}_{eff}}{r_t-(1-\alpha)\dot{\delta}_{eff}}\right)^{\xi}\right] \tag{8–12}$$

where δ'_{ut} and t'_c denote the rate–dependent evaluations of the ultimate tensile displacement and tensile strength of contact, respectively. r_δ and r_t are referred to as displacement and stress components of r_G.

Note as the product of Equation 8–11 and 8–12 should give the dynamic fracture energy, the exponents of η and ξ have to be taken into account.

Two approaches can be possibly adopted to build the rate–dependent model:

- Partial rate–dependency (RD–P); only the ultimate tensile displacement of contact is changing with the contact opening speed, while the contact tensile strength is fixed.

- Full rate–dependency (RD–F); both the contact tensile strength and ultimate displacement change in terms of the contact opening speed.

Since any development of the contact model is needed to be consistent with the original numerical methodology outlined in Chapter 5, the linear–decaying irreversible cohesive law is still used. In this framework, the two models of rate–dependency are illustrated as follows.

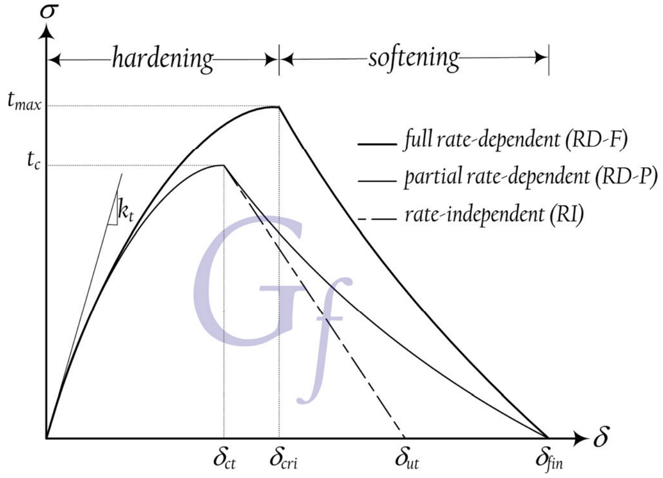

Figure 8–7: Rate–dependent cohesion law of contact

8.4.2. *Partial rate–dependent model*

In the RD–P model, tensile peak strength of contact is fixed at t_c = 75.0 *MPa*. In the softening stage, the ultimate tensile displacement of contact is momentarily updated through Equation 8–11, where δ_{ut} = 7.54 μm. As soon as contact displacement exceeds δ'_{ut}, contact fails and its displacement is taken as the contact final displacement, δ_{fin}. From this instant on, contact will carry no tension whatever its displacement is.

Like the classical CFM formulation, the rate–dependent tensile stress of cohesive contact is expressed through

$$\sigma = \begin{cases} k_t \delta_{eff} \, exp(-\delta_{eff} / \delta_{ct}) & \delta_{eff} \le \delta_{ct} \\ t_c (1-D) & \delta_{ct} < \delta_{eff} \le \delta'_{ut} \\ 0 & \delta_{eff} > \delta_{fin} \end{cases} \qquad (8\text{–}13)$$

where

$$\delta_{ct} = e \frac{t_c}{k_t} \qquad (8\text{–}14)$$

is constant. The damage variable, *D*, is determined by the same manner as described in Section 5.1.1. The unloading–reloading cycles are also handled based on the suggestions outlined there

a. *Influence of rate–dependency parameters*

RD–P's specific parameters are r_δ and η. Assuming three different values for η as 1.0, 1.5, and 2.5, the variation of v_{cr} versus r_δ is investigated. In these calculations, the crack is only allowed to propagate along the specimen centerline. The prescribed boundary displacement, Δ, is fixed at 0.14 *mm*, i.e., W = 7570 *N/m*. Five values of r_δ are chosen: 2.5, 5, 10, 20, and 100 *m/s*. The very large value of r_δ = 100 *m/s* implies that the model essentially behaves as the rate–independent simulation. Figure 8–8 presents the variation of the crack propagation velocity versus the natural logarithm of r_δ.

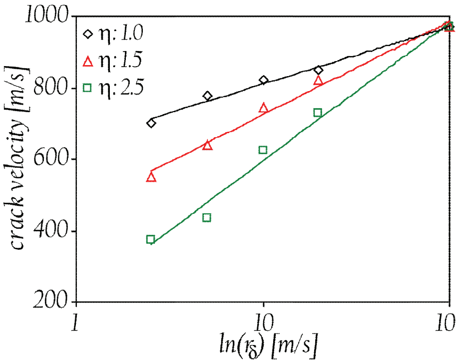

Figure 8–8: Sensitivity of crack propagation velocity to rate–dependency parameters

Clearly, decreasing r_δ slows down the crack propagation. In addition, increasing η makes the results more sensitive to r_δ, where the inclination of the fitted lines gets steeper. All the solutions expectedly converge to the RI prediction, i.e., v_{cr} = 916 *m/s*, when r_δ = 100 *m/s*.

b. *Reproduction of experimental data*

The experimental data fit, depicted in Figure 8–2, offers v_{cr} = 654 *m/s* for W = 7570 *N/m*. Figure 8–8 suggests that if r_δ equals 2.5, 5.0, and 10.0 *m/s* respectively for η = 1.0, 1.5, and 2.5, the simulation will produce v_{cr} as 654 *m/s*. Using these parameters, three RD–P simulations are designed as named in Table 8–2. In each simulation, main crack is allowed to bifurcate for Δ = 0.16 *mm*, where the crack will deviate from the centerline shortly after propagation. That is why the numerical results under Δ = 0.16 *mm* may not be comparable to the experiments and should be examined cautiously.

Table 8–2: Details of the partial rate–dependent simulations

RD–P1	RD–P2	RD–P3
r_δ = 2.5 *m/s* and η = 1.0	r_δ = 5.0 *m/s* and η = 1.5	r_δ = 10.0 *m/s* and η = 2.5

As Figure 8–9 (next page) presents, the simulations results show the same tendency as the experimental data. As manifestly observed, the RD–P predictions are much closer to the test data than those of the RI model are. There still exist certain deviations, where the curvature of the line fitted to the laboratory data is not appropriately reproduced.

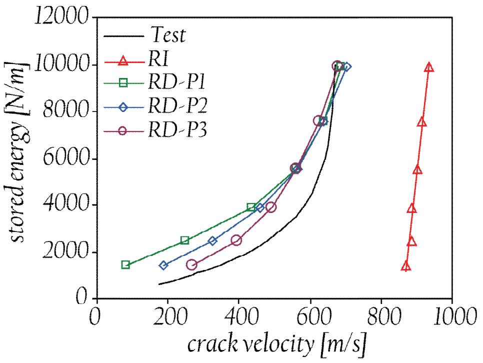

Figure 8–9: Crack propagation speed predicted by the RD–P models listed in Table 8–2

Nevertheless, the trend of curvature produced by RD–P2 is the most comparable one to the experimental data.

The rate parameters are scaled for $\Delta = 0.14$ *mm*. Assuming $\eta = 1.5$, if the process done in Section a is repeated to fit the laboratory data but for $\Delta = 0.06$ *mm*, this time r_δ is obtained as 9.0 *m/s*. Using this set of the rate parameters, crack propagation is again simulated. The results, labeled RD–P4, are compared to the test data and those of RD–P2 in Figure 8–10. It reveals that the RD–P simulation is not able to properly reproduce the test measurements, as the deviation is still existing. The reason may be attributed to the significance of the local stress increase, which is basically absent in the RD–P model.

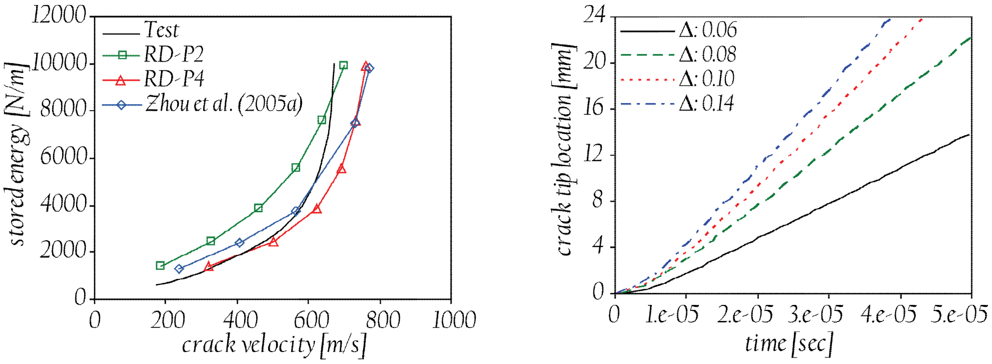

Figure 8–10: Variation of crack propagation speed predicted by the model RD–P2 and 4 (left) and crack tip location versus time for the model RD–P4 (right)

As seen in Figure 8–10, the lines fitted to the results of RD–P2 and RD–P4 follow nearly the same trend of curvature, although r_δ is changed. Therefore, r_δ does not affect on the curvature of the fitted lines. Considering this and the conclusion made in Section a, η is known as the factor determining the hyperbolic shape and curvature of the fitted lines. The numerical predictions by Zhou et al. (2005a) are also plotted. They modeled the fracture behavior of the PMMA plated through adopting an FEM–based scheme called Cohesive Element Model assuming the crack–tip ultimate deformation to be rate–dependent. As seen, their predictions are similar to those of RD–P when the true curvature of the test data is not well reproduced. One may think that the RD–P model may lead to better predictions through changing η or r_δ. Unfortunately, that is not helpful. In case using so small r_δ, the final displacement of contacts becomes unacceptably large and sometimes exceeds the total boundary displacement of the specimen, i.e., 2Δ. If increasing η very much, the crack may behave in a *stop–go* fashion and eventually stop further running. Figure 8–11 demonstrates this phenomenon, where failure instant for the contacts, located on the crack path, is plotted versus their distance from the crack initiation point, for $\eta = 2.5$ and $r_\delta = 1.0$ and 2.5 *m/s*. It shows that far contacts break earlier than near ones do, implying that the crack–tip locks, while the contact points beyond it start separating. This event causes the particles to inter–lock and to overlap each other that finally renders the calculation unstable. Figure 8–11 shows that this situation is more critical as r_δ decreases.

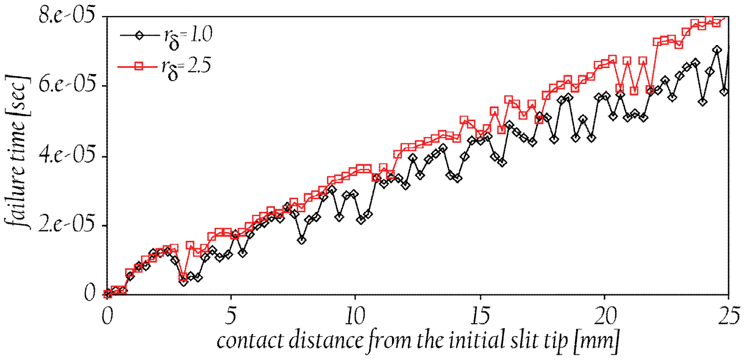

Figure 8–11: Failure time of contacts versus their distance from the initial slit tip for η = 2.5

All the discussions made lead to this conclusion that the RD–P model cannot reproduce the real energy dissipation occurring in the dynamic fracture event. Therefore, increasing both the contact strength and ultimate deformation is necessary to produce the actual fracture energy, and consequently to limit the fracture propagation velocity.

8.4.3. *Full rate–dependent model*

Several experimental investigations (e.g. Li and Bazant 1997a, 1997b; Costanzo and Walton 1998; Allen and Searcy 2001; Kubair et al. 2003; Xu et al. 2003; Ivankovic et al. 2004) suggest that fast cracking results in both local stress and deformation increase in the crack–tip zone. Consequently, contact peak strength as well as its ultimate displacement is expected to change with the contact opening speed. To establish corresponding contact law, the tensile stress of contact is assumed as

$$\sigma = \begin{cases} k_t \delta_{eff}\, exp(-\delta_{eff}/\delta'_{ct}) & \delta_{eff} \le \delta'_{ct} \\ t_{max}(1-D) & \delta_{cri} < \delta_{eff} \le \delta'_{ut} \\ 0 & \delta_{eff} > \delta_{fin} \end{cases} \tag{8–15}$$

where

$$\delta'_{ct} = e\frac{t'_c}{k_t} \tag{8–16}$$

In the hardening stage (see Figure 8–7), the contact tensile strength is momentarily updated by Equation 8–12, where $t_c = 75.0\ MPa$. As soon as contact reaches the cohesive softening phase, its instantaneous tensile stress and displacement are recorded as t_{max} and δ_{cri}, respectively. Given these values and δ'_{ut} obtained from Equation 8–11 where $\delta_{ut} = 7.54\ \mu m$, the damage variable ($D$), and subsequently the contact cohesive stress are evaluated.

Note that if a simple linear equation was adopted in Equation 8–15 to represent the contact hardening process, the contact opening speed would be prevented to evolve significantly due to constantly high stiffness of contact. To resolve this inconvenience, contact must lose its stiffness as its displacement evolves. Therefore, an exponential hardening behavior is assumed, where its decaying stiffness allows the separation of contact to accelerate, and consequently lets its opening speed be numerically defined.

a. *Influence of rate–dependency parameters*

Fixing r_δ and η as they are in RD–P4, the influence of r_t and ξ on the RD–F model response is examined. For this purpose, assuming two levels of r_t as 2.0 and 3.0 *m/s*, the variation of v_{cr} versus ξ is investigated. In these calculations, the crack is only allowed to propagate along the plate centreline. The prescribed boundary displacement, Δ is fixed at 0.14 *mm*, where $W = 7570$ N/*m*, and the experimentally observed speed is estimated as 654 *m/s* (Figure 8–2).

Figure 8–12 presents the variation of the crack propagation velocity versus ξ varying from 0.1 to 0.4. Clearly, increasing ξ slows down the fracture propagation. In addition, the higher r_t gives less sensitive results to ξ, specifically when $\xi < 0.3$. For the lowest ξ, both the simulations tend to the same predictions, which is, as expected, very near the RD–P4 result, i.e., $v_{cr} = 734$ *m/s*.

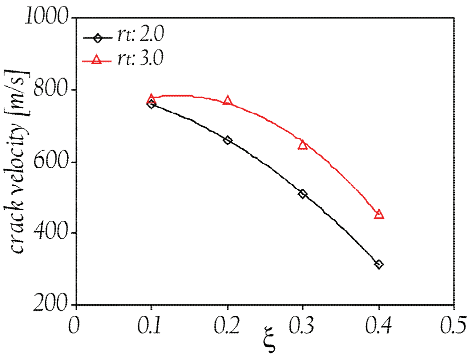

Figure 8–12: Sensitivity of crack propagation velocity, predicted by the RD–F model, to rate–dependency parameters

b. *Reproduction of experimental data*

As Figure 8–12 suggests, the experimental measurement of crack velocity, i.e., 654 *m/s*, can be reproduced, if taking ξ as 0.2 and 0.3 respectively for $r_t = 2.0$ and 3.0. Using these parameters, two RD–F runs are implemented, as named in Table 8–3 (next page). Their results, in terms of W versus v_{cr}, are illustrated in Figure 8–13, where the single crack is allowed to bifurcate only for $\Delta = 0.16$ *mm*.

Table 8–3: Details of the full rate–dependent simulations

RD–F1	RD–F2
$r_\delta = 9.0$ *m/s* and $\eta = 1.5$	$r_\delta = 9.0$ *m/s* and $\eta = 1.5$
$r_t = 2.0$ *m/s* and $\xi = 0.2$	$r_t = 3.0$ *m/s* and $\xi = 0.3$

The numerical results show very much the same pattern with the experimental data. The RD–F predictions are so closer to the test data than those by the RD–P model are. The RD–F2 simulation decreases crack propagation speed too much under high pre–strain. This means that $\xi = 3$ is so large, that causes contacts located at the crack–tip zone not to break under very high tensile stresses. The RD–F1 results provide the best fit, as they properly reproduce the experimental measurements all over the stored energy values.

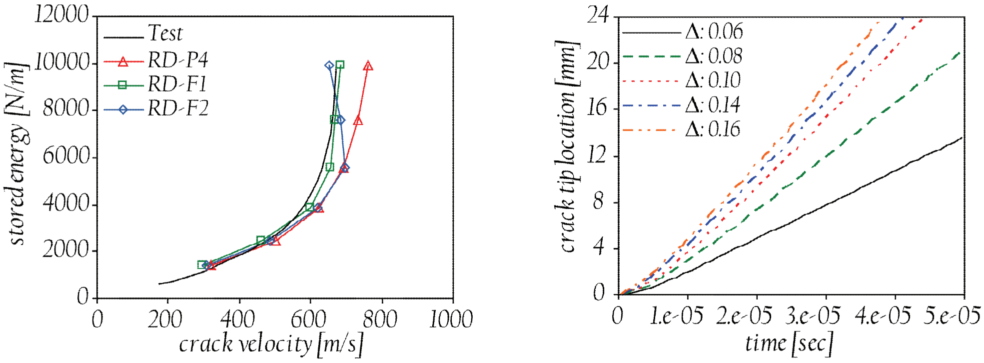

Figure 8–13: Variation of crack propagation speed predicted by the model RD–F1 and 2 (left) and crack tip location versus time for the optimal model of RD–F1 (right)

In order to observe how the rate parameters control contact response, variation of cohesive stress within a contact point, located at $x = 12$ *mm*, is plotted versus its effective displacement. Figure 8–14 and 8–15 present these curves for the RD–P4 and RD–F1 models under different levels of Δ. As manifested in both the plots, the contact ultimate displacement is much larger than its static value, i.e., $\delta_{ut} = 7.54$ μm.

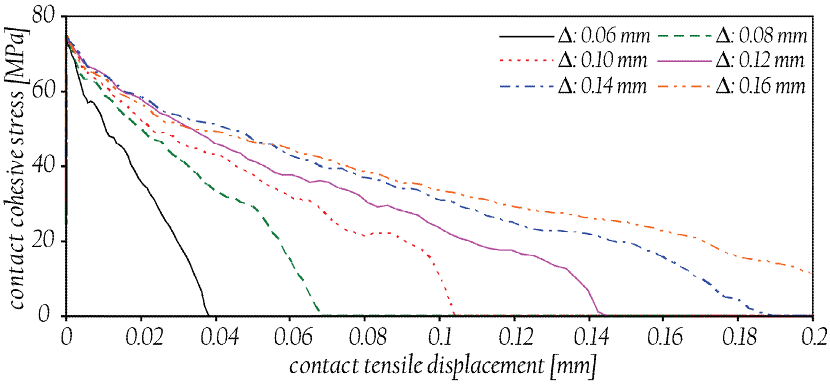

Figure 8–14: Contac cohesive stress versus contact displacement for the RD–P4 simulation

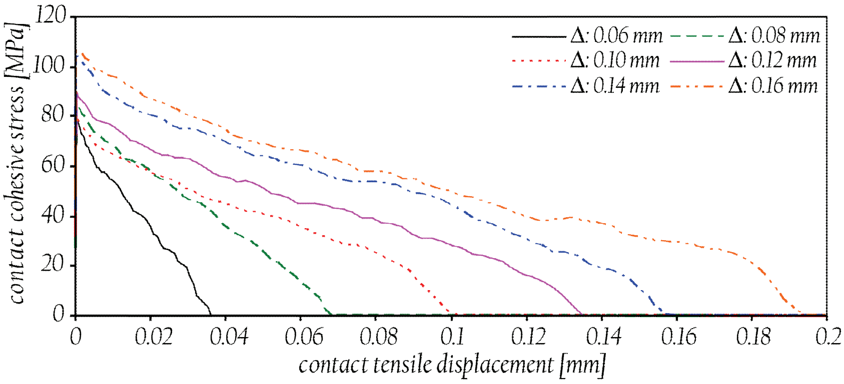

Figure 8–15: Contact cohesive stress versus contact displacement for the RD–F1 simulation

The RD–P4 model gives δ_{fin} as 0.24 *mm* for the total boundary displacement of 0.32 *mm* (Δ = 0.16 *mm*). δ_{fin} predicted by the RD–F1 simulation is smaller, i.e., 0.19 *mm*, where the contact peak strength is increased and reaches 1.42t_c (= 106.5 *MPa*) under the highest pre-strain (see Table 8–4 for details). For low pre-strain, i.e., $\Delta < 0.1$ *mm*, the contact strength increase is insignificant and RD–F1 follows the RD–P4 predictions (see Figure 8–13).

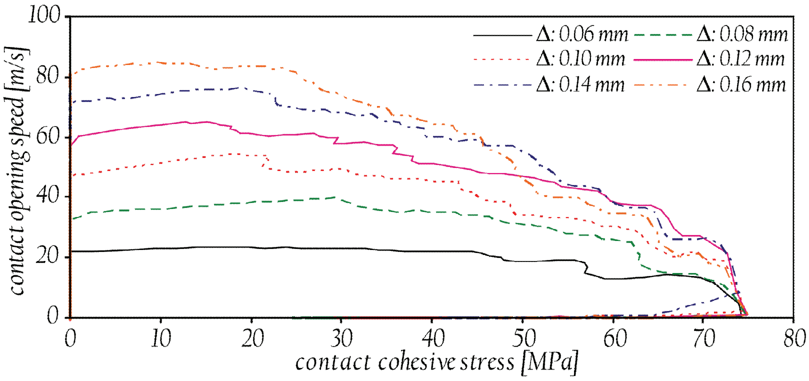

Figure 8–16: Contact opening speed versus contact cohesive stress for the RD–P4 simulation

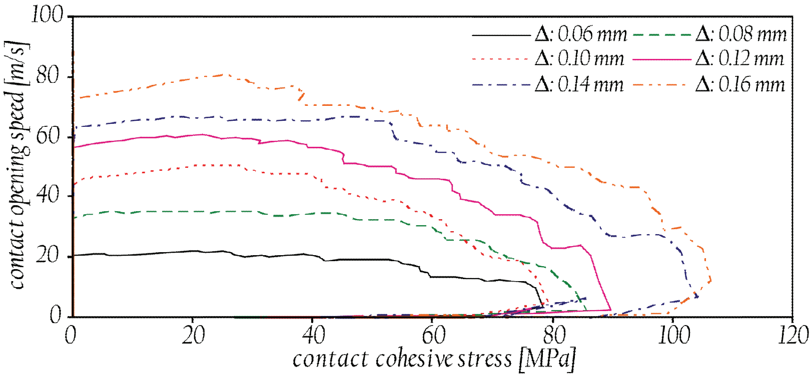

Figure 8–17: Contact opening speed versus contact cohesive stress for the RD–F1 simulation

Figure 8–16 and 8–17 show the variation of the contact opening speed versus its stress. As seen, the contact opening speed approaches a steady value as the contact undergoes the cohesive softening stage. This verifies the assumption made for Equation 8–5. The RD–F1 model further than the RD–P4 simulation limits the contact opening speed for the high Δ values that results in lower crack propagation velocity.

Table 8–4 summarizes the RD–F1 results in terms of the maximum–recorded cohesive strength (t_{max}) and the final tensile displacement (δ_{fin}) of the contact. The contact fracture energy (G_f) is subsequently obtained from the area under the curves in Figure 8–15.

Table 8–4: Details of the full rate–dependent simulations

Δ [mm]	W [N/m]	v_{cr} [m/s]	t_{max} [MPa]	δ_{fin} [mm]	G_f [N/mm]
0.06	1391	295	78.41	0.037	1387
0.08	2472	463	85.74	0.068	2855
0.10	3863	601	79.27	0.100	4022
0.12	5562	654	89.60	0.140	5883
0.14	7571	670	104.28	0.160	8094
0.16	9888	684	106.49	0.195	1018

The equality of W and G_f demonstrates that all the strain energy stored in the model is consumed through the contact fracturing. Thus, the RD–F1 contact model can reproduce the real energy release of fracturing process. Note that calculated G_f is a little larger than W, because Equation 8–2, which is adopted for the analytical evaluation of W, is valid for a regular rectangular plate. In the actual case, as the pre–existing slit makes the plate stress increase locally, the real amount of the stored strain energy is larger than that estimated by Equation 8–2.

c. *Crack bifurcation*

As discussed in Section 8.3.5, crack bifurcation is not numerically permitted when low or moderate pre–strain is applied. For this purpose, infinite strength is assumed for all the contacts not located on the plate centerline. As the specimen is loaded to the highest extent (Δ= 0.16 *mm*), all the contacts are allowed to break to provide the possibility of crack branching. The RI and RD–F predictions for branching are schematically presented in Figure 8–18.

a. rate–independent model (RI) **b. full rate–dependent model (RD–F1)**

Figure 8–18: Qualitative presentation of crack bifurcation patterns

Post–processing tools of UDEC are not effective for fracture visualization. None of the built–in facilities, e.g. stress/deformation contour or nodal displacement/velocity vector, satisfactorily represent material splitting. Furthermore, due to extremely small extent of particle separation compared to the model dimensions, presentation of the fractured particle assemblage is not representative either. That is why fracturing process has been shown only schematically.

The images, shown in Figure 8–18, are drawn out from post–fracture arrangement of the particles. They show that while the rate–independent simulation produces very chaotic crack dissemination, the rate–dependent model provides much more realistic predictions. Nevertheless, the bifurcation pattern is still different from the laboratory observation (compare Figure 8–18b with Figure 8–3).

8.4.4. *Discussion on rate–dependency parameters*

As ξ is much smaller than η ($\xi = 0.2$ and $\eta = 1.5$), the simulation suggests that material strength against fracturing is less influenced by loading rate than its deformation is. This is in agreement with the numerical investigation of Zhou and Molinari (2004a), where they observed that strength increase in ceramics is limited to 15% as the strain rate varies from 40 to 5000 s^{-1}.

Equation 8–10 provides an interpretation for the parameters of r_δ and r_t in terms of the material properties and model mesh size. The parametric study done shows that η and ξ determine how sensitive the results of the rate–dependent model are to the contact opening rate. Choosing very high η may engage the numerical fracture process with the stop–go type instabilities. High ξ may produce excessively large cohesive stress at the fracture process zone, which suppresses fracture propagation acceleration.

Consequently, an optimum set of the rate–dependency parameters, e.g. those of RD–F1, exists that reproduces the experimental data. However, despite of the classical micro–parameters of the CFM, the rate–dependency parameters are deprived of clear physical interpretation and their uniqueness is still under question. Nevertheless, they are doubtlessly necessary for CFM modeling of dynamic fracture.

8.5. **Conclusion**

Validity and adequacy of the CFM for dynamic fracture simulation was examined through modeling the fracture response of PMMA. It showed that the CFM does not reproduce the experimental fracture propagation velocity, unless loading rate effects get appropriately introduced into the cohesive contact model. Two approaches were adopted to reach this purpose, namely partial rate–dependent (RD–P) and full rate–dependent (RD–F) model. In the both, contact opening speed was the parameter representing the rate effects.

RD–P assumed that only contact ultimate displacement changes with its opening speed, while contact peak strength is fixed. Although its predictions were much better than the rate–independent model, certain deviations from the experimental data still existed. The results suggested that the RD–P contact model cannot reproduce actual amount of energy released through dynamic fracture propagation.

In the RD–F simulation, both the peak strength and effective displacement of contact are assumed to be dependent of the contact opening speed. Using this, the experimental fracture propagation speed was properly reproduced over the whole range of the applied load. The results demonstrated that the RD–F contact model can manage energy release process during the dynamic fracture event.

While the rate–independent model led to a very messy crack dissemination, introducing the rate effects into the contact model improved the CFM predictions for fracture bifurcation. However, distinct differences between the numerical and laboratory patterns of crack branching were still observed.

The obtained results emphasize the necessity of the rate–dependent contact model in order to effectively predict the dynamic fracture behavior of brittle materials.

CHAPTER 9

Dynamic fracturing in heterogeneous rock material

The most critical parameter characterizing fast crack propagation is dynamic fracture toughness. It refers to the resistance of a material against fracture under high-rate loading. Accurate measurement of dynamic fracture toughness of rock is of clear importance to understand correctly the mechanism of crack initiation and propagation within rock. These issues are in direct relation with the stability and durability of underground structures under dynamic loads caused by earthquake, blast and explosion. However, the standard methods used to measure dynamic fracture toughness of metals cannot be applied simply to rock material because of the special specimen geometry they require (Fowell and Xu 1993; Ouchterlony 1989).

As explained in Chapter 2, fracture tests on rock material usually resort to compression-induced tension in order to avoid pre-mature failure due to gripping in purely tensile testing. As an example, the three point bending specimen with the Split-Hopkinson Pressure Bar (SHPB) apparatus and the bar-impact testing machine, have been extensively used. Recently, the Semi-Circular Bend (SCB) specimen, originally used by Chong and Kuruppu (1984), has been adopted by Chen et al. (2009) because of its relative ease in terms of sample preparation and experiment setup.

A disconcerting point regarding fracture toughness is that different test methods may result in different measurements. The reason is often addressed to the undesired influences of specimen's geometry, boundary condition and loading nature on the test results. How to obtain a unique dynamic fracture toughness as a reliable material property is still subjected to open discussions.

Since numerical methods have provided a powerful tool to study dynamic fracture, they can potentially aid the experimental methods for measurement verification or performing appropriate corrections (e.g. Maigre and Rittel 1995). This chapter shows how the CFM, as a numerical method, is able to evaluate the validity of dynamic fracture toughness measured in laboratory. As a representative case, the semi–circular bend test method (Chen et al. 2009) is chosen. As seen later, simulations of the tests will demonstrate how some factors may affect on the test results, and finally suggests that few critical points must be considered to guarantee the test accuracy.

9.1. **Semi–Circular Bend (SCB) dynamic fracture toughness test**

In this section, the experimental work done by Chen et al. (2009) on dynamic fracture behavior of the SCB specimens is presented. More explanations about the test are published by Dai et al. (2008) and Dai et al. (2009).

9.1.1. *Sample preparation*

To make the SCB specimens, rock cores (40 *mm* nominal diameter) were drilled from Laurentian granite blocks, and sliced into discs with an average thickness of 16 *mm*. A circular diamond saw was used to cut a disc into two half–discs and to create a 4 by 1 *mm* notch on each half–disc. The material was chosen since its mineralogical and mechanical characteristics are well investigated (e.g., Nasseri and Mohanty 2008). Table 9–1 lists the mechanical properties of the specimens used.

Table 9–1: Mechanical properties of Laurentian granite

Young's modulus, E	92.0 GPa	Poisson's ratio, ν	0.21
fracture energy, G_f	25.1 N/m	density, ρ	2630 kg/m^3
Mode-I fracture toughness, K_{IC}	1.52 $MPa\sqrt{m}$	tensile strength, σ_t	13.2 MPa

The dominant constituents of Laurentian granite are feldspar (60%) and quartz (33%). The mineral grain size of the granite varies from 0.2 to 2 *mm* with average grain sizes of 0.5 and 0.4 *mm* for quartz and feldspar, respectively. Biotite grain size is of the order of 0.3 *mm* and constitutes 3–5% of the rock.

9.1.2. *SHPB test setup*

The SCB specimen is tested by a SHPB machine whose schematic configuration is presented in Figure 9–1, where R, B, and a respectively denote the radius, thickness, and depth of the notch. Two steel pins, spanning S, are placed between the transmitted bar and specimen to minimize the disturbances that the specimen surface friction may make.

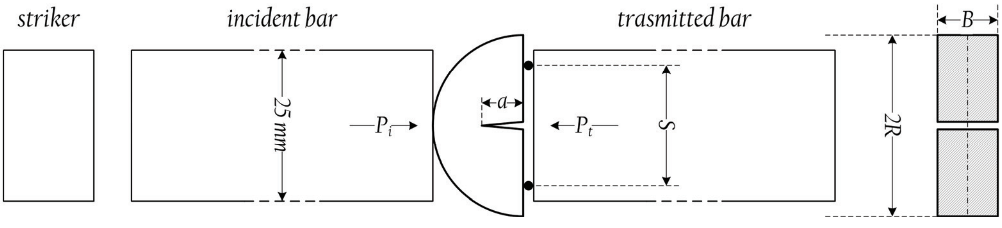

Figure 9–1: Schematics of the SHPB test setup and the SCB sample (Chen et al. 2009)

The striker bar is launched by a low-pressure gas gun to impact the incident bar, resulting in an incident stress wave. The incident pulse propagates along the incident bar before it hits the sample, resulting in the reflected and transmitted stress waves. The forces applied to the specimen by the incident and transmitted bars are denoted as P_i and P_t. Details of the SHPB testing and related formulation have been review in Chapter 3.

9.1.3. *Measurement*

The stress intensity factor for the Mode-I fracture in the SCB specimen is obtained as

$$K_{Id}(t) = \psi \frac{SP(t)}{BR^{1.5}} \tag{9-1}$$

where $P(t)$ is the time-varying loading force. ψ is a dimensionless factor, which depends on the specimen geometry. For the sample used, $\psi = 0.9615$ (Dai et al. 2009). Since the specimen is in dynamic equilibrium, the forces applied on both sides of the sample are identical during the test. Thus, $P(t) = P_i = P_t$ (see Chapter 3 for details). The dynamic fracture toughness, K_{ICd}, corresponds to the maximum loading force, P_{max}.

The test results suggested that $K_{Id}(t)$ evolves with a nearly linear trend, as its slope can be used to represent the average loading rate as follows, where t_d is when $K_{Id} = K_{ICd}$.

$$\dot{\kappa} = \frac{K_{ICd}}{t_d} \tag{9-2}$$

9.1.4. *Test results*

Figure 9-2 presents the measured dynamic fracture toughness at different loading rates, where it increases almost linearly with increasing loading rates. This phenomenon has been frequently observed in other test methods as well (e.g. Li 1999; Zhang et al. 1999).

The fitted line predicts that the minimum dynamic fracture toughness is 1.35 $MPa\sqrt{m}$ for a loading rate close to zero. This is in fair agreement with the static fracture toughness of Laurentian granite, which is 1.52 $MPa\sqrt{m}$ (Table 9-1).

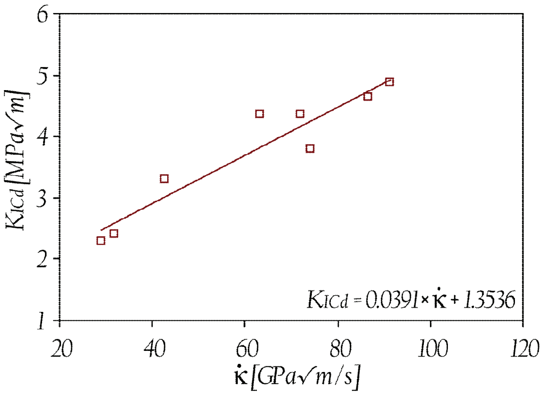

Figure 9-2: Results of the SCB dynamic fracture toughness (Chen et al. 2009)

9.2. **Simulation of the SCB dynamic fracture toughness test**

9.2.1. *Model geometry and boundary condition*

As reviewed in Chapter 2, rock fracture happens in mineral structure whose scale is in the order of 10^{-4} to $10^{-3}\,m$. This means that a model, composed of particles with the size of $10^{-4}m$, should reproduce rock fracture behavior. Therefore, particle size for the simulation of Laurentian granite is taken as its average mineral size, i.e., 0.5 *mm*.

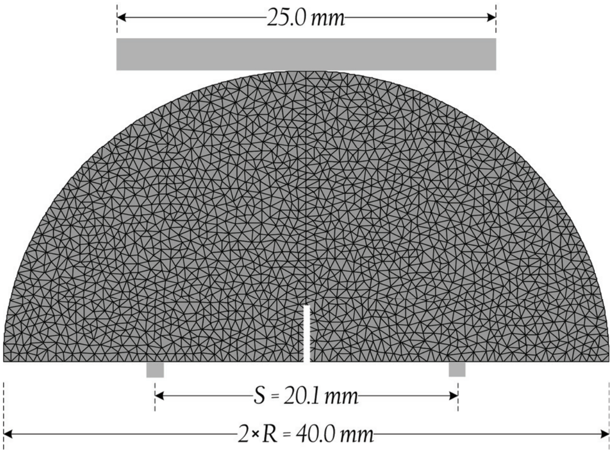

Figure 9–3: Model geometry and boundary condition

Presented in Figure 9–3, the geometry and boundary condition of the model are the same with the experiment. The model contains a 4 *mm* long slit along the centerline. The SCB model is made of 3480 irregular triangular particles with the average edge size of $d_p = 0.5$ *mm*, where each particle consists of one CST. As the area in contact between the specimen and the support pins is reported about 1 *mm*, the pins are estimated by two fixed steel squares with 1 *mm* edge length.

The SHPB incident bar is simulated by the upper steel plate. It moves down to model the bar dynamic load, where its time–dependent velocity is

$$v(t)=\begin{cases} v_d\dfrac{t}{t_0} & t\le t_0 \\ v_d & t>t_0 \end{cases} \tag{9–3}$$

v_d is the applied dynamic velocity and t_0 is the *arise time* to reach the applied velocity which is assumed $20\mu s$ for all the simulations. Equation 9–3 suggests that the applied velocity gradually increases to v_d. This is to help the specimen reach stress equilibrium. For this purpose, t_0 should be at least five times longer than the time needed for wave transmission through the specimen (Ma et al. 2010). Respecting the suggestions made in Chapter 4, the time step is taken as 5×10^{-10} *sec*, which secures the analysis stability.

9.2.2. *Micro–parameters*

The orthotropic cohesive law was fully explained in Chapter 5. Since the SCB specimen is subjected to the Mode–I fracturing, contact shear failure is not expected to occur. Therefore, the numerical fracture process should be controlled only by the contact tensile parameters. Consequently, the contact cohesion and friction angle should be assumed large enough to prevent any shear failure in contacts. They are taken as the uniaxial compressive strength and internal friction angle of Laurentian granite as reported by Nasseri and Mohanty (2008), i.e., 220 *MPa* and 50°, respectively. A comparison with the upper bound of the micro–parameters in the Augig granite simulation (Table 6–3) confirms the adequate largeness of these estimations.

Given Equation 5–30, the tensile stiffness coefficient of contact in plane–stress is calculated as $k_t = 3.63\times10^7$ *MPa/mm*. Since no shear failure is assumed, the shear stiffness coefficient of contact is assumed as k_t.

To obtain the contact tensile strength, t_c, a series of static fracture tests are arranged, where t_c varies from 1 to 8 times the rock tensile strength, σ_t. Given $G_f = 25.1$ *N/m*, the ultimate tensile displacement of contact, δ_{ut}, is obtained through Equation 5–11 for each simulation, as listed in Table 9–2.

In order to secure quasi–static equilibrium for the model, the local damping factor, α, is fixed at 0.2, and v_d is assumed 2 *mm/sec*. The kinetic friction angle between the steel loading plate, support pins, and the rock specimen is assumed 5° (e.g., Li et al. 2009).

Table 9–2: Details of static fracture toughness tests

t_c [*MPa*]	13.2	26.4	52.8	79.2	105.6
δ_{ut} [*mm*]	3.805	1.903	0.951	0.634	0.476
K_{IC} [$MPa\sqrt{m}$]	1.051	1.237	1.362	1.618	2.032

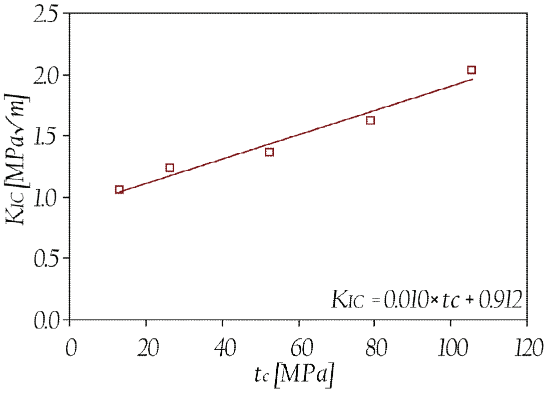

Figure 9–4: Variation of static fracture toughness versus contact tensile strength

The results are presented in Table 9–2 and Figure 9–4. They demonstrate a clear linear dependence between the static fracture toughness, K_{IC}, and the contact tensile strength, t_c. Note that the equation of the fitted line suggests that K_{IC} never comes below 0.912

$MPa\sqrt{m}$, even if t_c is zero. This is due to the resistance that the model exhibits against loading, which is mainly raised by the inertia effects and, as seen later, by the slip friction between the specimen and the support pins.

Given $K_{IC} = 1.52\ MPa\sqrt{m}$, the fitted line equation predicts $t_c = 66.0\ MPa$ ($\delta_{ut} = 0.761\ mm$). Repeating the simulation with the obtained micro–parameters exactly gives target K_{IC}.

9.2.3. *Calculation results using rate–independent contact model*

First, the simulation is performed by using the classical CFM. Three groups of simulation are designed, which are labeled as RI(ϕ : 0), RI(ϕ : 5), and RI(ϕ : 10). The values in the parentheses indicate the friction angle assumed for the specimen boundary surface, i.e., the interface of the loading plate and pins with the specimen. Each group includes five runs with different applied dynamic velocities as v_d = 200, 400, 600, 800 and 1000 *mm/s*. In all the simulations, no numerical damping is applied, i.e., $\alpha = 0$. This is to restrict the model to release energy only through contact failure and not particle viscosity.

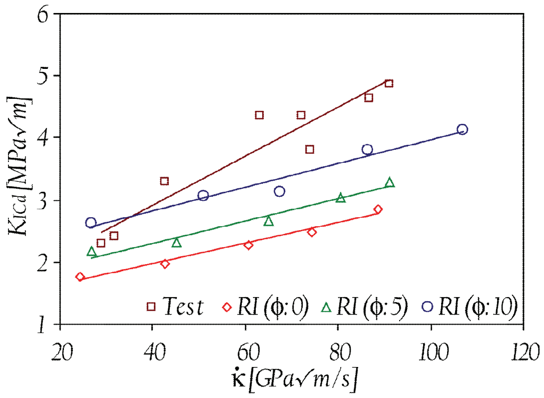

Figure 9–5: Variation of dynamic fracture toughness versus loading rate and specimen surface friction for rate–independent models

The results are presented in Figure 9–5. The difference between the fracture toughness predicted by the classical CFM and that measured by the test is apparent. However, the experimentally observed rate–sensitivity of the fracture toughness is partly captured, where K_{ICd} predicted increases with the loading rate increase for all the simulations. Nevertheless, the fitted lines to the simulation data are all less steep than that of the test results.

Figure 9–5 also suggests that the boundary surface friction highly influences the SCB test results, i.e., higher friction assumed on the specimen boundary surface, larger fracture toughness predicted. This signifies that the friction between the SCB specimen and the loading bars can potentially alter the measurements. The reason can be explored in the specimen motion mode. When the incident wave strikes the specimen, it splits in half, and each part laterally slides over the pins. Therefore, the slip friction between the pins and the specimen is mobilized, which disturbs the fracture opening process, and consequently increases the sample resistance against fracturing. As seen, the fitted lines to the data of the different groups have the same slope. This implies that the specimen surface friction does not control the model sensitivity to the applied loading rate.

9.2.4.*Calculation results using rate–dependent contact model*

a. Influence of rate–dependency parameters

Since the dependence of measured K_{ICd} on loading rate is nearly linear (Figure 9–2), the partial rate–dependent model (RD–P) sounds sufficient for our purpose. To find the corresponding rate parameters, i.e., r_δ and η, a series of CFM situations are arranged to evaluate how numerical predictions are sensitive to the rate–parameters. For this purpose, r_δ is changed from 100 to 1000 *m/s* and η from 1 to 3, where the specimen surface friction is assumed 5°, and v_d is fixed at 1000 *mm/s*.

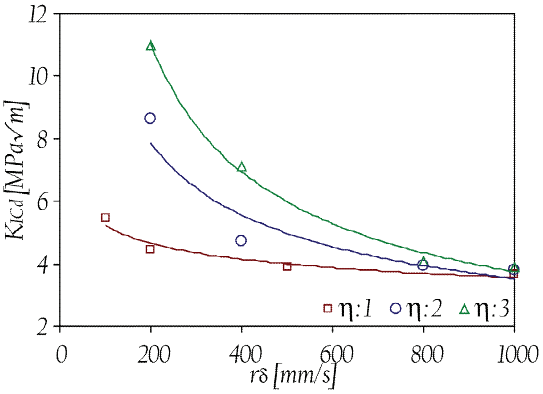

Figure 9–6: Variation of dynamic fracture toughness versus rate parameters

The results are plotted in Figure 9–6. It shows that increasing η or decreasing r_δ leads to increasing K_{ICd}. In addition, increasing η makes the CFM predictions more sensitive to r_δ.

If the loading rate, calculated by Equation 9–2, was plotted for all the points of Figure 9–6, it would be seen to vary between 90 and 100 *GPa√m/s* for which experimental $K_{ICd} \approx 5$ *MPa√m* (Figure 9–2). Figure 9–6 suggests that the best combination of the rate–parameters to get the dynamic fracture toughness of 5 *MPa√m* is $\eta = 2$ and $r_\delta = 400$ *mm/s*.

b. Reproduction of experimental results

Given $\eta = 2$ and $r_\delta = 400$ *mm/s*, the SCB specimen is again simulated. The obtained results, labeled as RD(ϕ : 5), are compared to the experimental data and those of the rate–independent model in Figure 9–7 (next page). The results clearly show that the RD model reproduces the test data much better than the RI model did. As seen, the slope of the fitted line to the RD model data is nearly as steep as the one fitted to the experimental data. This means that the RD model, unlike RI, is able to predict the actual rate–varying fracture toughness of the SCB specimens. As the selected rate–parameters make the RD model reproduce the laboratory data, the validity of the approach leading η and r_δ, is verified.

The results of the RI and RD models are listed in Table 9–3 in detail. For every v_d value, t_d obtained from the rate–dependent model is longer than that from the rate–independent one. The difference becomes greater as the loading rate increases. This demonstrates that the energy absorbing capacity of the RD model is larger than that of RI.

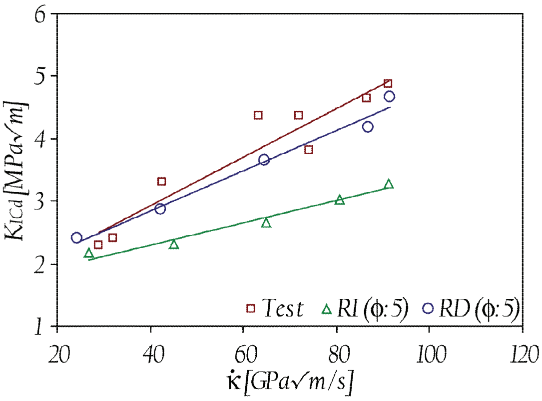

Figure 9–7: Variation of dynamic fracture toughness versus loading rate for rate–independent and rate–dependent models

Table 9–3: Results of the RI and RD simulations

	rate–independent model (RI)			rate–dependent model (RD)		
v_d [mm/s]	t_d [sec]	κ [GPa√m/s]	K_{ICd}[MPa√m]	t_d [sec]	κ [GPa√m/s]	K_{ICd}[MPa√m]
200	8.11e–5	26.76	2.17	9.86 e–5	24.34	2.40
400	5.11 e–5	45.21	2.31	6.74 e–5	42.43	2.86
600	4.09 e–5	65.04	2.66	5.68 e–5	64.44	3.66
800	3.76 e–5	80.59	3.03	4.82 e–5	86.93	4.19
1000	3.61 e–5	91.14	3.29	5.10 e–5	91.57	4.67

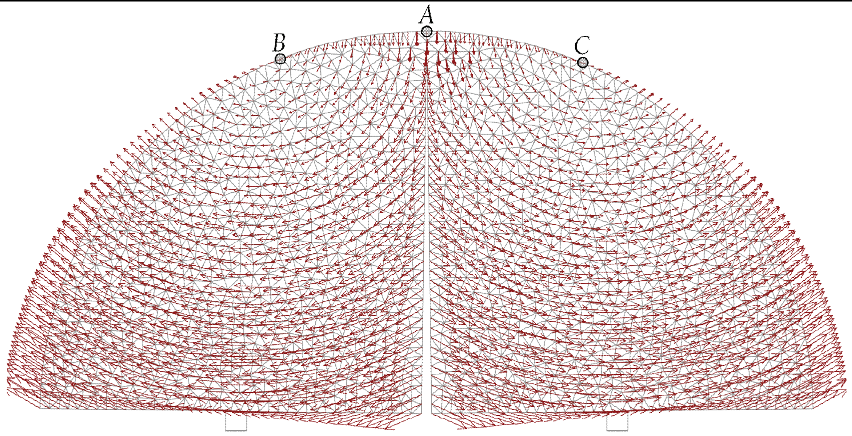

Figure 9–8: Nodal displacement vectors of particle assemblage

Figure 9–8 depicts the nodal displacement vectors of the particle assemblage under v_d = 1000 m/s. As seen, the centre of rotation of each specimen half is located neither at the pins nor at the contact point with the incident bar (point A). It is at the points B and C, which have no displacement. The plot also shows that both the halves are sliding over the support pins. This demonstrates that the slip friction between the specimen and the pins is an unavoidable matter of the SCB test.

To explore the friction effects from an energy point of view, an energy analysis is performed, where the total boundary loading work supplied to the system, W, the total strain energy stored in the assemblage, U_c, the current kinetic energy of the system, U_k, the total dissipated energy through the specimen surface friction, W_j, are continuously calculated by UDEC. The total energy released by fracture propagation will be therefore:

$$W_f = W - U_c - U_k - W_j \tag{9–4}$$

Figure 9–9 offers the energy analysis output for the RD model under v_d = 1000 *m/s*, and assuming 5° surface friction angle. It shows that the amount of energy dissipated through the specimen surface friction (≈ 6.40 *N.mm*) is rather comparable to the total fracture energy (≈ 9.96 *N.mm*), although the friction angle assumed is very small. This again emphasizes how significantly the frictional effects influence the SCB test results.

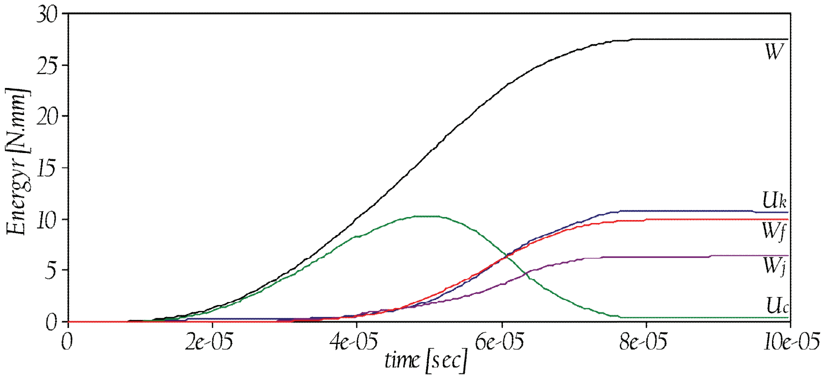

Figure 9–9: Variation of different components of energy versus time for v_d = 1000 mm/s.

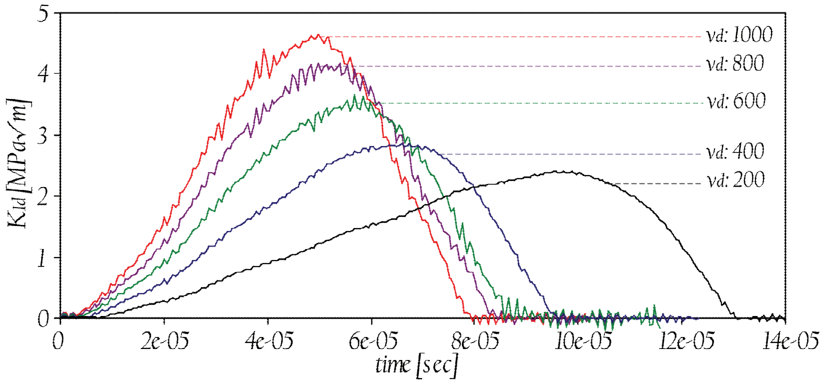

Figure 9–10: Variation of stress intensity factor predicted by the RD model under different values of applied dynamic velocity

Variation of the stress intensity factor versus time for the RD model is plotted in Figure 9–10. Comparison of the results when v_d = 1000 *m/s* with Figure 9–9 indicates that the model strain energy as well as the stress intensity factor reaches their peaks at 50 *μs*. However, Figure 9–11b (next page) demonstrates that the fracture just starts propagating

25 μs after the loading bar touches the specimen, when $K_{Id} = 2.33\ MPa\sqrt{m}$. This means that the peak of K_{Id} (= 4.67 $MPa\sqrt{m}$), which is experimentally reported as the dynamic fracture toughness, does not correspond with the instant of fracture initiation. The simulation suggests that the actual toughness value, regarding fracture initiation, is much lower than the laboratory measurement. The same is observed under $v_d = 200\ mm/s$, where the fracture starts propagating at 55 μs when $K_{Id} = 1.40\ MPa\sqrt{m}$, but the peak value (= 2.40 $MPa\sqrt{m}$) happens some time later at 97 μs.

Under $v_d = 1000\ mm/s$, the fracture propagation ends at about 70 μs. From 80 μs on, the specimen does not bear any more load, and all the energy components get nearly constant (Figure 9–9). Note that since the specimen is still in contact with the pins, the friction work (W_j) slightly evolves and consequently the kinetic energy decays.

Details of the fracture propagation are illustrated in Figure 9–11, where the contacts fully damaged are colored in brown thick lines, and those in cohesive softening stage are plotted by thin red lines. It reveals that the fracture propagates much faster under high–rate than low–rate loading. Moreover, the cohesive zone, ahead the crack tip, broadens, as the loading rate increases.

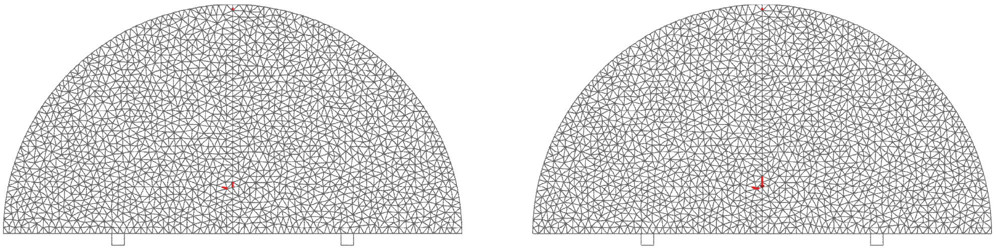

pre–peak (55 µs) pre–peak (25 µs)

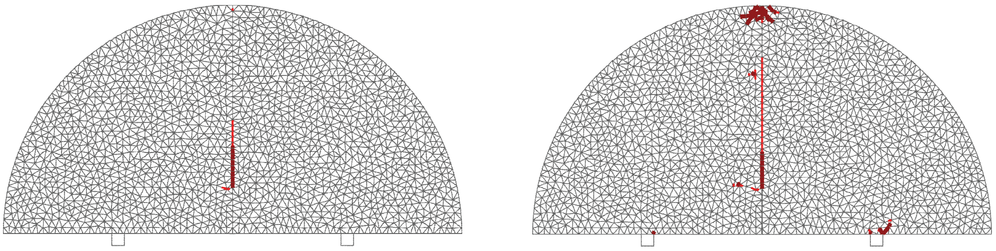

peak (97 µs) peak (50 µs)

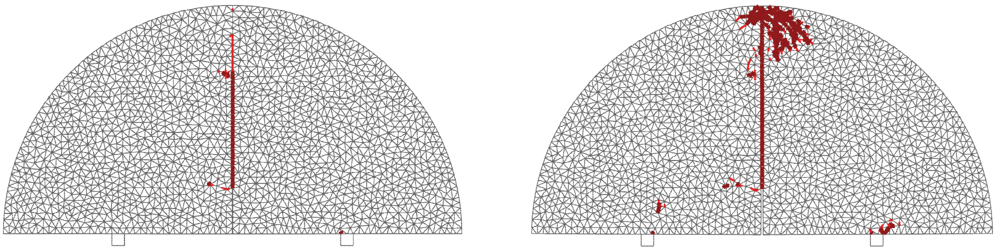

post–peak (118 µs) post–peak (70 µs)

a. $v_d = 200$ mm/s b. $v_d = 1000$ mm/s

Figure 9–11: Details of fracture propagation under the lowest and the highest applied dynamic velocities

Figure 9–11b indicates that the high–rate loading may cause local damages around where the specimen touches the loading bars. Note, since particles arrangement thereby contacts orientation is quite arbitrary, the individual failure pattern of each specimen half may differ from the other half. That is why the failure examples are unsymmetrical.

9.3. Conclusion

The semi–circular bend (SCB) dynamic fracture toughness tests were simulated by the CFM. The obtained results emphasized the necessity and importance of the rate–dependent contact model for the simulation of dynamic fracture toughness. In addition, they indicated that the friction between the rock specimen and loading bars plays an important role in the test results. Therefore, it has to be managed carefully in order to secure the measurement accuracy.

The results suggested that the frictional effects must be eliminated to have the most precise measurement. However, since this is practically impossible, numerical modeling may assist to correct the experiment measurements. For this purpose, the fracture toughness test can be reproduced by the CFM, when the frictional boundary condition is introduced. Keeping all the input parameters and loading condition fixed but setting the friction to be zero, the simulation is repeated which eventually provides the correct dynamic fracture toughness of the SCB test.

More importantly, the simulation revealed that the maximum dynamic force, which is recorded in the test to calculate dynamic fracture toughness, does not correspond with the instant of fracture initiation. For both the low and high loading rates, fracturing is triggered far before the applying dynamic force (or correspondingly stress intensity factor) reaches its peak value. This is a point of concern as it means that the actual dynamic fracture toughness of material is overestimated by the laboratory measurements.

CHAPTER 10

Conclusions and research outlook

This thesis was dedicated to expand our knowledge about rock failure and fracture, particularly with focus on micromechanical effects. The thesis demonstrated the capability and effectiveness of the DEM as a numerical tool for fracture research. This is a promising sign suggesting the DEM for tackling intrinsically discontinuous problems.

As discussed in Chapter 3, the DEM can be potentially coupled with other continuous numerical method, e.g. FEM and FDM, in order to handle the particles. As an example, UDEC is an FDM–DEM coupled code, which solves each particle using the FDM formulation and handles particle interaction by the DEM. Very recently, Mahabadi et al. (2010a, b) have presented a combined FEM–DEM simulation concerning almost the same objectives we followed. Although their research is still ongoing (at the time of the thesis preparation) and hence the results are not entirely presented, those published agree with our statement regarding the advantages of DEM modeling.

Results obtained at each chapter are listed at the end of the chapter. However, here are the results brought together to provide a recapitulation of the thesis objectives and its achievements.

10.1. Summary of conclusions

The investigations on rock fracture and failure by the CFM have been carried out in the last four chapters, where we started with static failure response of rock and ended to its dynamic fracture behavior.

The DEM calibration has been a matter of discussion for a long time since the bonded particle modeling was introduced. Chapter 6 investigated how the micromechanical properties of rock control its compressive and tensile behavior. It showed that the CFM micro–parameters can be calibrated such that the model, not only quantitatively but also qualitatively, reproduces the rock standard properties measured in laboratory for both hard and weak rock.

Using the CFM calibrated micro–parameters, the numerical simulation properly fitted the static test data in terms of the Young's modulus, the Poisson's ratio, unconfined compressive strength, internal cohesion, internal friction angle, and tensile strength measured by the Brazilian split test. This suggests that the particle/contact model adopted in the CFM embodies the actual properties of rock microstructure.

Sensitivity of the results to particle size, numerical loading rate, and numerical damping applied has been also evaluated. Furthermore, the numerical circumstances, necessary for securing the quasi–static state of analysis, have been discussed in detail.

Chapter 7 introduced the use of the CFM in modeling the shear response of the plaster–made joint specimens. As reported, the predictions for the single–teeth joint were hopeful. Shear strength, dilation and asperity crushing were properly predicted, where no additional modification or effort was required.

For the double–teeth joint, the model fitted the pre–failure response and peak shear strength. However, there was a qualitative deviation between the experiment and numerical reproduction under high normal pressure, where post–peak behavior of the model is more brittle than that of the laboratory sample. Nevertheless, the model succeeded to fully predict the laboratory results when low normal pressure is applied.

Chapter 8 was dedicated to the examination of DEM modeling for dynamic fracture analysis in homogeneous isotropic materials. This purpose has been reached through modeling the fracture response of the PMMA plates.

The simulations revealed that the rate–independent contact model was not able to predict the experimental fracture propagation velocity. This made us believe that the loading rate effects have to be introduced appropriately into the cohesive contact model. Two conducts were adopted to embody this idea, labeled as RD–P and RD–F, where the contact opening speed was taken as the parameter representing rate effects.

RD–P assumes that only the contact ultimate displacement is rate–dependent whilst the contact peak strength is fixed. Although the RD–P predictions were much better than those of the rate–independent model, there still existed distinct deviations from the experimental data. The results suggested that the RD–P contact model cannot reproduce the actual amount of energy released through dynamic fracture propagation.

In the RD–F simulation, both the peak strength and effective displacement of contact are assumed as dependent of the contact opening speed. As reported, the RD–F model properly reproduced the PMMA fracture propagation speed.

Introducing the rate effects into the contact model improved the CFM predictions for crack bifurcation. However, distinct differences between the numerical and experimental crack branching were still observed.

Having all the numerical progresses achieved, Chapter 9 aimed to examine rock fracture behavior under dynamic loading. The semi–circular bend dynamic fracture toughness test was simulated to reach this purpose. The obtained results indicated the necessity of the rate–dependent contact model for the simulation of rock dynamic fracture toughness.

The simulation demonstrated how DEM modeling can help us assess the validity of rock dynamic tests. The two investigated matters concerning the test validity were the effect of friction between rock specimen and loading bars and the true instant of fracture initiation.

The simulations indicated that the specimen surface friction with the loading bar (more importantly with the support pins) causes the test to overestimate the dynamic fracture toughness. As suggested in Chapter 9, since it is practically impossible to fully remove the frictional effects, numerical modeling hopefully can help us correct the experimental measurements.

More importantly, the simulation revealed that the maximum dynamic stress intensity factor occurs far beyond the instant of fracture initiation. Whether low or high loading rate is applied, fracture is initiated when the dynamic stress intensity factor is approximately half its maximum value. This is a point of serious concern as implies that the actual dynamic fracture toughness of material is nearly half of the laboratory reported value.

10.2. **Critical considerations**

Beside the results presented, the study specifically provides some critical suggestions, which are believed as necessary for any discontinuous modeling of fracture and fragmentation.

10.2.1. *Particle size*

Physical interpretation of particle varies with the microstructural characteristics of the simulated material. For rocks, particle size is basically a matter of their physical texture. Simulation of coarse large–grained rocks needs bigger particles than that of fine–grained ones. Since rock fracture expectedly passes through mineral interface, the weakest grains or mineral cement (if any), the rock fragments are at least as small as one or several minerals. Therefore, DEM particles, which numerically represent the fragmented pieces of failed rock, do not need to be smaller than the rock grains size.

For isotropic homogeneous material, e.g. PMMA, particles size should respect the considerations suggested by continuum models, e.g. it should be a reasonable fraction of the stress wavelength or the length of the fracture process zone. However, here is also a lower bound for particle size. Since the contact stiffness represents the stiffness of material existing in the fracture cohesive zone, only one particle is allowed to be placed within the cohesive zone thickness. Otherwise, the material located in this zone would be modeled less stiffly than reality because there would exist several contacts over the zone thickness, which act as springs in series. Therefore, particles size must not be smaller than the thickness of the fracture cohesive zone.

10.2.2. *Necessity of a representative contact model*

Since macroscopic response of any bonded particle assemblage is dominantly controlled by contact (or bond) constitutive model, this model must be appropriately adopted to allow the assemblage to simulate material physical response. Therefore, simulation of rock, as an anisotropic brittle material, needs a contact model providing these qualities. That is why the CFM contact model is orthotropic, cohesive, frictional, and rate-dependent. All these items are necessary for rock failure modeling. If neglecting contact orthotropy, the assemblage is no longer able to follow different compressive and tensile behaviors as physical rock does. Contact cohesiveness is required to provide real rock fracture energy, and contact friction is to present real slip behavior of broken fragments past each other. However, contact model should meet all these needs by using the fewest micro-parameters possible.

10.2.3. *Physical interpretation of numerical micro-parameters*

Each particle or contact micro-parameter should have a physical interpretation in terms of material mechanical properties. The aim for DEM modeling is to not only fit or reproduce laboratory data but also explore how the micromechanics of material produces its macroscopic behavior.

The developed closed-form expressions along with the CFM calibration process described how each CFM micro-parameter is related to rock standard properties in the rate-independent simulation. For example, it was shown that rock tensile strength and cohesion are much controlled by contact tensile strength, which numerically represents the tensile strength of mineral cement or weak grains through which material fractures. It was also revealed that rock internal friction angle is dominantly affected by the friction acting over the grains surfaces. Since contact friction starts acting after contact cohesion is exceeded, the mentioned examples support the idea suggesting that the mobilization of rock internal cohesion and friction angle is not coincident, where the former is activated first, and then the latter.

10.2.4. *Numerical process of fracture energy release*

No numerical damping must be applied to dynamic fracture simulations. We believe that the key for any successful simulation of fracture is that the adopted numerical model must be able to reproduce the actual amount of energy released in the material fracturing process. Very importantly, this issue must not be disturbed or manipulated at all by the application of any artificial (numerical) damping, e.g. local or Rayleigh damping. In other words, all the energy dissipation in a particle assemblage must occur only and only through the rupture of bonding elements (contacts).

10.2.5. *Necessity of rate–dependent model for fracture in micro–scale*

The thesis results supported the use of the rate–dependent contact (crack) model for dynamic fracture simulation. This approach is to let contact appropriately reproduce the actual amount of energy released during material fracturing process. Otherwise, numerical energy released through contact failure is held constant whatever the applied loading rate is. There are two points that we should pay attention to in rate–dependent simulation: physical interpretation of rate–dependent parameters and scale of modeling.

The results obtained from dynamic fracture simulation suggest that the rate–dependent parameters somehow express the sensitivity of dynamic fracture response to loading rate. However, the essence of this sensitivity is not clear yet. While the SHPB test on the granite SCB specimens suggested a linear rate–dependency, the test on the PMMA plates demonstrated a nonlinear asymptotic response. It is not vividly known how much these behaviors are related to material microstructure, and how much to the test circumstances such as boundary condition and specimen geometry. Therefore, admitting the observed rate–dependency as a material property is still under question for us.

The simulations suggested that the RD–P model, with only contact displacement increase, is sufficient when a linear rate–dependency is observed. However, it is not able to satisfactorily reproduce nonlinear asymptotic rate–dependencies. The RD–F model is then needed, which allows both the contact strength and displacement to increase with loading rate.

Although the rate–dependent model is needed for micro–scale simulation, its necessity for modeling at the scale of crystallites is not approved. As mentioned, we believe that the key point in accurate simulation of fracture is that the simulation properly reproduces the actual amount of energy released through material fracturing process. If current computational facilities let us establish a particle assemblage with a particle size in the order of material crystallites, the assemblage would be able to reproduce all the micro–cracking events happening in the fracture process zone. Since this model produced more fracture energy than the CFM does, it could possibly match the actual amount of energy released in the fracture process zone without the rate–dependent assumption.

10.3. **Research perspective**

With a particular focus on the contact constitutive model, this study was specifically dedicated to the application of the 2D DEM for the micromechanical investigation of rock material. The proposed model was established based on two main assumptions, i.e., elastic particle and orthotropic cohesive contact. The results of the DEM simulations were very promising in terms of their capability and adequacy for qualitative and quantitative prediction of rock failure behavior. These achievements offer a bright prospect for failure modeling by the DEM and encourage us for further attempts. In this framework, we suggest the following topics as the future continuation of this stream of research.

10.3.1. *Three-dimensional modeling*

As a pioneer attempt to assess the DEM applicability for fracture and fragmentation purposes, the thesis had to focus on 2D analysis, which inevitably prevented us from a comprehensive view over the problem. This issue gets more serious, when a 3D Lattice simulation has very recently shown that the thickness of the SCB specimen (examined in Chapter 9) influences the dynamic toughness measurement (Zhao et al. accepted).

The DLL files, provided for the CFM, are basically developed in 3D space and can be therefore imported directly into the 3D version of UDEC (3DEC). However, physical interpretation of the micro-parameters in 3D space may be slightly different from one in 2D. Furthermore, a 3D assemblage, composed of arbitrarily packed particles, must be generated by the 3D Delaunay triangulation, which is engaged with some additional efforts.

10.3.2. *Particle geometry*

The CFM makes use of triangular particles. As the arrangement of particle facets may affect on the mobilization of contact friction, the simulation of compressive and tensile failure of rock would be expectedly affected by the particle geometry. Hence, other particle geometries, e.g. quadrilateral, can be introduced to research this effect.

10.3.3. *Heterogeneity of particles*

The research presented assumed all particles to have the same elastic properties. In order to have a more genuine representation of heterogeneous rock material, a restricted variety of the properties can be randomly attributed to the particles through the statistical distributions, e.g. Weibull distribution. As Ma et al. (2010) have very recently shown, rock heterogeneity level, represented by the Weibull distribution parameters, affects on the sensitivity of rock behavior to loading rate.

10.3.4. *Particle crushing*

This study assumed that rock rupture is exclusively dominated by contact failure. Although this assumption is close to reality, grain crashing is sometimes reported in rock failure, particularly for highly stressed rock media (e.g. Guimaraes et al. 2007; Zang et al. 2000). This issue can be examined by introducing a continuum damage model into particle constitutive law, which is allowed in UDEC.

The aforementioned research suggestions may require developing new particle/contact constitutive models or defining additional micro–parameters. However, the critical considerations, discussed earlier, must be always respected in order to guarantee the effectiveness of any numerical study aiming rock micro–mechanical research.

References

ABAQUS. (2005). "Abaqus reference manuals." Providence, RI.

Abdollahi, A. (1996). "Investigation of objectivity in the application of the FEM to RC structures – II." Computers and Structures, 58(6), 1183–1211.

Abdulle, A., and Weinan, E. (2003). "Finite difference heterogeneous multi-scale method for homogenization problems." Journal of Computational Physics, 191(1), 18–39.

Abraham, F. F. (2005). "Unstable crack motion is predictable." Journal of the Mechanics and Physics of Solids, 53(5), 1071–1078.

Abraham, F. F. (2006). "Unstable crack motion is predictable (vol 53, pg 1071, 2005)." Journal of the Mechanics and Physics of Solids, 54(1), 233–235.

Agrawal, P., and Sun, C. T. (2004). "Fracture in metal–ceramic composites." Composites Science and Technology, 64(9), 1167–1178.

Alber, M. and Brardt, A. (2003). Factors influencing fracture toughness KIC from simple screening tests. Int. J. Rock Mech. Min. Sci.; 40: 779–784.

Alder, B. J., and Wainwright, T. E. (1959). "Studies in Molecular Dynamics. I. General Method." J. Chem. Phys, 31(2), 459.

Alfaiate, J., Pires, E. B., and Martins, J. A. C. (1997). "A finite element analysis of non–prescribed crack propagation in concrete." Computers and Structures, 63(1), 17–26.

Ali, A. (1996). "FEM analysis of concrete structures subjected to mode–I and mixed–mode loading conditions." Computers and Structures, 61(6), 1043–1055.

Allen, D. H. and C. R. Searcy (2001). "Micromechanically–based model for predicting dynamic damage evolution in ductile polymers." Mechanics of Materials 33(3): 177–184.

Al–Shayea, N.A., Khan, K. and Abduljauwad, S.N. (2000). Effects of confining pressure and temperature on mixed–mode (I–II) fracture toughness of a limestone rock. Int. J. Rock Mech. Min. Sci.; 37: 629–643.

Anderson, T. (1995). Fracture mechanics: fundamentals and applications, CRC press, Boca Raton.

Andreev, K., and Harmuth, H. (2003). "FEM simulation of the thermo–mechanical behavior and failure of refractories – A case study." Journal of Materials Processing Technology, 143–144, 72–77.

ANSYS Inc. (2008). http://www.ansys.com/

Ariffin, A. K., Huzni, S., Nor, M. J. M., and Mohamed, N. A. N. (2006). "Hybrid finite–discrete element simulation of crack propagation under mixed mode loading condition." Fracture and Strength of Solids Vi, Pts 1 and 2, 306–308, 495–499.

Arnold, D. N. (1981). "Discretization by Finite–Elements of a Model Parameter Dependent Problem." Numerische Mathematik, 37(3), 405–421.

Asadpoure, A., Mohammadi, S., and Vafai, A. (2006). "Modeling crack in orthotropic media using a coupled finite element and partition of unity methods." Finite Elements in Analysis and Design, 42(13), 1165–1175.

Asadpoure, A., and Mohammadi, S. (2007). "Developing new enrichment functions for crack simulation in orthotropic media by the extended finite element method." International Journal for Numerical Methods in Engineering, 69(10), 2150–2172.

Asferg, J. L., Poulsen, P. N., and Nielsen, L. O. (2007a). "A consistent partly cracked XFEM element for cohesive crack growth." International Journal for Numerical Methods in Engineering, 72(4), 464–485.

Asferg, J. L., Poulsen, P. N., and Nielsen, L. O. (2007b). "A direct XFEM formulation for modeling of cohesive crack growth in concrete." Computers and Concrete, An Int. Journal, 4(2), 83–100.

Ashby, M.F. and Hallam, S.D. (1986). The failure of brittle solids containing small cracks under compressive stress states. Acta Metall.; 34: 497–510.

Atkinson, B. K. (1984). Subcritical crack growth in geological materials. J. Geophys. Res.; 89: 4077–4114.

Atkinson, B. K. (1987). Introduction to fracture mechanics and its geophysical applications. In: Atkinson, B. K. (ed.) 1991. Fracture mechanics of rock. Academic press geology series. Academic Press, London: 1–26.

Atkinson, B. K. (1991). Fracture mechanics of rock. Academic press geology series. Academic Press, London.

Atkinson, C., Smelser, R.E. and Sanchez, J. (1982). Combined mode fracture via the cracked Brazilian disk test. Int. J. Fract.; 18: 279–291.

Ayatollahi, M. R. and M. R. M. Aliha (2006). "On determination of mode II fracture toughness using semi–circular bend specimen." Int. Journal of Solids and Structures 43(17): 5217–5227.

Azevedo, N. M., J. V. Lemos, et al. (2008). "Influence of aggregate deformation and contact behavior on discrete particle modeling of fracture of concrete." Engineering Fracture Mechanics 75(6): 1569–1586.

Babadagli, T. (2005). "Analysis of the displacement in fractal lattices with different number of grids." Fractals–Complex Geometry Patterns and Scaling in Nature and Society, 13(3), 207–213.

Babuska, I., and Suri, M. (1992). "On Locking and Robustness in the Finite–Element Method." Siam Journal on Numerical Analysis, 29(5), 1261–1293.

Babuska, I., Melenk, J. M. (1997) "The partition of unity method." International Journal for Numerical Methods in Engineering, 40 (4), 727–758.

Barenblatt, G. I. (1962). "The mathematical theory of equilibrium cracks in brittle fracture." Advances in Applied Mechanics 7: 55–129.

Barkhatov, V. A. (2007). "Solving wave equations by the finite–difference time–domain method: Basic relationships for a two–dimensional problem." Russian Journal of Nondestructive Testing, 43(9), 605–618.

Barr, B. and Derradj, M. (1990). Numerical study of a shear (mode II) type test specimen geometry. Eng. Fract. Mech.; 35: 171–180.

Barton, N. (1971). A relationship between joint roughness and joint shear strength. Proceedings of the international symposium on rock fracture, Nancy, France.

Barton, N. (1976). "Review of a new shear strength criterion for rock joints." Eng Geol 7: 287332.

Barton, N. and V. Choubey (1977). "The shear strength of rock joints in theory and practice." Rock Mech 10: 154.

Barton, N., S. Bandis, et al. (1985). "Strength, deformation and permeability of rock joints." Int J Rock Mech Min Sci Geomech Abstr 22: 121–140.

Bayoui, M.R., Klepaczko, J.R., and Bassion, M.N. (1984). "Determination of Fracture Toughness JIc Under Quasi-Static and Dynamic Loading Conditions Using Wedge Loaded Specimens." Journal of Testing and Evaluation (JTE) ASME, 12 (5):316.

Bažant, Z.P. and Pfeiffer, P.A. (1986). Shear fracture tests of concrete. Matér. Constr.; 16: 111–121.

Bearman, R. A. (1999). The use of the point load test for the rapid estimation of Mode I fracture toughness. Int. J. Rock Mech. Min. Sci.; 36: 257–263.

Bearman, R. A., Pine, R. J. and Willis, B. A. (1989). Use of fracture toughness testing in characterising the comminution potential of rock. Today's Technology for the Mining and Metallurgical Industries, Symp. of MMIJ/IMM, Kyoto, Japan: 161–181.

Bedford, A. and D. S. Drumheller (1996). Introduction to Elastic Wave Propagation, John Wiley and Sons.

Belytschko, T., Chiapetta, R. L., and Bartel, H. D. (1976). "Efficient Large-Scale Nonlinear Transient Analysis by Finite-Elements." International Journal for Numerical Methods in Engineering, 10(3), 579–596.

Belytschko, T., Lu, Y., and Gu, L. (1992). "Element free Galerkin methods." Comput. Mech., 37, 229–256.

Belytschko, T., Gu, L., and Lu, Y. Y. (1994a). "Fracture and Crack-Growth by Element Free Galerkin Methods." Modeling and Simulation in Materials Science and Eng., 2(3A), 519–534.

Belytschko, T., Lu, Y. Y., and Gu, L. (1994b). "Element-free Galerkin methods." International Journal for Numerical Methods in Engineering, 37(2), 229–256.

Belytschko, T., Lu, Y. Y., Gu, L., and Tabbara, M. (1995). "Element-Free Galerkin Methods for Static and Dynamic Fracture." Int. Journal of Solids and Structures, 32(17-18), 2547–2570.

Belytschko, T., Krongauz, Y., Organ, D., Fleming, M., and Krysl, P. (1996). "Meshless methods: An overview and recent developments." Comp. Methods in App. Mechanics and Eng., 139(1-4), 3–47.

Belytschko, T., and Tabbara, M. (1996). "Dynamic fracture using element-free Galerkin methods." International Journal for Numerical Methods in Engineering, 39(6), 923–938.

Belytschko, T., Krysl, P., and Krongauz, Y. (1997). "A three-dimensional explicit element-free Galerkin method." International Journal for Numerical Methods in Fluids, 24(12), 1253–1270.

Belytschko, T., Black, T. (1999). "Elastic crack growth in finite elements with minimal remeshing." International Journal for Numerical Methods in Engineering, 45(5), 601–620

Belytschko, T., and Fleming, M. (1999). "Smoothing, enrichment and contact in the element-free Galerkin method." Computers & Structures, 71(2), 173–195.

Belytschko, T., Organ, D., and Gerlach, C. (2000). "Element-free Galerkin methods for dynamic fracture in concrete." Computer Methods in Applied Mechanics and Eng., 187(3-4), 385–399.

Belytschko, T., Chen, H., Xu, J. X., and Zi, G. (2003). "Dynamic crack propagation based on loss of hyperbolicity and a new discontinuous enrichment." International Journal for Numerical Methods in Engineering, 58(12), 1873–1905.

Belytschko, T., Loehnert, S., Song, J.-H. (2007). "Multi-scale aggregating discontinuities: A method for circumventing loss of material stability." International Journal for Numerical Methods in Engineering 73 (6), pp. 869–894

Bennett, J. (1991). "A Weibull brittle material failure model for the ABAQUS computer program." Contract: W-7405-ENG-36.

Benz, W., and Asphaug, E. (1994). "Impact Simulations with Fracture .1. Method and Tests." Icarus, 107(1), 98–116.

Benz, W., and Asphaug, E. (1995). "Simulations of Brittle Solids Using Smooth Particle Hydrodynamics." Computer Physics Communications, 87(1–2), 253–265.

Berton, S. (2003). "Numerical simulation of the durability mechanics of cement–based materials," PhD thesis, University of California, Davis.

Bhagat, R. B. (1985). "Mode I fracture toughness of coal." Geotechnical and Geological Engineering 3(3): 229–236.

Block, G., M. Rubin, et al. (2007). "Simulations of dynamic crack propagation in brittle materials using nodal cohesive forces and continuum damage mechanics in the distinct element code LDEC." International Journal of Fracture 144(3): 131–147.

Bobet, A. and Einstein, H.H. (1998). Fracture Coalescence in Rock–type Materials under Uniaxial and Biaxial Compression. Int. J. Rock Mech. Min. Sci.; 35: 863–888.

Bocca, P., Carpinteri, A., and Valente, S. (1990). "Size effects in the mixed mode crack propagation: Softening and snap–back analysis." Engineering Fracture Mechanics, 35(1–3), 159–170.

Bocca, P., Carpinteri, A., and Valente, S. (1991). "Mixed mode fracture of concrete." International Journal of Solids and Structures, 27(9), 1139–1153.

Bonnet, M., Maier, G., and Polizzotto, C. (1998). "Symmetric Galerkin boundary element methods." Applied Mechanics Reviews, 51(11), 669–703.

Bonora, N. (1997). "A nonlinear CDM model for ductile failure." Engineering Fracture Mechanics (UK), 58(1–2), 11–28.

Brace, W.F. and Bombolakis, E.G. (1963). A Note on Brittle Crack Growth in Compression. J. Geophys. Res; 68: 3709–3713.

Brandtzaeg, A. (1927). "Failure of Material Composed of Non Isotropic Elements." Det. Kgl. Norske. Videnskabers Selskabs, Grandheim.

Broberg, K. B. (1999). Cracks and Fracture. Academic Press, Cambridge.

Brooker, D. C., and Ronalds, B. F. (2001). "Prediction of ductile failure in tubular steel members using ABAQUS." International Society of Offshore and Polar Engineers, P.O. Box 189, Cupertino, CA, 95015–0189, USA.

Brown, E.T. (1981). Rock Characterization, Testing and Monitoring, ISRM Suggested Methods, Pergamon Press, Oxford.

Buehler, M. J., van Duin, A. C. T., and Goddard, W. A. (2006). "Multiparadigm modeling of dynamical crack propagation in silicon using a reactive force field." Physical Review Letters, 96(9), 1–4.

Cai, J. G., and Zhao, J. (2000). "Effects of multiple parallel fractures on apparent attenuation of stress waves in rock masses." Int. Journal of Rock Mechanics and Mining Sciences, 37(4), 661–682.

Cai, M. (2008). "Influence of intermediate principal stress on rock fracturing and strength near excavation boundaries––Insight from numerical modeling." Int. Journal of Rock Mechanics and Mining Sciences 45(5): 763–772.

Camacho, G. T. and M. Ortiz (1996). "Computational modeling of impact damage in brittle materials." International Journal of Solids and Structures 33(20–22): 2899–2938.

Camacho, G. T. and M. Ortiz (1997). "Adaptive Lagrangian modeling of ballistic penetration of metallic targets." Computer Methods in Applied Mechanics and Engineering 142(3–4): 269–301.

Camborde, F., C. Mariotti, et al. (2000). "Numerical study of rock and concrete behavior by discrete element modeling." Computers and Geotechnics 27(4): 225–247.

Campbell, J., Vignjevic, R., and Libersky, L. (2000). "A contact algorithm for smoothed particle hydrodynamics." Computer Methods in Applied Mechanics and Engineering, 184(1), 49–65.

Cavin, P., Gravouil, A., Lubrecht, A. A., and Combescure, A. (2005). "Automatic energy conserving space–time refinement for linear dynamic structural problems." International Journal for Numerical Methods in Engineering, 64(3), 304–321.

Chang, S.-H., Lee, C.-I. and Jeon, S. (2002). Measurement of rock fracture toughness under modes I and II and mixed-mode conditions by using disc-type specimens. Eng. Geol.; 66: 79–97.

Chen, J. S., Pan, C., Wu, C. T., and Liu, W. K. (1996). "Reproducing Kernel Particle Methods for large deformation analysis of non-linear structures." Computer Methods in Applied Mechanics and Engineering, 139(1-4), 195–227.

Chen, R., K. Xia, et al. (2009). "Determination of dynamic fracture parameters using a semicircular bend technique in split Hopkinson pressure bar testing." Eng. Fract. Mech. 76(9): 1268–1276.

Chen, S. G., and Zhao, J. (1998). "A study of UDEC modeling for blast wave propagation in jointed rock masses." International Journal of Rock Mechanics and Mining Sciences, 35(1), 93–99.

Chen, S. G., Cai, J. G., Zhao, J., and Zhou, Y. X. (2000). "Discrete element modeling of an underground explosion in a jointed rock mass." Geotechnical and Geological Eng., 18(2), 59–78.

Chen, Y. Q., Yao, Z. H., and Zheng, X. P. (2002). "3-D numerical simulation of fracture processes in heterogeneous brittle materials." Acta Mechanica Solida Sinica, 15(4), 332–341.

Cheng, Y. M. (1998). "Advancements and improvement in discontinuous deformation analysis." Computers and Geotechnics, 22(2), 153–163.

Cheung, K. S., and Yip, S. (1990). "Brittle-Ductile Transition in Intrinsic Fracture-Behavior of Crystals." Physical Review Letters, 65(22), 2804–2807.

Chiang, D. Y. (1997). Experimental study on the degradation of shear behavior of tooth-shaped joints. Civil Engineering Department. Taipei, Taiwan, Tamkang University. Master thesis.

Chilton, L., and Suri, M. (1997). "On the selection of a locking-free hp element for elasticity problems." International Journal for Numerical Methods in Engineering, 40(11), 2045–2062.

Chiou, Y. J., Lee, Y. M., and Tsay, R. J. (2002). "Mixed mode fracture propagation by manifold method." International Journal of Fracture, 114(4), 327–347.

Chlup, Z., P. Flasar, et al. (2010). "Response of inherently brittle materials on higher loading rates." Engineering Fracture Mechanics 77(2): 359–366.

Cho, N., Martin, C. D., and Sego, D. C. (2007). "A clumped particle model for rock." International Journal of Rock Mechanics and Mining Sciences, 44(7), 997–1010.

Cho, S. H., and Kaneko, K. (2004). "Influence of the applied pressure waveform on the dynamic fracture processes in rock." Int. Journal of Rock Mechanics and Mining Sciences, 41(5), 771–784.

Cho, S. H., Ogata, Y., and Kaneko, K. (2003). "Strain-rate dependency of the dynamic tensile strength of rock." International Journal of Rock Mechanics and Mining Sciences, 40(5), 763–777.

Chong, K.P. and Kuruppu, M.D. (1984). New specimen for fracture toughness determination of rock and other materials. Int. J. Fract.; 26: 59–62.

Chu, L. F., Schatzinger, R. A., and Tham, M. K. (1998). "Application of wavelet analysis to upscaling of rock properties." Spe Reservoir Evaluation & Engineering, 1(1), 75–81.

Clough, R. W. (1960). "The finite element method in plane stress analysis." Proceedings of the Second ASCE Conference Electronic Computation, Pittsburg, PA.

Costanzo, F. and J. R. Walton (1998). "Numerical simulations of a dynamically propagating crack with a nonlinear cohesive zone." International Journal of Fracture 91(4): 373–389.

Costin, L.S. (1987). Deformation and failure. In: Atkinson, B.K. (ed.). 1991. Fracture Mechanics of Rock. Academic Press, New York: 167–215.

Courant, R.; Friedrichs, K.; and Lewy, H. (1967). "On the Partial Difference Equations of Mathematical Physics." IBM Journal. 11, 215–234.

Cox, S.J.D. and Scholz, C.H. (1988). Rupture Initiation in Shear Fracture of Rocks: An Experimental Study. J. Geophys. Res.; 93: 3307–3320.

Cundall, P. A. (1971) "A computer model for simulating progressive, large scale movements in blocky rock systems." Proceedings of the International Symposium on Rock Fracture, Nancy.

Cundall, P.A., Strack, O.D.L. (1979). "A discrete numerical model for granular assemblies." Geotechnique, 29(1), 47–65.

Cundall, P. A. (1987). "Distinct element models of rock and soil structure." Analytical and Computational Methods in Engineering Rock Mechanics: 129–163.

Cundall, P. A. (1988). "Formulation of a three–dimensional distinct element model––Part I. A scheme to detect and represent contacts in a system composed of many polyhedral blocks." Int. Journal of Rock Mechanics and Mining Science and Geomechanics Abstracts, 25(3), 107–116.

Cundall, P.A., and R.D. Hart, (1992). "Numerical modeling of discontinua." Eng Comp., 9, 101–113.

Curran, J.H., and G.I., Ofoegbu. (1993). "Modeling discontinuities in numerical analysis." In: Hudson JA, editor in–chief. Comprehensive rock engineering, vol. 1. Oxford: Pergamon Press, p. 443–68.

Dai, F., K. Xia, et al. (2008). "Semicircular bend testing with split Hopkinson pressure bar for measuring dynamic tensile strength of brittle solids." Review of Scientific Instruments 79(12): 123903–6.

Dai, F., R. Chen, et al. (2009). "A Semi–Circular Bend Technique for Determining Dynamic Fracture Toughness." Experimental Mechanics, In Press

Dai, F., K. Xia, et al. (2010). "Rate dependence of the flexural tensile strength of Laurentian granite." International Journal of Rock Mechanics and Mining Sciences, In Press, Corrected Proof.

Dally, J. W., W. L. Fourney, et al. (1985). "On the uniqueness of the stress intensity factor – crack velocity relationship." International Journal of Fracture 27(3–4): 159–168.

Damjanac, B., M. Board, et al. (2007). "Mechanical degradation of emplacement drifts at Yucca Mountain––A modeling case study: Part II: Lithophysal rock." International Journal of Rock Mechanics and Mining Sciences 44(3): 368–399.

Davies, J., Morgan, T.G. and Yim, A.W. (1986). The finite element analysis of specimens giving a mode II type of failure. Fracture Toughness and Fracture Energy of Concrete. In Wittmann, F.H. (ed.), Elsevier Science Publishers, Amsterdam: 209–211.

de Borst, R. (2008). "Challenges in computational materials science: Multiple scales, multi–physics and evolving discontinuities." Computational Materials Science, 43(1), 1–15.

De, S., and Bathe, K. J. (2000). "The method of finite spheres." Comp. Mechanics, 25(4), 329–345.

Delaunay, B. (1934). "Sur la sphère vide." Izvestia Akademii Nauk SSSR, Otdelenie Matematicheskikh i Estestvennykh Nauk 7: 793–800.

Diederich, M. S. (2000). Instability of hard rock masses: the role of tensile damage and relaxation University of Waterloo. PhD thesis.

Dienes, G. J., and Paskin, A. (1987). "Molecular Dynamic Simulations of Crack–Propagation." Journal of Physics and Chemistry of Solids, 48(11), 1015–1033.

Donze, F., and Magnier, S. A. (1995). "Formulation of a 3–D Numerical–Model of Brittle Behavior." Geophysical Journal International, 122(3), 790–802.

Donze, F. V., Magnier, S. A., Daudeville, L., Mariotti, C., and Davenne, L. (1999). "Numerical study of compressive behavior of concrete at high strain rates." Journal of Engineering Mechanics, 125(10), 1154–1162.

Dresen, G. and Guéguen, Y. (2004). In: Guéguen, Y. and Boutéca, M. (eds.). Mechanics of Fluid Saturated Rocks. Academic Press.

Du, J., Kobayashi, A. S., and Hawkins, N. M. (1989). "FEM dynamic fracture analysis of concrete beams." Journal of Engineering Mechanics, 115(10), 2136–2149.

Du, C. (1996). "An algorithm for automatic Delaunay triangulation of arbitrary planar domains." Advances in Engineering Software 27(1–2): 21–26.

Dugdale, D. S. (1960). "Yielding of steel sheets containing slits." Journal of the Mechanics and Physics of Solids 8(2): 100–104.

Dwivedi, R.D., Soni, A.K., Goel, R.K. and Dube, A.K. (2000). Fracture toughness of rocks under sub-zero temperature conditions. Int. J. Rock Mech. Min. Sci.; 37: 1267-1275.

Dyka, C. T., Randles, P. W., and Ingel, R. P. (1997). "Stress points for tension instability in SPH." International Journal for Numerical Methods in Engineering, 40(13), 2325-2341.

Dyskin, A.V., Sahouryeh, E., Jewell, R.J., Joer, H. and Ustinov, K.B. (2003). Influence of shape and loacations of initial 3-D cracks on their growth in uniaxial compression. Eng. Fract. Mech.; 70: 2115-2136.

Eker, E., and Akin, S. (2006). "Lattice Boltzmann simulation of fluid flow in synthetic fractures." Transport in Porous Media, 65(3), 363-384.

Elmarakbi, A.M., Hu, N., and Fukunaga, H. (2009). "Finite element simulation of delamination growth in composite materials using LS-DYNA." Composites Sci. and Tech., 69(14), 2383-2391.

Engelder, T. (1987). Joints and shear fractures in rock. In: Atkinson, B.K. (ed.). (1991. Fracture mechanics of rock. Academic press geology series. Academic Press, London: 27-69.

Erdogan, F. and Sih, G.C. (1963). On the crack extension in plates under plane loading and transverse shear. J. Basic Eng.; 85: 519-527.

Ernst, J. R., Holliger, K., Maurer, H., and Green, A. G. (2006). "Realistic FDTD modeling of borehole georadar antenna radiation: methodology and application." Near Surf. Geoph., 4, 19-30.

Espandar, E., and Lotfi, V. (2003). "Comparison of non-orthogonal smeared crack and plasticity models for dynamic analysis of concrete arch dams." Computers & Structures, Volume 81, Issue 14, Pages 1461-1474.

Evans, A.G. (1972). A method for evaluating the time dependent failure characteristics of brittle materials and its application to polycrystalline alumina. J. Mater. Sci.; 7: 1137-1146.

Eve, S., M. Gomina, et al. (2002). "Microstructural and mechanical behavior of polyamide fibre-reinforced plaster composites." Journal of the European Ceramic Society 22(13): 2269-2275.

Farkas, D., Van Swygenhoven, H., and Derlet, P. M. (2002). "Intergranular fracture in nanocrystalline metals." Physical Review B, 66(6), 601011-601014.

Fernandez-Mendez, S., and Huerta, A. (2004). "Imposing essential boundary conditions in mesh-free methods." Computer Methods in Applied Mechanics and Engineering, 193(12-14), 1257-1275.

Fineberg, J., S. P. Gross, et al. (1991). "Instability in dynamic fracture." Physical Review Letters 67(4): 457-460.

Follansbee, P.S., (1985). "The Hopkinson Bar," Mechanical Testing, Metals Handbook, 9th ed,8, American Society for Metals, Metals Park, OH,198-217.

Fowell RJ, Xu C. (1993). "The cracked chevron-notched Brazilian disc test geometrical considerations for practical rock fracture toughness measurement". International Journal of Rock Mechanics and Mining Science Goemechanical Abstract 30(7): 821-824.

Fowell, R. J. and C. Xu (1994). "The use of the cracked Brazilian disc geometry for rock fracture investigations." International Journal of Rock Mechanics and Mining Sciences & Geomechanics Abstracts 31(6): 571-579.

Fowell, R.J. (1995). Suggested methods for determining Mode I fracture toughness using cracked chevron notched Brazilian disc specimens. Int. J. Rock Mech. Min. Sci. Geomech. Abst.; 32: 57-64.

Freund, L. B. (1990). Dynamic Fracture Mechanics, Cambridge University Press

Fukui, K., S. Okubo, et al. (2004). "Some aspects of loading-rate dependency of Sanjome andesite strengths." International Journal of Rock Mechanics and Mining Sciences 41(7): 1215-1219.

Fulk, D. A., and Quinn, D. W. (1996). "An analysis of 1-D smoothed particle hydrodynamics kernels." Journal of Computational Physics, 126(1), 165-180.

Gao, H., and Klein, P. (1998). "Numerical simulation of crack growth in an isotropic solid with randomized internal cohesive bonds." J of the Mechanics and Physics of Solids, 46(2), 187-218.

Germanovich, L.N. and Dyskin, A.V. (2000). Fracture mechanics and instability of openings in compression. Int. J. Rock Mech. Min. Sci.; 37: 263–284.

Glaser, S.D. and Nelson, P.P. (1992). Acoustic Emission Produced by Discrete Fracture in Rock. Int. J. Rock Mech. Min. Sci. and Geomech. Abstr.; 29: 253–265.

Gmouh, A., S. Eve, et al. (2003). "Changes in plaster microstructure by pre–stressing or by adding gypsum grains: microstructural and mechanical investigations." Materials Science and Engineering: A 352(1–2): 325–332.

Gong, Q. M., and Zhao, J. (2007). "Influence of rock brittleness on TBM penetration rate in Singapore granite." Tunnelling and Underground Space Technology, 22(3), 317–324.

Gong, F. (2010). “Experimental study of rock mechanical properties under coupled static–dynamic loads and dynamic strength criterion”, PhD Thesis, China Changsha, Central South University.

Goodman, R., Taylor, R., and Brekke, T. (1968). "A model for the mechanics of jointed rock." J Soil Mech Div ASCE 94, SM3(6), 37–59.

Grasselli, G., J. Wirth, et al. (2002). "Quantitative three–dimensional description of a rough surface and parameter evolution with shearing." International Journal of Rock Mechanics & Mining Sciences 39: 789–800.

Gray, G.T., (1999). “Classic Split–Hopkinson Pressure Bar Technique,” LA–UR–99–2347, Los Alamos National Laboratory.

Gray, G.T. and Blumenthal, W.R., (1999). “Split–Hopkinson Pressure Bar Testing of Soft Mateirals,” LA–UR–99–4878, Los Alamos National Laboratory.

Gray, J. P., Monaghan, J. J., and Swift, R. P. (2001). "SPH elastic dynamics." Computer Methods in Applied Mechanics and Engineering, 190(49–50), 6641–6662.

Gray, J. P., and Monaghan, J. J. (2004). "Numerical modeling of stress fields and fracture around magma chambers." Journal of Volcanology and Geothermal Research, 135(3), 259–283.

Gray, L. J., Phan, A. V., and Kaplan, T. (2004). "Boundary integral evaluation of surface derivatives." Siam Journal on Scientific Computing, 26(1), 294–312.

Griebel, M., S. Knapek, et al. (2007). Numerical simulation in molecular dynamics: numerics, algorithms, parallelization, applications, Springer.

Guidault, P. A., Allix, O., Champaney, L., and Navarro, J. P. (2007). "A two–scale approach with homogenization for the computation of cracked structures." Comp. Struct., 85(17–18), 1360–1371.

Guimaraes, M. S., J. R. Valdes, et al. (2007). "Aggregate production: Fines generation during rock crushing." International Journal of Mineral Processing 81(4): 237–247.

Gunsallus, K. L. and F. H. Kulhawy (1984). "A comparative evaluation of rock strength measures." Int. Journal of Rock Mechanics and Mining Sciences & Geomechanics Abstracts 21(5): 233–248.

Guo, H. (1990). Rock cutting using fracture mechanics principles. PhD Thesis, University of Wollongong, NSW, Australia.

Guo, H., Aziz, N.I. and Schmidt, L.C. (1993). Rock fracture toughness determination by the Brazilian test. Eng. Geol.; 33: 177–188.

Haberfield, C. M. and I. W. Johnston (1989). Relationship between fracture toughness and tensile strength for geomaterials. the 12th International Conference Soil Mechanics & Foundation Engineering, SMFE, Rio De Janeiro, Brazil.

Haidar, K., Dube, J. F., and Pijaudier–Cabot, G. (2003). "Modeling crack propagation in concrete structures with a two scale approach." International Journal for Numerical and Analytical Methods in Geomechanics, 27(13), 1187–1205.

Hakami, H. and Stephansson, O. (1990). Shear fracture energy of Stripa granite – results of controlled triaxial testing. Eng. Fract. Mech.; 35: 855–865.

Han, J. G., Ren, W. X., and Huang, Y. (2005). "A multivariu-ble wavelet-based finite element method and its application to thick plates." Finite Elements in Analysis and Design, 41, 821-833.

Hans, J. and M. Boulon (2003). "A new device for investigating the hydromechanical properties of rock joints." Int. Journal for Numerical and Analytical Methods in Geomechanics 27: 513-548.

Harison, J. A., B. O. Hardin, et al. (1994). "Fracture toughness of compacted cohesive soils using ring test." Journal of Geotechnical Engineering - ASCE 120(5): 872-891.

Hart, R. D., J. Lemos, et al. (1987). Block motion research: analysis with the distinct element method, Itasca Consulting Group/Agbabian Associates, DNA-TR-88-34-V2.

Hart, R., Cundall, P. A., and Lemos, J. (1988). "Formulation of a three-dimensional distinct element model--Part II. Mechanical calculations for motion and interaction of a system composed of many polyhedral blocks." International Journal of Rock Mechanics and Mining Science & Geomechanics Abstracts, 25(3), 117-125.

Hasnaoui, A., Van Swygenhoven, H., and Derlet, P. M. (2003). "Dimples on nanocrystalline fracture surfaces as evidence for shear plane formation." Science, 300(5625), 1550-1552.

Hatzor, Y. H., Arzi, A. A., Zaslavsky, Y., and Shapira, A. (2004). "Dynamic stability analysis of jointed rock slopes using the DDA method: King Herod's Palace, Masada, Israel." International Journal of Rock Mechanics and Mining Sciences, 41(5), 813-832.

Haussler-Combe, U., and Korn, C. (1998). "An adaptive approach with the Element-Free-Galerkin method." Computer Methods in Applied Mechanics and Engineering, 162(1-4), 203-222.

Hazzard, J. F. and Young R. P. (2000a). "Micromechanical modeling of cracking and failure in brittle rocks." Journal of Gheophysical Research 105: 16683-16697.

Hazzard, J. F., and Young, R. P. (2000b). "Simulating acoustic emissions in bonded-particle models of rock." International Journal of Rock Mechanics and Mining Sciences, 37(5), 867-872.

He, Y. M., Chen, X. F., Xiang, J. W., and He, Z. J. (2007). "Adaptive multiresolution finite element method based on second generation wavelets." Finite Elem. in Analysis and Design, 43, 566-579.

Hentz, S., Donze, F. V., and Daudeville, L. (2004). "Discrete element modeling of concrete submitted to dynamic loading at high strain rates." Computers Structures, 82(29-30), 2509-2524.

Herrmann, H. J., Hansen, A., and Roux, S. (1989). "Fracture of disordered, elastic lattices in two dimensions." Physical Review B, 39(1), 637-648.

Hettich, T., Hund, A., and Ramm, E. (2008). "Modeling of failure in composites by X-FEM and level sets within a multi-scale framework." Computer Methods in Applied Mechanics and Engineering, 197(5), 414-424.

Hildyard, M. W., and Young, R. P. (2002). "Modeling seismic waves around underground openings in fractured rock." Pure and Applied Geophysics, 159(1-3), 247-276.

Hillerborg, A. Modeer, M., and Petersson, P. (1976). "Analysis of crack formation and crack growth in concrete by means of fracture mechanics and finite elements." Cem Concr Res 6, 773-782.

Hoagland, R.G., Hahn, G.T. and Rosenfield, A.R. (1973). Influence of Microstructure on Fracture Propagation in Rock. Rock Mechanics; 5: 77-106.

Hoek, E. and Bieniawski, Z.T. (1984). Brittle fracture propagation in rock under compression. Int. J. Fract.; 26: 276-294.

Hoek, E. and E. T. Brown (1998). "Practical estimates of rock mass strength." International Journal of Rock Mechanics and Mining Sciences 34: 1165-1186.

Holliger, K., Musil, M., and Maurer, H. R. (2001). "Ray-based amplitude tomography for crosshole georadar data: a numerical assessment." Journal of Applied Geophysics, 47(3-4), 285-298.

Horii, H. and Nemat-Nasser, S. (1985). Compression-Induced Microcrack Growth in Brittle Solids: Axial Splitting and Shear Failure. J. Geophys. Res.; 90: 3105-3125.

Hou, T. Y., and Wu, X. H. (1997). "A multi-scale finite element method for elliptic problems in composite materials and porous media." Journal of Computational Physics, 134(1), 169-189.

Hrennikoff, A. (1941). "Solution of problems of elasticity by the framework method." Journal of Applied Mechanics, 169–175.

Hsiung SM. (2001). "Discontinuous deformation analysis (DDA) with nth order polynomial displacement functions." Rock mech. in the national interest, Swets & Zeitlinger Lisse, 1437–44.

Hsiung, S. M., and Shi, G. (2001). "Simulation of earthquake effects on underground excavations using discontinuous deformation analysis (DDA)." Rock Mech. in the National Interest, 1413–20.

Hu, C., Bai, J., and Ghosh, S. (2007). "Micromechanical and macroscopic models of ductile fracture in particle reinforced metallic materials." Modeling and Simulation in Materials Science and Engineering, 15(4).

Huang, X., B. C. Haimson, et al. (1993). "An investigation of the mechanics of rock joints--Part I. Laboratory investigation." International Journal of Rock Mechanics and Mining Sciences & Geomechanics Abstracts 30(3): 257–269.

Huang, S., K. Xia, et al. (2010). "An Experimental Study of the Rate Dependence of Tensile Strength Softening of Longyou Sandstone." Rock Mechanics and Rock Engineering, In Press.

Hudson, J.A. and Harrison, J.P. (1997). Engineering rock mechanics: an introduction to the principles. Elsevier, Oxford.

Ichikawa, Y., Kawamura, K., Uesugi, K., Seo, Y. S., and Fujii, N. (2001). "Micro- and macrobehavior of granitic rock: observations and viscoelastic homogenization analysis." Computer Methods in Applied Mechanics and Engineering, 191(1–2), 47–72.

Inglis, C.E. (1913. Stresses in a plate due to the presence of cracks and sharp corners. Trans. Inst. Naval Archit.; 55: 219–230.

Ingraffea, A.R. (1981). Mixed Mode fracture initiation in Indiana limestone and Westerly granite. In: Proc. 22nd US Symp. Rock Mech., Cambridge, MA.: 186–191.

Irwin, G.R. (1958). Fracture. In: Handbuch der Physik. Springer Verlag, Berlin, Vol. 6.

Itasca (2008). PFC (Particle Flow Code). Theory and Background Volume. Minneapolis, MN: ICG, Itasca Consulting Group Inc.

Itasca (2009). UDEC (Universal Distinct Element Code). Theory and Background Volume. Minneapolis, MN: ICG, Itasca Consulting Group Inc.

Ivankovic, A., K. C. Pandya, et al. (2004). "Crack growth predictions in polyethylene using measured traction-separation curves." Engineering Fracture Mechanics 71(4–6): 657–668.

Izumi, M., Mihashi, H. and Nomura, N. (1986). Fracture toughness of concrete for mode II Fracture Toughness and Fracture Energy of Concrete. In Wittmann, F.H. (ed.), Elsevier Science Publishers, Amsterdam: 347–354.

JafarGandomi, A., and Takenaka, H. (2007). "Efficient FDTD algorithm for plane-wave simulation for vertically heterogeneous attenuative media." Geophysics, 72(4), H43–H53.

Jafari, M. K., K. Amini Hosseini, et al. (2003). "Evaluation of shear strength of rock joints subjected to cyclic loading." Soil Dynamics and Earthquake Engineering 23(7): 619–630.

Jensen, R. P., Bosscher, P. J., Plesha, M. E., Edil, T. B. (1999) "DEM simulation of granular media-structure interface: effects of surface roughness and particle shape" Int. J. Numer. Anal. Met. Geomechanics 23: 531–547

Jeong, J., H. Adib-Ramezani, et al. (2006). "Tensile strength of the brittle materials, probabilistic or deterministic approach?" Strength of Materials 38(1): 72–83.

Jiang, Q. H., and Yeung, M. R. (2004). "A model of point-to-face contact for three-dimensional discontinuous deformation analysis." Rock Mechanics and Rock Engineering, 37(2), 95–116.

Jiao, Y., Zhang, X., Liu, Q., and Chen, W. (2007a). "Simulation of rock crack propagation using discontinuous deformation analysis method." Yanshilixue Yu Gongcheng Xuebao/Chinese Journal of Rock Mechanics and Engineering, 26(4), 682–691.

Jiao, Y. Y., Zhang, X. L., Zhao, J., and Liu, Q. S. (2007b). "Viscous boundary of DDA for modeling stress wave propagation in jointed rock." International Journal of Rock Mechanics and Mining Sciences, 44(7), 1070–1076.

Jimenez-Hornero, F. J., Giraldez, J. V., and Laguna, A. (2005). "Description of sorbing tracers transport in fractured media using the lattice model approach." Journal of Contaminant Hydrology, 81(1-4), 187-204.

Jing, L., Stephansson, O., and Nordlund, E. (1993). "Study of rock joints under cyclic loading conditions." Rock Mechanics and Rock Engineering, 26(3), 215-232.

Jing, L., Nordlund, E., and Stephansson, O. (1994). "A 3-D constitutive model for rock joints with anisotropic friction and stress dependency in shear stiffness." International Journal of Rock Mechanics & Mining Sciences, 31(2), 173-178.

Jing, L., Tsang, C. F., and Stephansson, O. (1995). "DECOVALEX – an international co-operative research project on mathematical models of coupled THM processes for safety analysis of radioactive waste repositories." Int. J of Rock Mechanics & Mining Sciences, 32(5), 389-398.

Jing, L., and Hudson, J. A. (2002). "Numerical methods in rock mechanics." International Journal of Rock Mechanics and Mining Sciences, 39(4), 409-427.

Jing, L. (2003). "A review of techniques, advances and outstanding issues in numerical modeling for rock mechanics and rock engineering." Int. J of Rock Mech. Mining Sciences, 40(3), 283-353.

Jing, L., and O. Stephansson, (2007). “Fundamentals of Discrete Element Methods for Rock Engineering”, Theory and Application, Elsevier.

Johnson, G. R., Stryk, R. A., and Beissel, S. R. (1996). "SPH for high velocity impact computations." Computer Methods in Applied Mechanics and Engineering, 139(1-4), 347-373.

Jumikis, A. R. (1979). Rock Mechanics. Trans. Tech. Publ., Series on rock and soil mechanics, U.S.A.: 216-219.

Jun, Z., W. Yang, et al. (2006). "Mode-I fracture toughness of PMMA at high loading rates." Journal of Materials Science 41(24): 8363-6.

Kaiser, P. K., and Tang, C. A. (1998). "Numerical Simulation of Damage Accumulation and Seismic Energy Release During Brittle Rock Failure-Part II: Rib Pillar Collapse." Int. J. Rock Mech. Min. Sci, 35(2), 123-134.

Kaminski, M. (2005). "Homogenization-based finite element analysis of unidirectional composites by classical and multiresolutional techniques." Computer Methods in Applied Mechanics and Engineering, 194(18-20), 2147-2173.

Karami, A., and Stead, D. (2008). "Asperity degradation and damage in the direct shear test: A hybrid FEM/DEM approach." Rock Mechanics and Rock Engineering, 41(2), 229-266.

Karedla, R. S. and J. N. Reddy (2007). "Modeling of crack tip high inertia zone in dynamic brittle fracture." Engineering Fracture Mechanics 74(13): 2084-2098.

Katona. (1983). "A simple contact-friction interface element with applications to buried culverts." Int J Numer Anal Methods Geomech, 7(3), 71-84.

Katsman, R., and Aharonov, E. (2006). "A study of compaction bands originating from cracks, notches, and compacted defects." Journal of Structural Geology, 28(3), 508-518.

Kazerani, T., G. Zhao, et al. (2010a). "Dynamic Fracturing Simulation of Brittle Material using the Distinct Lattice Spring Method with a Full Rate-Dependent Cohesive Law." Rock Mechanics and Rock Engineering 43(6): 717-726.

Kazerani, T. and J. Zhao (2010). "Micromechanical parameters in bonded particle method for modeling of brittle material failure." Int. J Num. Analit. Meth. in Geomech., DOI: 10.1002/nag.884.

Kazerani, T., Yang, Z.Y. and Zhao, J. (2010b), “Investigation of failure mode and shear strength of rock joints using discrete element method”, accepted in EUROCK 2010, Lausanne, Switzerland.

Kemeny, J. (2005). "Time-dependent drift degradation due to the progressive failure of rock bridges along discontinuities." Int. Journal of Rock Mechanics and Mining Sciences, 42(1), 35-46.

Kemeny, J.M. and Cook, N.G.W. (1987). Crack Models for the Failure of Rocks in Compression. In: Proc. of the 2nd Int. Conf. on Constitutive Laws for Eng. Materials, Arizona, USA.: 879-887.

Kennedy, M. and D. Krouse (1999). "Strategies for improving fermentation medium performance: a review." Journal of Industrial Microbiology and Biotechnology 23(6): 456-475.

Khoei, A. R., and Nikbakht, M. (2007). "An enriched finite element algorithm for numerical computation of contact friction problems." Int. Journal of Mechanical Sciences, 49(2), 183-199.

Kidane, A. and A. Shukla (2010). "Quasi-Static and Dynamic Fracture Initiation Toughness of Ti/TiB Layered Functionally Graded Material under Thermo-Mechanical Loading." Engineering Fracture Mechanics, 77 (3), 479-491.

Kim, Y. I., Amadei, B., and Pan, E. (1999). "Modeling the effect of water, excavation sequence and rock reinforcement with discontinuous deformation analysis." International Journal of Rock Mechanics and Mining Sciences, 36(7), 949-970.

Kim, Y. and Y. J. Chao (2007). "Effect of loading rate on dynamic fracture initiation toughness of brittle materials." International Journal of Fracture 145(3): 195-204.

Klein, P., and Gao, H. (1998). "Crack nucleation and growth as strain localization in a virtual-bond continuum." Engineering Fracture Mechanics, 61(1), 21-48.

Ko, J., Kurdila, A. J., and Pilant, M. S. (1995). "A class of finite element methods based on orthonormal, compactly supported wavelets." Computational Mechanics, 16(4), 235-244.

Kohlhoff, S., Gumbsch, P., and Fischmeister, H. F. (1991). "Crack-Propagation in Bcc Crystals Studied with a Combined Finite-Element and Atomistic Model." Philosophical Magazine a-Physics of Condensed Matter Structure Defects and Mechanical Properties, 64(4), 851-878.

Kolsky, H., (1949). “An Investigation of the Mechnical Properties of Materials at Very High Rates of Loading,” Proc. Roy. Soc. Lond. B.,62,676-700.

Kolsky, H., (1963). “Stress Waves in Solids”, Dover, New York.

Kozicki, J. (2007). "Application of Discrete Models to Describe the Fracture Process in Brittle Materials," Doctoral thesis, Gdansk University of Technology.

Krivtsov, A.M. and Wiercigroch, M. (2001). "Molecular Dynamic Simulation of Mechanical Properties for Polycrystal Materials." Materials Physics and Mechanics, 3(1), 45-51.

Krivtsov, A.M. (2003). "Molecular dynamics simulation of impact fracture in polycrystalline materials." Meccanica, 38(1), 61-70.

Krysl, P., and Belytschko, T. (1999). "The Element Free Galerkin method for dynamic propagation of arbitrary 3-D cracks." Int Journal for Numerical Methods in Engineering, 44(6), 767-800.

Kubair, D. V., P. H. Geubelle, et al. (2003). "Analysis of a rate-dependent cohesive model for dynamic crack propagation." Engineering Fracture Mechanics 70(5): 685-704.

Kuna-Ciska, H., and Skrzypek, J. J. (2004). "CDM based modeling of damage and fracture mechanisms in concrete under tension and compression." Eng. Fract. Mech., 71(4-6), 681-698.

Kuruppu, M.D. (1997). Fracture toughness measurement using chevron notched semi-circular bend specimen. Int. J. Fract.; 86: L33-L38.

Labuz, J.F., Shah, S.P. and Dowding, C.H. (1983). Post peak tensile load-displacement response and the fracture process zone in rock. In: Proc. 24th US Symp. Rock Mech. 421-428.

Labuz, J.F., Shah, S.P. and Dowding, C.H. (1985). Experimental analysis of crack propagation in granite. Int. J. Rock Mech. Min. Sci. and Geomech. Abstr.; 22: 85-98.

Ladanyi, B. and G. Archambault (1977). Shear strength and deformability of filled indented joints. International symposium: the geotechnics of structurally complex formations. Capri: 37126.

Lawn, B. (1993). Fracture of brittle solids. Cambridge University Press, Cambridge.

Lee, H. S., Y. J. Park, et al. (2001). "Influence of asperity degradation on the mechanical behavior of rough rock joints under cyclic shear loading." Int. J of Rock Mech. and Min. Sci. 38(7): 967–980.

Lee, Y. and V. Prakash (1999). "Dynamic brittle fracture of high strength structural steels under conditions of plane strain." International Journal of Solids and Structures 36(22): 3293–3337.

Lei, W. D., Teng, J., Hefny, A. M., and Zhao, J. (2006). "Transmission ratio (T–n) in the radian direction normal to joints in 2–D compressional wave propagation in rock masses." Journal of University of Science and Technology Beijing, 13(3), 199–206.

Lemos, J. V., Hart, R. D., Cundall, P. A. (1985). "A Generalized Distinct Element Program for Modeling of Jointed Rock Masses", Proc. Int. Symp. Fundamentals of Rock Joints, Bjorkliden, Sweden, 335–343.

Lemos, J. V. (1993). "Numerical modelling of fractured media applied to underground gas storage". Short Course on Underground Storage of Gases, LNEC, Lisboa, 122–139.

Lemos, J. V. (1994). "Computational topics in discrete element modeling". Applications of Computational Mechanics in Geotechnical Engineering (Ed. Vargas et al.), Balkema, 371–384,

Lesnic, D., Elliott, L., Ingham, D. B., Clennell, B., and Knipe, R. J. (1997). "A mathematical model and numerical investigation for determining the hydraulic conductivity of rocks." International Journal of Rock Mechanics and Mining Sciences, 34(5), 741–759.

Li, Y. N. and Z. P. Bazant (1997a). "Cohesive crack with rate–dependent opening and visco–elasticity: I. Mathematical model and scaling." International Journal of Fracture 86(3): 247–265.

Li, Y. N. and Z. P. Bazant (1997b). "Cohesive crack model with rate–dependent opening and visco–elasticity: II. Numerical algorithm, behavior and size effect." International Journal of Fracture 86(3): 267–288.

Li HB. (1999). "Experimental and theoretical studies on mechanical properties of granite under dynamic compressive loads". PhD thesis, I RSM Chinese Academy of Sciences.

Li, H. B., Zhao, J., and Li, T. J. (2000). "Micromechanical modeling of the mechanical properties of a granite under dynamic uniaxial compressive loads." International Journal of Rock Mechanics and Mining Sciences, 37(6), 923–935.

Li, L. Y., Che, F. X., and Liu, D. A. (2004a). "Fracture behaviors of multi–crack in rock–like material." Advances in Fracture and Failure Prevention, Pts 1 and 2, 261–263, 1523–1528.

Li, M. T., Feng, X. T., and Zhou, H. (2004b). "2D vector cellular automata model for simulating fracture of rock under tensile condition." Advances in Fracture and Failure Prevention, Pts 1 and 2, 261–263, 705–710.

Li QM, Lu YB, Meng H. (2009). "Further investigation on the dynamic compressive strength enhancement of concrete–like materials based on split Hopkinson pressure bar tests. Part II: Numerical simulations". International Journal of Impact Engineering 36: 1327–1334.

Liang, Z. Z., Tang, C. A., Li, H. X., and Zhang, Y. B. (2004). "Numerical simulation of the 3D failure process in heterogeneous rocks." International Journal of Rock Mechanics and Mining Sciences, 41(3), 419–419.

Libersky, L. D., and Petschek, A. G. (1991). "Smooth particle hydrodynamics with strength of materials." Advances in the Free–Lagrange Method Including Contributions on Adaptive Gridding and the Smooth Particle Hydrodynamics Method, 248–257.

Lilliu, G., and van Mier, J. G. M. (2003). "3D lattice type fracture model for concrete." Engineering Fracture Mechanics, 70(7–8), 927–941.

Liszka, T., and Orkisz, J. (1979). "Finite difference method at arbitrary irregular grids and its application in applied mechanics." Comput. Struct., 11(1–2), 83–95.

Liszka, T., and Orkisz, J. (1980). "The Finite–Difference Method at Arbitrary Irregular Grids and Its Application in Applied Mechanics." Computers & Structures, 11(1–2), 83–95.

Liszka, T. J., Duarte, C. A. M., and Tworzydlo, W. W. (1996). "hp–Meshless cloud method." Computer Methods in Applied Mechanics and Engineering, 139(1–4), 263–288.

Liu, W. K., Chen, Y., Uras, R. A., and Chang, C. T. (1996). "Generalized multiple scale reproducing kernel particle methods." Comp. Methods in App. Mechanics and Engineering, 139(1–4), 91–157.

Liu, W. K., Hao, W., Chen, Y., Jun, S., and Gosz, J. (1997a). "Multiresolution reproducing kernel particle methods." Computational Mechanics, 20(4), 295–309.

Liu, W. K., Li, S., and Belytschko, T. (1997b). "Moving least–square reproducing kernel methods (I) methodology and convergence." Computer Methods in Applied Mechanics and Engineering, 143(1–2), 113–154.

Liu, C., Y. Huang, et al. (1998). "Enhanced mode–II fracture toughness of an epoxy resin due to shear banding." Acta Materialia 46(16): 5647–5661.

Liu, D., Wang, S. and Li, L. (2000). Investigation of fracture behavior during rock mass failure. Int. J. Rock Mech. Min. Sci.; 37: 489–497.

Liu, X. L., and Lemos J. V. (2001). “Procedure for contact detection in discrete element analysis”, Advances in Engineering Software, Vol. 32(5), 409–415.

Liu, G. R., and Gu, Y. T. (2004). "Boundary meshfree methods based on the boundary point interpolation methods." Engineering Analysis with Boundary Elements, 28(5), 475–487.

Liu, J. X., Deng, S. C., and Liang, N. G. (2008). "Comparison of the quasi–static method and the dynamic method for simulating fracture processes in concrete." Comp. Mechanics, 41(5), 647–660.

Lockner, D.A., Moore, D.E. and Reches, Z. (1992). Microcrack interaction leading to shear fracture. In: Tillerson and Wawersik (eds.). Rock Mechanics. Balkema, Rotterdam: 807–816.

Lockner, D.A. (1995). Rock Failure. In: Rock Physics and Phase Relations, AGU Reference Shelf; 3: 127–146.

Lorig, L. J., Brady, B. H. G., and Cundall, P. A. (1986). "Hybrid distinct element–boundary element analysis of jointed rock." Int. Journal of Rock Mechanics and Mining Sciences and, 23(4), 303–312.

Lotfi, V. and R. Espandar (2004). "Seismic analysis of concrete arch dams by combined discrete crack and non–orthogonal smeared crack technique." Engineering Structures 26(1): 27–37.

Lu, Y. Y., Belytschko, T., and Tabbara, M. (1995). "Element–Free Galerkin Method for Wave–Propagation and Dynamic Fracture." Computer Methods in Applied Mechanics and Engineering, 126(1–2), 131–153.

Ma, G., Dong, A., Li, J. (2006a). "Modeling strain rate effect for heterogeneous brittle materials." Transactions of Tianjin University 12 (SUPPL.), .79–82

Ma, J., Lu, H., Wang, B., Hornung, R., Wissink, A., and Komanduri, R. (2006b). "Multi–scale simulation using generalized interpolation material point (GIMP) method and molecular dynamics (MD)." Cmes–Computer Modeling in Engineering & Sciences, 14(2), 101–117.

Ma, G., X. Wang, et al. (2010). "Modeling Strain Rate Effect of Heterogeneous Materials Using SPH Method." Rock Mechanics and Rock Engineering 43(6): 763–776.

Mahabadi, O., B. Cottrell, et al. (2010a). "An Example of Realistic Modeling of Rock Dynamics Problems: FEM/DEM Simulation of Dynamic Brazilian Test on Barre Granite." Rock Mechanics and Rock Engineering 43(6): 707–716.

Mahabadi, O. K., G. Grasselli, et al. (2010b). "Y–GUI: A graphical user interface and pre–processor for the combined finite–discrete element code, Y2D, incorporating material heterogeneity." Computers and Geosciences 36(2): 241–252.

Mahtab, M. A., and Goodman, R. E. (1970). "Three–Dimensional Finite Element Analysis of Jointed Rock Slopes." Proc., Second Congress of the International Society of Rock Mechanics, Belgrade, 353–360.

Maier, G., and Frangi, A. (1998). "Symmetric boundary element method for "discrete" crack modeling of fracture processes." Comp. Assisted Mechanics and Eng. Sciences, 5(3), 201–226.

Maigre H, Rittel D. (1995). “Dynamic fracture detection using the force–displacement reciprocity: application to the compact compression specimen”. International Journal of Fracture 73(1): 67–79.

Markus Peters, K. H. (2005). "Numerical aspects of the eXtended Finite Element Method." 355–6.

Medina, D. F., and Chen, J. K. (2000). "Three–dimensional simulations of impact induced damage in composite structures using the parallelized SPH method." Composites Part a–Applied Science and Manufacturing, 31(8), 853–860.

Melenk, J. M., and Babuska, I. (1996). "The partition of unity finite element method: Basic theory and applications." Computer Methods in Applied Mechanics and Engineering, 139(1–4), 289–314.

Melin, S. (1989). Why are crack paths in concrete and mortar different from those in PMMA. Matér. Constr.; 22: 23–27.

Menouillard, T., Réthoré, J., Combescure, A., and Bung, H. (2006). "Efficient explicit time stepping for the eXtended Finite Element Method (X–FEM)." 911–939.

Menouillard, T., Réthoré, J., Moës, N., Combescure, A., and Bung, H. (2007). "Mass lumping strategies for X–FEM explicit dynamics: Application to crack propagation." n/a.

Mergheim, J., Kuhl, E., and Steinmann, P. (2005). "A finite element method for the computational modeling of cohesive cracks." 276–289.

Miller, R., Tadmor, E. B., Phillips, R., and Ortiz, M. (1998). "Quasicontinuum simulation of fracture at the atomic scale." Model. and Simulation in Materials Sci. and Eng., 6(5), 607–638.

Miller, R. E., and Tadmor, E. B. (2007). "Hybrid continuum mechanics and atomistic methods for simulating materials deformation and failure." MRS Bulletin, 32(11), 920–926.

Min, K. B., and Jing, L. R. (2003). "Numerical determination of the equivalent elastic compliance tensor for fractured rock masses using the distinct element method." International Journal of Rock Mechanics and Mining Sciences, 40(6), 795–816.

Moes, N., J. Dolbow, et al. (1999). "A finite element method for crack growth without re–meshing." International Journal for Numerical Methods in Engineering 46(1): 131–150.

Molinari, J. F., and Ortiz, M. (2002). "Three–dimensional adaptive meshing by subdivision and edge–collapse in finite–deformation dynamic–plasticity problems with application to adiabatic shear banding." International Journal for Numerical Methods in Engineering, 53(5), 1101–1126.

Molinari, J. F., Gazonas, G., Raghupathy, R., Rusinek, A., and Zhou, F. (2007). "The cohesive element approach to dynamic fragmentation: The question of energy convergence." International Journal for Numerical Methods in Engineering, 69(3), 484–503.

Monaghan, J. (1988). "An Introduction to SPH." Computer Physics Communications, 48(1), 89–96.

Moore, D.E. and Lockner, D.A. (1995). The role of microcracking in shear–fracture propagation in granite. J. Struct. Geol.; 17: 5–114.

Mora, P., and Place, D. (1994). "Simulation of the Frictional Stick–Slip Instability." Pure and Applied Geophysics, 143(1–3), 61–87.

Morris, J. P., Rubin, M. B., Block, G. I., and Bonner, M. P. (2006). "Simulations of fracture and fragmentation of geologic materials using combined FEM/DEM analysis." International Journal of Impact Engineering, 33(1–12), 463–473.

MSC.Software. (2007). " What's New: Marc 2007 r1." http://www.mscsoftware.com/

Müller, W. (1984). Bruchzähigkeitsmessungen an Gesteinen. Diplomarbeit, Institut für Geophysik, Ruhr–University Bochum, Germany.

Müller, W. and Rummel, F. (1984). Bruchzähigkeitsmessungen an Gesteinen. Bericht zu den BMFT–FE–Vorhaben 03E–3068–B, Ruhr–University Bochum, Germany.

Mullins, M., and Dokainish, M. A. (1982). "Simulation of the (001) Plane Crack in Alpha–Iron Employing a New Boundary Scheme." Philosophical Magazine a–Physics of Condensed Matter Structure Defects and Mechanical Properties, 46(5), 771–787.

Munjiza, A., Owen, D. R. J., and Bicanic, N. (1995). "A Combined Finite–Discrete Element Method in Transient Dynamics of Fracturing Solids." Engineering Computations, 12(2), 145–174.

Munjiza, A., Andrews, K. R. F., and White, J. K. (1999). "Combined single and smeared crack model in combined finite–discrete element analysis." International Journal for Numerical Methods in Engineering, 44(1), 41–57.

Munjiza, A., and John, N. W. M. (2002). "Mesh size sensitivity of the combined FEM/DEM fracture and fragmentation algorithms." Engineering Fracture Mechanics, 69(2), 281–295.

Munjiza, A. (2004). The Combined Finite–Discrete Element Method, John Wiley and Sons, Ltd, University of London.

Munjiza, A., Bangash, T., and John, N. W. M. (2004). "The combined finite–discrete element method for structural failure and collapse." Engineering Fracture Mechanics, 71(4–6), 469–483.

Muravin, B., and Turkel, E. (2006). "Multiple crack weight for solution of multiple interacting cracks by meshless numerical methods." International Journal for Numerical Methods in Engineering, 67(8), 1146–1159.

Murphy, N. and A. Ivankovic (2005). "The prediction of dynamic fracture evolution in PMMA using a cohesive zone model." Engineering Fracture Mechanics 72(6): 861–875.

Nagarajan, A., Mukherjee, S., and Lutz, E. (1996). "The boundary contour method for three-dimensional linear elasticity." Journal of Applied Mechanics, Transactions ASME, 63(2), 278–286.

Nasseri, M. H. B., A. Schubnel, et al. (2007). "Coupled evolutions of fracture toughness and elastic wave velocities at high crack density in thermally treated Westerly granite." International Journal of Rock Mechanics and Mining Sciences 44(4): 601–616.

Nasseri, M. H. B. and B. Mohanty (2008). "Fracture toughness anisotropy in granitic rocks." International Journal of Rock Mechanics and Mining Sciences 45(2): 167–193.

Nayroles, B., Touzot, G., and Villon, P. (1992). "Generalizing the finite element method: Diffuse approximation and diffuse elements." Computational Mechanics, 10(5), 307–318.

Nemat-Nasser, S., Isaacs, J.B., andStarrett, J.E., (1991). "Hopkinson Techniques for Dynamic Recovery Experiments," Proc. Roy. Soc. Lond. A.,435,371–391.

Nguyen, T. S. and A. P. S. Selvadurai (1998). "A model for coupled mechanical and hydraulic behavior of a rock joint." Int J Numer Anal Meth Geomech 22: 29–48.

Nicholas, T., (1982). "Material Behavior at High Strain Rates," Impact Dynamics, John Wiley and Sons, New York, Chap. 6.

Nicolazzi, L. C., Barcellos, C. S., Fancello, E. A., and Duarte, C. A. M. (2005). "Generalized boundary element method for galerkin boundary integrals." Engineering Analysis with Boundary Elements, 29(5), 494–510.

Nishioka, T. (1995). "Recent developments in computational dynamic fracture mechanics." Dynamic Fracture Mechanics: 1–60.

Nishioka, T., H. Tokudome, et al. (2001). "Dynamic fracture-path prediction in impact fracture phenomena using moving finite element method based on Delaunay automatic mesh generation." International Journal of Solids and Structures 38(30–31): 5273–5301.

NIST/SEMATECH (2003, 6/23/2010). "E-handbook of statistical methods." Retrieved 8/11/2010, from www.itl.nist.gov/div898/handbook.

Onate, E., Idelsohn, S., Zienkiewicz, O. C., and Taylor, R. L. (1996a). "A finite point method in computational mechanics: Applications to convective transport and fluid flow." Int. J. Numer. Methods Eng., 39, 3839–3866.

Onate, E., Idelsohn, S., Zienkiewicz, O. C., Taylor, R. L., and Sacco, C. (1996b). "A stabilized finite point method for analysis of fluid mechanics problems." Computer Methods in Applied Mechanics and Engineering, 139(1–4), 315–346.

Onate, E., Perazzo, F., and Miquel, J. (2001). "A finite point method for elasticity problems." Computers & Structures, 79(22–25), 2151–2163.

Ouchterlony, F. (1982). Review of fracture toughness testing of rock. SM Archives; 7: 131–211.

Ouchterlony F. (1989). “On the background to the formulas and accuracy of rock fracture toughness measurements using ISRM standard core specimens”. International Journal of Rock Mechanics and Mining Science Goemechanical Abstract 26(1): 13–23.

Ouchterlony, F. (1988). Suggested methods for determining the fracture toughness of rock. International Journal of Rock Mechanics and Mining Science Goemechanical Abstract; 25: 71–96.

Pan, X. D., and Reed, M. B. (1991). "Coupled distinct element–finite element method for large deformation analysis of rock masses." Int. J of Rock Mech. and Min, Sci. Geom. Abs., 28, 93–99.

Pan, E. N., Chen, C. S., and Amadei, B. (1997). "A BEM formulation for anisotropic half–plane problems." Engineering Analysis with Boundary Elements, 20(3), 185–195.

Pandolfi, A., P. Krysl, et al. (1999). "Finite element simulation of ring expansion and fragmentation: The capturing of length and time scales through cohesive models of fracture." International Journal of Fracture 95(1–4): 279–297.

Pandolfi, A., P. R. Guduru, et al. (2000). "Three dimensional cohesive–element analysis and experiments of dynamic fracture in C300 steel." Int. J of Solids and Structures 37(27): 3733–3760.

Park, N., Park, P., Hong, C. and Jeon, S. (2001). Crack propagation and coalescence under uniaxial loading. In: Särkka P. and Eloranta P. (eds.). Rock Mechanics, a challenge for society. Proceedings of the ISRM Regional Symposium EUROCK 2001, Espoo: 271–276.

Park, H. J. and S. H. Park (2010). "Extension of Central Composite Design for Second–Order Response Surface Model Building." Communic. in Statis. – Theory and Methods 39(7): 1202–1211.

Paskin, A., Gohar, A., and Dienes, G. J. (1980). "Computer–Simulation of Crack–Propagation." Physical Review Letters, 44(14), 940–943.

Paskin, A., Som, D. K., and Dienes, G. J. (1983). "The Dynamic Properties of Moving Cracks." Acta Metallurgica, 31(11), 1841–1848.

Paterson, M. S. (1978). Experimental rock deformation, the brittle field. , Springer–Verlag.

Patton, F. (1996). Multiple modes of shear failure in rock. Proceedings of the 1st congress of ISRM. Laboratorio nacional de engenharia civil, Lisboa. 1: 50913.

Pedro, M. A. A., and Belytschko, T. (2005). "Analysis of three–dimensional crack initiation and propagation using the extended finite element method." 760–788.

Perazzo, F., Lohner, R., and Perez–Pozo, L. (2008). "Adaptive methodology for meshless finite point method." Advances in Engineering Software, 39(3), 156–166.

Petit, J.–P. and Barquins, M. (1988). Can natural faults propagate under Mode II conditions. Tectonics; 7: 1243–1256.

Pinho, S. T., L. Iannucci, et al. (2006). "Formulation and implementation of decohesion elements in an explicit finite element code." Composites Part A: App. Sci. and Manufacturing 37(5): 778–789.

Plesha, M. E. (1987). "Constitutive models for rock discontinuities with dilatancy and surface degradation." Int. Journal for Numerical and Analytical Methods in Geomechanics 11(4): 345–362.

Pollard, D.D. and Aydin, A. (1988). Progress in understanding jointing over the past century. Geol. Soc. Am. Bull.; 100: 1181–1204.

Popelar, C., C. Anderson, et al. (2000). "An experimental method for determining dynamic fracture toughness." Experimental Mechanics 40(4): 401–407.

Poschel, T., and Buchholtz, V. (1995). "Molecular–Dynamics of Arbitrarily–Shaped Granular Particles." Journal De Physique I, 5(11), 1431–1455.

Potyondy, D. O. and P. A. Cundall (2004). "A bonded–particle model for rock." International Journal of Rock Mechanics and Mining Sciences 41(8): 1329–1364.

Potyondy, D. O. (2007). "Simulating stress corrosion with a bonded–particle model for rock." International Journal of Rock Mechanics and Mining Sciences, 44(5), 677–691.

Prabel, B., Combescure, A., Gravouil, A., and Marie, S. (2007). "Level set X-FEM non-matching meshes: application to dynamic crack propagation in elastic-plastic media." 1553-1569.

Prisco, M., and Mazars, J. (1996). "Crush-crack a non-local damage model for concrete." Mechanics of Cohesive-Frictional Materials, 1(4), 321-347.

Qi, C., M. Wang, et al. (2009). "Strain-rate effects on the strength and fragmentation size of rocks." International Journal of Impact Engineering 36(12): 1355-1364.

Rabczuk, T., and Eibl, J. (2003). "Simulation of high velocity concrete fragmentation using SPH/MLSPH." International Journal for Numerical Methods in Engineering, 56(10), 1421-1444.

Rahman, S., and Rao, B. N. (2002). "Probabilistic fracture mechanics by Galerkin meshless methods – part II: reliability analysis." Computational Mechanics, 28(5), 365-374.

Ramesh, K.T. andNarasimhan, S., (1996). "Finite Deformations and the Dynamic Measurement of Radial Strains in Compression Kolsky Bar Experiments," Int. J. Solids Struct.,33,3723-3738.

Randles, P. W., and Libersky, L. D. (1996). "Smoothed particle hydrodynamics: Some recent improvements and applications." Comp. Methods in App. Mech. and Eng., 139(1-4), 375-408.

Rao, Q. (1999). Pure shear fracture of brittle rock. Doctoral thesis, Division of Rock Mechanics, Luleå University, Sweden.

Rao, B. N., and Rahman, S. (2002). "Probabilistic fracture mechanics by Galerkin meshless methods – part I: rates of stress intensity factors." Computational Mechanics, 28(5), 351-364.

Rao, Q., Sun, Z., Stephansson, O., Li, C. and Stillborg, B. (2003). Shear fracture (Mode II) of brittle rock. Int. J. Rock Mech. Min. Sci.; 40: 355-375.

Rashid, Y. R. (1968). "Ultimate Srength Analysis of Pre-stressed Concrete Pressure Vessels." Nuclear Engineering and Design, 7, 334-344.

Ravi-Chandar, K. and W. G. Knauss (1984). "An experimental investigation into dynamic fracture: II. Microstructural aspects." International Journal of Fracture 26(1): 65-80.

Reches, Z. and Lockner, D.A. (1994). Nucleation and growth of faults in brittle rocks. J. Geophys. Res.; 99-B9: 18,159-18,173.

Remmers, J. J. C., R. de Borst, et al. (2008). "The simulation of dynamic crack propagation using the cohesive segments method." Journal of the Mechanics and Physics of Solids 56(1): 70-92.

Rethore, J., Gravouil, A., and Combescure, A. (2005a). "A combined space-time extended finite element method." International Journal for Numerical Methods in Engineering, 64(2), 260-284.

Rethore, J., Gravouil, A., and Combescure, A. (2005b). "An energy-conserving scheme for dynamic crack growth using the eXtended finite element method." Int. J Num. Meth. Eng., 63(5), 631-659.

Reuschle, T. (1998). "A network approach to fracture: The effect of heterogeneity and loading conditions." Pure and Applied Geophysics, 152(4), 641-665.

Ribeaucourt, R., Baietto-Dubourg, M. C., and Gravouil, A. (2007). "A new fatigue frictional contact crack propagation model with the coupled X-FEM/LATIN method." Computer Methods in Applied Mechanics and Engineering, 196(33-34), 3230-3247.

Rosch, F., Rudhart, C., Roth, J., Trebin, H. R., and Gumbsch, P. (2005). "Dynamic fracture of icosahedral model quasicrystals: A molecular dynamics study." Physical Review B, 72(1), 1-9.

Ruiz, G., M. Ortiz, et al. (2000). "Three-dimensional finite-element simulation of the dynamic Brazilian tests on concrete cylinders." Int. J for Num. Methods in Engineering 48(7): 963-994.

Saadaoui, M., P. Reynaud, et al. (2000). "Slow crack growth study of plaster using the double torsion method." Ceramics International 26(4): 435-439.

Saez, A., and Dominguez, J. (2001). "Dynamic crack problems in three-dimensional transversely isotropic solids." Engineering Analysis with Boundary Elements, 25(3), 203-210.

Sagong, M. and Bobet, A. (2002). Coalescence of multiple flaws in a rock-model material in uniaxial compression. Int. J. Rock Mech. Min. Sci.; 39: 229-241.

Sahraoui, S., A. El Mahi, et al. (2009). "Measurement of the dynamic fracture toughness with notched PMMA specimen under impact loading." Polymer Testing 28(7): 780–783.

Sall, J., L. Creighton, et al. (2007). JMP Start Statistics: A Guide to Statistics and Data Analysis Using JMP, Fourth Edition, SAS Press.

Sammis, C.G. and Ashby, M.F. (1986). The failure of brittle porous solids under compressive stress states. Acta metal.; 34: 511–526.

Sands, C. M., Henderson, R. J., and Chandler, H. W. (2007). "A three dimensional computational model of the mechanical response of a dual–phase ceramic." Comp. Mat. Sci., 39(4), 862–870.

Sansoz, F., and Molinari, J. F. (2007). "Size and microstructure effects on the mechanical behavior of FCC bicrystals by quasicontinuum method." Thin Solid Films, 515(6), 3158–3163.

Sato, M. (2006). "Finite–difference time–domain numerical analysis of elastic wave fields using both elastic and velocity potential variables." Japanese Journal of Applied Physics Part 1–Regular Papers Brief Communications & Review Papers, 45(5B), 4453–4461.

Schlangen, E., and van Mier, J. G. (1992a). "Experimental and numerical analysis of micro–mechanisms of fracture of cement–based composites." Cem. and Conc. Comp., 14(2), 105–118.

Schlangen, E., and van Mier, J. G. M. (1992b). "Simple Lattice Model for Numerical–Simulation of Fracture of Concrete Materials and Structures." Materials and Structures, 25(153), 534–542.

Schlangen, E., and Garboczi, E. J. (1997). "Fracture simulations of concrete using lattice models: computational aspects." Engineering Fracture Mechanics, 57(2–3), 319–332.

Schmidt, R.A. (1980). A microcrack model and its significance to hydraulic fracturing and fracture toughness testing. In: Proc. 21st US Symp. Rock Mech.: 581–590.

Schöpfer, M. P. J., S. Abe, et al. (2009). "The impact of porosity and crack density on the elasticity, strength and friction of cohesive granular materials: Insights from DEM modeling." International Journal of Rock Mechanics and Mining Sciences 46(2): 250–261.

Schroder, C. T., and Scott, W. R. (2000). "A finite–difference model to study the elastic–wave interactions with buried land mines." Transactions on Geosci. and Remote Sensing, 38, 1505–12.

Schubert, F., Peiffer, A., Kohler, B., and Sanderson, T. (1998). "The elastodynamic finite integration technique for waves in cylindrical geometries." J. of Acoustical Soc. of America, 104(5), 2604–14.

Sfantos, G. K., and Aliabadi, M. H. (2007). "Multi–scale boundary element modeling of material degradation and fracture." Comp. Methods in App. Mechanics and Engineering, 196(7), 1310–1329.

Sharon, E., S. P. Gross, et al. (1996). "Energy dissipation in dynamic fracture." Physical Review Letters 76(12): 2117–2120.

Shen, B. (1995). The mechanism of fracture coalescence in compression – experimental study and numerical simulation. Eng. Fract. Mech.; 51: 73–85.

Shen, Y. T., and Yi, X. M. (2000). "Wavelet–numerical method in crack analysis." Applied Mathematics and Mechanics–English Edition, 21(10), 1139–1144.

Shet, C. and N. Chandra (2002). "Analysis of Energy Balance When Using Cohesive Zone Models to Simulate Fracture Processes." J of Engineering Materials and Technology 124(4): 440–450.

Shetty, D. K., A. R. Rosenfield, et al. (1987). "Mixed–mode fracture in biaxial stress state: Application of the diametral–compression (Brazilian disk) test." Eng. Frac. Mech. 26(6): 825–840.

Shi, G. H. (1988). "Discontinuous deformation analysis, a new numerical model for the statics and dynamics of block systems." PhD thesis, Univ. of California, Berkeley, Berkeley, Calif.

Shi, G. H. (1991). "Manifold method of material analysis." Transactions of the 9th Army Conference on Applied Mathematics and Computing, U.S. Army Research Office, Minneapolis, MN, 57–76.

Shioya, T. and F. Zhou (1995). "Dynamic fracture toughness and crack propagation in brittle material." Constitutive Relation in High/Very High Strain Rates: 105–112.

Shioya, T., F. Zhou, and R. Ishida (1995). “Micro-cracking process in brittle crack propagation.” DYMAT J 2. 105–118.

Shiryaev, A. and Kotkis, A.M. (1982). Methods for determining fracture toughness of brittle porous materials. Industrial Laboratory; 48: 917–918.

Shyu K. (1993). "Nodal-based discontinuous deformation analysis," UC Berkeley. PhD thesis.

Simmons, G. and Richter, D. (1976). Microcracks in rocks. In: Stens, R.G.J. (ed.). The physics and chemistry of minerals and rocks. Wiley, New York.: 105–136.

Singh, R.N. and Sun, G.X. (1989). Relationships between fracture toughness, hardness indices and mechanical properties of rock. Mining Dep. Magazine, Univ. of Nottingham, England: 49–62.

Singh, I. V., and Jain, P. K. (2005a). "Parallel EFG algorithm for heat transfer problems." Advances in Engineering Software, 36(8), 554–560.

Singh, I. V., and Jain, P. K. (2005b). "Parallel meshless EFG solution for fluid flow problems." Numerical Heat Transfer Part B-Fundamentals, 48(1), 45–66.

Sneddon, I.N. (1945. The stress distribution in the neighbourhood of a crack in an elastic solid. Proc. Camb. Phil. Soc.; 42: 229–260.

Sofianos, A. I., and Kapenis, A. P. (1998). "Numerical evaluation of the response in bending of an underground hard rock Voussoir beam roof." International Journal of Rock Mechanics and Mining Sciences, 35(8), 1071–1086.

Song, J., and Kim, K. (1996). "Micromechanical modeling of the dynamic fracture process during rock blasting." Int. J of Rock Mech. and Min. Sci. and Geomech. Abstr., 33(4), 387–394.

Soparat, P., and Nanakorn, P. (2008). "Analysis of cohesive crack growth by the element-free Galerkin method." Journal of Mechanics, 24(1), 45–54.

Souley, M., Homand, F., and Thoraval, A. (1997). "The effect of joint constitutive laws on the modeling of an underground excavation and comparison with in situ measurements." International Journal of Rock Mechanics and Mining Sciences, 34(1), 97–115.

Spanos, P. D., and Rao, V. R. S. (2001). "Random field representation in a biorthogonal wavelet basis." Journal of Engineering Mechanics, 127(2), 194–205.

Stanchits, S., Backers, T., Stephansson, O. and Dresen, G. (2003). Comparison of Acoustic Emission Events and Micromechanics of granite under Mode I and Mode II loading. In: Makurat, A. and Curri, P. (eds.). EURO-Conference on Rock Physics and Geomechanics – Micromechanics, Flow and Chemical Reactions. 7–11 September 2003, Delft, Netherlands.

Starfield, A. M., and Cundall, P. A. (1988). "Towards a Methodology for Rock Mechanics Modeling." Int. J, Rock Mech. Min. Sci. and Geomech., 25(3), 99–106.

Stefan Loehnert, T. B. (2007). "A multi-scale projection method for macro / micro-crack simulations." 1466–1482.

Stéphane, B., Phu, V. N., Cyrille, D., Amor, G., and Hung, N.-D. (2007). "An extended finite element library." 703–732.

Stolarska, M., Chopp, D.L., Moes, N. and Belyschko, T. (2001). "Modeling crack growth by level sets in the extended finite element method." 943–960. Int J Numer Meth Eng. 51. 943–960.

Strouboulis, T., Zhang, L., and Babuska, I. (2007). "Assessment of the cost and accuracy of the generalized FEM." International Journal for Numerical Methods in Engineering, 69(2), 250–283.

Sukop, M. C. and D. T. Thorne (2006). Lattice Boltzmann modeling: an introduction for geoscientists and engineers, Birkhäuser.

Sukumar, N., Moran, B., and Belytschko, T. (1998). "The natural element method in solid mechanics." International Journal for Numerical Methods in Engineering, 43(5), 839–887.

Sukumar, N., Chopp, D. L., and Moran, B. (2003a). "Extended finite element method and fast marching method for three-dimensional fatigue crack propagation." Eng. Fract. Mech., 70, 29–48.

Sukumar, N., Srolovitz, D. J., Baker, T. J., and Preost, J. H. (2003b). "Brittle fracture in polycrystalline microstructures with the extended finite element method." 2015–2037.

Suri, M. (1996). "Analytical and computational assessment of locking in the hp finite element method." Computer Methods in Applied Mechanics and Engineering, 133(3–4), 347–371.

Swartz, S.E. and Taha, N.M. (1990). Mixed mode crack propagation and fracture in concrete. Eng. Fract. Mech.; 35: 137–144.

Szabo, B. A. (1990). "The P–P and H–P Versions of the Finite–Element Method in Solid Mechanics." Computer Methods in Applied Mechanics and Engineering, 80(1–3), 185–195.

Szymczak, P., and Ladd, A. J. C. (2004). "Microscopic simulations of fracture dissolution." Geophysical Research Letters, 31(23), 1–4.

Tadmor, E. B., Ortiz, M., and Phillips, R. (1996a). "Quasicontinuum analysis of defects in solids." Philosophical Magazine A: Physics of Condensed Matter, Structure, Defects and Mechanical Properties, 73(6), 1529–1563.

Tadmor, E. B., Phillips, R., and Ortiz, M. (1996b). "Mixed atomistic and continuum models of deformation in solids." Langmuir, 12(19), 4529–4532.

Takano, N., and Okuno, Y. (2004). "Three–scale finite element analysis of heterogeneous media by asymptotic homogenization and mesh superposition methods." International Journal of Solids and Structures, 41(15), 4121–4135.

Tan, Y., D. Yang, et al. (2008). "Study of polycrystalline Al2O3 machining cracks using discrete element method." International Journal of Machine Tools and Manufacture 48(9): 975–982.

Tan, Y., D. Yang, et al. (2009). "Discrete element method (DEM) modeling of fracture and damage in the machining process of polycrystalline SiC." Journal of the European Ceramic Society 29(6): 1029–1037.

Tang, C. A., and Kaiser, P. K. (1998). "Numerical Simulation of Cumulative Damage and Seismic Energy Release During Brittle Rock Failure–Part I:Fundamentals." Int. J. Rock Mech. and Min. Sci., 35(2), 113–121.

Tang, C.A., Lin, P., Wong, R.H.C. and Chau, K.T. (2001). Analysis of crack coalescence in rock–like materials containing three flaws – Part II: numerical approach. Int. J. Rock Mech. Min. Sci.; 38: 925–939.

Taylor, L. M. (1983). "BLOCKS, A block motion code for geomechanics studies." Sandia National Laboratories.

Tedesco, J. W., Ross, C. A., and Kuennen, S. T. (1993). "Experimental and numerical analysis of high strain rate splitting tensile tests." ACI Materials Journal, 90(2), 162–169.

Terada, K., Asal, M., and Yamagishi, M. (2003). "Finite cover method for linear and non–linear analyses of heterogeneous solids." International Journal for Numerical Methods in Engineering, 58(9), 1321–1346.

Terada, K., and Kurumatani, M. (2005). "An integrated procedure for three–dimensional structural analysis with the finite cover method." International Journal for Numerical Methods in Engineering, 63(15), 2102–2123.

Terada, K., Ishii, T., Kyoya, T., and Kishino, Y. (2007). "Finite cover method for progressive failure with cohesive zone fracture in heterogeneous solids and structures." Computational Mechanics, 39(2), 191–210.

Thallak, S., Holder, J. and Gray, K.E. (1993). The pressure dependence of apparent hydrofracture toughness. Int. J. Rock Mech. Min. Sci. and Geomech. Abstr.; 30: 831–835.

Thiercelin, M. and Roegiers, J.M. (1986). Fracture toughness with the modified ring test. In: Proc. 27th US Symp. Rock Mech., Alabama: 284–290.

Tomar, V., Zhai, J., and Zhou, M. (2004). "Bounds for element size in a variable stiffness cohesive finite element model." Int. Journal for Numerical Methods in Engineering, 61(11), 1894–1920.

Ulusay, R. and J. A. Hudson, Eds. (2007). The complete ISRM suggested methods for rock characterization, testing and monitoring: 1974–2006. Ankara, Turkey, Commission on Testing Methods, International Society of Rock Mechanics.

Vernerey, F. J., Liu, W. K., Moran, B., and Olson, G. (2008). "A micromorphic model for the multiple scale failure of heterogeneous materials." J of the Mech. and Phys. of Solids, 56, 1320–47.

Wang, Q.Z. and Xing, L. (1999). Determination of fracture toughness Kic by using the flattened Brazilian disk specimen for rocks. Eng. Fract. Mech.; 64: 193–201.

Wang, Y. C., Yin, X. C., Ke, F. J., Xia, M. F., and Peng, K. Y. (2000). "Numerical simulation of rock failure and earthquake process on mesoscopic scale." Pure and App. Geoph., 157(11–12), 1905–1928.

Wang, Q.Z., Jia, X.M., Kou, S.Q., Zhang, Z.X. and Lindqvist, P.–A. (2003). More accurate stress intensity factor derived by finite element analysis for the ISRM suggested rock fracture toughness specimen – CCNBD. Int. J. Rock Mech. Min. Sci.; 40: 233–241.

Wang, T. L., and Tang, X. M. (2003). "Finite–difference modeling of elastic wave propagation: A nonsplitting perfectly matched layer approach." Geophysics, 68(5), 1749–1755.

Wang, Q., W. Li, et al. (2006a). "A Method for Testing Dynamic Tensile Strength and Elastic Modulus of Rock Materials Using SHPB." Pure and Applied Geophysics 163(5): 1091–1100.

Wang, Y. C., Abe, S., Latham, S., and Mora, P. (2006b). "Implementation of particle–scale rotation in the 3–d Lattice Solid Model." Pure and Applied Geophysics, 163(9), 1769–1785.

Wanne, T. S. and R. P. Young (2008). "Bonded–particle modeling of thermally fractured granite." International Journal of Rock Mechanics and Mining Sciences 45(5): 789–799.

Watkins, J. (1983). Fracture toughness test for soil–cement samples in Mode II. Int. J. Fract.; 23: 135–138.

Watkins, J. and Liu, K.L.W. (1985). A finite element study of the short beam test specimen under mode II loading. Int. J. Cement Composites and Lightweight; 7: 39–47.

Wawersik, W. R. and C. Fairhurst (1970). "A study of brittle rock fracture in laboratory compression experiments." International Journal of Rock Mechanics and Mining Science & Geomechanics Abstracts 7(5): 561–564.

Wawrzynek, P. A., and Ingraffea, A. R. (1989). "An interactive approach to local remeshing around a propagating crack." Finite Elements in Analysis and Design, 5(1), 87–96.

Wearing, J. L., and Burstow, M. C. (1994). "Elastoplastic Analysis Using a Coupled Boundary–Element Finite–Element Technique." Engineering Analysis with Boundary Elements, 14(1), 39–49.

Weerheijm, J. and J. C. A. M. Van Doormaal (2007). "Tensile failure of concrete at high loading rates: New test data on strength and fracture energy from instrumented spalling tests." International Journal of Impact Engineering 34(3): 609–626.

Wei, L., and Hudson, J. A. (1988). "A hybrid discrete–continuum approach to model hydro–mechanical behavior of jointed rocks." Eng Geol, 49, 317–325.

Westergaard, H.M. (1939). Bearing Pressures and Cracks. J. Appl. Mech.; 24: 361–364.

Whittaker, B.N., Singh, R.N. and Sun, G. (1992). Rock Fracture Mechanics, Principles, Design and Applications. Developments in Geotechnical Engineering, 71. Elsevier, Amsterdam.

Whittles, D. N., S. Kingman, et al. (2006). "Laboratory and numerical investigation into the characteristics of rock fragmentation." Minerals Engineering 19(14): 1418–1429.

Williams, J. R., and Mustoe, G. G. W. (1987). "Modal methods for the analysis of discrete systems." Computers and Geotechnics, 4(1), 1–19.

Winter, R. (1983). Bruchmechanische Gesteinsuntersuchungen mit dem Bezug zu hydraulischen Frac–Versuchen in Tiefbohrungen. Dissertationsschrift der Ruhr–Universität Bochum.

Wolfel. (2007). "ATENA Non–linear Simulation of Concrete and Reinforced Concrete ". http://www.woelfel.de/wtpeng/atena/atena.hhtml

Wong, R.H.C., Chau, K.T., Tang, C.A. and Lin, P. (2001). Analysis of crack coalescence in rock–like materials containing three flaws – Part I: experimental approach. Int. J. Rock Mech. Min. Sci.; 38: 909–924.

Wu, C. D., and Lin, J. F. (2008). "Multi–scale particle dynamics in nanoimprint process." Applied Physics a–Materials Science & Processing, 91(2), 273–279.

Xia, K. (2006). "Scaling of fracture energies: The rationalization of different laboratory measurements." Geophys. Res. Lett. 33.

Xia, K., M. H. B. Nasseri, et al. (2008). "Effects of microstructures on dynamic compression of Barre granite." International Journal of Rock Mechanics and Mining Sciences 45(6): 879–887.

Xu, X. P. and A. Needleman (1994). "Numerical simulations of fast crack growth in brittle solids." Journal of the Mechanics and Physics of Solids 42(9): 1397–1434.

Xu, X. P. and A. Needleman (1995). "Numerical simulations of dynamic interfacial crack growth allowing for crack growth away from the bond line." Int. Journal of Fracture 74(3): 253–275.

Xu, X. P. and A. Needleman (1996). "Numerical simulations of dynamic crack growth along an interface." International Journal of Fracture 74(4): 289–324.

Xu, C., T. Siegmund, et al. (2003). "Rate–dependent crack growth in adhesives: I. Modeling approach." International Journal of Adhesion and Adhesives 23(1): 9–13.

Yacoub–Tokatly, Z., Barr, B. and Norris, P. (1989). Mode III fracture – a tentative test geometry. In: Shah, S.P., Swartz, S.E. and Barr, B. (eds.). Fracture of Concrete and Rock – recent developments. Elsevier, University Press, Cambridge, UK: 596–604.

Yang, Z. Y. and D. Y. Chiang (2000). "An experimental study on the progressive shear behavior of rock joints with tooth–shaped asperities." Int. J of Rock Mech. and Min. Sci. 37(8): 1247–1259.

Yang, Z. J., and Chen, J. (2005). "Finite element modeling of multiple cohesive discrete crack propagation in reinforced concrete beams." Engineering Fracture Mechanics, 72(14), 2280–2297.

Yee, K. (1966). "Numerical solution of initial boundary value problems involving Maxwell's equations in isotropic media." Antennas and Propagation, IEEE Transactions (1988), 14(3), 302–7.

Yokoyama, T. and K. Kishida (1989). "A novel impact three–point bend test method for determining dynamic fracture–initiation toughness." Experimental Mechanics 29(2): 188–194.

Yoon, J. (2007). "Application of experimental design and optimization to PFC model calibration in uniaxial compression simulation." Int. J of Rock Mechanics and Mining Sciences 44(6): 871–889.

Yu, L., Chouteau, M., Boerner, D. E., and Wang, J. (1998). "On the imaging of radio–frequency electromagnetic data for cross–borehole mineral exploration." Geoph. J Int., 135(2), 523–541.

Zang, A., Wagner, F.C., Stanchits, S., Janssen, C. and Dresen, G. (2000). Fracture process zone in granite. J. Geophys. Res.; 105–B10: 23654–23661.

Zaratian, B. (1997). Microsoft Visual C++ Owners Manual (Programming), Microsoft Press.

Zhai, J., V. Tomar, et al. (2004). "Micromechanical Simulation of Dynamic Fracture Using the Cohesive Finite Element Method." J of Engineering Materials and Technology 126(2): 179–191.

Zhai, Y., G. Ma, et al. (2008). "Dynamic failure analysis on granite under uniaxial impact compressive load." Frontiers of Architecture and Civil Engineering in China 2(3): 253–260.

Zhang, G.X., Sugiura, Y., Hasegawa, H. (1997). "Manifold method and its applications to engineering." Proceedings of The second International Conference on Analysis of Discontinuous Deformation, New York.

Zhang, X., and Lu, M. W. (1998). "Block–interfaces model for non–linear numerical simulations of rock structures." International Journal of Rock Mechanics and Mining Sciences, 35(7), 983–990.

Zhang Z. X., Kou S. Q., Yu J, Yu, Y, Jiang L. G., Lindqvist P. A. (1999). "Effects of loading rate on rock fracture". International Journal of Rock Mechanics and Mining Science 36(5): 597–611.

Zhang, X., Lu, M. W., and Wegner, J. L. (2000). "A 2-D meshless model for jointed rock structures." International Journal for Numerical Methods in Engineering, 47(10), 1649–1661.

Zhang, Z. X. (2002). "An empirical relation between mode I fracture toughness and the tensile strength of rock." International Journal of Rock Mechanics and Mining Sciences 39(3): 401–406.

Zhang, X. L., Jiao, Y. Y., Liu, Q. S., and Chen, W. Z. (2007). "Modeling of stability of a highway tunnel by using improved DDA method." Yantu Lixue/Rock and Soil Mechanics, 28(8), 1710–1714.

Zhao, J. (1997a). "Joint surface matching and shear strength part A: joint matching coefficient (JMC)." International Journal of Rock Mechanics and Mining Sciences 34(2): 173–178.

Zhao, J. (1997b). "Joint surface matching and shear strength part B: JRC-JMC shear strength criterion." International Journal of Rock Mechanics and Mining Sciences 34(2): 179–185.

Zhao, J., Zhou, Y. X., Hefny, A. M., Cai, J. G., Chen, S. G., Li, H. B., Liu, J. F., Jain, M., Foo, S. T., and Seah, C. C. (1999). "Rock dynamics research related to cavern development for ammunition storage." Tunnelling and Underground Space Technology, 14(4), 513–526.

Zhao, J. and H. B. Li (2000). "Experimental determination of dynamic tensile properties of a granite." International Journal of Rock Mechanics and Mining Sciences 37(5): 861–866.

Zhao, X. B., Zhao, J., Hefny, A. M., and Cai, J. G. (2006). "Normal transmission of S-wave across parallel fractures with Coulomb slip behavior." J. of Eng. Mechanics-Asce, 132(6), 641–650.

Zhao, G. F. (2010). “Development of micro-macro continuum-discontinuum coupled numerical method” PhD thesis, EPFL.

Zhao, G. F., T. Kazerani, et al. (accepted). "Numerical study of the semi-circular bend dynamic fracture toughness test by using discrete element models Engineering Fracture Mechanics" Engineering Fracture Mechanics

Zhou F. (1996). “Study on the macroscopic behavior and the microscopic process of dynamic crack propagation”. PhD dissertation, The University of Tokyo

Zhou, F. and J. F. Molinari (2004a). "Stochastic fracture of ceramics under dynamic tensile loading." International Journal of Solids and Structures 41(22-23): 6573–6596.

Zhou, F., and J. F. Molinari (2004b). "Dynamic crack propagation with cohesive elements: A methodology to address mesh dependency." International Journal for Numerical Methods in Engineering, 59(1), 1–24.

Zhou, F., J. F. Molinari, et al. (2005a). "A rate-dependent cohesive model for simulating dynamic crack propagation in brittle materials." Engineering Fracture Mechanics 72(9): 1383–1410.

Zhou, F.., Molinari, J. F., and Ramesh, K. T. (2005b). "A cohesive model based fragmentation analysis: effects of strain rate and initial defects distribution." International Journal of Solids and Structures, 42(18-19), 5181–5207.

Zhou, X. P. and H. Q. Yang (2007). "Micromechanical modeling of dynamic compressive responses of mesoscopic heterogenous brittle rock." Theoretical and App. Fracture Mechanics 48(1): 1–20.

Zhou Y. X. and J. Zhao (2011) “Advances in Rock Dynamics and Applications”. CRC Press, Oxford

Zhu, W. C., and Tang, C. A. (2006). "Numerical simulation of Brazilian disk rock failure under static and dynamic loading." Int. Journal of Rock Mechanics and Mining Sciences, 43(2), 236–252.

Zi, G., and Belytschko, T. (2003). "New crack-tip elements for XFEM and applications to cohesive cracks." International Journal for Numerical Methods in Engineering, 57(15), 2221–2240.

Zienkiewicz, O. B., B. Dullage,C. Stagg, K. (1970) "Analysis of nonlinear problems in rock mechanics with particular reference to jointed rock systems." Proceedings of the Second International Congress on Rock Mechanics, Belgrade.

Zienkiewicz, O.C., Hinton, E., Biccanic, N., Fejzo, P. (1980). "Computational Models for the Transient Dynamic Analysis of Concrete Dams." Dams and Earthquake, Inst. of Civil Engineers, London.

Tohid KAZERANI

Rock Mechanic Laboratory (LMR)
School of Architecture, Civil and Environmental Engineering (ENAC)
Swiss Federal Institute of Technology at Lausanne (EPFL)

Bâtiment GC D1–414, Station 18, 1015, Lausanne, Switzerland

Phone: +41 21 601 24 61, Email: tohid.kazerani@epfl.ch
url: http://people.epfl.ch/kazerani

Born August 1980. Male. Single

Research Interests

- Rock dynamics, rock fracture and fragmentation
- Discrete element method, computational micromechanics
- Nonlinear finite element method, plasticity, fluid–structure interaction

Education

- ScD of Civil Engineering in Rock Mechanics (2006–2011), Ecole Polytechnique Fédéral de Lausanne (EPFL), Lausanne, Switzerland. Supervisor: Prof. Jian Zhao
  Thesis title:
  Micromechanical study of rock fracture and fragmentation under dynamic loads using discrete element method

- MSc of Structural Engineering (2003–2005), Amirkabir University of Technology, Tehran, Iran. Supervisor: Prof. Vahid Lotfi
  Thesis title:
  Nonlinear dynamic analysis of concrete arch dams including dam–reservoir interaction

- BSc of Civil and Environmental Engineering, First Class Honors (1998–2003), Amirkabir University of Technology, Tehran, Iran

Teaching Experiences

- Discontinuum–based modeling for underground structures (2009, 2010), a short course instructed for the “master of advanced studies on tunneling”, EPFL
- Teaching assistantship for rock mechanics and course instructor in numerical modeling sessions (2007–2010), undergraduate level course, EPFL
- Supervising students for semester and diploma projects (2009, 2010), EPFL

Academic Experiences

- Reviewer of Tunneling and Underground Space Technology (international journal)
- Delegate of the “Swiss society for soil and rock mechanics” (SGBF) in the ISRM international symposium (11.2008), Tehran, Iran
- Member of organizing committee in the European rock mechanics symposium of the ISRM (06.2010), Lausanne, Switzerland
- Visiting Research Assistant (09.2010), Russian Academy of Science, St. Petersburg, Russia
- Presentation at two international conferences:
  The 5th Asian Rock Mechanics Symposium (ARMS 2008), Tehran, Iran
  The European rock mechanics symposium (EUROCK2010), Lausanne, Switzerland

Work Experience

- **Research assistance at the EPFL**
  Research assistance at the rock mechanics laboratory (LMR) (2007–2011), Static and dynamic analysis of rock material and rock joint, including laboratory work at the EPFL and mutual collaborations with the Nanyang Technological University of Singapore and the Tamkang University of Taiwan
- **Engineering experiences**
  Six month internship in the dam and hydropower plant design department (2005), Mahab-Ghodss consulting engineering company, Tehran, Iran
  Structural engineer and designer, Parseh construction company (2003-2004), Mashhad, Iran

Computer Skills

Programming:	C++, Maple
Modeling:	3DEC, UDEC, FLAC, PFC, ANSYS, SAP, ETABS, SAFE
Graphics:	AutoCAD, Photoshop, Illustrator
Office suite:	MS–Office, MS–Visio

Languages

Persian (native), English (fluent), French (intermediate)

Publications

- **Articles in peer–reviewed journals**

  Kazerani, T. and J. Zhao (2010). "Micromechanical parameters in bonded particle method for modeling of brittle material failure." *International Journal for Numerical and Analytical Methods in Geomechanics*: DOI: 10.1002/nag.884

  Kazerani, T., G. F. Zhao, and J. Zhao (2011). "Dynamic fracturing simulation of brittle material using the Distinct Lattice Spring Method with a full rate–dependent cohesive law." *Rock Mechanics and Rock Engineering* 43,6: 717–726

  Zhao, G. F., T. Kazerani, and J. Zhao (2011). "Numerical study of the semi–circular bend dynamic fracture toughness test by using discrete element models" *Engineering Fracture Mechanics* (in press)

- **Articles submitted in journals**

  Kazerani, T and J. Zhao, "Simulation of dynamic fracturing in brittle materials using discrete element method and a full rate–dependent logic for cohesive contact", *Engineering Fracture Mechanics*

  Kazerani, T., Z.Y. Yang, and J. Zhao "A discrete element model for prediction of shear strength and degradation of rock joint by using compressive and tensile test data", *International Journal of Rock Mechanics and Mining Sciences*

- **Articles in conferences**

  Kazerani, T and J. Zhao (2008). "A bonded particle modeling for rock material", Proceeding, 5th Asian Rock Mechanics Symposium (ARMS 2008), Tehran, Iran

  Kazerani, T., Z.Y. Yang, and J. Zhao (2010). "Investigation of failure mode and shear strength of rock joints using discrete element method", Proceeding, European Rock Mechanics Symposium (EUROCK 2010), Lausanne, Switzerland

- **Book chapters**

  Kazerani, T. (2011). "Discontinuum–based Numerical Modeling of Rock Dynamic Fracturing and Failure", chapter 13 at "Advances in Rock Dynamics and Applications", Taylor & Francis, ISBN: 9780415613514, 660 pages (in press)

References

- **Professor Jian Zhao**
  Laboratoire de mécanique des roches (LMR), Ecole Polytechnique Fédéral de Lausanne (EPFL)
  Address: LMR-ENAC-EPFL / Bâtiment GC C1-413
  Station 18, CH-1015, Lausanne, Switzerland
  Phone: +41 21 693 2321, 2372, Fax: +41 21 693 4153, Email: jian.zhao@epfl.ch
  url: http://people.epfl.ch/jian.zhao
- **Professor Vahid Lotfi**
  Department of civil engineering, Amirkabir University of Technology
  Address: No.717, Faculty of Civil Eng., 424, Hafez Ave., Tehran, Iran, 15914
  Phone: +98 21 6454 3017, Email: vahlotfi@aut.ac.ir
  url: http://civil.aut.ac.ir/vlotfi-english
- **Dr. Carlos Carranza-Torres, associate professor**
  Department of civil engineering, University of Minnesota, Duluth Campus
  Address: 260 Swenson Civil Engineering / 1405 University Drive
  Duluth, MN 55812, Minnesota, USA
  Phone: +1 218 726 6460, Email: carranza@d.umn.edu
  url: http://www.d.umn.edu/civileng/